THE UNIVERSITY
of EDINBURGH

A study of the molecular regulation of trypanosomatid phosphofructokinases as drug targets.

James R. H. Kinkead

Thesis presented for the Degree of Doctor of Philosophy

The University of Edinburgh

January 2018

Abstract

The trypanosomatid parasites T. brucei, T. cruzi and Leishmania spp. are responsible for the 'neglected diseases' Human African Trypanosomiasis, Chagas disease and Leishmaniasis respectively. In their human infective form in the bloodstream all three trypanosomatid parasites rely heavily on glycolysis for ATP production. Phosphofructokinase (PFK) catalyses the third step of the glycolytic pathway in all organisms using aerobic respiration. It facilitates the phospho transfer from ATP to fructose 6-phosphate (F6P) to make the products fructose 1,6-bisphosphate (F16BP) and ADP. RNAi knockout of *T. brucei* PFK has shown the enzyme is essential for survival of the bloodstream form parasites. Trypanosomatid PFKs have a unique set of structural and regulatory differences compared to the mammalian host enzyme. These differences, coupled with the availability of trypanosomatid PFK crystal structures present an opportunity for the structure-based design of specific inhibitors against the enzyme.

Here we present an enzymatic characterisation of recombinant PFKs from *T. brucei*, *T. cruzi* and *Leishmania infantum* trypanosomatids, their regulation by the allosteric activator AMP, and their inhibition by drug-like inhibitor compounds. Inhibitor compounds ('CTCB compounds') were designed against T. brucei PFK with the aim of developing novel treatments against Human African Trypanosomiasis (HAT). We describe the testing, ranking and biophysical characterisation of these compounds as part of a Wellcome Trust Seeding Drug Discovery program. We found that CTCB inhibitor compounds bound to an allosteric pocket unique to trypanosomatid PFKs. We show that the compounds are specific; neither competing with the natural substrates ATP or F6P nor inhibiting the human PFK enzyme.

We describe the development and testing of highly potent and specific low molecular weight PFK inhibitors that translate to both killing of cultured *T. b. brucei* parasites and a cure of stage I HAT in mice models. We describe the tight, 1:1 binding of these compounds with trypanosomatid PFKs, and the thermodynamic characteristics of binding through various biophysical assays. We also show the unprecedented characterisation of the reverse PFK reaction by trypanosomatid and human forms of the enzymes. We found that PFK can also carry out the reverse enzymatic reaction, under physiologically relevant concentrations of ADP and F16BP to produce F6P and ATP. We show that the reverse reaction is also subject to allosteric regulation by AMP, and can be inhibited by the CTCB compounds with a similar potency to the forward reaction. Finally, we describe the mechanism of allosteric activation by AMP and inhibition by the drug-like compounds against trypanosomatid PFKs.

Lay summary

Protozoan parasites are microscopic organisms that invade larger organisms (known as the host) where they survive and reproduce at the expense of the host. The protozoan parasite species '*Trypanosoma brucei', 'Trypanosoma cruzi'* and '*Leishmania infantum'* are responsible for the human diseases 'African Sleeping Sickness', 'Chagas disease' and 'Leishmaniasis' respectively. These diseases are caused by the parasites gaining entry to the human bloodstream through the bite of an insect 'vector' carrying the parasite. African Sleeping Sickness has two disease stages; In the first the parasites enter the human bloodstream and replicate. After some time, the parasites move from the bloodstream into the tissue of the brain and spinal cord – the second stage of the disease. The parasites can survive and reproduce both in the insect 'vector' and in the human 'host' organisms. We know that for the '*Trypanosoma brucei'* parasites to survive in the human bloodstream, it relies on a pathway called glycolysis. This is an important pathway involving the breakdown of sugar (glucose) to produce energy in many organisms. Sugar is plentiful in the human bloodstream and this is the parasites main source of energy while it is in the bloodstream. Specifically, a protein known as phosphofructokinase (PFK) is an essential enzyme in the glycolysis pathway. Enzymes are proteins that speed up a chemical reaction. The chemical reaction involves starting molecules known as 'substrates'. Enzymes speed up reactions by binding these substrate molecules and facilitating their change to the end products of the reaction before releasing them. PFK carries out an important step in the glycolysis pathway, without this enzyme, the Trypanosoma brucei parasites cannot survive in the human bloodstream.

Because it is essential for survival of the parasites in the human bloodstream, this PFK enzyme was chosen as a target to design drugs to treat African Sleeping Sickness. This requires drug compounds to be designed, produced and tested for their ability to inhibit the activity of the Trypanosoma brucei PFK enzyme and kill the parasite. Humans also possess this PFK enzyme and so it is important that the drugs only inhibit the activity of the parasitic PFK enzyme. Importantly, the parasite PFK enzyme has a unique structure compared to the human enzyme form. This offers an opportunity to design drug molecules with specific properties that mean they only bind and inhibit the parasitic PFK enzyme and not the human form.

The primary aim of the work outlined in this thesis is to give a description of the effect of these inhibitor compounds on the activity of the PFK enzyme. This involved ranking the compounds according to how well they inhibited PFK activity, and providing a description of how the inhibitor compounds bind to the PFK protein. The aim of this was to provide information to

improve the design of the inhibitors to fit and inhibit the PFK enzyme better. To achieve this aim the Trypanosoma brucei PFK protein was produced by and harvested from large amounts of bacteria grown in the lab. The inhibitor compounds were then tested against the pure PFK protein in a number of experiments or 'assays' which measured the effect of the compounds on the PFK activity. We show that drug compounds designed against the parasitic PFK enzymes are effective inhibitors of the enzyme activity, and also lead to the death of living parasites in the laboratory. We also describe how and where the inhibitor compounds bind the PFK enzyme, and show that the compounds bind the parasitic PFK enzyme specifically over the human form.

The secondary aim of this thesis was to draw comparisons between the PFK enzymes from the Trypanosoma brucei, Trypanosoma cruzi and Leishmania infantum species in terms of their activity. The aim of this work was to further our understanding of the reliance that each parasite species places on the PFK enzyme for survival. We show how PFKs from these three parasitic species differ from each other in terms of the speed at which the enzyme carries out its role in glycolysis.

Biological enzymes are often regulated by certain chemicals found within the cells of organisms. These chemical regulators can speed up or slow down the activity of the enzyme, and in the case of PFK, are important in controlling the overall speed of the pathway in which they are part of. We describe how the PFK enzymes are regulated by a chemical activator of the enzyme, and compare the effect of this enzyme regulator across the PFK enzymes from the three parasitic species. Furthermore, we show how the parasitic PFK enzyme can run in reverse – carrying out the opposite chemical reaction under conditions that may occur in the parasite organism. This has not been reported before, and the PFK enzyme is traditionally not thought to be able to run in the reverse direction.

Finally, we link together all of our observations regarding the activity and inhibition of the parasitic PFK enzymes to develop a model for how the enzyme works and how it is regulated on a molecular level. We show that the inhibitor compounds designed against the Trypanosoma brucei parasite PFK enzyme are effective at killing parasites grown in the lab, and that the compounds lead to a cure of the first stage of the African Sleeping Sickness disease in the bloodstream of mice.

Declaration.

I declare that the research presented in this thesis and the thesis itself is solely my own work, completed at the University of Edinburgh, except where otherwise stated. This thesis has not been submitted, in whole or in part, for any other degree.

James Kinkead.

Acknowledgements.

I would firstly like to thank my primary supervisor Prof. Malcolm Walkinshaw for providing me with the opportunity to carry out this PhD project. He has provided support from day one and has on many occasions encouraged a belief in myself inside and outside the laboratory. It has been a pleasure and a privilege to work for the Walkinshaw lab and I would also like to thank Dr Iain McNae and Dr Jaqueline Dornan for their support, knowledge and guidance.

I am grateful for the Wellcome trust who funded the Seeding Drug Discovery project in which I was employed as a research technician, and from which the majority of my thesis work stems from.

I would like to especially thank Prof. Paul Michaels whose incredible encyclopaedic knowledge of everything Trypanosomes has been a tremendous resource throughout my PhD. I would also like to thank members of the Edinburgh Protein Production Facility – Dr Martin Wear, Dr Liz Blackburn and Dr Matthew Nowicki, without whom many of the biophysical techniques would not have run so smoothly.

I have worked alongside some extremely encouraging people in the Swann Building 3rd floor labs. A special thanks to Dr Willie Yen, Dr Simon Varzandeh and Dr Valdeko Kruusvee for sharing their knowledge and advice throughout. Thanks to Dr Peter Fernandes especially whom I collaborated with on many experiments and who has also provided excellent mentorship outside the laboratory.

There are not enough moments in life to give thanks to friends and family who provide an undying source of support and relief through trying times. I would like to take the opportunity to thank my mother and father for working so hard to provide for my sisters and I, and for supporting us in everything we do. To Marcus Price who has helped me through many difficult times simply by being himself, and to Daniel, Cammy, John, Lewis, Heather and Maddy who have all provided moments to savour in the past four years and more. A special thank you also to Dr Tanmay Gupta who provided plentiful distraction outside the lab. Tanmay, the world is yours.

Finally, I dedicate every word of this thesis to Kate. Her selflessness, support and patience has been invaluable in seeing me through this period and she makes every moment in life worthwhile.

Beyond the walls of intelligence, life is defined.

List of abbreviations.

1,3 BPGA	1,3-bisphosphoglycerate
2xTY	2x tryptone yeast extract broth media
6PGA	6-Phosphogluconate
6PGL	6-Phosphogluconolactone
AAT	Animal African Trypanosomiasis
ADP	Adenosine 5'-diphosphate
AMP	Adenosine 5'-monophosphate
AS	Allosteric Sigmoidal (plot)
ATP	Adenosine 5'-triphosphate
BSA	Bovine Serum Albumin
BSF	Bloodstream form
CL	Cutaneous Leishmaniasis
CNS	Central nervous system
CTCB	Center for Translational and Chemical Biology
CV	Column Volumes
DHAP	Dihydroxyacetone phosphate
DLS	Dynamic Light Scattering
DMSO	Dimethyl suphoxide
DNDi	Drugs for Neglected Diseases initiative
DTT	Dithiothreitol
EC_{50}	Half maximal killing (efficacy) concentration
EDC	1-ethyl-3-(3-dimethylaminopropyl) carbodimide
EDTA	Ethylenediaminetetraacetic acid
Ex/Em	Excitation/Emmission (wavelength)
F16BP	Fructose 1,6-bisphosphate
F26BP	Fructose 2,6-bisphosphate
F6P	Fructose 6-phosphate
FBP	Fructose 1,6-bisphosphate
FBPase	Fructose 1-6-bisphosphatase
FCC	Flux control coefficient
FCS	Fetal Calf Serum
FF	Fast flow (IMAC column)
FT	Flowthrough
G3P	Glyceraldehyde 3-phosphate
G3PDH	Glycerol 3-phosphate dehydrogenase
G6P	Glucose 6-phosphate
G6PDH	Glucose 6-phosphate dehydrogenase
GDP	Guanosine 5'-diphosphate
GK	Glycerokinase
GMP	Guanosine 5'-monophosphate
GOL	Glycerol
GTP	Guanosine 5'-triphosphate

h	Hill coefficient
HSA	Human Serum Albumin
HAT	Human African Trypanosomiasis
HBS	HEPES buffered saline
HEPES	4-(2-hydroxyethyl)-1-piperazineethanesulfonic acid
His_6	Hexa-histidine (tag)
HK	Hexokinase
HTS	High Throughput Screening
IC_{50}	Half maximal inhibitory concentration
IgG	Immunoglobumlin G
IMAC	Immobilised metal ion affinity chromatography
IPTG	Isopropyl β-D-1-thiogalactopyranoside
k_a	Association rate constant
K_{cat}	Enzyme turnover number
k_d	Dissociation rate constant
K_d	Equilibrium constant
kDa	Kilodalton
K_{half}	Micahelis constant (allosteric sigmoidal plots)
K_m	Micahelis constant
KNF	Koshland-Nemethy-Filmer (cooperativity model)
k_{off}	Dissociation rate constant (SPR)
k_{on}	Association rate constant (SPR)
Kpsi	Kilo-pounds per square inch
LB	Lysogeny broth
*Li*PFK	*Leishmania infantum* phosphofructokinase
MALDI-TOF	Matrix-Assisted Lazer Desorption/Ionization Time Of Flight
mAu	UV Milli-absorbance units
Mg^{2+}	Magnesium
ML	Muccocutaneous Leishmaniasis
MM	Michaelis-Menten
MOA	Mode of action
MS	Mass Spectrometry
MWC	Monod-Wyman-Changeux (cooperativity model)
MWCO	Molecular weight cut off
NADH	β-nicotinamide adenine dinucleotide
ND	Not determined
NECT	Nifurtimox-Eflornithine combination therapy
NHS	N-hydroxysuccinimide
NIH	National Institute of Health
NTA	Nitrilotriacetic acid
OD	Optical density
P20	TWEEN 20 surfactant

PCR	Polymerase chain reaction
PDB	Protein Data Bank
PEG	Polyethylene glycol
PEP	Phosphoenolpyruvate
PFK	Phosphofructokinase
PFK-1	6-phosphofructo-1-kinase
PFK-L	Phosphofructokinase liver isoform
PFK-M	Phosphofructokinase muscle isoform
PFK-P	Phosphofructokinase platelet isoform
PGAM	Phosphoglycerate mutase
PGI	Phosphoglucoisomerase
PGK	Phosphoglycerate kinase
pI	Isoelectric point
Pi	Free phosphate
Ppi	Pyrophosphate
PPP	Pentose phosphate pathway
PYK	Pyruvate kinase
RMSD	Root Mean Square Deviation
RNAi	RNA interference
RPM	Revolutions per minute
RT	Room Temperature
RU	Resonance Units
SA	Specific activity
SDD	Seeding Drug Discovery
SDS	Sodium dodecyl sulphate
SDS- PAGE	SDS polyacrylamide gel electrophoresis
SEC	Size exclusion chromatography
SOC	Super optimal broth with catabolic repressor
*Tb*PFK	*Trypanosoma brucei* phosphofructokinase
TCA	Tricarboxylic acid
*Tc*PFK	*Trypanosoma cruzi* phosphofructokinase
TDA	Thermal denaturation assay
TEA	Triethanolamine
TEV	Tobacco etch virus
TIM	Triose phosphate isomerase
Tm	Transition melting temperature
UoE	University of Edinburgh
UV	Ultraviolet
VL	Visceral Leishmaniasis
V_{max}	Maximal velocity
WC	Whole cell
WHO	World Health Organisation

Contents

Chapter 1: Introduction - phosphofructokinase and Human African Trypanosomiasis.

Chapter 1: Introduction - phosphofructokinase and Human African Trypanosomiasis.

1.1. Introduction.

The main aim of the work outlined in this thesis is to give a description of the molecular regulation of the glycolytic enzyme phosphofructokinase (PFK) in trypanosomatids. This overriding aim has two parts; firstly to investigate and describe the 'physiological' molecular regulation of phosphofructokinase by its substrates, known and potential effectors and metabolic intermediates. The purpose of this study was to provide an understanding of the underlying activity and regulation of the enzyme, as a target for developing drugs against trypanosomatids. This leads to the second focus of this project; to provide a description of the molecular inhibition of *Trypanosoma brucei* PFK by small molecules designed against the enzyme. This chapter introduces the diseases caused by trypanosomatids, explains the reasoning for selection of phosphofructokinase as a target for anti-trypanosomatid drug development and outlines the role of the enzyme within the parasites.

1.2. Human African Trypanosomiasis.

The work described in this thesis was carried out as part of a Wellcome Trust funded 'Seeding Drug Discovery' (SDD) project awarded to the Walkinshaw Group at the University of Edinburgh. This study aimed to identify and design small molecule inhibitors against the glycolytic enzyme phosphofructokinase in *T. brucei* parasites. The overall outcome was to develop novel drug candidates against Human African Trypanosomiasis (HAT). The work described in this thesis was carried out by the author in a research technician role working on the SDD project. Compound synthesis was carried out by Selcia Ltd, *in vitro* parasite culture work by Dr L. Yen and *in vivo* mouse work by Dr D. Malik at the University of Edinburgh.

The parasitic kinetoplastid *Trypanosoma brucei* is the cause of Human African Trypanosomiasis (HAT) or 'sleeping sickness' – a blood-borne disease spread by the bite of tsetse flies (*Glossina* spp.) carrying the parasite (Brun et al., 2010). *T. brucei* has 3 morphologically similar pathogenic subspecies; *T. b. gambiens* which causes HAT endemic to west Africa, *T. b. rhodesiense* causing an acute form of HAT in south and east Africa and *T. b. brucei* which is pathogenic to wild game and domestic mammals (African Animal Trypanosomiasis –AAT or 'Nagana disease') but not man (Brun et al., 2010; Stich, Abel, & Krishna, 2002). **Figure 1.1** shows the prevalence of the human

pathogenic foci across Africa. HAT is fatal if left untreated, and is a major cause of underdevelopment in countries where the disease is endemic (Brun et al., 2010; Stich et al., 2002). Poor, rural areas are worst affected due to increased likelihood of transmission from hunting, fishing and farming activities, where the natural habitat of the tsetse fly vector is coupled with pools of asymptomatically infected animals with *T. b. gambiense* and *T. b. rhodesiense* (Brun et al., 2010).

Modern vector control and population surveillance initiatives have reduced cases of the *T. b. gambiense* disease by 69% and *T. b. rhodesiense* reported cases by 4% between 1997 – 2006 in the 24 countries where the diseases are endemic (Barrett, 2006; Brun et al., 2010). Underreporting masks the true number of cases; a record low of 2,800 cases were reported in 2014 however the actual number of people infected is estimated at 20,000, with 65 million people at risk (http://www.who.int/).

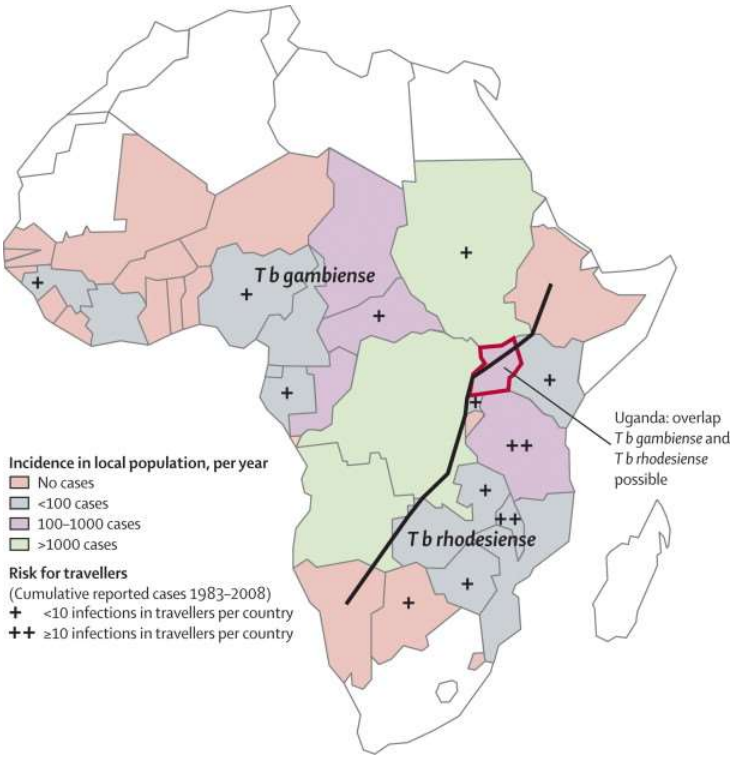

Figure 1.1: Distribution map of human pathogenic Trypanosomiasis cases across Africa.

Black line separates areas where the *T. b. gambiense* and *T. b. rhodesiense* foci prevail. Adapted from Brun et. al, 2010.

1.2.1 Trypanosomatids and 'neglected diseases'.

The trypanosomatid parasites *T. brucei*, *T. cruzi* and *Leishmania* spp. are the causative agents of HAT, American trypanosomiasis (Chagas disease) and Leishmaniosis diseases in humans worldwide. A high proportion of affected individuals coupled with a lack of sufficient drug development to treat HAT, Chagas Disease and Leishmaniasis has led the World Health Organisation to describe these as 'neglected diseases'(Brun et al., 2010). While HAT and Chagas are 2-stage diseases, three forms of Leishmaniasis occur; Visceral Leishmaniasis (VL) or 'kala-azar', cutaneous Leishmaniasis (CL) and mucocutaneous Leishmaniasis (ML). **Table 1.1** provides a summary of these three neglected diseases.

	African Trypanosomiasis[1]	**Chagas Disease[2]**	**Leishmaniosis[3]**
Parasite(s) responsible	*T. b. gambiense* (HAT) *T. b. rhodesiense* (acute HAT) *T. vivax/congolense* (African Animal Trypanosomiasis – 'AAT') *T. b brucei* (AAT- livestock) *T. evansi* (AAT – livestock) *T. equiperdum* (AAT – Horses)	*T. cruzi.* Kala-azar disease results from other zoonosis animal reservoirs of disease.	>20 *Leishmania* spp. VL: *L. donovani, L. infantum.* CL: *L. tropica, L. peruviana, L. mexicana, L. infantum.* *ML: L. amazonensis, L. braziliensis, L. panamensis.* Zoonosis: *L. major*.
Disease vector	Tsetse fly (Glossina spp.) bite – blood meal. Animal reservoirs (*T. b. rhodesiense*) – wild and domestic.	Triatomine 'kissing bug' – various species. Bite and contact with faeces. Animal reservoirs – wild and domestic.	Female phlebotomine Sandfly bite – blood meal. Reservoirs in 70 animal species.
Prevalence	Estimated 20,000 new cases annually. 65 million at risk.	6 – 7 million infected currently.	0.7 – 1 million new cases annually. 20-30,000 deaths annually.
Areas affected	Sub-Saharan Africa (*T. b. rhodesiense/gambiense/brucei*). South America and Asia (*T. b. evansi, T. vivax*) [4].	Initially endemic to S. America. 21 Latin American countries. New cases recently in USA, Canada and Europe due to migration of people – vector is absent outside S. America.	VL: 98 countries. Most prevalent in Brazil, Ethiopia, Kenya, Somalia, Sudan, Bangladesh and India. CL: Americas, Mediterranean, Middle East and Central Asia. ML: Bolivia, Brazil, Peru and Ethiopia.

Disease stages	Stage I (1.5 yrs.): Proliferation of parasites in bloodstream and lymphatic system. Generalised fever, headaches and lymphadenopathy. Stage II (1.5 yrs.): Parasites invade CNS. Disruption of sleep cycle, neuropsychiatric disorders and death if untreated.	Acute stage (2 months): parasites proliferate in bloodstream. Unspecific symptoms, characteristic skin lesions and eye swelling. Chronic stage (1+ yrs.): Parasites invade heart and muscles of digestive system. Cardiac and digestive disorders. Sudden death in later years due to heart and CNS failure.	VL: Fever, weight loss, enlargement of spleen and anaemia. CL: Skin lesions on exposed parts of body. Lifelong scars and disability. ML: Destruction of mucous membranes (Nose, mouth and throat).
Primary treatment	Stage I: Pentamidine, Suramin. Stage II: Eflornithine, Melarsoprol, Nifurtimox.	Benzimidazole, Nifurtimox. Most affective if treated in acute stage.	Dependant on disease type and location. VL: Paromomycin, liposomal amphotericin B, pentavalent antrimonials. CL: Paromomycin, Fluconazole and Pentamidine.

Table 1.1: Fact file on HAT, Chagas and Leishmaniosis neglected diseases.

1. WHO factsheet 259 Jan 2017. 2. WHO factsheet 340 Jan. 2017. 3 WHO factsheet 375 Jan 2017. (http://www.who.int/) 4. (Morrison, Vezza, Rowan, & Hope, 2016a).

1.2.2 AAT – Animal African Trypanosomiasis.

Animal African Trypanosomiasis (AAT) or 'Nagana disease' is caused by multiple species and strains of trypanosomes but two species predominate ; *T. congolense* and *T. vivax* in sub-Saharan Africa and *T. vivax* in south America are responsible for the most significant infections. *T. b. evansi* and *T. b. brucei* are also pathogenic to animals. Both *T. vivax* and *T. b. evansi* have developed mechanical transmission allowing them to spread out with the African tsetse fly transmission areas to South America and Asia respectively (Morrison, Vezza, Rowan, & Hope, 2016b). The disease affects wild game animals as well as domestic cattle and pig livestock and is a major contributing factor to economic underdevelopment in rural areas (Brun et al., 2010; Stich et al., 2002).

The majority of knowledge on African Trypanosomiasis is based on research into the *T. brucei* species and mice models of the disease. While the *T. b. brucei* subspecies is pathogenic in animals, the case for more focus on *T. congolense* and *T. vivax* studies has been made (Morrison et al., 2016b). Despite the wealth of knowledge they have provided in the study of HAT,

traditional mice models of *T. brucei* infection are becoming insufficient in making advances against AAT. Differences in the host (bovine) immune response, the regulation of parasite antigenic variation (VSGs) and differences in *T. congolense* and *T. vivax* drug uptake and resistance require a more focused approach on these species over *T. brucei* to advance progress on vaccines or drugs against AAT.

1.2.3 Trypanosomatidae phylogenetic tree.

Figure 1.2 shows a phylogenetic tree of the major disease causing species of Trypanosomatidae responsible for African trypanosomiasis, Chagas disease and Leishmaniasis. The three *T. brucei* subspecies (*T. b. brucei, T. b. rhodesiense* and *T. b. gambiense*) are not monophyletic; while *T. b. brucei* and *T. b. rhodesiense* differ only by a single gene that confers resistance to a lytic factor in human blood serum (*T. b. rhodesiense*), *T. gambiense* has evolved on a separate phylogenetic branch (Richardson et al., 2017).

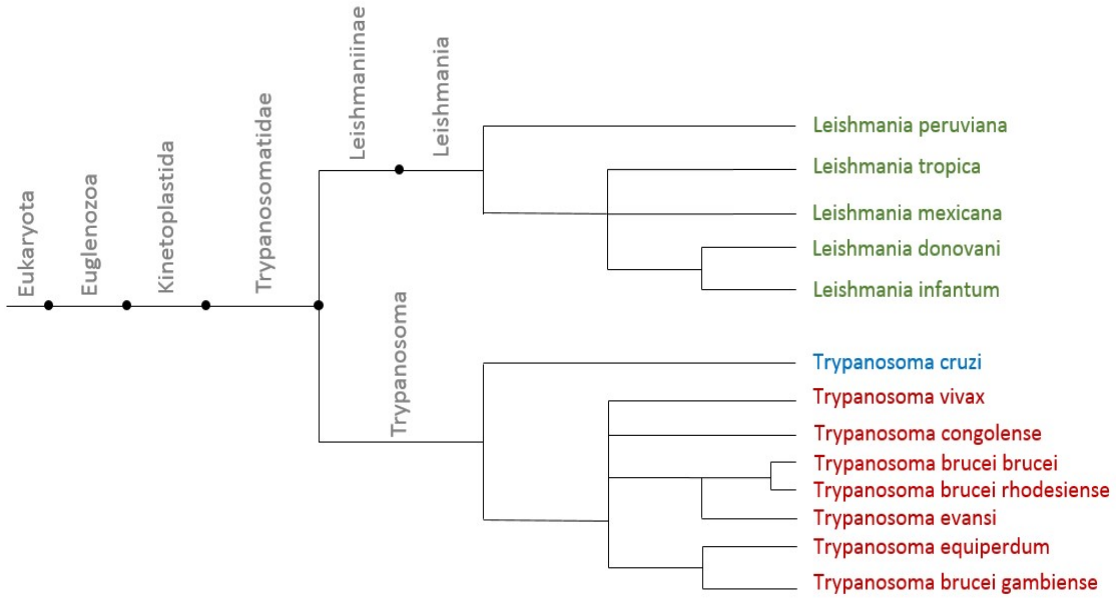

Figure 1.2: Phylogenetic tree of main pathogenic members of the Trypanosomatidae group.

Main causative species of African trypanosomiasis (red), Chagas disease (blue) and Leishmaniasis (green) are included.

1.2.4 Epidemiology of T. brucei infection in HAT.

Trypanosomes are protists belonging to the family Trypanosomatidae. They are unicellular organisms ~15 – 30 µm in length. They contain a nucleus, a single mitochondrion that spans from the posterior to anterior end of the parasite and a concentrated circular mitochondrial DNA density inside the kinetoplast. The parasite moves via a single flagellum – a semi-rigid structure made up of a doublet of microtubules ('axoneme') and a paraflagellar rod. The flagellum is connected to the mitochondrial genome via a basal body attached to the kinetoplast (**figure 1.3**) (Matthews, 2005). The parasite contains membrane-bounded organelles called glycosomes in which the first seven steps of glycolysis occur.

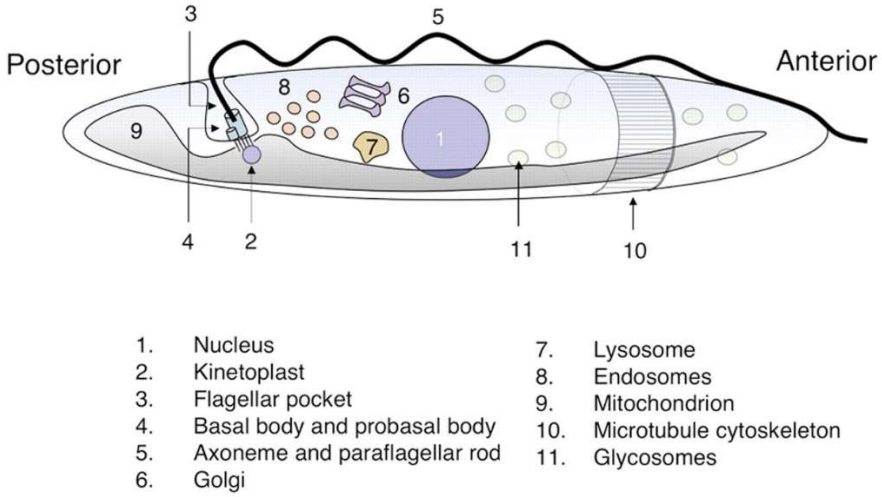

Figure 1.3: Structural architecture of typical Trypanosomatidae parasite.

Image adapted from Matthews, 2005.

The *T. brucei* parasite uses both male and female tsetse flies as a transmission vector. The fly must take a blood meal from an infected animal. The parasite undergoes a number of complex life-cycle changes in both the insect and mammalian host stages, as summarised in **figure 1.4**.

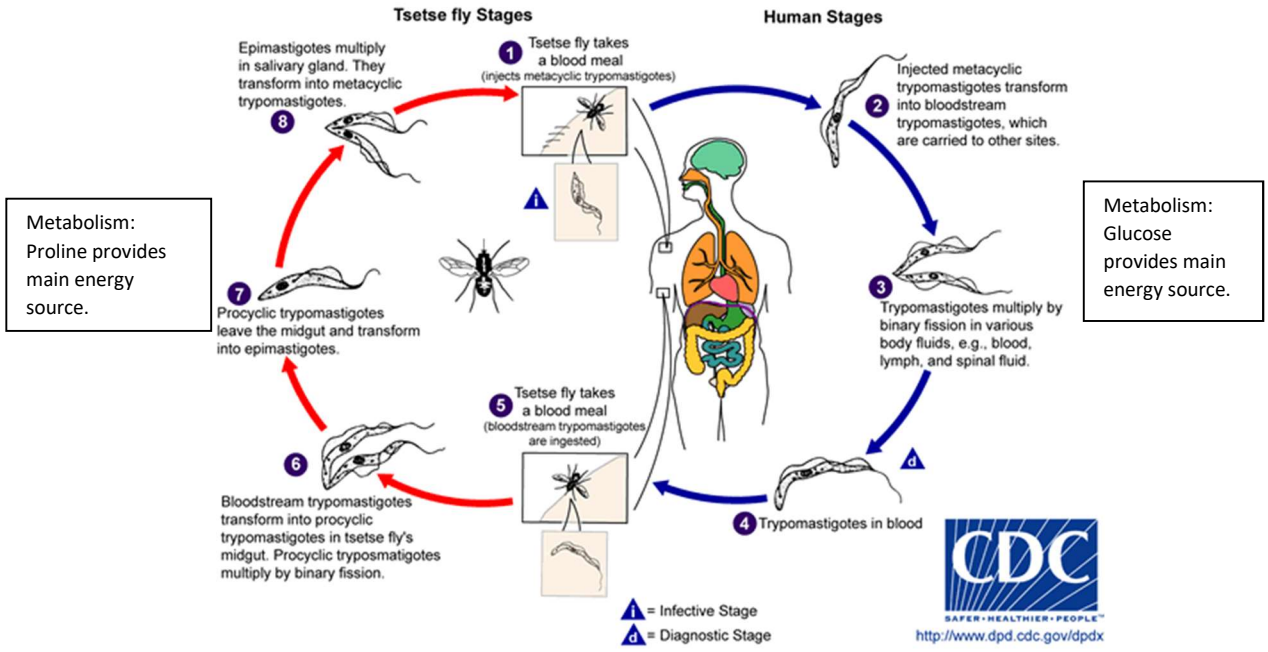

Figure 1.4: Insect vector and human host life cycle stages for Trypanosoma brucei.

Adapted from (http://www.cdc.gov/parasites/sleepingsickness/biology.html)

In the tsetse fly gut the formerly bloodstream form (BSF) trypomastigotes differentiate for 3-5 weeks before entering the salivary gland where they develop into an infective 'metacyclic' form. Only 0.1% of tsetse fly vectors will develop a fully mature infective parasite for transmission. It is the metacyclic form of the parasite that is transferred when the tsetse fly takes a blood meal from mammals. In the bloodstream, the *T. brucei* trypanosomes must overcome immune responses and prevent overconsumption of host resources from over proliferation; over proliferation will lead to host death and lessens transmission potential.

The first hurdle (immune system detection) is overcome through antigenic variation – trypanosomes constantly vary the expression of variant surface glycoproteins (VSG) to prevent immune system detection (Vickerman, 1978)(Taylor & Rudenko, 2006). Over proliferation is avoided by a density-dependant developmental switch from a proliferative 'slender' form to a non-proliferative (G0/G1 arrested) 'stumpy' form (Silvester, McWilliam, & Matthews, 2017). Stumpy *T. brucei* parasites halt antigenic variation, but instead have a greater rate of endocytosis to clear potential IgG-VSG immune interactions (Mclintock, Turner, & Vickerman, 1993).

Two differentiated disease stages are a product of the trypanosomatid life cycle while in the human host:

Stage I. The first stage ('haemolymphatic stage') of the disease is caused by parasites inhabiting the blood and lymphatic systems. The parasites avoid lytic factors and immune detection through variable expression of cell-surface glycoproteins, which are encoded by >2000 genes in *T. b. brucei* (Taylor & Rudenko, 2006). Human blood serum contains a lytic factor against trypanosomes. The non-pathogenic *T. brucei* subspecies *T. b. brucei* differs with the human pathogenic *T. b. rhodesiense* only by a single gene that encodes resistance to this lytic factor. Many of the glycoproteins are recognised by the immune system but those that are not allow the parasite to proliferate within the host. This stage is characterised by generalised fever, headaches and lymphenopathy (swollen lymph nodes) and can last up to 1 ½ years in the case of *T. b. gambiense*.

Stage II. The second stage ('meningoencephalitic stage') disease is caused by invasion of the central nervous system (CNS) by the parasite. The parasite remains extracellular and crosses the blood-brain barrier through gaps in intercellular junctions into the brain parenchyma (Masocha, Rottenberg, & Kristensson, 2007). Clinical characteristics include disruption of the sleep cycle through circadian rhythm complications, neuropsychiatric disorders and eventually death if left untreated. This stage can last up to 1 ½ years in the case of *T. b. gambiense* infections. *T. b. rhodesiense* infections cause an acute form of the disease in which the death of the host can occur within weeks or months from initial infection.

1.2.5 Diagnosis of HAT.

Initial diagnosis of first stage HAT is based on identification of the parasite in the blood in the form of finger pricks and laboratory testing including immunological 'CATT card' test and PCR identification (Biéler et al., 2016). Diagnosis, as well as treatment differs between the first and second stages of the disease. Second stage HAT requires more training and expertise as CNS lumbar punctures are required to identify the parasites and/or an elevation in white blood cells (Stich et al., 2002). Diagnosis therefore requires a high level of material and human resources and a stable infrastructure for screening and treatment. This is a difficulty in many of the rural and economically deprived areas where the disease is endemic. Increased research into better diagnostic methods is required and prompted the WHO's 'FIND' (Foundation for Innovative New Diagnostics) programme in 2006 (Brun et al., 2010) (Biéler et al., 2016).

1.2.6 Current treatment of HAT.

Historically, dyes such as 'trypan red' and arsenic-based chemicals that showed killing of trypanosomes were amongst the first disease-specific treatments (coined 'Chemiotherapy') to arise (Alsford et al., 2012a; Ehrlich, 1913). Amazingly, some current HAT treatments such as the trypan-red based drug 'Suramin' and the arsenic compound 'Melarsoprol' are still related to these original chemicals (Alsford et al., 2012b). The main treatments for HAT fall into those which can be used to treat the stage I form of the disease (Pentamidine and Suramin) and those which treat the stage II form of the disease as the parasites enter the CNS (Eflornithine, Nifurtimox and Melarsoprol). A summary of the current HAT treatments is given in **table 1.2**.

As seen in **table 1.2**, there are many major drawbacks to the current treatments for first and second stage HAT caused by *T. b. rhodesiense* and *T. b. gambiense.* Generally, stage I treatments are relatively non-toxic but have poor blood brain barrier (BBB) penetration. Stage II treatments have good BBB penetration but are highly toxic and in some cases lethal (Masocha et al., 2007). All of the current treatments have serious drug-related side effects, and in some cases such as the widely used Melarsoprol, these can be fatal. Drug resistance and treatment failure rates are increasing, and have been reported for Suramin since the 1950's (Pepin & Milord, 1994), although recently this has been disputed as treatment failure and not resistance (Wiedemar et al., 2017). Resistance to Pentamidine and Melarsoprol is due to a loss of a membrane transporter (de Koning, 2008) (Alsford et al., 2012b) (Munday et al., 2014). Side effects likely stem from untargeted modes of action; Melarsoprol is known to inhibit 80 assays out of a total of 370 listed in PubChem (Brimacombe et al., 2014).

Difficulties also arise in drug delivery; administration requires complex dosing schemes via intravenous or intramuscular injection – making treatment difficult in the rural areas in which the disease is endemic (Brun et al., 2010; Yun, Priotto, Tong, Flevaud, & Chappuis, 2010). In 2009 a combinatorial therapy named 'NECT' (Nifurtimox-Eflornithine Combination Therapy) was introduced. NECT offers significant advantages over Eflornithine monotherapy as a stage II *T. b. gambiense* treatment; patients are 50% less likely to develop serious side effects compared to Eflornithine monotherapy, and the cost of the total treatment, due to lower dosing schedules, is much smaller at €39 per patient compared to Eflornithine at a cost of €107 per patient (Yun et al., 2010). Reported efficacy is also improved with NECT – with 98% cure rates being reported over 92% for Eflornithine monotherapy (Yun et al., 2010). Using combinational therapies such as NECT also reduce the likelihood of parasite resistance over using Melarsoprol and Eflornithine monotherapies. Despite these advantages, NECT still has a human and material resource-heavy

treatment schedule, and is much less effective for treating 1st or 2nd stage HAT cause by *T. b. rhodesiense.* The need for an orally available, targeted and selective treatment for both stages of the disease in *T. b. rhodesiense* and *T. b. gambiense* is evident.

Drug	Stage of disease	Mode of action validated?	Side effects
T. b. gambiense			
Pentamidine (1940s) 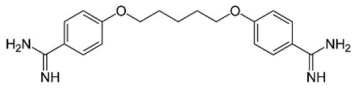	1st	Multiple targets. Binds nucleotides. Accumulates to millimolar concentrations and disrupts trypanosomes mitochondrial membrane potential [1]	Gastrointestinal problems, hypoglycaemia, diarrhoea, nausea and vomiting.
Eflornithine (1990s) 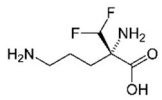	2nd	Yes – blocks polyamine biosynthetic pathway [2].	Effects human polyamine biosynthetic pathway. Convolutions, diarrhoea, nausea, vomiting and anaemia
Melarsoprol* (1949) 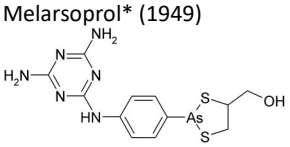	2nd	Yes – converted to melarsen oxide in body – promiscuous inhibitor of many metabolic pathways [3].	Encephalopathic syndromes – 5-10 % fatality rate. Skin reaction, neuropathies.
'NECT' – Nifurtimox + Eflornithine combination therapy (2009)	2nd	Yes – see Nifurtimox and Eflornithine monotherapies	As with monotherapies but Eflornithine symptoms 50% less likely than monotherapy [4].
T. b. rhodesiense			
Suramin (1920s) 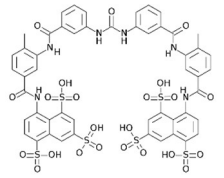	1st	No	Hypersensitivity, albuminuria, haematuria, neuropathy.
Melarsoprol (1949)	2nd	Yes – see above	See above
Others			
Nifurtimox ǂ 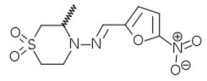	2nd	2 possible MOA – see section **1.2.7.** Current treatment for Chagas disease	Anorexia, weight loss, nausea, vomiting, vertigo. 50% of patients cannot complete treatment.
Fexinidazole (phase II trials 2012) 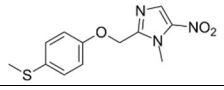	Active in 1st and 2nd stage HAT models	No	None reported in rat models.
SCYX-7158 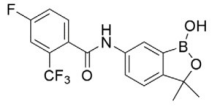	Cure in 2nd stage HAT models	No	Minimal effects in pre-clinical evaluation [5].

Table 1.2: current treatments for human African Trypanosomiasis (HAT).

** Where Eflornithine is not available or not currently registered as a 1st stage treatment for T. b. gambiense. ǂ Where Eflornithine and Melarsoprol are not effective*

[1] (Lanteri, Tidwell, & Meshnick, 2008a). [2] (Van Bogaert & Haemers, 1989).[3] (Verlinde et al., 2001). [4] (Yun et al., 2010). [5] (Barrett & Croft, 2012).

1.2.7 Trypanosomatid drug uptake and mechanisms of current HAT treatments.

Current treatments for HAT can be grouped into 2 categories; those that are used for treating the haemolymphatic (stage I) form of the disease, and those used for the meningoencephalitic (stage II) phase of the disease. They differ in both their mechanism of action (MOA) and uptake into the parasite cell.

Stage I treatments:

Suramin; Suramin is large (1.3 KDa) and has a negative charge so cannot pass through lipid membrane barriers by passive diffusion. Uptake is likely facilitated by trypanosome endocytosis. A recent study confirmed that the genes encoding 4 lysosomal proteins, an adaptin complex ('AP1') that facilitates endosomal clathrin-mediated trafficking and a BSF-specific invariant surface glycoprotein 'ISG75' were required to maintain the efficacy of Suramin against cultured *T. brucei* parasites lacking the gene (Alsford et al., 2012b). Suramin's specific MOA is still unknown.

Pentamidine; Pentamidine's MOA involves multiple targets. It is known to bind nucleotides, and accumulates to millimolar concentrations in the trypanosome where it disrupts the mitochondrial membrane potential (Lanteri, Tidwell, & Meshnick, 2008b). Potential targets have been found : two P-type ATPases and a plasma membrane H^+-ATPase (Alsford et al., 2012b). Uptake of Pentamidine was first found to be related to an adenosine transporter ('AT1'), the loss of which has been observed in drug resistant strains (Carter & Fairlamb, 1993). Recently the role of an aquaglyceroporin '*Tb*AQP2' has been found to also play a role in resistance (Munday et al., 2014).

Stage II treatments:

Melarsoprol; Melarsoprol's mode of action is related to the formation of a stable adduct with the kinetoplastid-specific antioxidant 'trypanothione'. This complex is named 'Mel T' and its toxic nature that inhibits a number of metabolic pathways is also responsible for its significant side effects in humans (Alsford et al., 2012b). Similar to Pentamidine, Melarsoprol's uptake and resistance is related to the adenosine transporter 'AT1' and '*Tb*AQP2' aquaglyceroporin in trypanosomes (Carter & Fairlamb, 1993) (Munday et al., 2014). Treatment failure rates for Melarsoprol is an increasing problem (de Koning, 2008).

Eflornithine; Eflornathine irreversibly inhibits ornithine decarboxylase – an enzyme involved in Polyamine synthesis. Polyamine synthesis is essential for the trypanosome's cell growth and replication (Van Bogaert & Haemers, 1989). Elfornithine's MOA is thought to be trypanostatic and not trypanocidal. Its uptake and emerging resistance is facilitated by 'AAT6' - a member of an amino acid transporter family (Vincent et al., 2010).

Nifurtimox; Nifurtimox is the primary treatment for American trypanosomiasis (Chagas disease). Activation of the prodrug to a toxic product and resistance is facilitated by a mitochondrial type 1 nitroreductase (Wilkinson, Taylor, Horn, Kelly, & Cheeseman, 2008)(Hall, Bot, & Wilkinson, 2011). Two schools of thought remain on the drug's downstream MOA;

- It forms a nitro-anion radical metabolite that damages the parasite's DNA, similar to the MOA of antibacterial 'nitrofuran' compounds (Gutteridge, 1985).
- It results in the production of toxic superoxide anions and hydrogen peroxide (H_2O_2) from the inhibition of the parasitic antioxidant enzyme 'trypanothione reductase' (Marr & Docampo, 1986).

The unknown MOA, significant side effects and complex dosing and administration regimes of the current HAT treatments present the need for new, orally administered drug candidates to fight the disease. Coupled with evidence of emerging resistance to some of the drugs, the need to feed new effective drug candidates into the drug discovery pipeline is evident.

1.3. Glycolysis as a target for anti-trypanosomatid drugs.

1.3.1 Trypanosomatid metabolism and reliance on glycolysis.

The glycolytic pathway is a promising target for anti-trypanosomatid drugs, as reviewed by Barros-Alvarez et al. (2014) and Verlinde et al. (2001). Bloodstream-form (BSF) *T. brucei* trypanosomes rely solely on aerobic glycolysis for their ATP production (Barros-Alvarez et al., 2014). BSF trypanosomes adapt to use aerobic glycolysis for energy production in the bloodstream. Mitochondrial metabolism, the respiratory chain and the TCA cycle are all severely repressed in this life cycle stage. In *T. brucei* promastigotes, 40% of the enzymes contained within the glycosomes are glycolytic enzymes, this proportion increases to 90% in the BSF stage where glucose supplies are plentiful (Barros-Alvarez et al., 2014). Each of the glycolytic enzymes in BSF *T. brucei* have been validated as essential for parasite survival through RNAi knockdown experiments (Albert et al., 2005; Caceres, Michels, & Hannaert, 2010). Starving BSF *T. brucei* cultures of glucose, or incubating cultures with the glucose transporter inhibitor 'Phloretin' causes cell death within minutes (Seyfang & Duszenko, 1991). Amino acids and lipids are still taken up in BSF trypanosomes, but are used for anabolic processes and cell material synthesis, not ATP production (Barros-Alvarez et al., 2014).

In the bloodstream, *T. brucei* trypanosomes undergo a density-dependant developmental switch from 'slender' to 'stumpy' forms. Aside from the morphological and cell cycle changes associated with this switch, the parasites upregulate a number of metabolic proteins. In preparation for transmission into the Tsetse fly salivary and gut as procyclic trypanosomes, *T. brucei* parasites activate their mitochondrion. A number of metabolic proteins are upregulated in the switch to stumpy forms to prepare for this, and a great deal of evidence now suggests that BSF *T. brucei* parasites are capable of a rapid switch to alternate energy metabolism – reviewed by ((Zikova, Verner, Nenarokova, Michels, & Lukes, 2017). Stumpy form parasites have been found to be dominant over slender forms in late state HAT infections in mice (MacGregor, Savill, Hall, & Matthews, 2011). It is thought that this stage allows for immediate changes in metabolic pathways used once the parasite moves to a new environment, such as the fly midgut or, as recently reported, the host skin tissue (Tanowitz, Scherer, Mota & Figueiredo, 2017) or adipose tissue where fatty acid metabolism genes are upregulated (Capewell et. al, 2016). While this emerging evidence suggests alternative metabolic pathways are used by *T. brucei* parasites within the human host, it is clear that in the bloodstream the parasites are heavily reliant on glycolysis. This presents a window of opportunity for drug development against the infective form of the parasite.

1.3.2 The glycosome and glycolytic enzyme targets.

Trypanosomes contain membrane-bounded organelles called glycosomes where 7 out of the 10 glycolytic enzymes are found. Glycosomes in BSF *T. brucei* trypanosomes are highly specialised – 90% of the protein content is made up of glycolytic enzymes (P. A. M. Michels, Bringaud, Herman, & Hannaert, 2006). **Figure 1.5** shows the compartmentalisation of glycolysis and related metabolic pathways in *T. brucei, T. cruzi and Leishmania* spp. glycosomes. The localisation of essential glycolytic enzymes within these organelles coupled with the evolutionally divergence between the enzymes in parasite and man has resulted in unique structural and functional differences in the glycosomal proteins that can be exploited in drug discovery against trypanosomes. Compartmentalisation provides a unique glycolytic environment; there is no net ATP production within *T. brucei* glycosomes, meaning an ATP/ADP balance is maintained within the organelles. A constant NAD^+/NADH balance is also maintained, and the organelle is said to be in equilibrium. Other metabolic pathways are also found within glycosomes, such as the pentose phosphate pathway (PPP), an extension of the glycolytic pathway to produce succinate, and routes for nucleotide sugar synthesis (**figure 1.5**).

Glycolytic flux within the glycosomes of BSF *T. brucei* is very high – inhibition of enzymes resulting in just a 50% reduction of glycolytic flux causes cell growth arrest and death of trypanosomes (Barros-Alvarez et al., 2014). The compartmentalised enzymes in trypanosomes are not subject to the regulatory mechanisms controlling glycolysis in many other cells (Verlinde et al., 2001); two examples are the regulation of hexokinase and PFK, which are heavily regulated in other organisms but not in trypanosomatids (Nwagwu & Opperdoes, 1982). Instead, the compartmentalisation of the first 7 steps of glycolysis means that net ATP production occurs outside the glycosome, and does not fuel hexokinase and PFK, therefore removing the need for regulation to prevent the 'turbo effect' (Haanstra et al., 2008). A long evolutionary divergence between trypanosomatids and mammals (Fernandes, Nelson, & Beverley, 1993) coupled with the unique regulatory and structural differences as a result of glycosomal compartmentalisation makes glycolysis an attractive target for anti-trypanosomatid drugs (Barros-Alvarez et al., 2014; Verlinde et al., 2001) . Each of the glycolytic enzymes in *T. brucei* have been kinetically characterised and sequence identity between human and parasite forms is as low as 21% (PFK) ranging to 55% for glyceraldehyde-3-phosphate dehydrogenase (GAPDH).

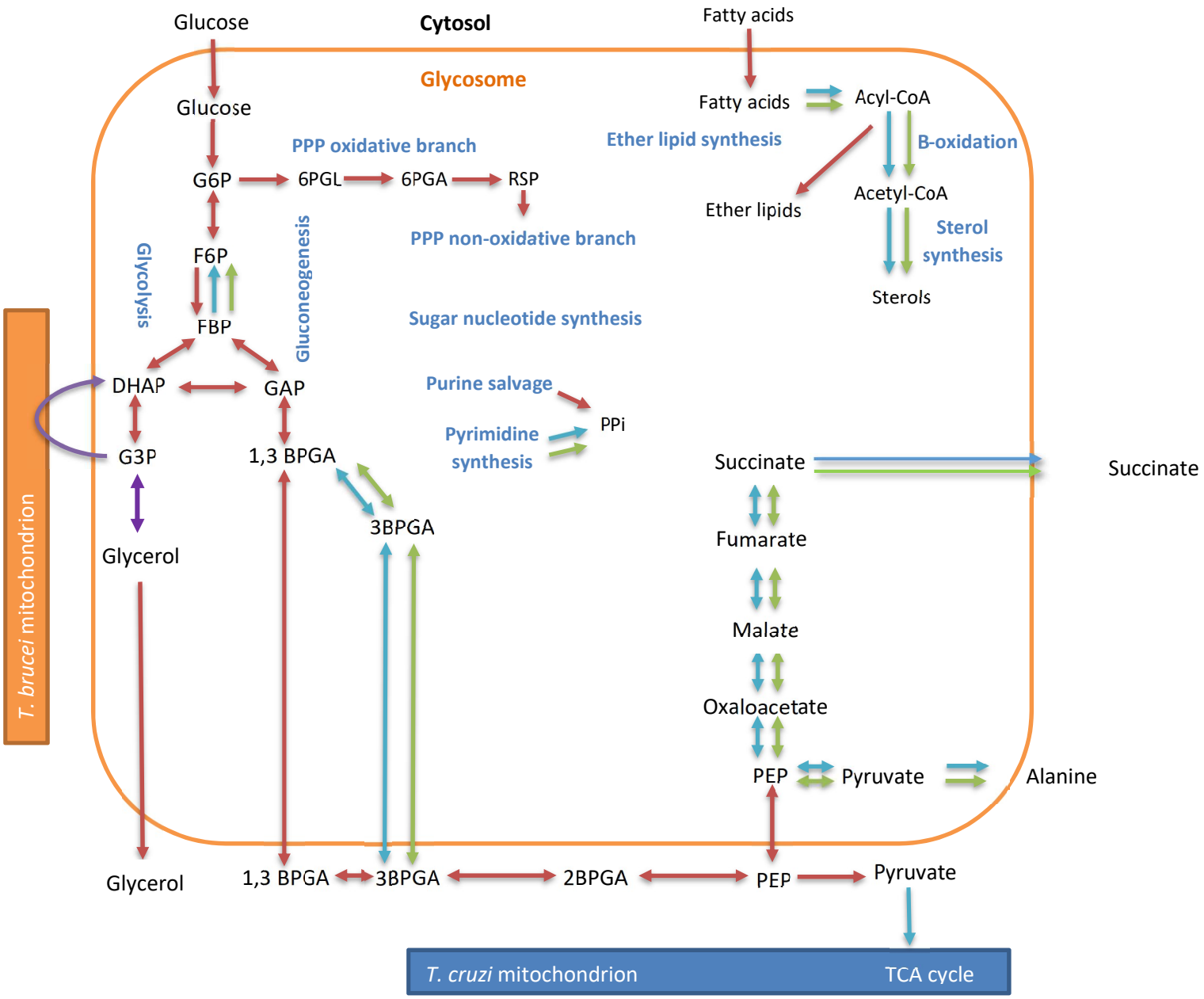

Figure 1.5: metabolic pathways localised to the glycosome and used in BSF T. brucei, T. cruzi and Leishmania spp. Names of pathways are shown in blue.

All species

Leishmania spp. only

T. cruzi only

T. brucei BSF only

1.3.3 Alternative metabolic pathways as anti-trypanosomatid targets.

Other transport and metabolic pathways linked to glycosomes also serve as targets of interest for developing anti-trypanosome drugs. Many of these pathways are predominant in the procyclic parasite stage in the tsetse fly midgut, and not expressed or only at low level in the bloodstream forms. These include the pentose phosphate pathway (PPP), an extension of the glycolytic pathway to allow production of succinate in the glycosome and synthetic routes for sugar nucleotide synthesis needed for glycosylation reactions (reviewed in Barros-Alvarez et al., 2014).

Glycosomal metabolism differs slightly between human pathogenic forms of *T. brucei*, *T. cruzi* and *Leishmania* spp. A considerably higher proportion of glucose is used in the PPP and succinate pathways in the *T. cruzi* glycosome compared to *T. brucei* and *Leishmania* spp. The *T. cruz*i mitochondrion is more developed than in BSF *T. brucei* as it possesses a TCA cycle and electron transfer chain in both life cycle stages (Barros-Alvarez et al., 2014). *T. cruzi* also contain the enzymes for an extended glucose catabolic pathway to produce succinate, in contrast to *T. brucei* which has a more 'glycolysis optimised' glycosome (Barros-Alvarez et al., 2014). Recent evidence however indicates that *T. brucei* BSF parasites, notably in stumpy but also in long-slender forms have a significantly more complete mitochondrial proteome than previously thought, although expressed at low level, in agreement with metabolic carbon products such as pyruvate, acetate, malate, fumarate and succinate being observed in cultured BSF *T. brucei* (Zikova, Verner, Nenarokova, Michels, & Lukeš, 2017)

Leishmania spp. live as 'amastigotes' in their pathogenic human stage in phagolysosomes of macrophages and other phagocytotic cells, which have an acidic, low glucose and high amino acid environment (Barros-Alvarez et. al, 2014). As such gluconeogenesis is predominant over glycolysis in *Leishmania* amastigotes. β-oxidation of fatty acids, for which the enzymes involved are contained within both the mitochondrion and glycosomes, provides the main source of energy for the amastigotes (Barros-Alvarez et. al, 2014). Purine salvage and pyrimidine synthesis is also facilitated by the glycosomes in *Leishmania* spp.

Targeting glycolysis remains an excellent option for developing drugs against *T. brucei* bloodstream parasites, however for *T. cruzi*, and *Leishmania* spp. alternative metabolic targets should be considered, as less reliance is placed on glycolysis for survival. Whether this is also true for *T. brucei* parasites occupying host environments such as adipose tissue remains to be determined.

1.3.4 Alternative metabolic pathways targeted in anti-trypanosomatid drug development.

The **pentose phosphate pathway** has been targeted for anti-trypanosome drugs through inhibition of glucose-6-phosphate dehydrogenase (G6PDH) and 6-phosphogluconate dehydrogenase (6PGDH) (see PPP oxidative branch, **figure 1.5**); Human steroids such as epiandrosterone un-competitively inhibit the *T. brucei* enzymes at low µM range, but with limited selectivity and do not inhibit the *Leishmania* spp. enzyme form (Cordeiro & Thiemann, 2010; Cordeiro, Thiemann, & Michels, 2009). Prodrug analogues of the substrate for 6-phosphogluconate (6PDH) have been shown to exhibit trypanocidal activity with ED_{50}'s of 0.008 – 43 µM (Dardonville et al., 2004). Targeting the PPP in trypanosomes leads to a supressed oxidative stress response that leads to increased H_2O_2 death in *T. brucei* (Barros-Alvarez et al., 2014).

Purine salvage enzymes Hypoxanthine-guanine phosphoribosyl transferase (HGPRT) and xanthine phosphoribosyl transferase (XPRT) have also been targeted with the drug Allopurinol showing trypanostatic activity in Chagas disease models in dogs (Koutinas et al., 2001) and mice (Gobbi et al., 2007). Subtle differences observed in the active sites of crystal structures of human and *T. cruzi* HGPRT lead to a screen for compounds yielding candidates with low µM ED_{50}'s and K_i's of 0.5-17 µM against the parasite (Freymann et al., 2000).

Low nanomolar inhibitors of the genetically validated anti-*T. brucei* target glycogen synthase kinase-3 (GSK-3) have recently been developed (Urich, Luksch, Frearson, Brenk, & Wyatt, 2014).

The **glycosomal membrane** is a permeability barrier for metabolites, cofactors (ATP, NADH), lipids and proteins larger than ~400-500 Da. Glycosomal membrane transporters are another promising target for anti-trypanosome drugs therefore, preventing the shuttling of material important for survival. Little is known about glycosomal transport of small molecule intermediates. Peroxisome protein transport has been researched extensively however (review available by Galland and Michels (Galland & Michels, 2010)). Low sequence similarity homologs of peroxisome transport proteins have been identified in *T. brucei* for two classes of transporters; ATP-binding cassette (ABC) transporters – of which 3 have been identified in *T. brucei* (Yernaux et al., 2006), and a mitochondrial carrier family (MCF) transporter – of which one has been identified in *T. brucei* (Colasante, Peña Diaz, Clayton, & Voncken, 2009). Two plasma membrane glucose transporters are known in *T. brucei:* THT1 which is expressed in BSF parasites and THT2 which is expressed in the insect form of the parasite are promising inhibitor targets (Bakker, Westerhoff, Opperdoes, & Michels, 2000; Seyfang & Duszenko, 1991).

1.3.5 Considerations for glycolytic target choice: metabolic flux.

The reliance of trypanosomes on glycolysis, and the rapid death of trypanosomes where the pathway has been blocked presents a promising target for anti-trypanosome drug compounds. As reviewed by Verlinde et al., there are two requirements for blocking the flux of an essential metabolic pathway; the targeted enzyme must exert sufficient control on the flux, and the affinity of the inhibitor against the target must be high enough to sufficiently block its activity(Verlinde et al., 2001).

Metabolic control analysis is a technique whereby the physiological effects of blocking one enzyme in a metabolic pathway can be quantified. A review of the process has been carried out by Cascante et al. (Cascante et al., 2002) and Bakker et al. (Bakker et al., 2000). Each enzyme within the system is given a flux control coefficient, described as:

Flux Control Coefficient (FCC) = change of flux / change in enzyme activity

Due to the 'summation theorem' for metabolic control analysis, in an ideal pathway the sum of the FCC values of all enzymes making up the system equal 1. Bearing this in mind, an ideal target for inhibition of glycolysis in trypanosomes should therefore have a relatively high FCC in the parasite, and a low FCC in the host organism. This is known as 'differential control analysis' and can be used to consider enzyme targets that may have high structural similarity between organisms to describe effect a drug has on one organism over the other– i.e. a drug may limit the flux of glycolysis in the target more than the host, killing the target organism without damaging the host cells (Haanstra et al., 2017). The flux control coefficients for *T. brucei*'s glycolytic enzymes are well known and data on the human counterparts is also becoming established (Haanstra et al., 2017)(Bakker et al., 2000).

A study by Bakker et al. (Bakker et al., 1999) using the transport inhibitor Phloretin showed that under normal blood glucose levels (5mM) the glucose transporter in *T. brucei* had partial control of flux (FCC = 0.3-0.5) and full control of flux (FCC =1) under low glucose levels (0.4mM). Therefore under physiological conditions the glucose transporter is one, but not the sole controlling component of glycolytic flux in *T. brucei*. A 51% reduction in glycolytic flux is required to kill trypanosomes. It was found that the hierarchy of FCC's corresponded to the effectiveness of inhibiting the glycolytic enzymes; inhibition of only 50% of the glucose transporter activity was required to reduce the glycolytic flux by 50%. Aldolase, glyceraldehyde-3-phosphate dehydrogenase, phosphoglycerate kinase and glycerol-3-phosphate dehydrogenase required 76-85% inhibition for a 50% decrease in flux and hexokinase, phosphofructokinase and pyruvate

kinase needed 93-97% inhibition for 50% flux reduction (Bakker et al., 2000). This hierarchy suggests the glucose transporter followed by aldolase, glyceraldehyde-3-phosphate dehydrogenase, phosphoglycerate kinase and glycerol-3-phosphate dehydrogenase would be the best glycolytic targets for anti-trypanosome drugs. A further study showed that 95% inhibition of aldolase, glyceraldehyde-3-phosphate dehydrogenase or phosphoglycerate kinase caused no clinical symptoms in human erythrocytes (Schuster & Holzhütter, 1995). PFK and PYK are lower on the list of glycolytic targets ranked on FCC values only.

The glucose transporter in *T. brucei* therefore appears like an interesting target – together with hexokinase it has a FCC value of 0.6, as well as a direct relationship between inhibition and reduction of glycolytic flux (Bakker et al., 2000)(Haanstra et al., 2017). Recent studies have shown that glucose transporters and glyceraldehyde-3-phosphate dehydrogenase are the most selective antiparasitic targets in terms of flux control, when comparing BSF *T. brucei* over human erythrocytes (Haanstra et al., 2017). In reality however the trypanosomes may compensate for THT1 inhibition (the glucose transporter found in blood-forms) by expressing the THT2 transporter (found in the insect-stage form) (Bakker et al., 2000). Much of the emerging HAT drug resistance is also related to transporter loss in resistant *T. brucei* strains (Alsford et al., 2012a).

Another major consideration for an anti-trypanosome target is the type of inhibition carried out by the drug molecule on the target. Inhibitors based on substrate analogues will be competitive and likely less effective in vivo, especially in the highly concentrated milieu of the glycosome (Bakker et al., 1999). If structural identity of the target enzyme is high between organisms, the target enzyme should ideally have unique allosteric sites or binding pockets into which a compound can bind and inhibit the enzyme.

In summary, an ideal antiparasitic target is an enzyme with high flux control in the parasite, but low control in the host cell, one which may have a unique pocket into which specific inhibitors can be developed without the need to compete with substrates. Inhibition of a non-essential enzyme will not kill the target organism. Similarly, if a high level of enzyme inhibition is required to elicit an effect on the cell (ie if the FCC is low), high doses of the compound will be required.

1.4. Phosphofructokinase: an excellent target for anti-trypanosomatid drugs.

Phosphofructokinase (PFK) or (6-phosphofructo-1-kinase – PFK-1) is an enzyme that phosphorylates the fructose-6-phosphate sugar to fructose 1,6-bisphosphate (F16BP) in the third step of glycolysis. The enzyme is responsible for a limiting step in glycolysis and the conversion of F6P to F16BP is considered to be essentially irreversible.

Both mammals and trypanosomes have two non-homologous PFKs – 'PFK-1' and 'PFK-2'. Fructose 1-6-bisphosphatase (FBPase) facilitates the reverse reaction of F16BP to F6P. In both mammals and trypanosomes PFK-1 catalyses the conversion on F6P to F16BP. Similarly, both mammalian and trypanosomatid PFK-2 catalyses the conversion of F6P to F26BP *and* the hydrolysis of F26BP as a bifunctional enzyme, known as PFK2/FBPase2 in mammals and a pair of enzymes – PFK2 and FPBase2 in trypanosomes. The difference is that in mammals, the production of F26BP acts as a positive regulator of glycolysis (through PFK-1) and inhibitor of glycogenesis (through FBPase-1). In trypanosomatids however, the production of F26BP by PFK-2 is strictly a positive regulator of glycolysis through stimulation of the downstream pyruvate kinase (PYK) enzyme. This is summarised in **figure 1.6**.

PFK2 and PFK1 are not homologous – in fact the PFK2 domain of mammalian PFK2/FBPase enzyme has greater structural identity with adenylate kinase than PFK1 (Rider et al., 2004). A total of 4 isoenzymes of the homodimeric PFK2/FBPase2 enzyme exist in mammals, each encoded by a separate gene that expresses several isoforms with differing regulatory properties (Rider et al., 2004). In trypanosomes, 4 genes encode PFK2 proteins in *T. brucei* and *L. major*. Four pairs of genes encode the PFK2 enzyme in *T.* cruzi (Chevalier et al., 2005). One of the mammalian isoenzymes – named 'PFKB3' is a promising target for cancer therapies (Yang & Hou, 2017).

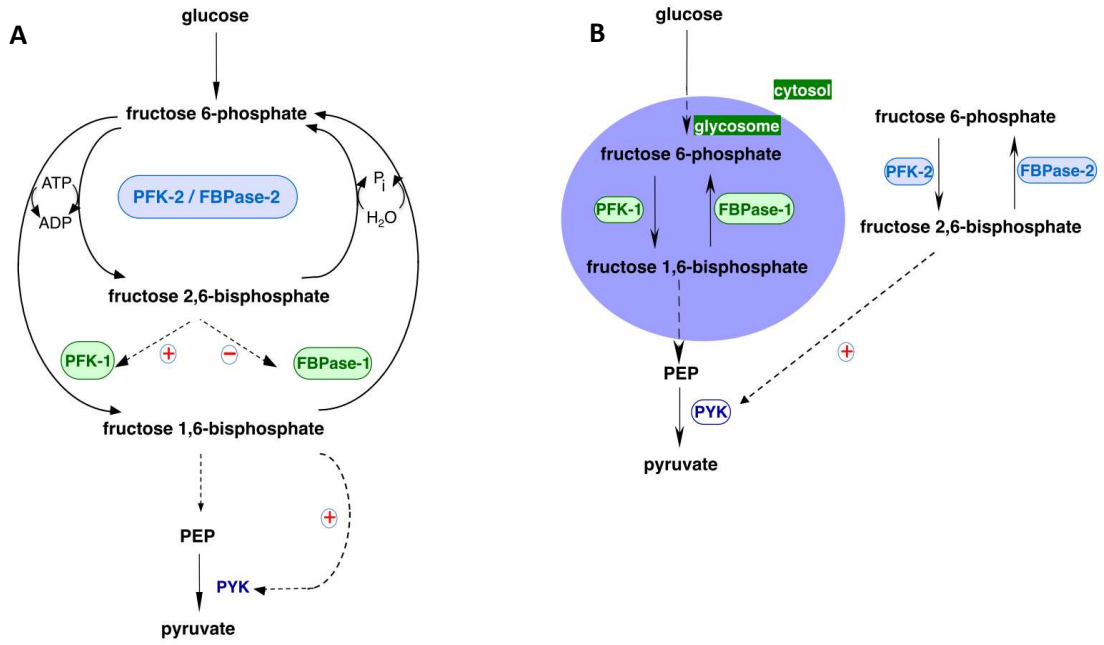

Figure 1.6: Roles of PFK1 and PFK2 enzymes in mammals and Trypanosomes.

A) Roles of PFK1 and PFK2 enzymes in mammalian cells. F26BP (produced by PFK2) acts directly as a positive regulator of PFK1 here. All enzymes within cytosol of cell. B) Roles of PFK1 and PFK2 enzymes in trypanosomatids – blue circle represents glycosome. F26BP here acts still as a positive regulator of glycolysis, but on the cytosolic PYK enzyme, not PFK1. Image adapted from (Chevalier et al., 2005).

The target of interest in the Wellcome Trust funded SDD project is PFK-1 in *T. brucei*. Despite a relatively low control of glycolytic flux (Bakker et al., 2000), PFK-1 remains an excellent candidate for anti-trypanosomatid drugs. We know that PFK-1 in trypanosomes is an essential enzyme as part of an essential pathway; in a study of *T. brucei* 427 bloodstream form parasites with tetracycline-inducible RNAi against PFK, it was found that knockdown of PFK resulted in cell death (**figure 1.7**) (Albert et al., 2005).

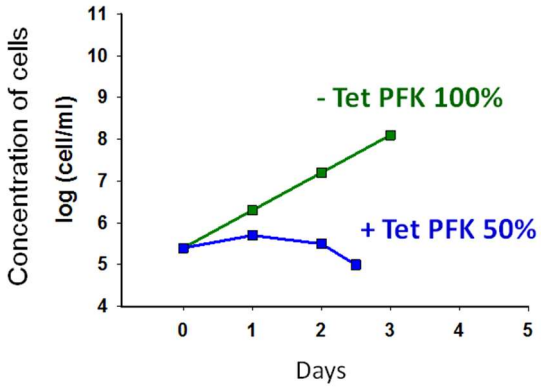

Figure 1.7: RNAi shows PFK is essential for BSF T. brucei survival.

Cultured T. b. brucei 427 cell line with tetracycline (Tet)-induced RNAi against PFK. Cell lines deficient in 50% of their PFK expression show lack of growth (blue). Image adapted from (Albert et al., 2005).

1.4.1 Evolution of phosphofructokinase-1

Phosphofructokinases can be assigned into one of two groups – ATP dependant (ATP-PFK) and PPi dependant (PPi-PFK) enzymes, according to the phospho donor they use. All PFKs evolved from a bacterial PFK-like ATP-dependant ancestor. Gene duplication and fusion events have led to a number of PFK types differing in structure and regulatory properties across species (McNae & Martinez-Oyanedel, 2009). The evolution of PFK in yeast, mammals, trypanosomes, bacteria and plants is summarised in **figure 1.8**. **Table 1.3** summarises the structural and regulatory properties of PFK enzymes from these species.

	Bacteria	**Yeasts**	**Trypanoso-matids**	**Mammals**	**Bacteria protists**	**Plants**
Organism	*E. coli*	*S. cerevisiae*	*T. brucei*	*H. sapiens*	*B. burgdorferi*	*S. tuberosum* (potato)
PFK family	ATP-dependant	ATP-dependant	ATP-dependant	ATP-dependant	PPi-dependant	PPI-dependant
Quaternary structure	Homotetramer (4 x 36 KDa)	Hetero-octamer (4X X 108 KDa, 4X 105 KDa)	Homotetramer (4 x 55 KDa)	3 isozymes – homo- and heterotetramers (4 X 82 KDa)	Homodimer (2 x 60 KDa)	Heterotetramer (2 x 64 KDa, 2 x 57 KDa)
Allosteric activators	ADP, GDP	AMP, ADP, F-2,6-BP, NH_4^+, Pi	AMP	AMP, ADP, F-2,6-BP	Non-allosteric	F-2,6-BP
Allosteric inhibitors	PEP	ATP, citrate, F-1,6-BP	None known	ATP, citrate, F-1-P, PEP	Non-allosteric	None known

Table 1.3: Fact file for Phosphofructokinase enzymes in ATP-dependant and PPi-dependant families.

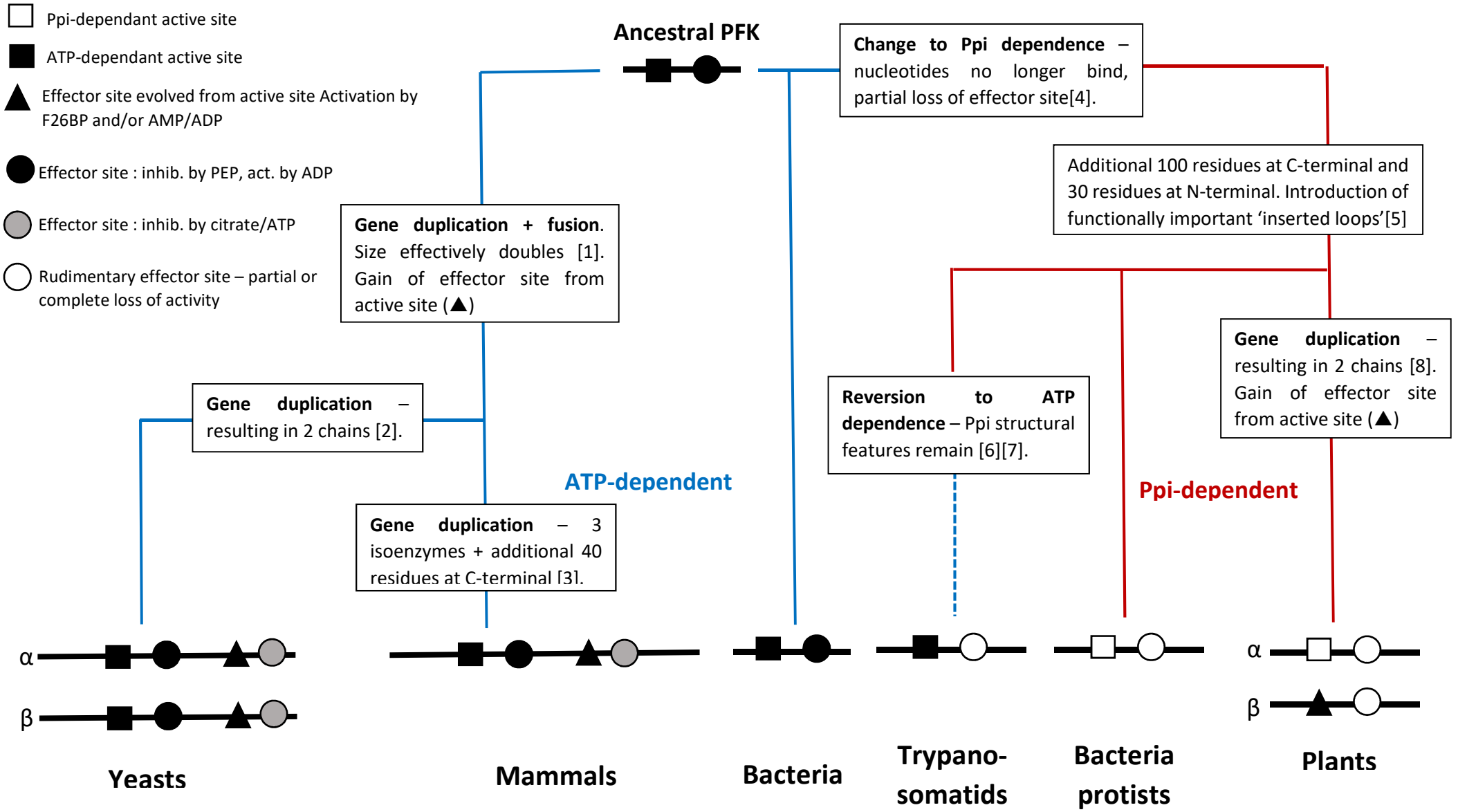

Figure 1.8: Summary of evolution of phosphofructokinase.

Image adapted from McNae et. al (2009). [1] Poorman et. al (1984). [2] Heinisch et. al (1989). [3]: Dunaway. (1983). [4]: Bapteste, Moreira and Philippe (2003). [5]: Moore et. al (2002). [6]: Michels et. al (1997). [7]: Martinez-Oyanedel et. al (2007). [8]: Carlisle et. al (1990).

1.4.2 Phosphofructokinase-1 in eukaryotes.

A great deal is known about the structure of prokaryotic PFKs from bacteria, however relatively little is known about the structure of eukaryotic PFKs. *Tb*PFK was the first eukaryotic PFK that has been described structurally in its active form (2HIG, 3F5M) (Martinez-Oyanedel et al., 2007; McNae & Martinez-Oyanedel, 2009). The yeast PFK hetero-octamer from *S. cerevisiae* has also been described structurally in its active form (3O8O) (Banaszak et al., 2011). Gene duplication and fusion events from a prokaryotic ancestor have resulted in eukaryotic PFKs having subunits roughly twice as large as their bacterial ancestor (**figure 1.8**). One eukaryotic PFK subunit consists of two halves, each of which are related to one ancestral bacterial PFK subunit, and form hetero- and homo-oligomeric enzymes (Schöneberg, Kloos, Brüser, Kirchberger, & Sträter, 2013). Each eukaryotic dimer corresponds in terms of size and fold to one bacterial tetramer as shown in **figure 1.9** below. Trypanosomatid PFKs of course are an exception to this due to their divergent ancestral path, though do have extensions on their C and N terminals relative to the bacterial ancestor (**figure 1.8**). Plant PFKs underwent a separate gene duplication event from eukaryotic PFKs that, similar to yeast PFKs, resulted in 2 chains per subunit (**figure 1.8**) (Carlisle et al., 1990).

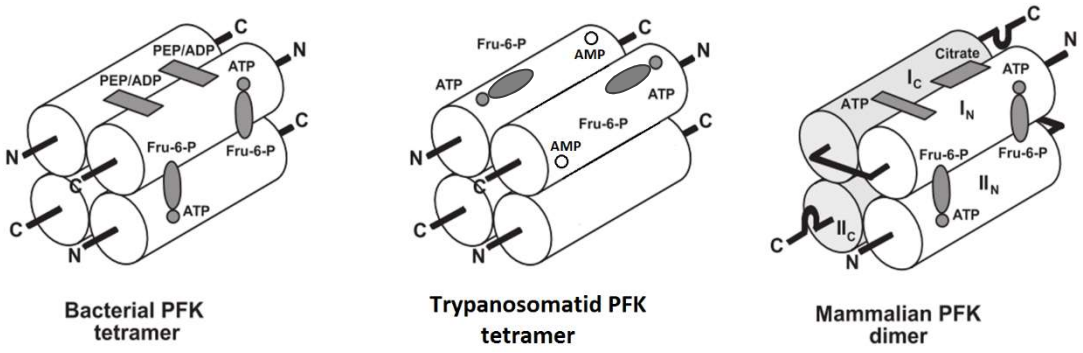

Figure 1.9: Model of an ancestral bacterial PFK tetramer compared to trypanosomatid PFK tetramer and mammalian PFK dimer. Substrate and effector sites are also shown as described by Archaga et. al (Arechaga, Martínez-Costa, Ferreras, Carrascosa, & Aragón, 2010). *I_C, I_N, II_C, and II_N correspond to the C- and N-terminal ends of each mammalian subunit ('I' and 'II').*

Rabbit muscle PFK was the first mammalian PFK structure to be partially solved (3O8L/N) (Banaszak et al., 2011). The smallest active form of a mammalian PFK has been shown to be a tetramer, but higher oligomeric and filamentous forms are also possible (Schöneberg et al., 2013). PFK is expressed in three isoforms from three separate chromosomes in humans; PFKM – solely expressed in skeletal muscle, PFKL – expressed mainly in the liver and PFKC (or 'PFKP')

– expressed mainly in platelet and fibroblast cells (G. a Dunaway, Kasten, Sebo, & Trapp, 1988). Residues known to be involved in ATP and F6P binding are well conserved across all species. The first complete crystal structure of a homotetrameric human PFKP has recently been published with ATP-Mg^{2+} (4XYJ) and ADP (4XYK) bound forms (Webb et al., 2015). It exists as a homotetramer (A_4).

1.4.3 Phosphofructokinase-1 in trypanosomatids.

To date, *T. brucei* PFK-1 is the only trypanosomatid PFK with published structures. **Figure 1.10** shows an identity matrix between the trypanosomatid PFK species investigated in this thesis and mammalian, bacterial and yeast PFKs.

	L. inf.	**T. bruc.**	**T. cong**	**T. vivax**	**T. cruzi**	E. coli	S. cere.	Rb (M)	Hs (M)
L. inf.	-	70.3	69.5	70.0	71.8	23.0	22.8	25.3	24.7
T. bruc.	70.3	-	87.7	79.8	76.9	24.8	25.5	24.4	23.6
T. cong.	69.5	87.7	-	81.6	77.3	25.1	24.6	23.6	22.7
T. vivax	70.0	79.8	81.6	-	78.7	26.4	24.5	24.7	24.2
T. cruzi	71.8	76.9	77.3	78.7	-	25.7	24.0	25.0	24.2
E. coli	23.0	24.8	25.1	26.4	25.7	-	34.4	40.2	40.8
S. cere.	22.8	25.5	24.6	24.5	24.0	34.4	-	42.9	42.7
Rb (M)	25.3	24.4	23.6	24.7	25.0	40.2	42.9	-	96.3
Hs (M)	24.7	23.6	22.7	24.2	24.2	40.8	42.7	96.3	-

L. inf. = *Leishmania infantum*. T. bruc. = *Trypanosoma brucei brucei*/ T. cong. = *T. congolense* (IL300 strain), S. cere. = *Saccharomyces cerevisiae*. Rb (M) = Rabbit muscle (*Oryctolagus cuniculus*). Hs (M) = *Homo sapiens* muscle.

Figure 1.10: Sequence identity matrix between trypanosomatid, mammalian, bacterial and yeast PFKs.

The trypanosomatid PFKs have ~70-88% identity with each other, but only ~20-25% identity with their mammalian counterparts. As discussed in **section 3.2.1, chapter 3**, the active site is well conserved across all PFK species. Despite this, several unique structural features beyond the active site of *T. brucei* PFK provide the opportunity for targeted inhibitor development and specificity against the trypanosomatid enzyme over the mammalian homolog.

1.4.4 Structure of *T. brucei* PFK-1.

T. brucei PFK is a homotetramer (dimer of dimers) of four 53 KDa subunits, 487 a.a. per subunit. Its crystal structure was the first eukaryotic PFK structure to be solved in its active form (Martinez-Oyanedel et al., 2007). Structures of the apoenzyme (2HIG) and ATP-bound enzyme (3F5M) have been solved. **Figure 1.11** shows the crystal structure of the ATP-bound *Tb*PFK tetramer.

Each subunit consists of 3 domains; 'A' domain (res. 8-94, 410-441) is a loosely packed domain and contains a feature unique to the *T. brucei* enzyme - the N-terminal 'embracing arm' that links neighbouring subunits in each dimer(McNae & Martinez-Oyanedel, 2009). A tightly packed 'B domain' (res. 95-233, 386-409) contains the ATP-binding portion of the active site, and a tightly packed 'C' domain (res. 234-385, 442-453) contains two more structural features unique to *T. brucei* PFK; an 'inserted loop' (res. 329-348) that donates two unique residues to the catalytic activity of the enzyme compared to other eukaryotic PFKs (McNae & Martinez-Oyanedel, 2009), and a C-terminal extension that forms 'reaching arms' that make contacts with adjacent subunits between the dimers (**figure 1.11A**). This structure is disordered in the apoenzyme form but ordered in the ATP-bound structure. These N- and C-terminal extensions are unique compared to other ATP-dependant PFKs and are likely a result of *T. brucei* PFKs PPi ancestral lineage. The *Tb*PFK inserted loop is unique to trypanosomatid PFKs, but is similar to an additional sequence in the *B. burgdorferi* bacterial PPi-PFK structure that forms a 'lid' over the active site (Martinez-Oyanedel et al., 2007).

The active site of *Tb*PFK is located between domains B+C. ATP binding occurs between a helix ('Helix 8') and another dynamic active site loop – the 'Arg173' loop (res. 170-178). Models based on the *E. coli* PFK structure show that F6P binding occurs in the cleft directly below the ATP binding site (Schirmer & Evans, 1990). Another dynamic loop important for catalytic activity is the 'Asp229 loop' (res. 225-257) which contributes an important aspartate residue required for phosphorylation of F6P (see **figure 1.12**).

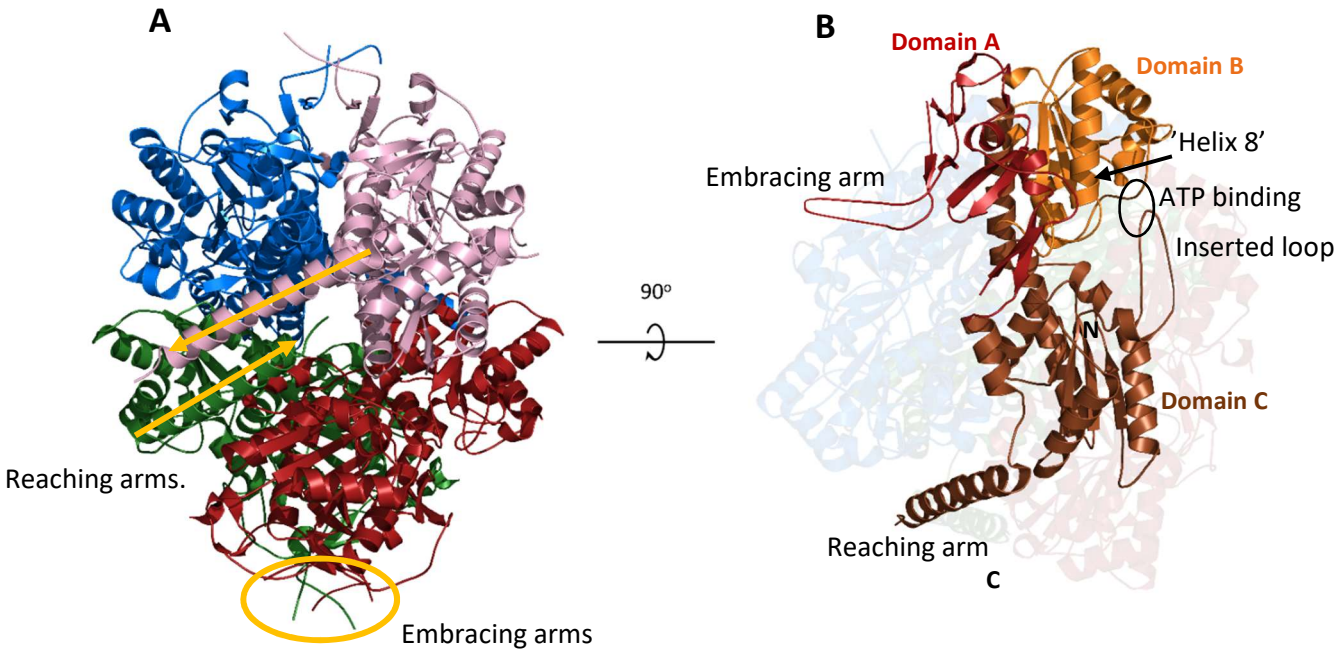

Figure 1.11: Structure of MgATP bound TbPFK holoenzyme (3F5M).

A) TbPFK tetramer – subunits coloured blue, pink, green and red. Orange arrows indicate C-terminal reaching arms between adjacent subunits. Orange circle indicates embracing arms of 2 neighbouring subunits in dimer. B) TbPFK monomer coloured according to domains; Domain A (res. 8-94, 410 – 411) – red, Domain B (res. 95 – 233, 386 – 409) – orange, and Domain C (res. 234 – 385, 442-453) – brown. Other subunits in tetramer are shown in background. ATP binding site has been circled.

1.4.5 Active site structure and catalytic mechanism of TbPFK-1.

The catalytic mechanism of bacterial ATP-dependant PFK from *E. coli* and *B. stearothermophilus* has been described by Evans et. al. (Evans, 1992). An aspartate residue-Asp127 (corresponding to Asp229 in *Tb*PFK) pulls the proton away from the -OH1 group of F6P, allowing the nucleophilic attack of the γ-phosphate of ATP (Evans, 1992) (**figure 1.12**). A central magnesium ion co-ordinates the binding of ATP to PFK and the transfer of the γ-phosphate from ATP to F6P.

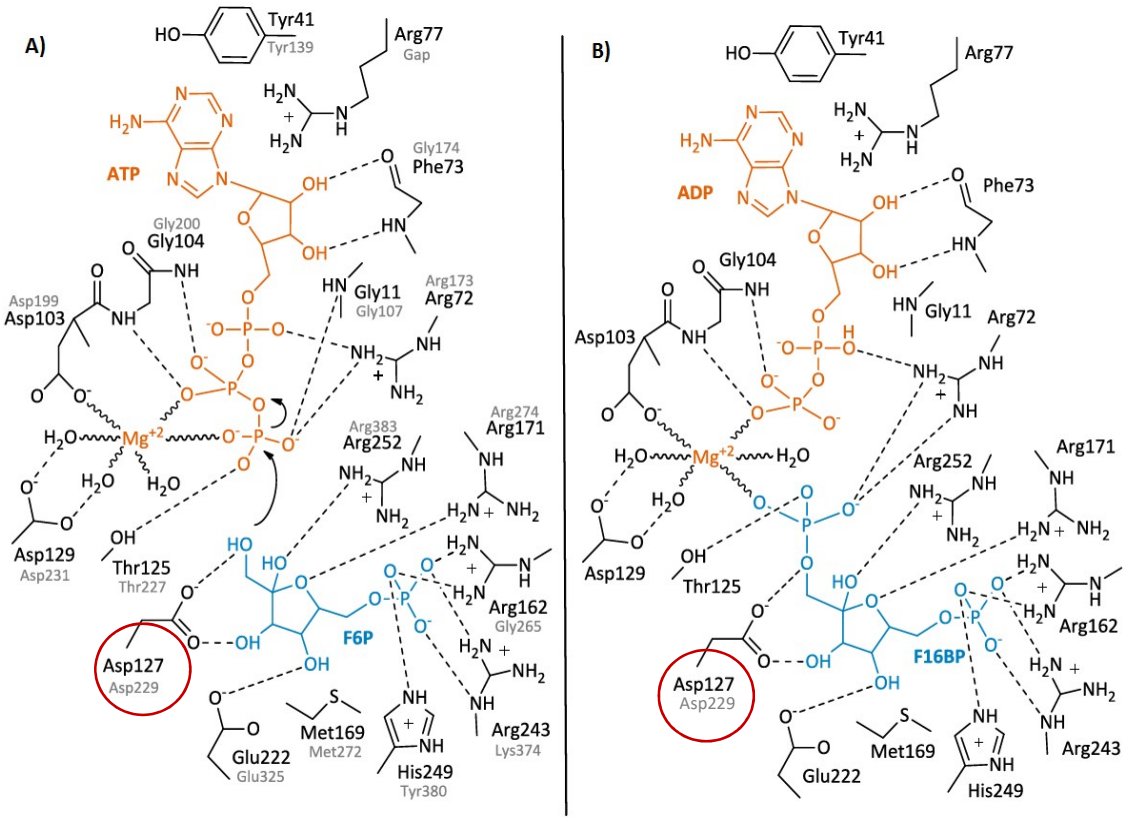

Figure 1.12: catalytic mechanism of bacterial ATP-dependant PFK.

Adapted from Evans et al(Evans, 1992). *Active site residues involved in ATP and F6P binding and phosphotransfer as modelled by Evans et. al using a 'hybrid' model of E.coli and B. stearothermophilus enzymes. Bacterial residues given in bold. Corresponding T. brucei PFK residues are given in grey underneath, as described by* (Martinez-Oyanedel et al., 2007). *Asp229 (TbPFK), part of the Asp229 loop, has been circled to highlight its importance in the catalytic activity of the enzyme.*

The active site of *Tb*PFK is formed by residues between the B and C domains. Known structural data suggest that the catalytic mechanism of *Tb*PFK is ordered – ATP binds first and induces a conformational change that accommodates F6P binding, as well as forming the putative allosteric pocket into which AMP binds (McNae & Martinez-Oyanedel, 2009). Prior to ATP binding the active site is in a more 'closed' conformation; S341 (from the 'inserted loop') and N230 (from the 'Asp229 loop') block the α- and γ-phosphates of ATP, respectively.

Upon ATP binding, there is a 3° conformational rotation from a 'hinge' point between domains A and C (**figure 1.13**). Strikingly, the C-terminal reaching arms become ordered in the ATP-bound structure, forming long subunit-spanning helices involved in holding the tetramer together in an active state (McNae & Martinez-Oyanedel, 2009).

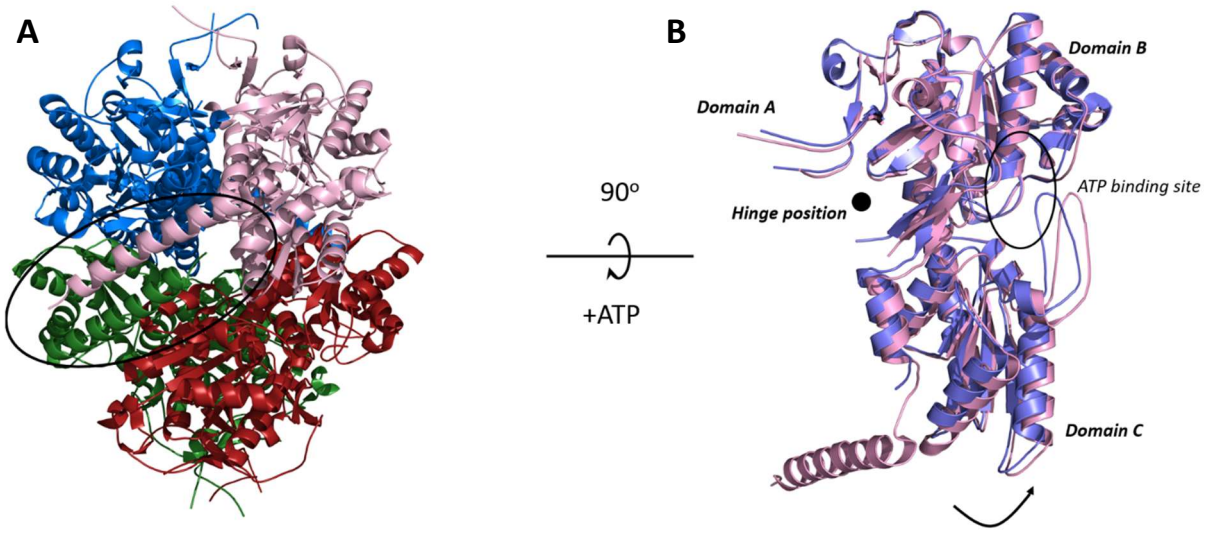

Figure 1.13: ATP binding to TbPFK-1 induces a conformational change in the tertiary structure.

A) MgATP-TbPFK structure (3F5M) consists of a homotetramer. ATP binding orders the C-terminal reaching arms (circled) that hold adjacent subunits together. B) Image B shows the pink subunit from image A rotated 90° on the plane of the paper. The same MgATP-bound monomer (pink) has been overlaid onto the apoenzyme (2HIG)((purple) monomer structure. ATP binding induces a 3° rotation around a hinge point.

The ATP-inducted rotation in domain C results in the movement and ordering of three dynamic loops near the active site; the 'Arg173 loop' 'inserted loop' and 'Asp229 loop' move away from the ATP pocket to accommodate F6P binding and γ-phosphate transfer (**figure 1.14**). The C-terminal helices (reaching arms) become ordered and hold the tetramer together tighter (McNae & Martinez-Oyanedel, 2009).

In the apo-enzyme structure the Asp229 loop – named so due to the catalytic importance of the Asp229 residue (**figure 1.12**) - sits in a conformation with the Asp229 residue pointed toward the ATP/F6P binding sites. In the ATP-bound structure the loop is repositioned away from the active site. The active site is opened up and F6P can bind.

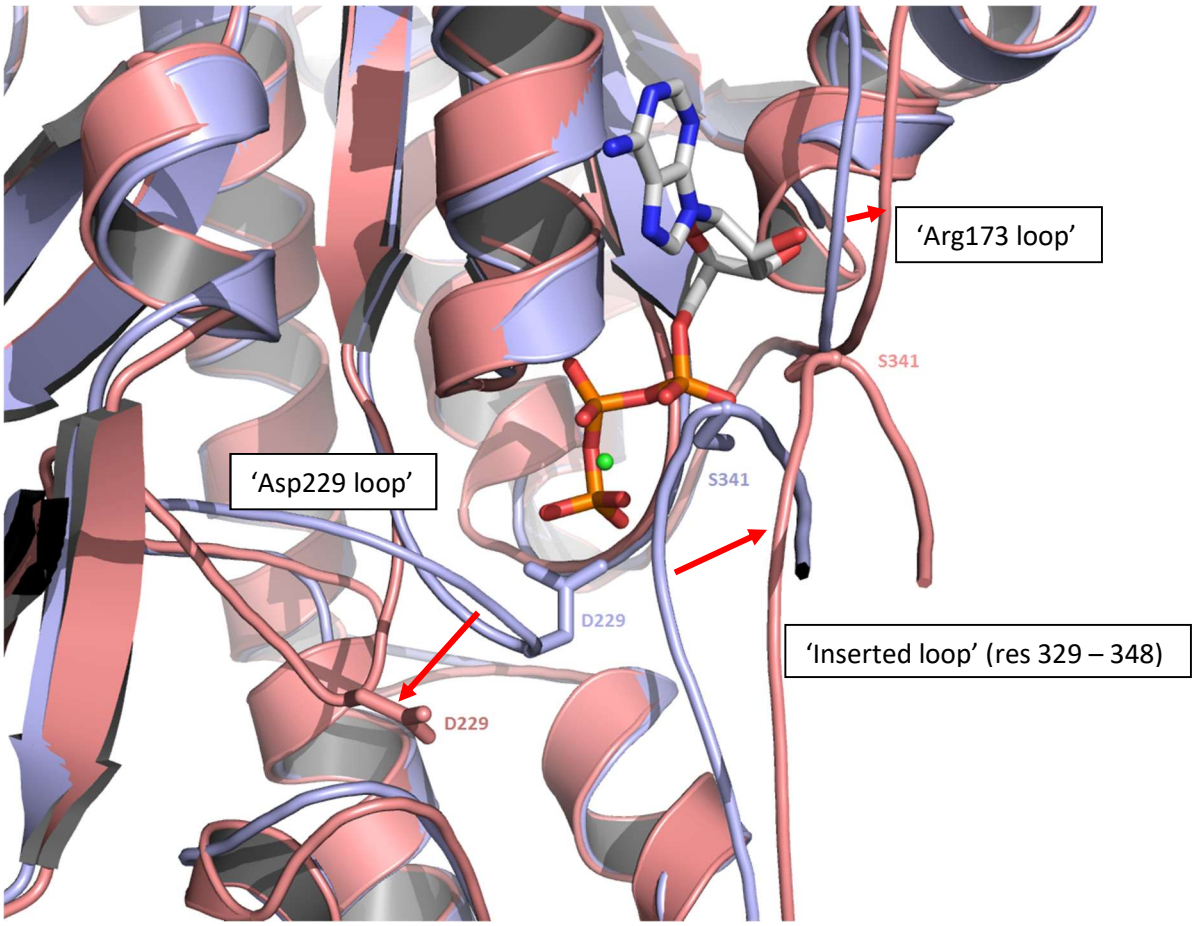

Figure 1.14: Conformational changes in TbPFK active site upon ATP binding.

*TbPFK Apo (**2HIG**) (purple) and ATP-bound (**3F5M**) (pink) crystal structures are shown in cartoon form. ATP (sticks with white carbons) is shown in its TbPFK crystal structure-bound position with Mg^{2+} (green sphere). The three main loops undergoing conformational change between the apo- and ATP-bound enzymes have been labelled and arrows (red) depict movement upon ATP-binding. The Asp229 ('D229') important in catalytic activity has been shown in stick form.*

1.4.6 F6P binding in trypanosomatid PFKs – Cooperativity models.

Cooperative binding of F6P has been observed at the lower concentrations of F6P titrations against PFK enzymes from *T. brucei* (Claustre et al., 2002), *T. cruzi* (Rodríguez, Lander, & Ramirez, 2009) and *L. donovani* (López et al., 2002) trypanosomatids. Two well-known models for describing cooperativity in enzymes are the Monod-Wyman-Changeux (MWC) 'symmetry' or 'concerted' model and the opposing Koshland-Nemethy-Filmer (KNF) or 'sequential' model (Koshland & Hamadani, 2002). **Figure 1.15** summarises the two models. The two models have conflicting features regarding the mechanism of cooperativity. The 'rules' for each model are as follows;

KNF model (sequential):

- Subunits in a multimeric protein can exist in either a low affinity or high affinity state, and switch between the two upon ligand binding.
- Ligand binding to one subunit induces a change from the inactive to active state.
- The switch of one subunit causes the neighbouring subunit to change to the high affinity state by making it more thermodynamically favourable to change its conformation. This happens in a sequential manner.

  Further rules added by the researchers Koshland and Hamadi state:
- Subunits in the oligomeric enzyme are identical to each other
- The conformational change is an intramolecular, tertiary structure rearrangement within the oligomer (Koshland & Hamadani, 2002).

MWC model (symmetry):

- Enzyme oligomers with identical subunits exist in a thermal equilibrium between T and R states, independent of ligand binding.
- The T and R states differ in affinity for the substrate – R generally having higher affinity. The equilibrium between the two states when no ligand is bound is called the isomerisation constant (L).

  L = [T]/[R]. Were T = inactive state, R = active state.
- Ligand can bind to either the T or the R state, with varying or identical affinities. The ratio of T and R state dissociation constants is expressed as constant *c*.

  $c = K_d^R/K_d^T$. If *c* = 1 both R and T states have the same affinity for the ligand. The smaller *c*, the more equilibrium shifts to the R state.
- All subunits of the oligomer change state at the same time, known as 'concerted transition'.
- Ligand binding effects the ratio of the two conformational states only.

A

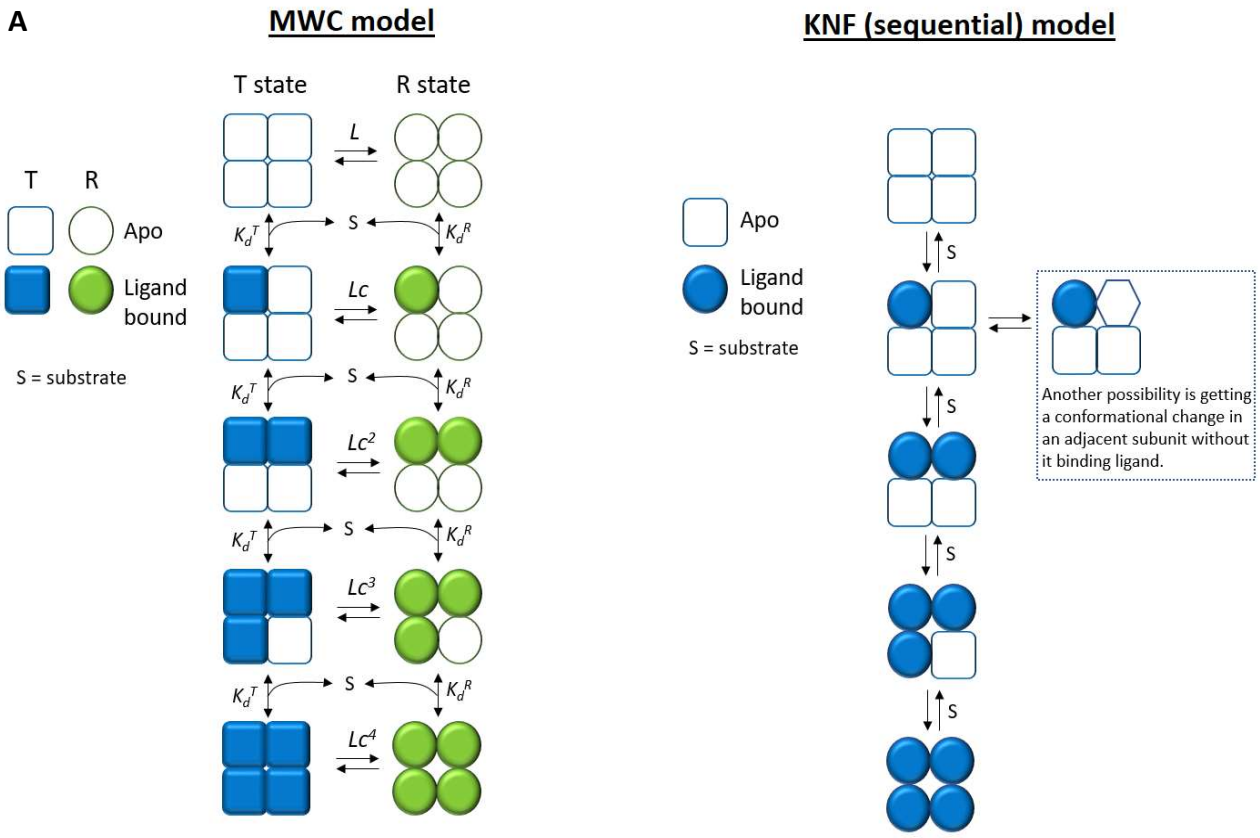

B

Monod-Wyman-Changeux (MWC) 'symmetry' model	**Koshland-Nemethy-Filmer (KNF) / sequential model**
Conformational change is in the whole protein (**quaternary** structure) between R and T states.	Conformational change between R and T states is at **tertiary** structure level.
Only used to describe **positive** cooperativity.	Describes both **positive** and **negative** cooperativity.
Takes into account **thermodynamics** of change in state.	Does not take into account thermodynamics of conformational switch.
Gives sigmoidal binding curve.	Gives sigmoidal binding curve.
Subunits change from T to R states independent of ligand binding	Subunits only change conformation when ligand binding occurs.

Figure 1.15: Two models for substrate cooperativity.

A) Cooperative binding schemes for MWC and KNF models.

B) Table comparing main principles for the opposing MWC and KNF models.

1.4.7 AMP activation of T. brucei PFK-1

The allosteric effector site for *Tb*PFK is located ~38Å from the active site. *Tb*PFK is allosterically activated solely by AMP but, unlike its bacterial ancestors it isn't affected by the activator ADP. Substitution of 2 amino acids compared to the *E. coli* PFK structure (Arg154 and Arg25 in E.coli, Tyr256 and Leu121 in *T. brucei*) explain this specificity for AMP; the unique residues in the *T. brucei* enzyme were originally thought to sterically hinder ADP binding (McNae & Martinez-Oyanedel, 2009). An unpublished structure of *Tb*PFK with AMP bound by Montserrat Valdivieso and Iain McNae at the University of Edinburgh revealed the binding mechanism of AMP (pers. comm. I McNae). **Figure 1.16** shows the position of the AMP binding site and the residues involved in AMP binding. Residues interacting with AMP are donated from two subunits in the dimer interface (**figure 1.16B**). This structure however revealed that the additional phosphate in ADP could theoretically be accommodated, as the orientation of AMP binding was different to previously modelled (per. comm. Iain McNae, UoE) (**Figure 1.16B**).

The C-terminal reaching arms that become ordered following ATP binding hold the tetramer together and span across adjacent subunits. The putative AMP binding site is located under the base of each reaching arm helix. It is possible that AMP binding is communicated across the tetramer via these helices (**figure 1.16A**).

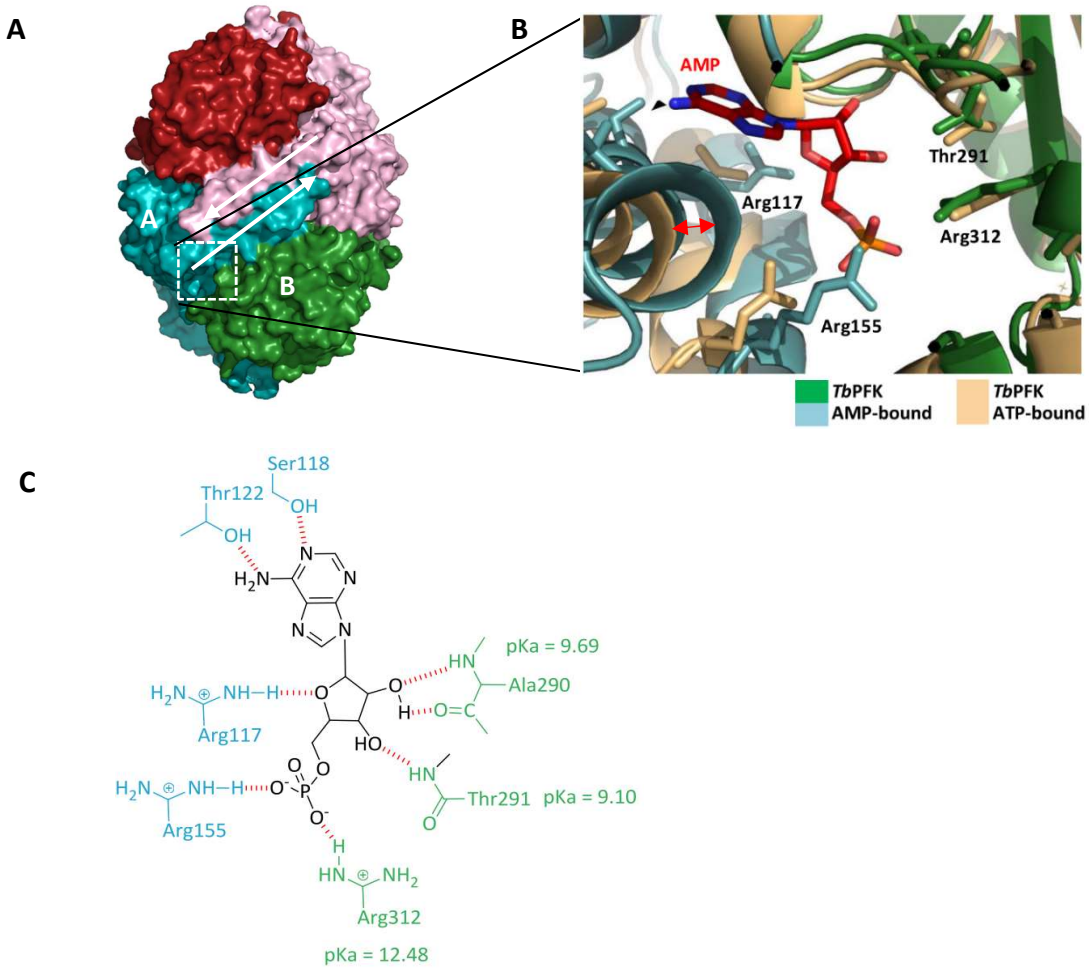

Figure 1.16: AMP binding may be communicated via the C-terminal reaching arms.

***A**) AMP-TbPFK structure (3F5M) in surface representation, subunits of the homotetramer have been coloured. Subunits A and B of a dimer have been labelled. The AMP binding site is located under the base of C-terminal reaching arm helices (boxed). White arrows indicate direction of 'reaching arm' helices proposed as communicating AMP binding across the tetramer. **B**) Binding orientation of AMP in AMP-TbPFK structure. MgATP-TbPFK structure overlaid (gold). Space for the additional phosphate in ADP can be seen between Arg155 and Arg312. A movement in the helix making up the reaching arms can be seen comparing the ATP-bound (gold) and AMP-bound (blue – subunit A) can be seen and is labelled with red arrow. **C**) Schematic of AMP binding to TbPFK. A subunit residues shown in green, B subunit residues in blue. Hydrogen bonds shown in red. Images in B and C by M. Valdivieso.*

1.4.8 Target specificity – unique structural features of T. brucei PFK.

All three human PFK isoforms have <26% identity with *Tb, Tc* and *Li*PFK and share 69-73% identity with each other (**figure 1.10, section 1.4.3**). The residues involved in the catalytic activity of eukaryotic ATP- PFKs are well conserved, as assessed in **section 3.2.1, chapter 3**. Compared to the mammalian isoforms, *Tb*PFK has two unique residues in its active site – S341 and N343 - contributed by the 'inserted loop' feature.

A unique pocket was found via crystal structures identified by a screen for drug-like inhibitor compounds against *Tb*PFK (Brimacombe et al., 2014). This so-called 'CTCB binding pocket' also has low identity (<35 %) with both the rabbit muscle and human isoforms of PFK but is conserved between *T. cruzi, L. infantum and T. brucei* PFKs and poses as an excellent target for structural design of specific inhibitor compounds with proximity to the enzyme's active site. Comparison of the apo- and ATP-bound crystal structures of *Tb*PFK show that the 'CTCB binding pocket' accommodates a leucine residue (Leu232) attached to the Asp229 loop in the apo-enzyme form (**figure 1.17**). Following ATP binding and conformational change of the Asp229 loop, this leucine is removed from the pocket. Interruption of this functionally important loop movement by a drug molecule sitting in the pocket therefore makes this a promising target for anti-*Tb*PFK drugs.

The 'Asp229' and 'inserted' loops also present a unique opportunity for interactions between the enzymes active site and inhibitor molecules.

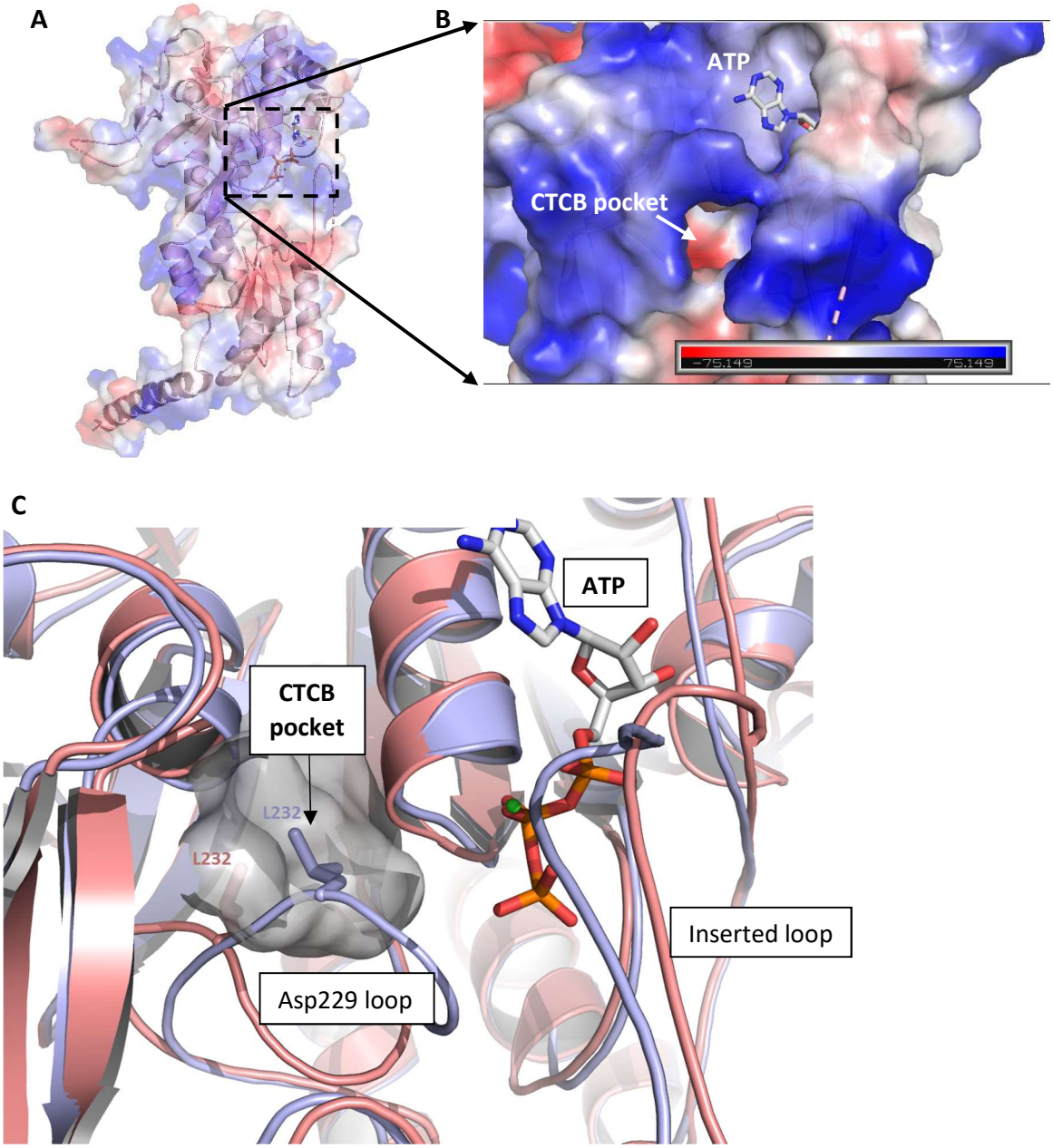

Figure 1.17: The CTCB inhibitor pocket normally accommodates a leucine residue.

A) TbPFK monomer (3F5M) with electrostatic charge potential surface representation. The CTCB binding pocket lies to the left of the ATP binding pocket. B) The CTCB pocket is a negatively charged cleft, surrounded by areas of positively charged residues. ATP shown in stick form. C) Apo (purple) and ATP-bound (pink) crystal structures of TbPFK monomers. Residues involved in the 'CTCB binding' pocket have been shown in surface form (grey). ATP shown as sticks, Mg^{2+} atom as green sphere. As can be seen, in the apoenzyme form a leucine (L232)(sticks) attached to the Asp229 loop occupies the CTCB binding pocket. All images generated in PyMol 2.0.

A distinct advantage of the CTCB binding pocket in designing anti-HAT drugs is that it is specific to the target organism; **Figure 1.18** below shows a sequence alignment of the residues making up the CTCB binding pocket, ATP binding site and F6P binding site between the three trypanosomatid PFKs, rabbit muscle PFK (*RbPFKM*) and human muscle PFK (*HsPFKM*). While the F6P and ATP binding sites are relatively well conserved between all species, the CTCB binding pocket has less than 33% identity between the trypanosomatid PFK and mammalian PFKs.

***Tb*PFK residue**	***Tc*PFK**	***Li*PFK**	***RbPFKM***	***Hs*PFKM**	
G107*	G	G	G	G	ATP binding *backbone interactions
R173 (Arg173 loop)	R	R	R	R	
G174*	G	G	C	C	
P175 (Arg173 loop)	P	P	K	K	
G198	G	G	G	G	
G200*	G	G	G	G	
T201	T	T	V	V	
K226	K	K	Q	Q	
S341 (Inserted loop)	S	S	K	K	
N343 (Inserted loop)	N	N	-	-	
R173	R	R	R	R	F6P binding
E325	E	E	E	E	
K374	K	K	R	R	
Y380	Y	Y	H	H	
R383	R	R	R	R	
Q202	Q	Q	L	L	'CTCB binding pocket'
P225	P	P	V	V	
K226	K	K	G	G	
T227	T	T	S	S	
D231	D	D	D	D	
L232	L	L	F	F	
I414	I	I	V	V	
A430	A	A	C	C	
T431	T	T	V	V	

Figure 1.18: Sequence alignment of ATP, F6P and CTCB compound binding pockets between trypanosomatid and mammalian PFKs.

Residue numbers relate to TbPFKs sequence. Red = unrelated or absent residue. Yellow = residue with related properties. Green = identical residue. Tb = T. brucei, Tc = T. cruzi, Li = L. infantum, Rs = rabbit muscle, Hs = H. sapiens muscle.

1.4.9 Target specificity – regulatory properties of trypanosomatid PFKs.

There are no known physiological inhibitors of trypanosomatid PFKs and only one allosteric activator, AMP (Claustre et al., 2002). PFK in trypanosomatids is contained within the membrane-bounded organelles, the 'glycosomes'. Compartmentalisation provides a unique environment that affects the regulatory properties of the PFK enzyme;

I) **PFK is insensitive to known effectors of other eukaryotic PFKs**. The glycosomal membrane is not entirely impermeable to metabolites, but known effectors of other eukaryotic PFKs (**Table 1.3**) such as citrate and F-2,6-BP have not been reported as regulators of trypanosomatid PFKs. Phosphoenolpyruvate (PEP) enters *T. cruzi* and *Leishmania* spp. glycosomes for succinate production, but this pathway is not present in BSF *T. brucei* glycosomes (see **fig 1.5**). ADP is present in the glycosome but while theoretically able to bind to the AMP effector site in *Tb*PFK structures, it demonstrated only very weak inhibition of the enzyme (IC_{50}^{ADP} = 7.3 mM) (described later in section **4.5.6**).

II) **The glycosomes have a specific ATP: ADP ratio.** The ATP:ADP ratio is kept balanced, and net ATP production occurs outside the glycosome. In silico analysis has shown that the ATP:ADP ratio inside the glycosome is different to that in the cytosol, and both vary according to the external glucose concentration (Barbara M Bakker et al., 2000). As comparisons of the apo- and ATP-bound structures of *Tb*PFK have shown, ATP binding induces an active conformational state. High ATP will cause a conformational switch from a low affinity T-state to a higher affinity R-state form of PFK. The glycolytic membrane is impermeable to nucleotides, and so the ATP:ADP ratio is maintained by the enzymes phosphoglycerate kinase (PGK), glycerol kinase (GK) and pyruvate phosphate dikinase (PPDK) (Deramchia et al., 2014).

III) In other eukaryotes **product feedback inhibition** is an important regulatory property for the glycolytic enzymes hexokinase and PFK, to prevent the build-up of intermediates (G6P, F6P and F16BP) in cells that may result from autocatalytic activation of the pathway by its net ATP production ('turbo-effect') (Teusink, Walsh, Van Dam, & Westerhoff, 1998). *T. brucei, T. cruzi and L. infantum* PFKs are not regulated by their products or by F26BP which is an important feedback regulator of mammalian glycolysis and glycogenesis. Trypanosomatid PYK is regulated by such metabolites, but is located in the

cytosol, not the glycosomes; There is no net production of ATP within glycosomes, and so hexokinase and PFK do not subject to product activation (turbo-effect). As such they do not need to be regulated as they are in organisms where these enzymes are not compartmentalised (Haanstra et al., 2008) See **table 1.3** for a comparison of PFK regulators across species.

1.5. Developing novel drugs against HAT.

Treating stage II HAT remains a challenge in developing new drugs against HAT – the parasites enter the CNS and the drug compound therefore must have features that allow it to cross the blood brain barrier. Uptake or diffusion through the trypanosomes cell membrane and glycosomal membrane adds further complications in delivering an inhibitor to a glycosomal target at an effective concentration. Emerging evidence of drug resistance in trypanosomatid strains due to the loss of membrane transporters is well documented (Alsford et al., 2012b). While this adds an additional challenge to drug development, it also stresses the need for a diverse pipeline of novel treatments against infectious trypanosomatids.

1.5.1 Finding novel inhibitors of TbPFK.

The initial development of inhibitors against *Tb*PFK was carried out by Claustre et. al in 2002. Analogs of 2,5 anhydro-D mannitols, similar in scaffold to F6P and F26BP, were designed and tested against recombinant *Tb*PFK. **Figure 1.19A** shows the chemical scaffold of these compounds and the chemical progression in potency. The compounds had relatively weak inhibitory activity, and had reversible binding with respect to saturating concentrations of ATP and F6P (Claustre et al., 2002). The best compound ('compound 8') had an IC_{50} of 0.45 mM against *Tb*PFK at saturating F6P and ATP concentrations (**figure 1.19A**).

In 2008 Nowicki et al. at the University of Edinburgh designed, synthesised and tested a range of furanose-based analogs against recombinant *Tb*PFK and *Leishmania mexicana* pyruvate kinase (*Lm*PYK). Initial compounds were based on the same F6P/F26BP analogs developed by Claustre et al. Advancement in potency against *Tb*PFK came firstly from the addition of various halobenzene combinations, resulting in a 3,4-dichlorobenzyl group which gave the best potency of the chemical series –IC_{50} = 0.41 mM against *Tb*PFK ('compound 2m' **figure 1.19B**). Additional increases in potency were achieved from testing the dihalogen benzene groups on a sugar amine based scaffold (**figure 1.19B**), the best compound achieving an IC_{50} of 23 µM ('compound 8e'). In models of 'compound 8e' binding to TbPFK, the furanose ring of the sugar amide structure bound in a similar orientation to F16BP in bacterial PFK crystal structures (Nowicki et al., 2008).

In 2014, a collaboration between the University of Edinburgh and the Chemical Genomics Center of the National Institutes of Health (NIH) carried out a screen of 330, 683 compounds against recombinant *T. brucei* and *T. cruzi* PFK enzyme activity (Brimacombe et al., 2014). More than 1000 hits were confirmed, and the 3,4-dichlorobenze group identified by Nowicki et al. in 2008 was a commonality in many of the most potent hits (Brimacombe et al., 2014). The group identified a novel para-amido sulphonamide scaffold (**figure 1.19C**). Increases in potency were achieved through addition of halo-benzyl combinations to this initial scaffold – see compounds 13, 14 and 18 in **figure 1.19C**. Halogens on the 3 and 4 positions of the benzyl group proved to be most potent, as previously confirmed by Nowicki et al. The next advancement in potency was achieved by testing dihalo combinations on the 3,4-position of the benzyl ring, with different groups on the sulphonamide scaffold (**figure 1.19C**). This yielded three of the most potent compounds – compounds '30', '39' and '42' with IC_{50} values of 0.37, 0.079 and 0.015 µM against *Tb*PFK respectively (**figure 1.19C**). The most potent compound '42' however showed a degree of competition with ATP when tested against *Tb*PFK, but showed no inhibition of rabbit muscle PFK. Unfortunately, compound 42 showed no toxicity against cultured BSF *T. b. brucei* 427 strain parasites. The resulting chemical series were good drug candidates; Compound '30' showed a promising EC_{50} of 16.3 µM against the *T. b. brucei* 427 parasites, and was selected as the compound of choice for further development, known as 'ML251' (Brimacombe et al., 2014). None of the compounds tested in the study showed significant human toxicity (EC_{50} > 46µM against human MRC-5 lung cell line). ML251 showed good aqueous solubility and plasma stability and was selected later as one of the initial chemical scaffolds in the Wellcome Trust funded seeding drug discovery programme (SDD) – the results of which are discussed in this thesis.

A: Claustre et al. (2002).

Scaffold 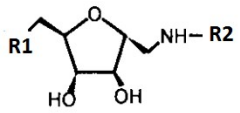	Compound name	R1	R2	Enzyme potency against *Tb*PFK (IC_{50})
	1		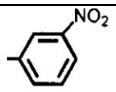	1.1 mM (saturating ATP/F6P)
	8	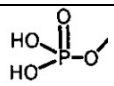	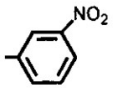	0.45 mM (sat. ATP/F6P)
	12	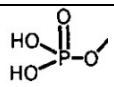		0.54 mM (sat. ATP/F6P)

B: Nowicki et al. (2008).

Scaffold Series I 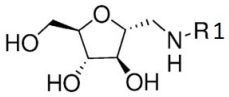	Compound name	R1	R2	Enzyme potency against *Tb*PFK (IC_{50})
	2b	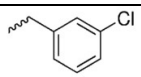		No inhibition
	2c	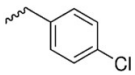		No inhibition
	2m	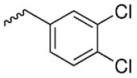		0.41 mM
Series II 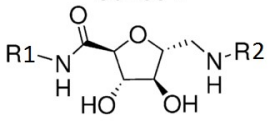	8e	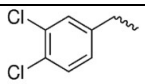	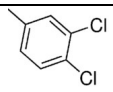	23 µM
	8h	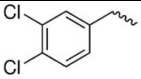		49 µM

C. NIH screen/Brimacombe et al. (2014).

Scaffold	Compound name	R1/ R1-R2	X	Enzyme potency against *Tb*PFK (IC_{50})
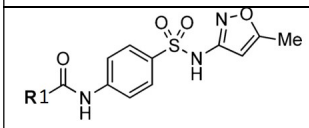	13	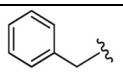		36.6 µM
	14	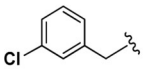		7.3 µM
	18	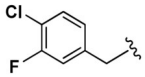		0.7 µM
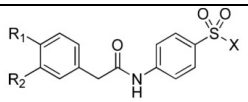	28	Cl-Cl		0.65 µM
	30 (ML251)	Cl-Cl	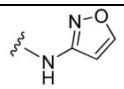	0.37 µM
	39	Cl-Cl	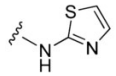	0.079 µM
	42	Cl-F	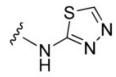	0.015 µM

Figure 1.19: Lead compound progression in initial studies of TbPFK inhibitors.

Compound naming is based on numbering system in each publication as stated. A) (Claustre et al., 2002)*. B)* (Nowicki et al., 2008)*. C)* (Brimacombe et al., 2014)*.*

1.5.2 Novel inhibitors of TbPFK – Wellcome Trust Seeding Drug Discovery project.

An initial screening project of 340, 000 small molecules against *T. brucei* PFK enzyme activity was carried out in collaboration with the Walkinshaw lab at the University of Edinburgh and the Chemical Genomics Center of the National Institutes of Health (NIH) (Brimacombe et al., 2014). This study identified >1,000 small molecule inhibitors of *T. brucei* PFK. From here, the Walkinshaw lab in collaboration with the medicinal chemistry company Selcia Ltd. undertook a structure-based design approach to developing compounds ('CTCB' compounds) from these chemical series as part of the Wellcome Trust-funded SDD project. Existing crystal structures of apo- and ATP-bound *T. brucei* PFK solved by Iain McNae allowed the identification of the unique pocket into which the initial inhibitors bound. This pocket will be referred to as the 'CTCB compound binding site'. **Figure 1.17** (**section 1.4.8**) shows the position of the CTCB pocket.

1.5.3 Recent drug development against HAT.

The 5-nitroimidazole compound 'Fexinidazole' and its 2 metabolite compounds sulfoxide and sulphone have trypanocidal activity against cultured *T. brucei* strains. The drug shows cures in chronic and acute HAT disease models in mice, is orally effective and has no reported side effects in rat studies (Kaiser et al., 2011). Fexinidazole is the most advanced novel HAT drug; it entered clinical development in 2009 and phase III trials started in 2016. A recent update has shown that it led to a 99% cure in patients with stage I HAT. Furthermore, it cured 91% of people with severe onset HAT. While this cure rate is lower than with NCET combination therapy (98% treatment rate), it has the significant advantage of being an orally prescribed pill, over the 16-injection intravenous infusion and oral administration of NCET combination therapy (Maxmen, 2017).

A new lead compound from Scynexis – 'SCYX-7158' is a benzoxaborole compound developed against *T. brucei* from optimisation of a benzoaborole-6-carboxamide series with good parasite killing but poor brain penetration. The compound clears *T. brucei* parasites from stage II HAT mice models after oral dosing (Barrett & Croft, 2012; Jacobs et al., 2011). SCYX-7158 entered phase I clinical trials in 2012.

Inhibitors of the N-myristoyltranferase enzyme involved in membrane targeting and activity of many biological proteins have been characterised as a drug target against *T. brucei*, and inhibitors have been successfully developed against it (Frearson et al., 2010). These inhibitors had good results against stage I HAT models but poor brain penetration prevented a stage II cure from the drugs. Recently, the inhibitor scaffold has been revisited and developed to a new series of compounds with greater brain penetration (Bayliss et al., 2017). -

Both Fexinidazole and SCYX-7158 have excellent HAT curing properties in mice models of stage I and II HAT and have shown low toxicity levels in human and mammalian cell lines (Barrett & Croft, 2012), however their mode of action is not currently known.

A series of brain-penetrant Indoline-2-carboxamide inhibitors of *T. brucei*, obtained by a phenotypic screen at the University of Dundee have also been reported (Cleghorn et al., 2015). These compounds allowed full cures in stage I mice and partial cures in stage II models, but had low dose tolerability (Cleghorn et al., 2015).

A broad spectrum inhibitor of the kinetoplastid proteasome named 'GNF6702' has recently been developed by a joint collaboration (Khare et al., 2016). The drug cleared infection in disease models of HAT (*T. brucei*), Chagas disease *(T. cruzi)* and Leishmaniasis (*Leishmania* spp.*)* in mice. It is a non-competitive inhibitor of the kinetoplastid proteasome, does not inhibit mammalian cell growth or proteasome, and is well tolerated in mice.

1.6. Thesis aims and outline.

1.6.1 Thesis aims.

The overall aim of this project was to test and characterise the molecular regulation of *Tb*PFK, alongside similar PFKs from *T. cruzi* and *Leishmania infantum* parasites. This included two main goals; I) The main focus of the work involved testing and characterising the inhibition of the enzyme by small molecule inhibitor compounds, alongside the Wellcome Trust funded 'Seeding Drug Discovery' (SDD) project carried out by the Walkinshaw group. *T. brucei* phosphofructokinase is a well-researched and validated target for trypanocidal drug development, as it is essential for survival of the bloodstream infective form of the parasite. The availability of crystal structures (2HIG, 3F5M) of the enzyme and the identification of the unique 'CTCB binding' pocket presents a unique opportunity for a structure-based drug design approach. An established expression construct and optimised purification protocol for recombinant *T. brucei* PFK, coupled with expert knowledge and equipment at the Edinburgh Protein Production Facility (EPPF) and Centre for Translational and Chemical Biology (CTCB) facilities at the University of Edinburgh allowed for excellent practical resources for carrying out the SDD project.

II) The secondary focus of this work was to advance current knowledge of the enzymatic activity and regulation of the PFK enzyme in the disease-causing *T. brucei*, *T. cruzi* and *Leishmania* spp. parasites. Specifically, to describe a mechanism of regulation of the trypanosomatid PFK enzymes.

To achieve these goals, the work outlined in this thesis has 4 specific aims;

1) Identification and optimisation of assays for high through-put testing of novel *Tb*PFK inhibitors. This included optimisation of orthogonal primary assays to carry out ranking of compounds against the PFK enzyme, alongside high throughput ranking through surface plasmon resonance (SPR) assays. This was carried out in parallel with assays ranking the potency of compounds against cultured parasites, to feed back information to aid with the ongoing design and development of inhibitors as part of the SDD project.
2) Characterisation of the binding properties of PFK inhibitors. This was achieved through biophysical assays to characterise the affinity, stoichiometry and thermodynamic parameters of compound binding with the *Tb*PFK target. Again, this fed back valuable information to the ongoing design of the inhibitors, and aided in the selection of compound candidates.

3) Characterisation of the molecular regulation of trypanosomatid PFK activity by inhibitor compounds. This was carried out through enzymatic and biophysical assays as well as structural analysis, to characterise the effect on enzymatic activity by the drug candidates. The goal of this work was to establish the mode of action (MOA) of the CTCB compounds against parasitic PFKs.
4) Describe the molecular regulation of trypanosomatid PFKs by physiological effectors. To advance the current knowledge of PFK enzymatic activity and regulation, provide a model for AMP activation of the enzyme and investigate the reversibility of the enzyme-catalysed reaction under physiologically relevant conditions. This was achieved through several enzymatic activity assays and biophysical techniques.

1.6.2 Outline of thesis.

Chapter 2 acts as a reference for the protocols, materials and methods used to obtain the information described in this thesis.

Chapter 3 describes the cloning, expression and purification of recombinant PFKs from *T. brucei, T. cruzi, T. vivax, T. congolense and L. infantum* Trypanosomatidae species. It also describes the biophysical characterisation, validation and quality assurance of the PFK enzymes to be used in the subsequent assays involved in the SDD project.

Chapter 4 describes and compares the kinetic activity and molecular regulation of the PFK enzyme from *T. brucei, T. cruzi* and *L. infantum.*

Chapter 5 shows the investigation and unprecedented description of the reverse reaction of trypanosomatid PFK under physiologically relevant conditions.

Chapter 6 describes the testing, development and characterisation of small molecule inhibitors of *Tb*PFK, as part of the Wellcome Trust-funded Seeding Drug Discovery (SDD) programme carried out by the Walkinshaw Group and the medicinal chemistry company Selcia Ltd.

Chapter 7 outlines a proposed mechanism of regulation of trypanosomatid PFKs through:

1. Cooperativity in F6P binding and regulation by AMP.
2. Inhibition by CTCB inhibitor compounds.

Chapter 7 also explains the outcome of the Seeding Drug Discovery programme project.

Chapter 2: Materials and Methods

This chapter is intended as a reference for the experimental procedures used to measure the data described in chapters 3 – 6.

2.1. Introduction.

The Wellcome Trust funded Seeding Drug Discovery project involved designing and testing small molecule inhibitors specifically against *T. brucei* PFK. As such, this was the main PFK protein being expressed and purified on a regular basis. However in order to carry out comparisons with PFK from other trypanosomatid species, *Trypanosoma brucei, Trypanosoma congolense, Trypanosoma vivax* and *Leishmania infantum* PFK constructs were cloned, expressed and purified (*T. vivax* and *T. congolense* PFKs were not successfully expressed at the time of writing).

2.2 Expression and purification of trypanosomatid PFKs.

2.2.1 Expression of trypanosomatid PFKs

T. brucei, T. cruzi and *L. infantum* PFK constructs in their expression plasmids were provided from previous studies by the Walkinshaw group at the University of Edinburgh. Typically, 1 – 2 µL of 100 – 150 ng/µL DNA was used to transform 50 µL chemically competent cells (according to protein construct – see **table 2.2** below). These were plated and grown at 37 ^{o}C overnight on LB agar plates with their corresponding antibiotic. A single colony was used to inoculate 50 ml of overnight starter culture media containing the corresponding antibiotic (**table 2.2**).

	Competent cell line	Grow-up media	Antibiotic used for selection
T. brucei PFK	C41(DE3)	2xTY	Kanamycin (50 µg/ml)
T. cruzi PFK	BL21 (DE3)	2xTY	Kanamycin (50 µg/ml)
T. congolense PFK	BL21(DE3)	LB or 2xTY	Kanamycin (50 µg/ml)
T. vivax PFK	ND	ND	ND
L. infantum PFK	C41(DE3)	2xTY	Carbenicillin (100 µg/ml)

Table 2.2: summary of conditions for growth and expression of parasitic PFKs.

ND = not done – *T. vivax* PFK could not be successfully transformed at the time of writing.

All PFK constructs were grown in 500 ml of media using the overnight starter culture to an OD of 0.8-0.9 in a shaking incubator at 250 RPM, 37 ^{o}C. Cells were cold shocked at 4 ^{o}C for 30 mins and induced at 18^{o}C for 16 hrs at 100 RPM using 1 mM IPTG. Cells were pelleted at 5000 rpm using a Beckmam Coulter Avanti J-26 centrifuge with a JLA-8.1000 rotor at 10^{o}C for 30 minutes.

2.2.2 Preparation of cell lysates for parasitic PFK purification

1 litre cell pellets were re-suspended in 30ml TEA buffer (50 mM TEA, 5 mM $MgCl_2$, 50 mM KCl, 10% glycerol, pH 7.4) supplemented with Roche cOmplete™ EDTA-free Protease Inhibitor Cocktail and ~5 mg of deoxyribonuclease (sigma DV25). Cells were lysed at 25 Kpsi using a Constant Cell Disruption Systems cell disruptor at 6 ^{o}C. The resulting lysate was centrifuged at 50,000 X g for 45 minutes using a Beckman Coulter Avanti® J-26 centrifuge with JA-25.50 rotor. The supernatant was then filtered using a 0.22 µm syringe filter on ice.

2.2.3 Purification of parasitic PFKs

All purifications were carried out at 6 ^{o}C in an ÄKTApurifier system (GE Healthcare). Filtered cell lysate was passed over a HiTrap IMAC FF column (GE Healthcare) charged with cobalt at 1 ml/min using a p960 sample pump module. Unbound sample was washed with 10 column volumes (CV) of wash buffer (as described in **2.2.2**). Two additional wash steps carried out at 1ml/min with a further 10 CV of wash buffer mixed with 8% then 20% elution buffer (50 mM TEA, 300 mM NaCl, 500 mM imidazole, 10 glycerol, pH 8.0). PFK was then eluted from the column with 15 CV of 100% elution buffer. 1 ml fractions were eluted in a 96-well block (Greiner BioOne 780270).

2.2.3.1 Size exclusion chromatography (SEC) – *T. brucei* and *T. cruzi* PFK purification.

Fractions containing PFK were collected, pooled and concentrated to a volume of 5 ml using a Vivaspin 6 column of molecular weight cut off (MWCO) 100 kDa (Sartorius). This sample was loaded manually into a 5 ml holding loop before being passed over a HiPrep Sephacryl™ S-200 16/60 column (GE Healthcare), pre-equilibrated with gel filtration buffer (20 mM TEA, 5 mM $MgCl_2$, 50 mM KCl, 10 % glycerol, pH 7.4). An example chromatogram for the Sephacryl S-200 16/60 column in given in **figure 2.1.** Sample and buffer flow rate was held at 0.5 ml/min over the duration. PFK was eluted off the column with 1.5 column volumes of gel filtration buffer and 2ml fractions corresponding to PFK were collected, pooled and concentrated to ~0.5 mg/ml using a Vivaspin 20 MWCO 30 kDa concentrating column (Sartorius).

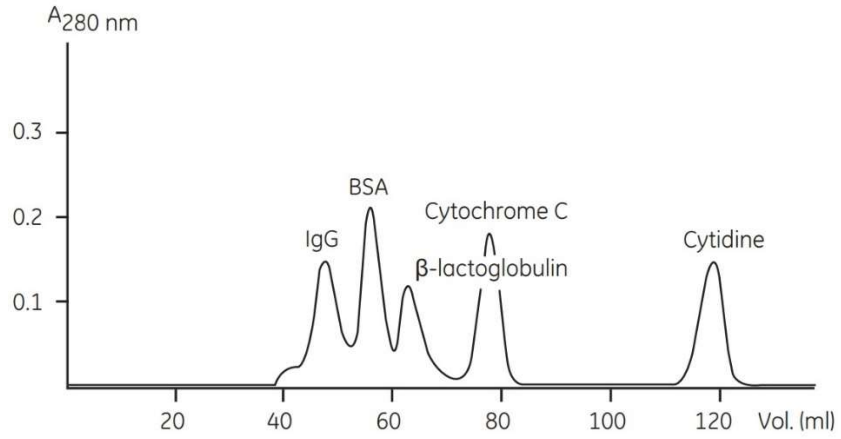

Figure 2.1: Chromatogram profile for Sephacryl S-200 16/60 SEC column.

Example chromatogram trace for IgG (160 kDa), BSA (67 kDa), B-lactoglobulin (35 kDa), cytochrome C (12.4 kDa) and cytidine (0.24 kDa). Adapted from General Electric Company Sephacryl S200 manual 2005-2009.

2.2.3.2 Desalting step – *L. infantum* PFK purification.

Pooled IMAC elutions of *L. infantum* PFK precipitated on Sephacryl and Sepharose-based size exclusion chromatography columns (data not shown) and so this step could not be used for *Li* PFK. The second stage for *Li*PFK therefore involved a simple desalt size exclusion chromatography step; 5ml of the pooled IMAC fractions were filtered using a 0.22 nm syringe filter and were loaded onto a 'HiPrep 26/10 Desalting' column (GE Healthcare) equilibrated with SEC buffer (20 mM TEA, 5mM $MgCl_2$, 50 mM KCl, pH 7.4) at 7 ^{o}C. The PFK was eluted with 1.5 column volumes of the same buffer. 2 ml fractions were eluted into a 96-well block (Greiner BioOne 780270). Fractions containing *Li*PFK were concentrated using a Vivaspin 6 100 kDa MWCO spin concentrator (Sartorius).

2.2.3.3 Measurement of protein concentration.

Protein concentration was measured using a 'NanoDrop Lite' spectrophotometer. Absorbance was measured at 280 nm and converted to concentration using the Beer-Lambert law; $A = \varepsilon * c * l$ where A = absorbance, ε = extinction coefficient of protein, c = concentration and l = path length. A table of extinction coefficients for each parasitic PFK is given in **table 2.3**. Only *T. brucei, T. cruzi* and *L. infantum* PFKs were successfully expressed and purified at the time of writing.

Species	Length (a.a)	MW (kDa)	pI	Extinction coeff. ($M^{-1}cm^{-1}$)
T. brucei	507	55.76	9.50	37860
T. congolense	507	55.59	9.15	37860
T. cruzi	505	55.81	9.23	40380

T. vivax	504	55.41	9.36	41870
L. infantum	510	57.07	8.99	56435

Table 2.3: Extinction coefficients for parasitic PFKs

2.2.4 MALDI-TOF Mass Spectometry confirmation.

Purified *Tc*PFK and *Li*PFKs were confirmed using MALDI-TOF mass spectrometry. An in-gel Trypsin digest was carried out; 5 µg of each protein sample was run on a 12% acrylamide SDS-PAGE gel and stained with InstantBlue stain (Expedion). Bands of interest were excised using a clean scalpel. SDS was removed from the gel using methanol and the protein was reduced using 20 mM DTT at 30 ^{o}C. Cysteines were alkylated using 50 mM iodoacetimide and the gel pieces dehydrated using 50% (v/v) acetonitrile and air dried. The trypsin digest was carried out in 50 mM ammonium bicarbonate buffer (pH 7.8) with 13.3 µg/ml trypsin (Sigma) for 16 hours at 30 ^{o}C.

The peptide samples were spotted onto a MS plate with a a-cyano-4-hydroxycinnamic acid (CHCA) matrix (Sigma) containing 0.3% trifluroacetic acid (TFA). MALDI-TOF mass spectrometry was carried out on a Bruker Ultraflex MALDI TOF TOF mass spectrometer at the School of Chemistry, UoE.

2.2. Phosphofructokinase kinetics and inhibition assays.

2.3.1 PYK/LDH linked enzyme assay.

This assay measures PFK's phosphotransferase activity by linking ADP-production to downstream pyruvate kinase (PYK) and lactate dehydrogenase (LDH) enzyme reactions, as shown in figure 2.2 below. The oxidation of NADH to NAD+ by LDH can be measured by reading the absorbance at 340 nm over time in a spectrophotometer.

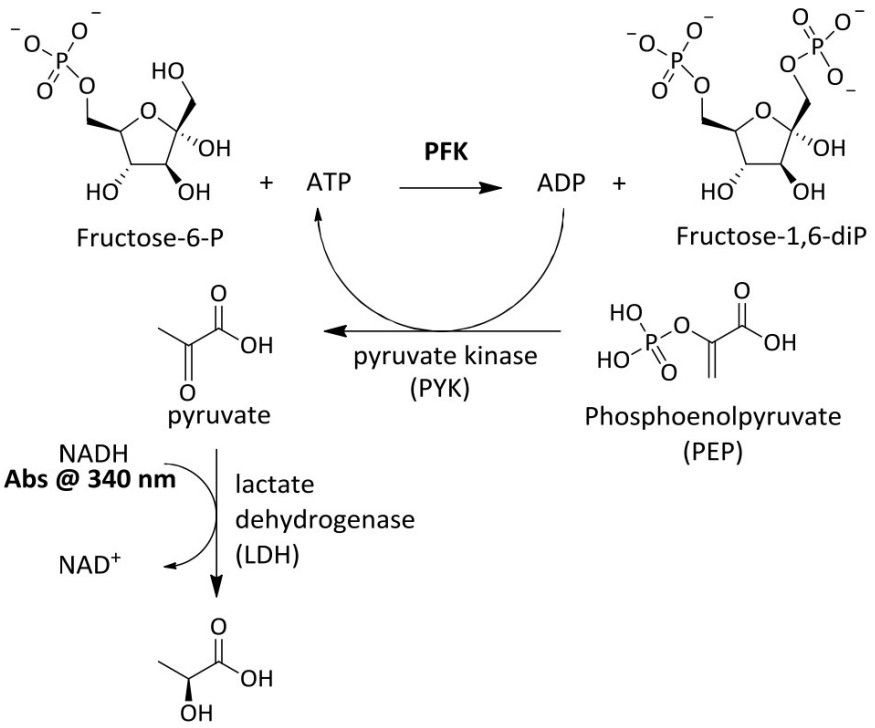

Figure 2.2: PYK/LDH linked enzyme assay reaction scheme

All PYK/LDH linked enzyme assays were performed at 25°C in a 96-well plate format using a Molecular Devices Spectramax® M5 Multimode Plate Reader. In all assays, each well had a final volume of 100 µL, plated in non-binding, clear 96-well F-bottom plates (Greiner BioOne 655901). Unless stated otherwise, all auxiliary enzymes and reagents used were purchased from Sigma-Aldrich. Human M1 pyruvate kinase (M1PYK) enzyme was recombinantly expressed and purified from *E. coli* at the University of Edinburgh. The expression plasmid containing DNA for M1 PYK was kindly provided by Dr Meng Yuan. Raw NADH absorbance readings were converted to concentration using the Beer-lambert law (A = Ɛcl) knowing ε340 NADH = 6220 M-1 cm-1. The gradient of the linear section of each absorbance over time curve was used to calculate the initial rate (μM^{-1} min^{-1}).

2.3.1.1 PYK/LDH linked enzyme assay for measuring PFK activity

A 2.5x 'assay mix' was made containing 4.8 mM PEP, 1.2 mM NADH , 20 U/ml PYK, 33 U/ml LDH and 2.5mM ATP in assay buffer (50 mM TEA, 10 mM $MgCl_2$, 100 mM KCl, , 10% glycerol, 0.005% $TWEEN_{20}$, , pH 7.4). For measuring activity 40 µl of assay mix was plated in a clear, non-binding 96 well plate (Greiner Bio-One cat. no. 655901) with 4-10 µl of the PFK sample (typically a 0.1

mg/ml stock) to be tested and 40 – 46 µl of assay buffer. This was to allow for variable protein stock concentrations to be tested. The reaction was started upon addition of 10 µl of 100mM F6P (10 mM final). Where required, *Tb*PFK was used as a positive control by adding 4 µl of a 0.1 mg/ml stock to 40 µl assay mix and 46 µl assay buffer. Absorbance at 340 nm was read with 20 second intervals for 10 minutes at 25 ^{o}C in 'kinetic mode' on the Spectramax© M5 Multicode plate reader.

2.3.1.2 PYK/LDH linked enzyme assay for measuring PFK inhibition

A 2.5X assay mix was made up in assay buffer (as in **2.3.1.1**) but with 12.5 mM ATP (5 mM final). A 2-fold serial dilution of 100X inhibitor compound stocks in 100% DMSO was carried out in a PCR plate. Inhibitor titrations were chosen according to known solubility or previous IC_{50} data, typically in the range of 100 – 0.78 µM, 20 – 0.16 µM or 5 – 0.04 µM (final concentration at 1% DMSO). 40 µL of assay mix, followed by 45 µL assay buffer, 4 µL of 0.1 mg/ml PFK and 1 µL of 100X serial diluted inhibitors were added to a non-binding, clear 96-well plate (Greiner Bio-One 655901) and incubated at room temperature for 10 minutes. The reaction was started by addition of 10 µL of 6 mM F6P. A known *Tb*PFK inhibitor ('CTCB-001' and later 'CTCB-405') was used as a positive control to a final concentration of 5 µM (>2x known IC_{50}). DMSO was used in place of inhibitor for negative controls. Where possible a multichannel pipette using non-binding tips (Tip-One cat. no. S1180) was used to reduce error. The A_{340} was measured using a Spectramax© M-5 multi-mode plate reader (Molecular Devices) in kinetic mode. Readings were taken over 10 minutes, 25 seconds apart at 25 ^{o}C. All compounds were tested in duplicate in the plate.

PFK inhibitors were checked for non-specific downstream inhibition of the auxiliary enzymes (PYK and LDH) by adding compounds to assay mix without ATP and starting the reaction with 0.4 mM (final) ADP (see **figure 2.2**).

2.3.1.3 Data analysis of PYK/LDH assay for measuring inhibition.

The gradient of the linear section of raw plots of NADH absorbance over time was converted to concentration over time using the Beer-lambert law (A = Ɛcl) knowing ε340 NADH = 6220 M-1 cm-1, for each concentration of CTCB inhibitor. The resulting enzyme velocity values were then plotted as a function of compound concentration using Kaleidagraph 4.0 software. The data was analysed using non-linear regression and a sigmoidal curve was fitted (**figure 2.3**) to determine the IC_{50} – the concentration of inhibitor that leads to 50% inhibition of maximal enzyme activity.

Kaleidagraph 4.0 uses the Levenberg-Marquardt algorithm in an iterative procedure to fit non-linear curves. The equation for the sigmoidal curve given in **figure 2.3** was fitted by using the positive control (100% inhibition of PFK – 5 µM CTCB 001 or '405) as the minimum velocity constraint (m1) and the negative control (no inhibition of PFK - 1% DMSO) as the maximum velocity constraint (m2) of the curve. The slope of the curve at the midpoint (m4) was set to 1.

$$velocity = \frac{m1 + (m2 - m1)}{(1 + (\frac{[inhibitor]}{IC_{50}})^{m4}}$$

Where m1 = Minimum velocity, m2 = maximum velocity and m4 = slope of curve at midpoint.

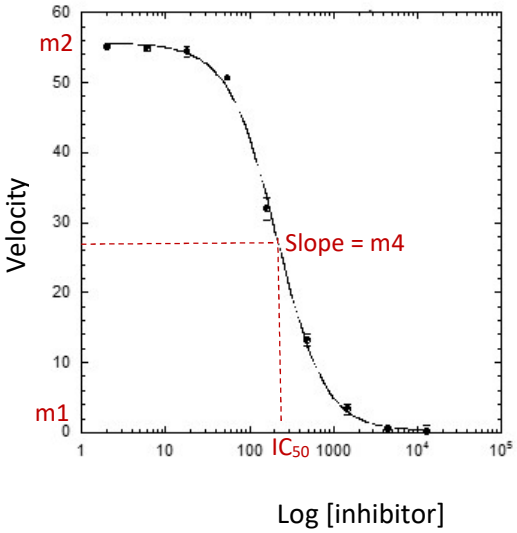

Figure 2.3: Sigmoidal plot equation for inhibition assays (PYK/LDH assay).

Equation used to plot dose-response curves and measure the IC_{50} of CTCB compounds against PFK. M1 = minimum velocity control (5 µM CTCB 001/405). M2 = max velocity control (DMSO).

2.3.1.4 PYK/LDH linked enzyme assay for enzyme kinetics and competition assays.

A 50 µl reaction mixture containing a 2-fold dilution series of either F6P or ATP was diluted in 2X assay mix (5mM PEP, 1.2 mM NADH, >20U/ml PYK, 33 U/ml LDH). To this 50 µl of 2X 'protein mix' was added containing 8 µg/ml PFK and a saturating concentration of F6P (10mM) or ATP (5mM) depending on the kinetic variable being measured. All stocks were buffered to pH 7.4 before use. When used AMP was added to the 2X 'assay mix' to a concentration of 1 mM (final concentration 0.5 mM) for F6P titrations. When tested against ATP titrations, AMP was added to the 'protein mix' (final concentration 0.5 mM). The AMP-assay or AMP-protein mix was allowed to incubate at room temperature for 10 minutes. Both assay mix and protein mix were

allowed to reach room temperature before addition to the plate. 96 well non-binding translucent plates (Greiner BioOne 655904) were used. Titration assays were carried out in triplicate. Upon addition of 50 µl of assay mix the A_{340} was measured in kinetic mode over 5 minutes with readings every 14 seconds at 25 °C.

When compound competition kinetics were investigated 100X, 100% DMSO stocks were added to either the 2X 'protein mix' or 'assay mix' and incubated at room temperature for 15 minutes before testing. Final concentrations of inhibitors were 0.5X, 1X and 2X their respective IC_{50} (as determined in enzyme-linked assay). DMSO was kept at 1% (v/v) (final) in all inhibition assays. The PFK concentration used was 4 µg/ml (final).

2.3.2 Aldolase/G3PDH/TIM linked enzyme assay

This assay measures PFK activity by linking the product fructose-1,6-biphosphate to the downstream enzymes aldolase, triose isomerase (TIM) and glycerol-3-phosphate dehydrogenase (G3PDH), as shown in **figure 2.4** below. All auxiliary enzymes and reagents were sourced from Sigma-Aldrich. Reaction volumes per well were 100 µL.

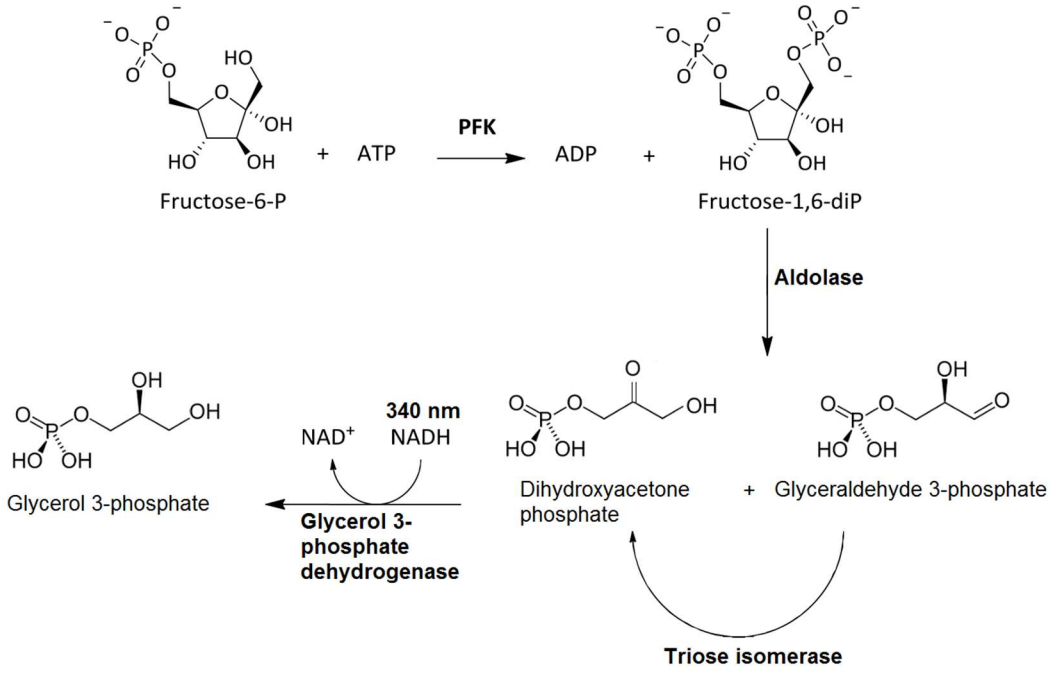

Figure 2.4: Aldolase/G3PDH/TIM linked enzyme reaction scheme.

2.3.2.1 Aldolase/G3PDH/TIM linked enzyme assay for measuring PFK activity.

A 2.5X 'assay mix' was made containing 5U/ml G3PD, 2.5 U/ml aldolase (A2714), 25 U/ml TIM, 1.25 mM NADH and 2.5 mM ATP using assay buffer (50 mM TEA, 100 mM KCl, 10 mM $MgCl_2$, 10% glycerol, pH 7.4). 40 µl of assay mix was plated in a clear, non-binding 96 well plate (Greiner Bio-One cat. no. 655901) with 4-10 µl of the PFK sample to be tested and 40 – 46 µl of assay buffer. This was to allow for variable protein stock concentrations to be tested. The reaction was started upon addition of 10 µl of 6mM F6P (0.6 mM final). Where required, TbPFK was used as a positive control by adding 4 µl of a 0.1 mg/ml stock to 40 µl assay mix and 46 µl assay buffer. Absorbance at 340 nm was read with 20 second intervals for 10 minutes in 'kinetic mode' at 25 ^{o}C on a Spectramax© M5 Multicode plate reader.

2.3.2.2 Aldolase/G3PDH/TIM linked enzyme assay for measuring PFK inhibition

A 2.5X assay mix was used as described above, with assay buffer (as in **2.3.2.1**) but with 12.5 mM ATP (5 mM final). A 2-fold serial dilution of 100X inhibitor compound stocks in 100% DMSO was carried out in a PCR plate. Inhibitor titrations were chosen according to known solubility or previous IC_{50} data, typically in the range of 100 – 0.78 µM, 20 – 0.16 µM or 5 – 0.04 µM (final concentration at 1% DMSO). 40 µL of assay mix, followed by 45 µL assay buffer, 4 µL of 0.1 mg/ml PFK and 1 µL of 100X serially diluted inhibitors were added to a non-binding, clear 96-well plate (Greiner Bio-One 655901) and incubated at room temperature for 10 minutes. The reaction was started by addition of 10 µL of 6 mM F6P. A known *Tb*PFK inhibitor ('CTCB-001' and later 'CTCB-405') was used as a positive control to a final concentration of 5 µM (>2x known IC_{50}). DMSO was used in place of inhibitor for a negative control. Where possible a multichannel pipette using non-binding tips (Tip-One cat. no. S1180) was used to reduce error. The A_{340} was measured in using a Spectramax© M-5 multi-mode plate reader (Molecular Devices) in kinetic mode. Readings were taken over 10 minutes, 25 seconds apart at 25 ^{o}C. All compounds were tested in duplicate. Data analysis was carried out as described in **section 2.3.1.3**.

When tested, human muscle PFK (PFK-M) was used as above at a concentration of 4 µg/ml. ATP was added to the 2.5X assay mix at a concentration of 2.5 mM (1mM final). PFK-M was expressed, purified and kindly donated by Dr P. Fernandes, UoE.

When used, ADP was added after 10 mins RT incubation of PFK with the assay mix containing ATP.

2.3.3 Data analysis for kinetic assays.

Kinetic data for PFK activity measured in the PYK/LDH, Aldolase/TIM and PGI/G6PDH (reverse) activity assays was analysed using GraphPad Prism ver. 6 software. PFK velocity was plotted as a function of substrate concentration and analysed by non-linear regression. Curves were fitted using Michaelis-Menten (**figure 2.5**) and/or allosteric sigmoidal (**Figure 2.6**) models. The concentration of substrate that provided the half maximal enzyme activity ($V_{max}/2$) was recorded as the K_m (Micaelis-Menten plots) and K_{half} (allosteric sigmoidal plots) values.

$$Velocity = \frac{Vmax * [Substrate]}{Km + [Substrate]}$$

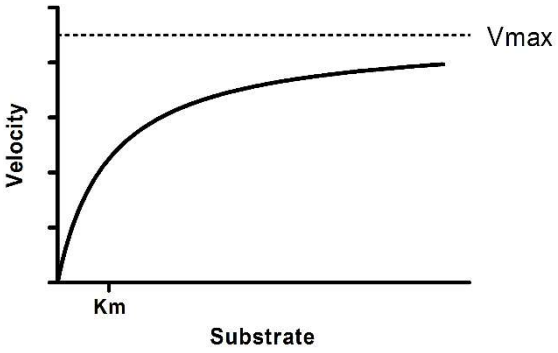

Figure 2.5: Michaelis-Menten plot equation.

$$Velocity = \frac{Vmax * [Substrate]^h}{(Khalf^h + [Substrate]^h)}$$

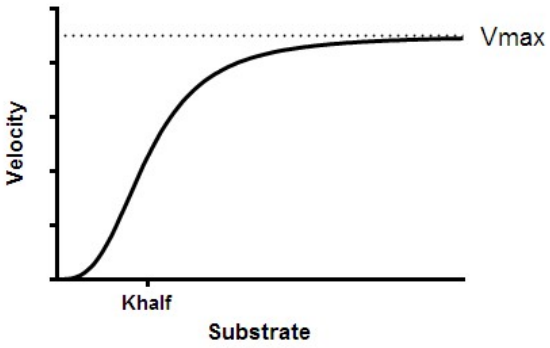

Figure 2.6: Allosteric sigmoidal plot equation.

2.3.4 ADP-Glo™ assay

This is an end-point assay manufactured by Promega (cat. No. V9102) that measures ADP produced in a kinase reaction. Following the kinase reaction, the addition of a reagent results in any unused background ATP being removed and the sequestering of the kinase reaction. A second reagent is then added to convert the remaining ADP to ATP which is coupled to the luciferase/luciferin reaction to produce light (**figure 2.7**). The assay was carried out in white,

non-binding 96-well plates (Greiner Bio-One 655904). 'Ultrapure' stocks of ATP and ADP provided by Promega were used to reduce background noise. All reagents additional to those provided in the Promega ADP-Glo™ kit where purchased from Sigma-Aldrich. Measured luminescence units can be converted to ADP concentrations through a standard ADP/ATP titration curve (**figure 2.8**). All ADP-Glo™ assays were carried out with a 25 µL kinase reaction volume at 25 °C.

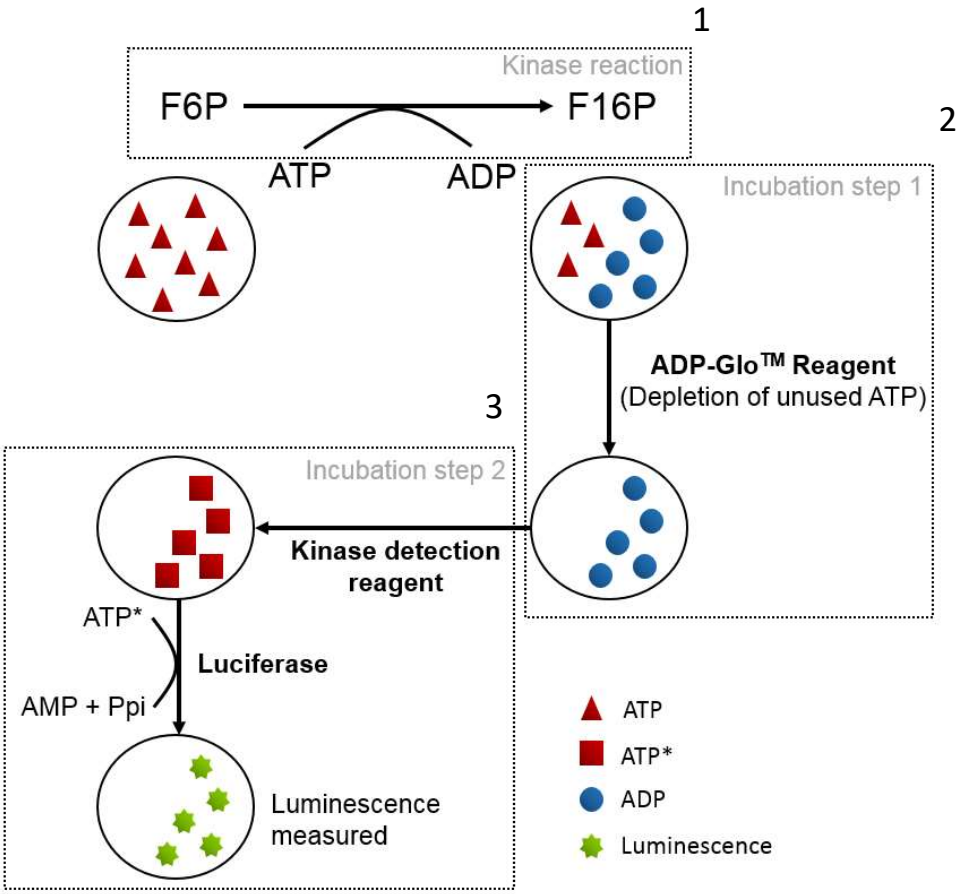

Figure 2.7 ADP-Glo™ assay reaction scheme

Assay is carried out in 3 steps: 1) Kinase reaction is run at 25 °C. 2) Incubation step 1: ADP-Glo reagent is added and background ATP is sequestered. 3) Incubation step 2: kinase detection reagent added. ADP is converted back into ATP and used in the luciferase/luciferin reaction and light is produced.

2.3.4.1 ADP-Glo™ assay for measuring PFK inhibition

A TEA-based assay buffer was used (50 mM TEA, 10 mM $MgCl_2$, 5 mM KCl, 0.1% w/v bovine serum albumin (BSA), 0.005% $Tween_{20}$, 1% DMSO, pH 7.4).. A 3-fold serial dilution of 250X inhibitor stocks carried out in 100% DMSO. 2 µL of these dilutions was added to 198 µL assay buffer and mixed well using a multichannel pipette. A visual inspection of these dilutions was

carried out to check for solubility at 1% DMSO. Concentration ranges of inhibitor compounds were chosen according to known solubility and/or IC_{50} data. Typical concentrations of compounds were 40 – 0.018 µM, and 14 – 0.006 µM (final concentration, 1% DMSO). The PFK reaction in the presence of inhibitor is carried out initially; 10 µL of 1 µg/ml PFK (final concentration 0.4 µg/ml) was added to 10 µl of the 1% DMSO inhibitor compound serial dilutions in a white, non-binding 96-well plate (Greiner BioOne 655904). CTCB-001 or CTCB-405 compounds were used as a positive control at a final concentration of 5 µM. Assay buffer containing 1% DMSO was added instead of inhibitor compound for the negative control. The protein/inhibitor mixture was incubated for 10 minutes at room temperature. The kinase reaction was started upon addition of a 5X ATP/F6P stock in assay buffer (final concentrations 0.5 mM F6P and 0.1 mM ATP). Plates were then sealed, centrifuged at 1000X RPM for 30 seconds and incubated at RT for 30 minutes. 25 µL of 'ADP-Glo™ Reagent' was then added to each well, mixed using a multichannel pipette and incubated at room temperature for 40 minutes. 50 µL of 'Kinase Detection Reagent' was added and incubated for 50 minutes at room temperature.

The luminescence was recorded using a Spectramax© M5 Multi-mode Plate Reader (Molecular Devices) in end-point mode, with 750 msec integration time.

2.3.4.2 Data analysis of ADP-Glo assay for measuring inhibition.

The raw luminescence values were converted to ADP concentration using a calibration curve for ADP standards (**figure 2.8**).

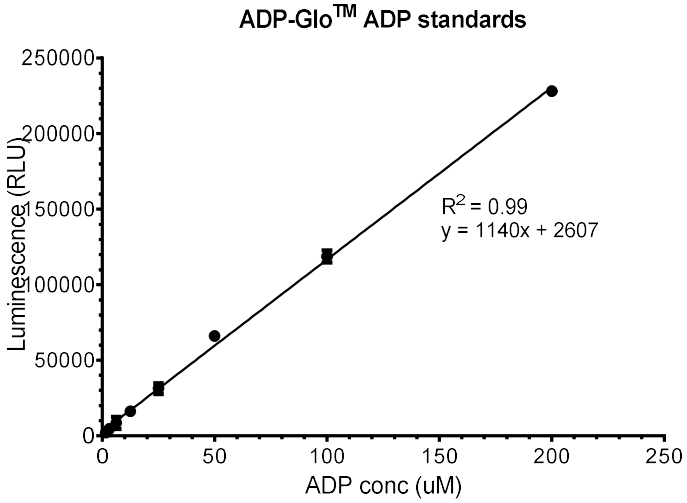

Figure 2.8: Calibration curve for ADP standards in ADP-Glo™ assay.

Carried out in ADP-Glo buffer (50 mM TEA, 10 mM $MgCl_2$, 5 mM KCl, 0.1% w/v (BSA), 0.005% $Tween_{20}$, 1% DMSO, pH 7.4) at 25°C.

The resulting ADP concentrations were plotted as a function of inhibitor compound concentration using Kaleidagraph 4.0 software. The data was analysed using non-linear regression and a sigmoidal curve was fitted (**figure 2.9**) to determine the IC_{50} – the concentration of inhibitor that leads to 50% inhibition of maximal enzyme activity. Kaleidagraph 4.0 uses the Levenberg-Marquardt algorithm in an iterative process to fit non-linear curves. The equation for the sigmoidal curve given in **figure 2.9** was fitted by using the positive control (100% inhibition of PFK – 5 µM CTCB 001 or '405) as the minimum constraint (m1) and the negative control (no inhibition of PFK - 1% DMSO) as the maximum constraint (m2) of the curve. The slope of the curve at the midpoint (m4) was set to 1.

$$velocity = \frac{m1 + (m2 - m1)}{(1 + (\frac{[inhibitor]}{IC_{50}})^{m4}}$$

Where m1 = Minimum velocity, m2 = maximum velocity and m4 = slope of curve at midpoint.

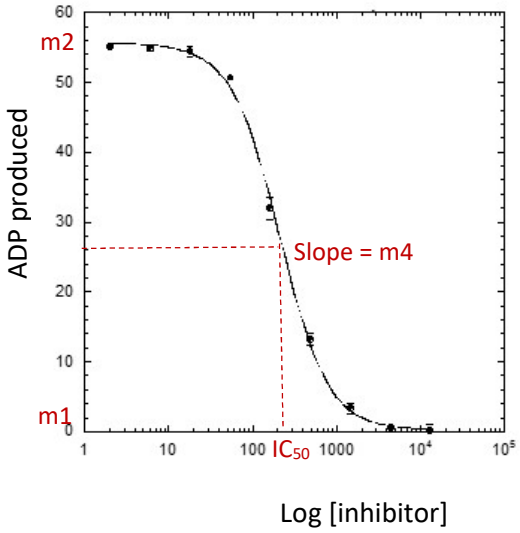

Figure 2.9: Sigmoidal plot equation for inhibition assays (ADP-Glo assay).

Equation used to plot dose-response curves and measure the IC_{50} of CTCB compounds against PFK. M1 = minimum ADP produced control (5 µM CTCB 001/405). M2 = max. ADP produced control (DMSO).

2.3.5 Kinase-Glo® assay

This is an end-point assay manufactured by Promega (cat. No. V6713) that measures ATP-consumption by a kinase reaction by linking any remaining ATP to the luciferase/luciferin reaction to produce light. Measured luminescence units were converted to ATP concentrations through a standard ATP titration curve (data not shown). All assays were carried out in white, non-binding flat-bottomed 96-well plates (Greiner BioOne 655904) with a final reaction volume of 50 µL.

2.3.5.1 Kinase-Glo® assay to measure PFK inhibition.

A TEA-based assay buffer was used (50 mM TEA, 10 mM $MgCl_2$, 5 mM KCl, 0.1% w/v BSA, 0.005% $Tween_{20}$, 1% DMSO, pH 7.4). A 3-fold serial dilution of 250X inhibitor stocks carried out in 100% DMSO. 2 µL of these dilutions was added to 198 µL assay buffer and mixed well using a multichannel pipette. A visual inspection of these dilutions was carried out to check for solubility at 1% DMSO. Concentration ranges of inhibitor compounds were chosen according to known solubility and/or IC_{50} data. Typical concentration ranges of compounds were 40 – 0.018 µM, and 14 – 0.006 µM (final concentration, 1% DMSO). The PFK reaction in the presence of inhibitor is carried out initially; 10 µL of 1 µg/ml PFK (final concentration 0.4 µg/ml) was added to 10 µl of the 1% DMSO inhibitor compound serial dilutions in a white, non-binding 96-well plate (Greiner BioOne 655904). CTCB-001 or CTCB-405 compounds were used as a positive control at a final concentration of 5 µM. Assay buffer containing 1% DMSO was added instead of inhibitor compound for the negative control. The protein/inhibitor mixture was incubated for 10 minutes at room temperature. The kinase reaction was started upon addition of a 5X ATP/F6P stock in assay buffer (final concentrations 0.5 mM F6P and 0.1 mM ATP). Plates were then sealed, centrifuged at 1000X RPM for 30 seconds and incubated at RT for 30 minutes. 25 µL of 'Kinase-Glo® Reagent' was then added to each well and incubated at RT for 30 minutes.

The luminescence was recorded using a Spectramax© M5 Multi-mode Plate Reader (Molecular Devices) in end-point mode, with 750 msec. integration time. Data was analysed as described in **section 2.3.4.2**.

2.3.5.2 Kinase Glo assay for measuring reverse PFK activity.

The reverse PFK assays were carried out in standard assay buffer (50 mM TEA, 10 mM MgCl2, 5 mM KCl, 0.1% w/v BSA, 0.005% $Tween_{20}$, 1% DMSO, pH 7.4). 40 µL of a PFK solution (final concentration 2 µg/ml) with ADP (final concentration 5mM) was incubated at room temperature for 10 minutes. The kinase reaction was started upon addition of 10 µL of a 5X F16BP stock (final concentration 5 mM) in assay buffer. All substrates were buffered to pH 7.4 before use. Plates were then sealed, centrifuged at 1000X RPM for 30 seconds and incubated at RT for 30 minutes. 25 µL of 'Kinase-Glo® Reagent' was then added to each well and incubated at RT for 30 minutes. Luminescence was measured as stated in **2.3.5.1**.

2.3. Phosphofructokinase reverse reaction assays.

2.4.1 PGI/G6PDH linked enzyme assay - reverse PFK activity.

This assay measures the formation fructose-6-phosphate (F6P) from F16BP as a product of reverse PFK activity by linking its production to the downstream enzymes phosphoglucose isomerase (PGI) and glucose-6-phosphate dehydrogenase (G6PDH) as shown in **figure 2.10** below. The reduction of NAD+ to NADH by the latter enzyme can be measured by recording absorbance at 340 nm. Glycerol kinase (GK) was used as an auxiliary kinase to prevent ATP accumulation. All reagents and auxiliary enzymes were purchased from Sigma Aldrich.

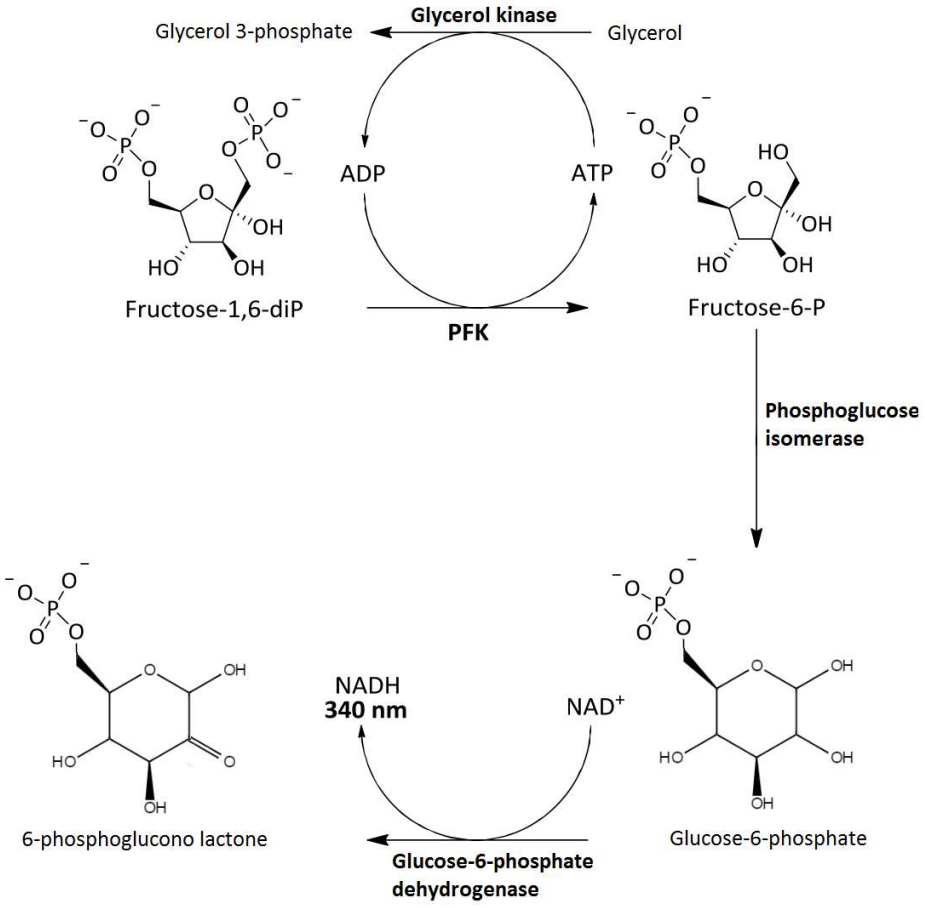

Figure 2.10: PGI/G6PDH linked enzyme assay reaction scheme.

2.4.1.1 PGI/G6PDH linked enzyme assay for measuring reverse PFK kinetics.

A 2.5X 'assay mix' containing 0.75 mM NAD+ (Sigma NAD100-RO), 10 U/ml G6PDH (Sigma/Roche G8529), 2.2 U/ml PGI (Sigma P9544) and 12.5 U/ml GK (Sigma G0774) was made up in assay buffer (50 mM TEA, 10 mM $MgCl_2$, 100 mM KCl, 10 % glycerol, 0.005 % $TWEEN_{20}$, pH 7.4). 40 µl

of assay mix was plated in a clear, non-binding 96 well plate (Greiner Bio-One cat. no. 655901) with 10 µL 20 µg/ml PFK and 10 µL 20mM ADP (or ADP titration). When used, AMP was added to a final concentration of 0.5 mM prior to the addition of ADP and the mixture was incubated for 10 minutes at room temperature. The reaction was started by addition of 20 µL of 50 mM F16BP (or 5X F16BP titration). Absorbance at 340 nm was read with 25 second intervals for 15 minutes at 25 ^{o}C in 'kinetic mode' on the Spectramax© M5 Multicode plate reader.

Data was analysed similar to that of the PYK/LDH and aldolase/TIM assays – see **section 2.3.3.**

2.4.1.2 PGI/G6PDH linked enzyme assay for measuring reverse PFK inhibition.

A 2-fold serial dilution of 100X inhibitor 'working' stocks in 100% DMSO was carried out in a PCR plate. Inhibitor titrations were chosen according to known solubility or previous IC_{50} data, typically in the range of 100 – 0.78 µM, 20 – 0.16 µM or 5 – 0.04 µM (final concentration at 1% DMSO). A 1.6X 'assay mix' (2 U/ml PGI, 0.5mM NAD+) was made up in assay buffer (10 mM $MgCl_2$, 50 mM TEA, 100 mM KCl, 10 glycerol, 0.005 % $TWEEN_{20}$, 1% DMSO, pH 7.4). 60 µl of assay mix was plated in a clear, non-binding 96 well plate (Greiner Bio-One cat. no. 655901) with 4 µL 0.1 U/µL G6PDH (Sigma no. G8529), 10 µL 20 µg/ml PFK, 1 µL of 100X inhibitor dilutions and 10 µL 20mM ADP. Plates were incubated for 10 minutes at room temperature. The reaction was started by addition of 20 µL of 10 mM F16BP. Absorbance at 340 nm was read with 25 second intervals for 15 minutes at 25 ^{o}C in 'kinetic mode' on the Spectramax© M5 Multicode plate reader.

Data was analysed with the same protocol as the inhibition assays in the PYK/LDH assay – see **section 2.3.1.3**.

2.4.2 Kinase-Glo® assay for measuring reverse reaction.

The same Promega Kinase-Glo® assay kit as described in **section 2.3.5.2** was also used to measure PFK reverse activity.

2.4. Biophysical analysis.

2.5.1 Dynamic light scattering of trypanosomatid PFKs.

Dynamic Light Scattering (DLS) involves focusing infra-red (IR) light on a sample of protein held in solution in a vertical capillary. The particles in solution move according to Brownian motion. The movement of particles scatters the infrared light and the diffraction pattern is measured on a detector behind the capillary (**figure 2.11**).

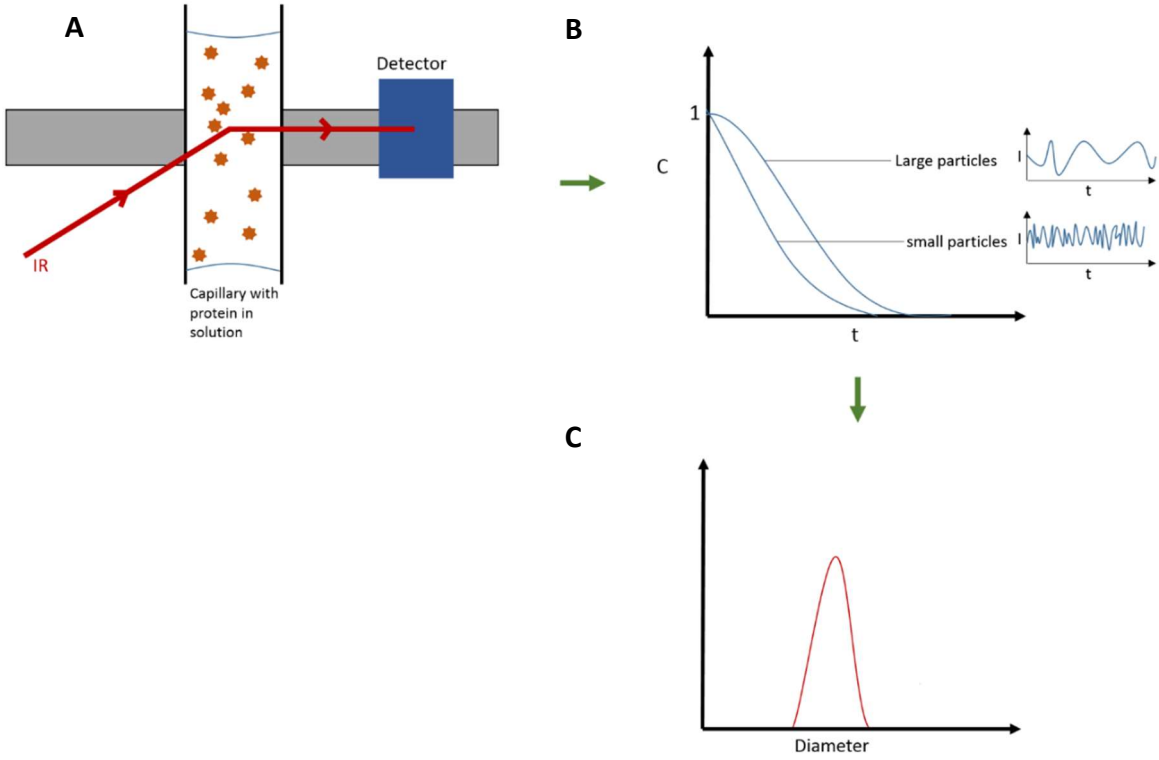

Figure 2.11: Schematic of dynamic light scattering steps.

A) Infra-red light is focused onto capillary containing protein molecules in solution. Scattering of light by diffusion of molecules is measured on a detector.

B) The correlation factor of the scatter (C) is plotted against time. The diffusion coefficient of the molecules is calculated from this plot. Smaller molecules have a faster exponential decay of the correlation factor than large particles.

C) Using the Stokes-Einstein equation, the radius of the particles can be calculated, and the distribution of different sizes particles within the population are plotted by 'intensity' and by 'volume'.

The rate at which spherical particles diffuse in solution is related to the size of the particles, and the two are linked by the Stokes-Einstein equation:

$$d = \frac{K_B T}{3\pi D \eta_0}$$ Stokes-Einstein equation

Where d = hydrodynamic diameter, K_B = Boltzmann constant, T = absolute temperature (Kelvin), D = diffusion coefficient and η_0 = viscosity of solution. Using this equation and the diffusion coefficient calculated from the plot of correlation factor against time (**figure 2.11B)**, the hydrodynamic diameter can be calculated. Assuming the protein particles to be roughly spherical in shape, this allows a calculation of the size of the protein molecules. The primary goal of DLS however is to assess the population of protein molecules. By plotting the populations of particles of various sizes (**figure 2.11C**), we can use DLS to show if a protein sample is monodisperse (a population of protein where the particles are all the same size) or if there are aggregates or contaminants in the sample (shown by a range of particles with differing hydrodynamic diameters).

All DLS experiments were carried out using a Zetasizer APS instrument (Malvern). 50 µL of sample was added per well in a 384-well plate . *T. brucei, T. cruzi* and *L. infantum* PFKs were tested at concentrations of 0.6, 0.7 and 0.5 mg/ml respectively. All samples were centrifuged at 4000 rpm for 10 minutes at 10 ^{o}C. All protein samples were tested in triplicate in a TEA – based buffer containing 20mM TEA, 10 mM $MgCl_2$, 50 mM KCl, pH 7.4. This buffer gave a viscosity of 1.14 cP – as calculated by the dedicated Zetasizer software. All analysis and graph plotting was carried out using this software.

2.5.2 Thermal Denaturation Assay (TDA).

Thermal Denaturation Assays (TDA) can be used to assess the thermal stability of proteins by measuring the transition melting temperature (T_m). The protein sample is subjected to an incremental temperature range in the presence of a environment-sensitive fluorescent dye such as SYPRO orange. Upon protein denaturation the protein unfolds and the surrounding dye is exposed the exposed hydrophobic residues, causing a rapid increase in fluorescence. A BioRad 'IQ5 ICycler' RT-PCR machine was used to carry out all TDA experiments. Sypro Orange (Life Technologies, S6650) fluorescent dye was used (ex/em 485/575 nm). Experiments were carried out in 96-well PCR plates (BioRad, 2239441) sealed with dedicated PCR seals (BioRad, MSB1001) with 50 µL assay volume.

2.5.2.1 TDA for measuring natural ligand binding.

The effect on thermal stability of *T. brucei, T. cruzi* and *L. infantum* PFKs in presence and absence of AMP, ADP, F6P and F16BP was carried out. The reaction buffer contained 50 mM TEA, 10 mM $MgCl_2$, 5 mM KCl, 10% glycerol and 0.005% $Tween_{20}$ at pH 7.4. A reaction volume of 50 µL was used, containing: 10 µL analyte (final concentration 1mM), 5 µL 50X Sypro orange dye (5X final) and 35 µL PFK (1.9 µM final). Each condition as tested in triplicate. A negative control containing buffer in place of an analyte, a background control (containing buffer and dye only) and an analyte control (containing only analyte and dye) were also carried out in triplicate. Plates were sealed, centrifuged at 1000 rpm for 30 seconds and subjected to a temperature range of 20 – 80 ^oC in 0.5 ^oC increments, with 30 second intervals between temperature increases. Plots of RFU v temperature and –d(RFU)/dt were exported from the BioRad software and plotted in Graphpad Prism to calculate the Tm. The average T_m and standard deviation was reported.

2.5.2.2: TDA for measuring ADP/AlF3/F16BP complex.

Various combinations of 1.25 mM solutions of ADP, AlF_3 and F16BP were made up in TEA buffer (50 mM TEA , 10 mM $MgCl_2$, 5 mM KCl, 10% glycerol, 0.005% $TWEEN_{20}$, pH 7.4). 40 µL of these solutions was added to the 96-well PCR plates with 5 µL of 50X Sypro orange. 5 µl of 20 µM *Tb*PFK was then added to each condition and allowed to incubate at room temperature for 15 minutes before the TDA protocol outlined in **section 2.5.2.1** was carried out.

2.5.2.3: TDA for determining K_d of *Tb*PFK for AMP.

A 1.5X 2-fold serial dilution series of AMP was made up in TEA buffer (50 mM TEA, 10 mM $MgCl_2$, 5 mM KCl, 10% glycerol, 0.005% $TWEEN_{20}$, pH 7.4). 35 µl of this AMP titration was added to each well in the 96 well PCR plate. 5 µL of 50X Sypro orange was added. 10 µL of trypanosomatid PFK was then added (2µM final). When used, ATP was added to the PFK stock to a concentration of 3.75 mM (0.75 mM final) and allowed to incubate with the protein for 10 minutes at room temperature. All stocks were buffered to pH 7.4 before use. Thermal melt temperatures were plotted against concentration of AMP and a curve was fitted using the Langmuir isotherm equation (below) for nonlinear regression in Graphpad Prism 6.0, shown in figure **4.15.**

$$Tm = \frac{Tm(AMPmax) * [AMP]}{(Kd + [AMP])} + c$$

Where c = T_m of PFK sample alone.

2.5.3 Surface Plasmon Resonance (SPR).

SPR assays measure the change in the angle of a wave of excited electrons known as a surface plasmon resonance (SPR) as polarised light is focused and refracted off a gold surface onto which a population of protein has been immobilised (**figure 2.12**). The SPR wave is sensitive to the amount of material on the gold surface – the refractive index. The binding of an analyte to this protein surface causes a change in the refractive index due to the build-up of material, and this changes the angle of the plasmon resonance. This change in angle is recorded in real time as resonance units (RU) (Wear, Blackburn, & Nowicki, 2009). As binding response is measured in real time, steady state kinetics, on and off rates can be determined. All SPR experiments were carried out on a GE Healthcare Biacore™ T200 instrument

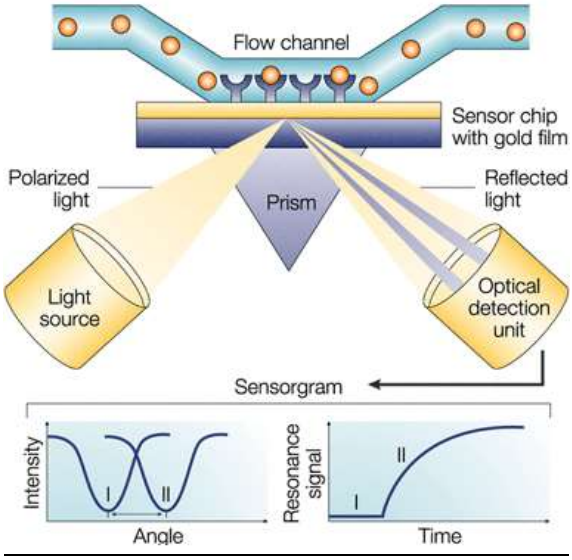

Figure 2.12: Surface plasmon resonance (SPR) schematic.

As material binds to immobilised protein on a gold surface, the change in the refractive index of the material leads to the change in angle of refracted light close to the protein surface (from I to II). This change is recorded and plotted as a response over time in a sensorgram. Image adapted from (Cooper, 2002).

2.5.3.1 Trypanosomatid PFK immobilisation for SPR assays.

Active N-terminally His_6-tagged *T. brucei, T. cruzi* and *L. infantum* PFK surfaces were generated by using a capture/stabilisation method optimised at the Centre for Translational and Chemical Biology (CTCB) at the University of Edinburgh(Wear & Walkinshaw, 2006)(Martin A. Wear, Nowicki, Blackburn, McNae, & Walkinshaw, 2017). Surface densities corresponding to ~1,500 –

13, 000 resonance units (RU) were immobilised on Ni^{2+}-nitrilotriacetic acid (NTA) sensor chips (GE Healthcare).

The surface was first primed with 500 µM $NiSO_4$. The dextran matrix on the chip was then activated using 0.2M 1-ethyl-3-(3-dimethylaminopropyl) carbodiimide (EDC) and 50 mM N-hydroxysuccinimide (NHS) to give reactive succinimide esters. EDC and NHS were injected at a rate of 5 $\mu L.min^{-1}$ for 500 seconds. 20 - 50 nM PFK in HBS buffer (10 mM HEPES, 150 mM NaCl, 0.05% P_{20}, pH 7.4) was washed over the surface at 30 ml/min until saturation in response was achieved. The PFK tetramers were captured via the N-terminal His_6 tags co-ordinating with the charged Ni^{2+} NTA groups (**figure 2.13**). 350 mM EDTA was washed over to strip any divalent ions off the surface, followed by ethaloamine (a primary amine) to quench any remaining active succinimide esters. **Figure 2.13** below summarises the surface preparation.

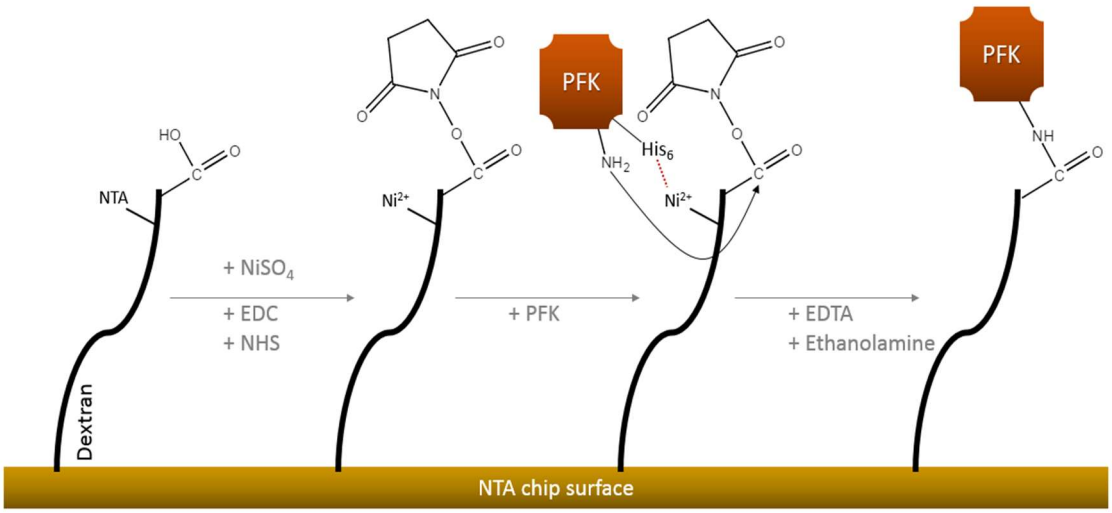

Figure 2.13: PFK is immobilised to the SPR chip via His-tag orientation and covalent binding with succinimide esters.

All SPR data analysis was carried out using the dedicated Biacore T200 evaluation software ver. 1.0 (GE healthcare). Steady state and kinetic parameters were calculated by fitting a 1:1 binding model to the sensorgram traces. Analyte binding responses reference subtracted and corrected for molecular weight.

2.5.3.2 SPR for measuring binding of PFK substrates and metabolites.

20 nM of *T. brucei, T. cruzi* and *L. infantum* PFK was used to create surfaces with ~3000 RU (*Tb*PFK *and Tc*PFK) and ~2400 RU (*Li*PFK). Substrates and other metabolic analytes were made

up and buffered in HBS buffer (10mM HEPES, 150 mM NaCl, 10 mM $MgCl_2$, 0.05 % $TWEEN_{20}$, pH 7.4). Analytes were made up in 2.5-fold serial dilutions with concentration ranges: AMP‡, ADP, ATP‡, GTP, GDP, F6P, F16BP, F26BP – 10 mM – 7.8 µM. Citrate, PPi, Phosphoenolpyruvate (PEP) – 20 mM – 156 µM. ‡1 mM when tested alongside another analyte. Analytes were tested against low density *Tb*PFK, *Tc*PFK and *Li*PFK surfaces of 1,500 – 300 RU. Analytes were washed over the surfaces at a rate of 30 $\mu L.min^{-1}$ with 30 second contact times and washed off with HBS running buffer (as above) for 30 seconds. When analytes were tested in the presence of AMP or ATP, these analytes were added to a concentration of 1 mM to the HBS running buffer and all analyte dilution series were made up in this buffer.

2.5.3.3 SPR for measuring binding of inhibitor compounds to PFK.

CTCB inhibitor compounds were screened against active *T. brucei* and *T. cruzi* PFK surfaces. 50 nM of PFK protein was used to create surfaces initially of 11,000 – 13, 000 RU. Later less crowded *Tb*PFK surfaces of ~1,500 RU were used. Compounds were first screened at 50 µM in HBS running buffer (10 mM HEPES; 150 mM NaCl, pH 7.4; 50 µM EDTA; 0.05 % P20; 1 % DMSO) and ranked compared to a normalised standard (CTCB-001 and CTCB-405). Run parameters were 30 µl.min-1, 15-second contact and 60-second dissociation times. Responses were corrected for molecular weight and bulk shift. Inhibitors which showed clean binding responses relative to the standard were further tested in a 2-fold dilution series ranging from 25 – 0.19 µM or 50 – 0.38 µM (solubility permitting) in HBS running buffer (as above). Steady state and kinetic parameters for a 1:1 binding model with mass transport correction were obtained using the dedicated Biacore T200 evaluation software.

2.5.3.4 SPR for measuring compound binding to human serum albumin (HSA).

Active His_6-*Tb*PFK surfaces were generated by using a capture/stabilization method (Wear & Walkinshaw, 2006). Surfaces of ~ 12,000 RU were immobilized on an NTA sensor chip. Additionally, monomeric human serum albumin (HSA) (Sigma A3782), fatty acid and globulin free, and purified to homogeneity in 10 mM HEPES; 150 mM NaCl, pH 7.4; 50 µM EDTA; 0.05 % P20, using a Superdex200 10/300 GL column) was immobilized to 12,600 RU using standard amine coupling chemistries . Single point screens at 50 µM were performed, with solvent correction, running simultaneously over both *Tb*PFK and HSA surfaces, with flow cell 1 (F_c1) as the bulk-shift reference surface, and responses corrected for molecular weight. Following visual assessment of each compound and ranking of response using CTCB 001 as the normalized standard selected compounds were run with a 2-fold dilution series (in the range from 50 µM – 0.39 µM) in HBS (10 mM HEPES; 150 mM NaCl, pH 7.4; 50 µM EDTA; 0.05 % P20; 1 % DMSO).

Run parameters were 30 µl.min^{-1}, 15 second contact and dissociation times (increased stabilization times were introduced between runs for compounds exhibiting slow multiphasic binding; see below). Kinetic and steady-state affinity values were fitted to 1:1 binding model with solvent correction. A two-state model was used to try and account for multiphasic binding behaviour against the HAS surface. Analytical-standard Warfarin (Sigma A2250) was used as a positive binding control against the HSA surface.

2.5.3.5 SPR for measuring compound binding thermodynamics against PFK.

To measure the thermodynamic properties of CTCB compound binding to PFK a low density (~1,500RU) and medium density (~6000 RU) surface of active T. brucei PFK were immobilised in pairs (Fc1 and Fc3 were left as reference cells for bulk-shift correction). Run parameters were 30 µl.min-1, 15-second contact and 60-second dissociation times. A 2-fold dilution series ranging 50 – 0.062 µM of CTCB compounds was carried out in HBS buffer (10 mM HEPES; 150 mM NaCl, pH 7.4; 50 µM EDTA; 0.05 % P20; 1 % DMSO). Each dilution series was run at 5 – 41 °C with 3°C increments. Steady state and kinetic parameters were measured by fitting a 1:1 binding model to sensorgrams using the dedicated Biacore T200 evaluation software. Thermodynamic parameters were calculated using van't Hoff plots of (InK_d against 1/T) and thermodynamic properties were calculated according to the van't Hoff equation :

$$InK_d = \left(\frac{\Delta H^\circ}{RT}\right) - \left(\frac{\Delta S^\circ}{R}\right) \quad \text{van't Hoff equation}$$

Where K_d = equilibrium dissociation constant, R = universal gas constant, T = absolute temperature (K) ΔH^o = enthalpy change and ΔS^o = entropy change. Taking the change in heat capacity of the system into account, the equation used was:

$$RTInK_d = \Delta H^\circ_{T^\circ} - T\Delta S^\circ_{T^\circ} + \Delta Cp^\circ(T - T_o) - T\Delta Cp^\circ In\left(\frac{T}{T_o}\right)$$

Where ΔCp^o = change in heat capacity and T_o is the reference temperature (298K) (Martin A. Wear et al., 2017). Van't Hoff plots were plotted using Kaleidagraph 4.0 software.

2.5.4 Isothermal titration calorimetry (ITC).

ITC measures the change of heat upon the binding of analyte to ligand in a thermally isolated (adiabatic) cell. The apparatus includes two cells: a sample cell containing the macromolecule(PFK) and a reference cell. The ligand (CTCB compound) is held in a syringe and titrated into the sample cell. A constant power is applied to the reference cell and acts as a feedback circuit to the sample cell. This maintains the two cells at the same temperature (ΔT=0). Upon binding of ligand to protein, heat is given out or taken in. This temperature difference

between the cells is detected by a calorimeter and the power applied to the sample cell is adjusted accordingly. The power used to maintain ΔT = 0 between the cells is the baseline. The change in reference power upon ligand and analyte interaction is measured as peaks (in endothermic reactions) or troughs (exothermic) showing the change in 'reference power' over time (µcal/sec). The heat evolved or absorbed during binding is quantified by integration of these peaks (**figure 2.14**)(Holdgate, 2001). ITC offers the ability to directly measure the enthalpy change from binding. As well as this ITC can be used to simultaneously measure the molar ratio (stoichiometry), the equilibrium constant (K_d) and entropy change (ΔS°) upon binding of ligand to protein.

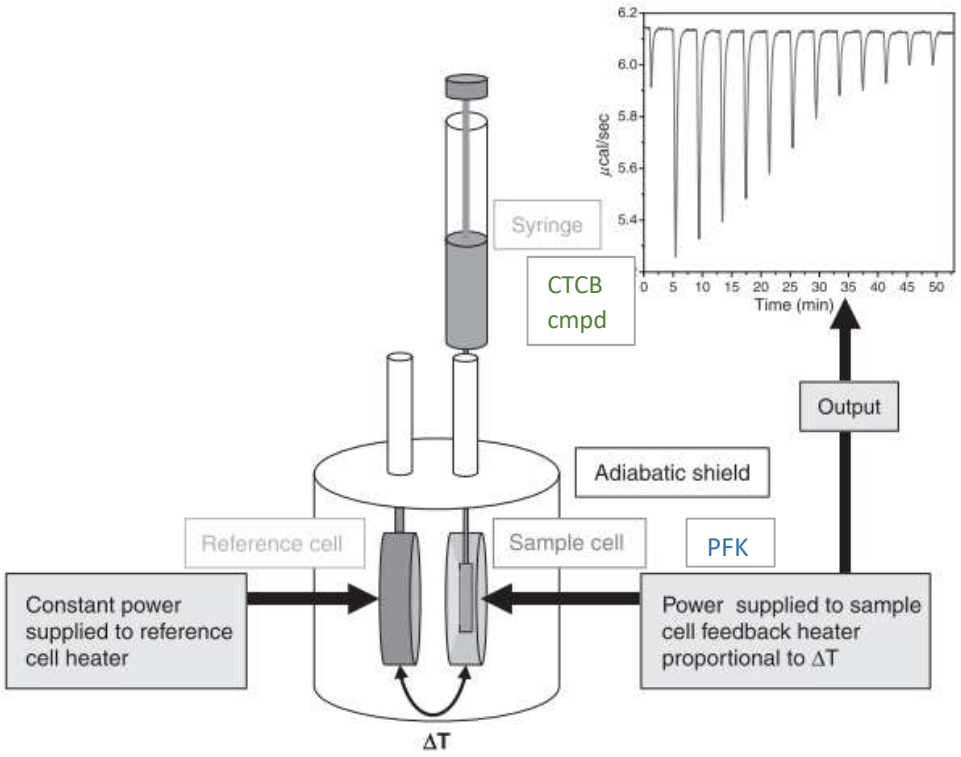

Figure 2.14: schematic of ITC for measuring CTCB compound binding.

CTCB compound is titrated into a cell containing PFK. The change in temperature ΔT is accurately measured by measuring the power (µcal/sec) required to heat or cool the sample cell so that ΔT=0 compared to the reference cell. Image adapted from Freyer & Lewis, 2008.

All ITC experiments were performed on a MicroCal auto-iTC200 with liquid handling robot (GE Healthcare). Both CTCB compounds and PFK protein were made up in HBS buffer (10 mM HEPES, 150 mM NaCl, 0.05 % P20, 1 % DMSO, pH 7.4). A 1:10 cell/syringe (protein/compound) ratio was

used for injections. Concentrations were adjusted according to compound stability and predicted K_d values. A Wiseman 'C-value' parameter of 10<C<100 was aimed for. To adjust for heat of dilution and check for buffer mismatch, controls where buffer was injected into protein and compound injected into buffer were carried out. 16 injections with 750 RPM stirring were carried out with 180 second delays between injections. Prior to syringe and cell filling, buffer, protein and compounds were stored at 15 ^{o}C, with injections carried out at 25 ^{o}C.

2.5.4.1: ITC data analysis.

Data was analysed using the dedicated MicroCal Origin® ITC analysis software. All raw injection peaks were adjusted for heat of dilution using the last 2 injections in each run. The raw injection peaks (**figure 2.15**) were baseline corrected and integrated to calculate the area underneath each peak (µcal). This data was plotted in Kcal per mole of injectant (y-axis, **figure 2.15**) against molar ligand : protein ratio (x-axis, **figure 2.15**). Curve fitting was carried out using the 'One set of sites' model. Curves were fitted by non-linear regression in an iterative process until the sum of squares (Chi^2) value was as low as possible. When ITC data was normalised (**section 6.4.6, chapter 6**), the stoichiometry ('N') parameter was fixed to 1.0 during curve fitting.

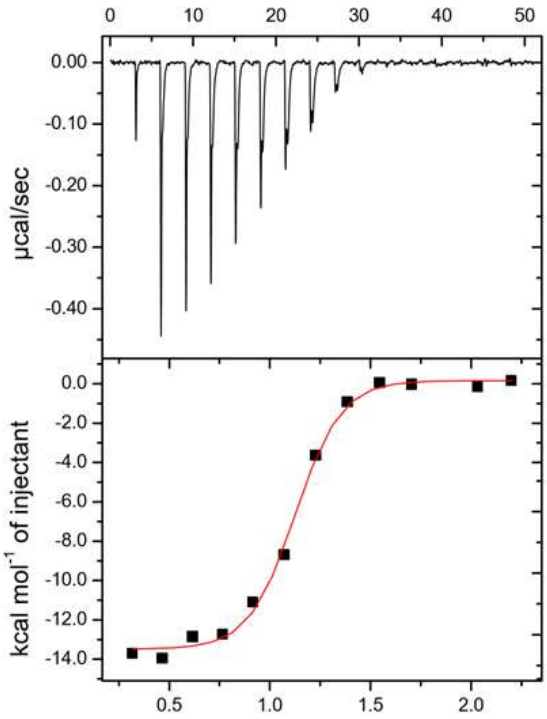

Figure 2.15: Example ITC analysis curves.

2.5. X-ray Crystallography

2.6.1 Robot screening

Automated robot crystal screens were conducted using an Art Robbins Instruments Gryphon LCP liquid handling robot. T. brucei PFK was used at a concentration of 3-4 mg/ml, mixed with 1mM ADP, F16BP and AlF_3 (sigma) in TEA buffer (20 mM TEA, 5 mM $MgCl_2$, 100 mM KCl, 10% glycerol, 0.005 % $Tween_{20}$, pH 7.4). 200 nL drops containing 100 nL of screening buffer and 100 nL of protein were plated in a 96-well microplate, sealed and crystals left to grow at 16 ^oC. Molecular Dimensions' 'JCSG-plus' screening kit was used.

2.6.2 AlF_3 co-crystallisation

Equimolar (1mM) concentrations of Aluminium fluoride trihydrate (AlF_3) (Sigma 23609), ADP and F16BP (> 99% purity, Sigma) were made and mixed in TEA buffer (as in **2.6.1**). Crystals were plated using the hanging drop method with a 1:1 and 1:2 protein: well conditions ratio in 1 µL drops. Varying pH and precipitant concentrations were used in each well conditions using MES-hydrate (2-(N-morpholino)ethanesulphonic acid) buffer (Sigma M2933), Imidazole (Fisher 288-32-4) and Poly (ethylene glycol) Mn 4000 (Sigma 81240) in a 24-well Linbro plate (Molecular Dimensions). **Table 2.5** shows an example plate layout. Crystal wells were sealed and left to grow at 16 ^oC. Smaller or 'needle-like' crystals were vortexed with glass beads and used as micro seeds for optimisation. When used, 200 nL of this micro seeding mixture was added to a 2 µL drop.

	pH 6.1	pH 6.3	pH 6.5	pH 6.7	pH 6.9	pH 7.1
12% PEG	240 µL 50% PEG4K 72.0 µL 1M MES 28.0 µL 1M IMIDAZOLE 400 µL 50% GOL 260 µL H_2O	240 µL 50% PEG4K 67.0 µL 1M MES 33.0 µL 1M IMIDAZOLE 400 µL 50% GOL 260 µL H_2O	240 µL 50% PEG4K 61.2 µL 1M MES 38.8 µL 1M IMIDAZOLE 400 µL 50% GOL 260 µL H_2O	240 µL 50% PEG4K 55.0 µL 1M MES 45.0 µL 1M IMIDAZOLE 400 µL 50% GOL 260 µL H_2O	240 µL 50% PEG4K 50.0 µL 1M MES 50.0 µL 1M IMIDAZOLE 400 µL 50% GOL 260 µL H_2O	240 µL 50% PEG4K 45.0 µL 1M MES 55.0 µL 1M IMIDAZOLE 400 µL 50% GOL 260 µL H_2O
14% PEG	280 µL 50% PEG4K 72.0 µL 1M MES 28.0 µL 1M IMIDAZOLE 400 µL 50% GOL 220 µL H_2O	280 µL 50% PEG4K 67.0 µL 1M MES 33.0 µL 1M IMIDAZOLE 400 µL 50% GOL 220 µL H_2O	280 µL 50% PEG4K 61.2 µL 1M MES 38.8 µL 1M IMIDAZOLE 400 µL 50% GOL 220 µL H_2O	280 µL 50% PEG4K 55.0 µL 1M MES 45.0 µL 1M IMIDAZOLE 400 µL 50% GOL 220 µL H_2O	280 µL 50% PEG4K 50.0 µL 1M MES 50.0 µL 1M IMIDAZOLE 400 µL 50% GOL 220 µL H_2O	280 µL 50% PEG4K 45.0 µL 1M MES 55.0 µL 1M IMIDAZOLE 400 µL 50% GOL 220 µL H_2O
16% PEG	320 µL 50% PEG4K 72.0 µL 1M MES 28.0 µL 1M IMIDAZOLE 400 µL 50% GOL 180 µL H_2O	320 µL 50% PEG4K 67.0 µL 1M MES 33.0 µL 1M IMIDAZOLE 400 µL 50% GOL 180 µL H_2O	320 µL 50% PEG4K 61.2 µL 1M MES 38.8 µL 1M IMIDAZOLE 400 µL 50% GOL 180 µL H_2O	320 µL 50% PEG4K 55.0 µL 1M MES 45.0 µL 1M IMIDAZOLE 400 µL 50% GOL 180 µL H_2O	320 µL 50% PEG4K 50.0 µL 1M MES 50.0 µL 1M IMIDAZOLE 400 µL 50% GOL 180 µL H_2O	320 µL 50% PEG4K 45.0 µL 1M MES 55.0 µL 1M IMIDAZOLE 400 µL 50% GOL 180 µL H_2O
18% PEG	360 µL 50% PEG4K 72.0 µL 1M MES 28.0 µL 1M IMIDAZOLE 400 µL 50% GOL 140 µL H_2O	360 µL 50% PEG4K 67.0 µL 1M MES 33.0 µL 1M IMIDAZOLE 400 µL 50% GOL 140 µL H_2O	360 µL 50% PEG4K 61.2 µL 1M MES 38.8 µL 1M IMIDAZOLE 400 µL 50% GOL 140 µL H_2O	360 µL 50% PEG4K 55.0 µL 1M MES 45.0 µL 1M IMIDAZOLE 400 µL 50% GOL 140 µL H_2O	360 µL 50% PEG4K 50.0 µL 1M MES 50.0 µL 1M IMIDAZOLE 400 µL 50% GOL 140 µL H_2O	360 µL 50% PEG4K 45.0 µL 1M MES 55.0 µL 1M IMIDAZOLE 400 µL 50% GOL 140 µL H_2O

Table 2.5: Example crystallography plating scheme for TbPFK.

GOL = glycerol, MES = 2-(N-morpholino)ethanesulphonic acid). PEG4K = polyethylene glycol Mn 4000.

2.6.3 X-ray crystallography data collection.

Crystals were sent to the Diamond Light Source synchrotron in Oxfordshire for remote data collection on the I04 and I24 beamlines. Data was auto-processed using EDNA and MOSFLM software.

Chapter 3 : Expression, purification and characterisation of trypanosomatid PFKs.

3.1. Introduction.

The work in this chapter describes the expression, purification and enzyme activity of *T. brucei, T. cruzi, L. infantum, T. congolense and T. vivax* PFK enzymes. The basis of the purification of the PFK enzymes mentioned above was pioneered by the work of Cronin and Tipton in 1985 who purified the enzyme from populations of bloodstream-form *T. brucei* parasites in rats (Cronin & Tipton, 1985). These researchers later described the dependence of Mg^{2+} ions for the enzymatic activity of *T. brucei* PFK, the lack of inhibition at ATP concentrations exceeding 2 mM, the co-operative relationship to F6P binding, and the steady state enzyme kinetics of the protein (Cronin & Tipton, 1987). Later work in purifying PFK was facilitated from the identification of the *Tb*PFK gene from genomic libraries (Michels et al, 1997) and the recombinant expression and purification in *E. coli* (Keillor et al., 2003).

3.2. Trypanosomatid PFK sequences.

The target for the Seeding Drug Discovery (SDD) programme was specifically *T. brucei* PFK due to its role in Human African Trypanosomiasis (HAT). Traditionally *T. b. brucei* strains have been studied for this purpose. This strain differs from the disease-causing *T. b. rhodesiense* and *T. b. gambiense* subspecies by the loss of a single gene that normally prevents lysis of the parasite in human blood, facilitating its use in the laboratory with greater ease. The *T. b. brucei* PFK enzyme is representative of the enzyme found in the human infective subspecies that cause HAT. Other trypanosomatid PFKs from *T. cruzi* (Chagas disease), *L. infantum* (Leishmaniasis), *T. congolense* and *T. vivax* (animal trypanosomiasis) were also expressed, purified and tested, as described throughout this thesis. Unfortunately, successful expression of *T. vivax* and *T. congolense* PFKs was not achieved before this thesis could be completed.

3.2.1 Sequence analysis of trypanosomatid PFKs.

Full length amino acid FASTA files were obtained from the Uniprot protein database (http://www.uniprot.org/) for *T. brucei, T. cruzi, T. congolense, T. vivax* and *L. infantum* PFKs. Sequence identity was analysed alongside other eukaryotic and prokaryotic PFKs (**table 3.1a**) and sequences were aligned to each other using the 'Clustal Omega' multiple alignment programme (http://www.ebi.ac.uk/Tools/msa/clustalo/). The trypanosomatid PFKs have a

relatively high identity of ~70 – 88% with each other, compared to ~23 – 26% identity with the mammalian and yeast PFKs. The active site is extremely well conserved across all the species outlined in **table 3.1A** (data not shown, see full alignment in **supplementary material**). A sequence alignment for the trypanosomatid PFKs is given in **figure 3.1**. A fact file of the 5 trypanosomatid PFK sequences is given in **table 3.1B**.

A

	L. inf.	**T. bruc.**	**T. cong**	**T. vivax**	**T. cruzi**	E. coli	S. cere.	Rb (M)	Hs (M)
L. inf.	-	70.3	69.5	70.0	71.8	23.0	22.8	25.3	24.7
T. bruc.	70.3	-	87.7	79.8	76.9	24.8	25.5	24.4	23.6
T. cong.	69.5	87.7	-	81.6	77.3	25.1	24.6	23.6	22.7
T. vivax	70.0	79.8	81.6	-	78.7	26.4	24.5	24.7	24.2
T. cruzi	71.8	76.9	77.3	78.7	-	25.7	24.0	25.0	24.2
E. coli	23.0	24.8	25.1	26.4	25.7	-	34.4	40.2	40.8
S. cere.	22.8	25.5	24.6	24.5	24.0	34.4	-	42.9	42.7
Rb (M)	25.3	24.4	23.6	24.7	25.0	40.2	42.9	-	96.3
Hs (M)	24.7	23.6	22.7	24.2	24.2	40.8	42.7	96.3	-

L. inf. = *Leishmania infantum*. T. bruc. = *Trypanasoma brucei brucei*/ T. cong. = *T. congolense* (IL300 strain), S. cere. = *Saccharomyces cerevisiae*. Rb (M) = Rabbit muscle (*Oryctolagus cuniculus*). Hs (M) = *Homo sapiens* muscle.

B

Species	Unirprot accession no.	Genomic DNA accession no. (EMBL)	PFK Length (a.a)
T. brucei brucei (strain 427)	O15648	AF008186	487
T. cruzi (strain CL Brener)	Q4E657	AAHK01000001	485
T. congolense (strain IL3000)	F9W8G2	CAEQ01001170	487
T. vivax (strain Y486)	G0TSZ6	HE573019	484
L. infantum (strain JPCM5)	A4I4W5	FR796461	486

Table 3.1: Sequence Identity matrix for selected eukaryotic and prokaryotic PFKs.

A) Identity matrix of amino acid sequences between PFKs in Trypanosomatid (bold), bacterial (E.coli), yeast (S. cerevisiae) and mammalian (O. cuniculus, H. sapiens) species. B) Details of database entries used in carrying out sequence analysis for trypanosomatid PFKs.

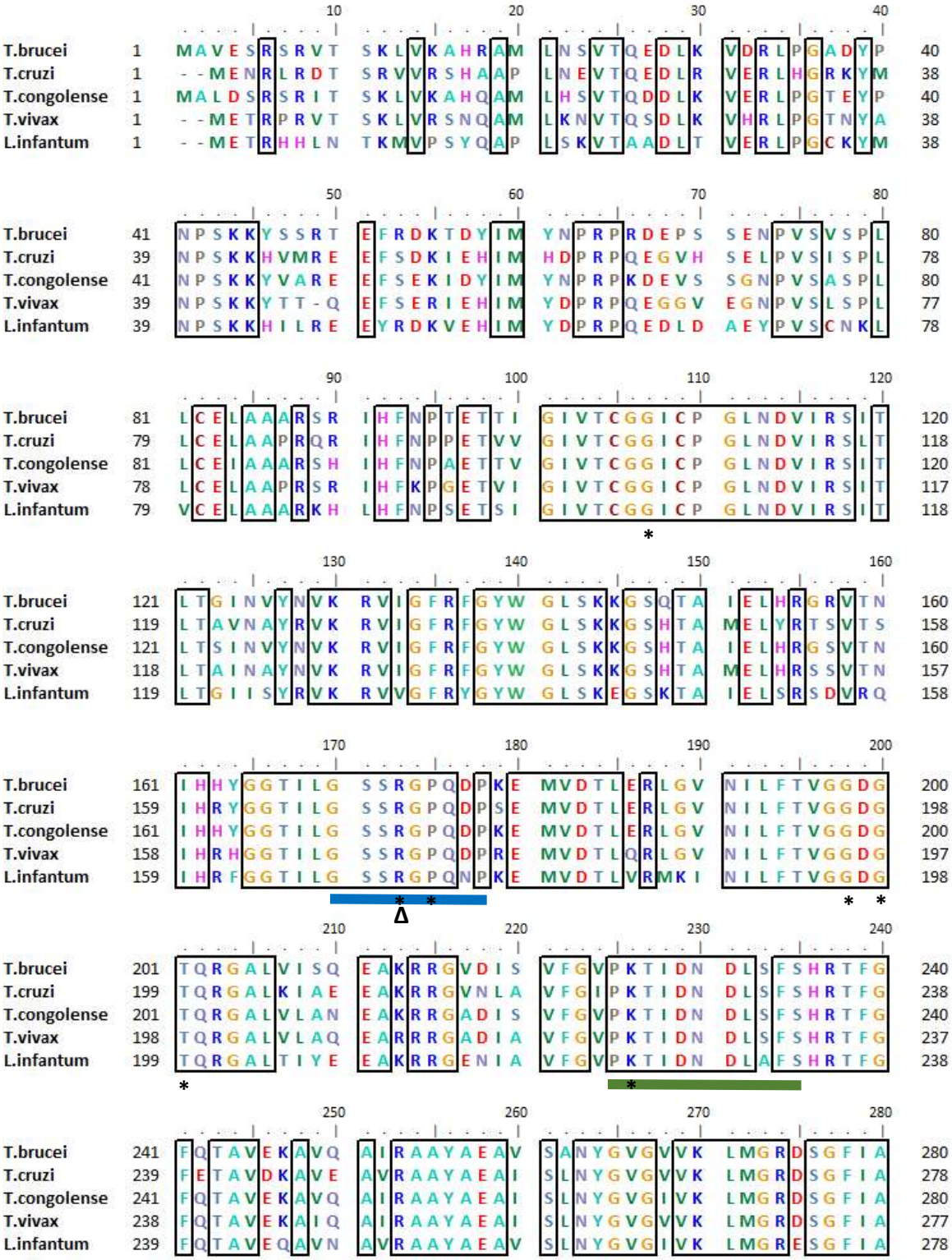
10 20 30 40
T.brucei 1 MAVESRSRVT SKLVKAHRAM LNSVTQEDLK VDRLPGADYP 40
T.cruzi 1 --MENRLRDT SRVVRSHAAP LNEVTQEDLR VERLHGRKYM 38
T.congolense 1 MALDSRSRIT SKLVKAHQAM LHSVTQDDLK VERLPGTEYP 40
T.vivax 1 --METRPRVT SKLVRSNQAM LKNVTQSDLK VHRLPGTNYA 38
L.infantum 1 --METRHHLN TKMVPSYQAP LSKVTAADLT VERLPGCKYM 38
50 60 70 80
T.brucei 41 NPSKKYSSRT EFRDKTDYIM YNPRPRDEPS SENPVSVSPL 80
T.cruzi 39 NPSKKHVMRE EFSDKIEHIM HDPRPQEGVH SELPVSISPL 78
T.congolense 41 NPSKKYVARE EFSEKIDYIM YNPRPKDEVS SGNPVSASPL 80
T.vivax 39 NPSKKYTT-Q EFSERIEHIM YDPRPQEGGV EGNPVSLSPL 77
L.infantum 39 NPSKKHILRE EYRDKVEHIM YDPRPQEDLD AEYPVSCNKL 78
90 100 110 120
T.brucei 81 LCELAAARSR IHFNPTETTI GIVTCGGICP GLNDVIRSIT 120
T.cruzi 79 LCELAAPRQR IHFNPPETVV GIVTCGGICP GLNDVIRSLT 118
T.congolense 81 LCEIAAARSH IHFNPAETTV GIVTCGGICP GLNDVIRSIT 120
T.vivax 78 LCELAAPRSR IHFKPGETVI GIVTCGGICP GLNDVIRSIT 117
L.infantum 79 VCELAAARKH LHFNPSETSI GIVTCGGICP GLNDVIRSIT 118
*
130 140 150 160
T.brucei 121 LTGINVYNVK RVIGFRFGYW GLSKKGSQTA IELHRGRVTN 160
T.cruzi 119 LTAVNAYRVK RVIGFRFGYW GLSKKGSHTA MELYRTSVTS 158
T.congolense 121 LTSINVYNVK RVIGFRFGYW GLSKKGSHTA IELHRGSVTN 160
T.vivax 118 LTAINAYNVK RVIGFRFGYW GLSKKGSHTA MELHRSSVTN 157
L.infantum 119 LTGIISYRVK RVVGFRYGYW GLSKEGSKTA IELSRSDVRQ 158
170 180 190 200
T.brucei 161 IHHYGGTILG SSRGPQDPKE MVDTLERLGV NILFTVGGDG 200
T.cruzi 159 IHRYGGTILG SSRGPQDPSE MVDTLERLGV NILFTVGGDG 198
T.congolense 161 IHHYGGTILG SSRGPQDPKE MVDTLERLGV NILFTVGGDG 200
T.vivax 158 IHRHGGTILG SSRGPQDPRE MVDTLQRLGV NILFTVGGDG 197
L.infantum 159 IHRFGGTILG SSRGPQNPKE MVDTLVRMKI NILFTVGGDG 198
* * * *
Δ
210 220 230 240
T.brucei 201 TQRGALVISQ EAKRRGVDIS VFGVPKTIDN DLSFSHRTFG 240
T.cruzi 199 TQRGALKIAE EAKRRGVNLA VFGIPKTIDN DLSFSHRTFG 238
T.congolense 201 TQRGALVLAN EAKRRGADIS VFGVPKTIDN DLSFSHRTFG 240
T.vivax 198 TQRGALVLAQ EARRRGADIA VFGVPKTIDN DLSFSHRTFG 237
L.infantum 199 TQRGALTIYE EAKRRGENIA VFGVPKTIDN DLAFSHRTFG 238
*
*
250 260 270 280
T.brucei 241 FQTAVEKAVQ AIRAAYAEAV SANYGVGVVK LMGRDSGFIA 280
T.cruzi 239 FETAVDKAVE AVRAAYAEAI SLNYGVGVVK LMGRDSGFIA 278
T.congolense 241 FQTAVEKAVQ AIRAAYAEAI SLNYGVGIVK LMGRDSGFIA 280
T.vivax 238 FQTAVEKAIQ AIRAAYAEAI SLNYGVGVVK LMGRDSGFIA 277
L.infantum 239 FQTAVEQAVN AVRAAYAEAV SLNYGVGIVK LMGRESGFIA 278

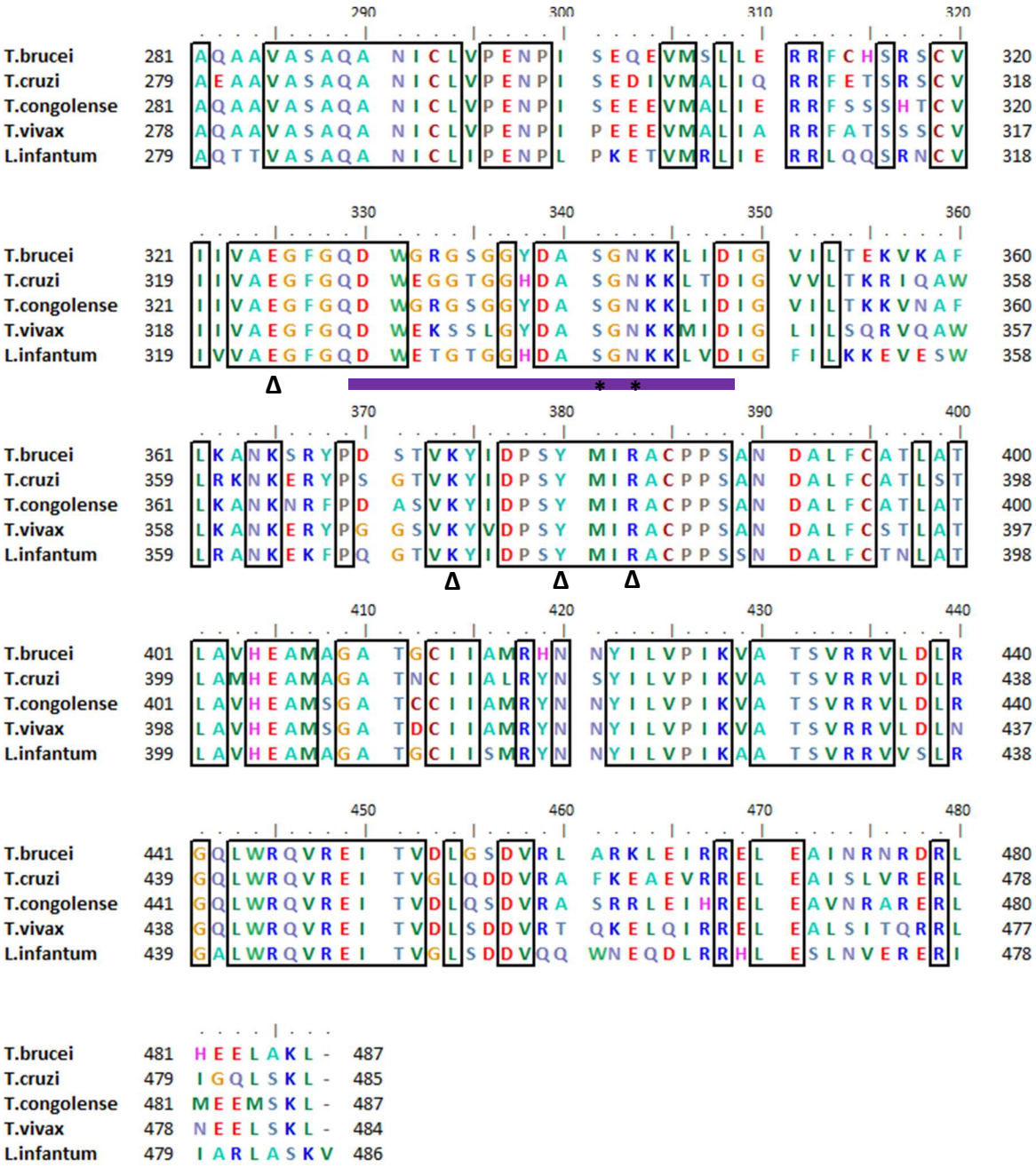

Figure 3.1: Sequence alignment of trypanosomatid PFKs.

*Amino acid sequence alignment of select trypanosomatid PFK monomers. Identical residues are boxed. Active site features of TbPFK including inserted loop 329-348 (purple), Arg173 loop 170-178 (blue) and Asp229 loop 225-235 (green) are underlined. Residues involved in ATP binding (*) and F6P binding (**Δ**) as described by McNae et. al are annotated beneath the sequence (McNae & Martinez-Oyanedel, 2009).*

Sequence alignments of the trypanosomatid PFKs tested in this thesis are shown in **figure 3.1**. There is 100% identity in residues involved in ATP and F6P binding (as described by McNae et. al) across all 5 species (McNae & Martinez-Oyanedel, 2009). The residues making up dynamic active site loops 'Arg173 loop' and 'Asp229 loop' have high identity across all species, as does the 'inserted loop' unique to trypanosomatid PFKs.

3.2.2 Sequence analysis against mammalian PFKs.

As the *T. b. rhodesiense/gambiense* parasites have infective life cycle stages in mammals, it is advantageous that the targeted pocket in trypanosomatid PFKs structure is either not present or sufficiently different in the mammalian equivalent, to prevent inhibition of the host enzyme. A sequence comparison of the residues involved in F6P and ATP binding, as well as the residues making up the 'CTCB binding pocket' in *T. brucei* PFK is given in **section 1.4.8, chapter 1.**

3.2.3 Recombinant trypanosomatid PFK enzyme sequence overview.

All recombinant trypanosomatid PFKs were cloned and purified with N-terminal His_6-tags ; *T. brucei, T. congolense, T. cruzi* and *T. vivax* PFKs all had the same thrombin-cleavable tag with a.a. sequence '**MGSSHHHHHHSSGLVPRGSH**'. *L. infantum* PFK had the TEV-cleavable site '**MSYYHHHHHHDYDIPTTENLYFQG**'. Characteristics of each sequence are given in **table 3.2**.

Species	Strain	Length (a.a)	MW (monomer) (kDa)	pI	Extinction coeff. ($M^{-1}cm^{-1}$)
T. b. brucei	427	507	55.76	9.50	37860
T. congolense	IL3000	507	55.59	9.15	37860
T. cruzi	CL Brener	505	55.81	9.23	40380
T. vivax	Y486	504	55.41	9.36	41870
L. infantum	JPCM5	510	57.07	8.99	56435

Table 3.2: Computed parameters for trypanosomatid PFK sequences.

All parameters computed using amino acid FASTA sequences and Expasy 'ProtParam' bioinformatics tool (http://web.expasy.org/protparam/). All sequence data include the His_6 affinity tag residues. All parameters calculated from a.a. sequence containing the N-terminal His_6 tag.

3.3. Cloning of trypanosomatid PFKs.

3.3.1 Cloning of T. congolense and T. vivax PFKs.

DNA sequences of *T. congolense* (1515 bp) and *T.* vivax (1512 bp) PFK with N-terminal His_6 tags were codon optimised for *E. coli* expression and synthesised into pMC vectors with Kanamycin resistance by Life Technologies 'GeneArt' services. Primers were designed for PCR amplification of the PFK insert from the pMC vector. The resulting DNA product was ligated into a pGEM®-T vector with coding for the beta-galactosidase enzyme and carbenicillin resistance. The vector was then transformed into DH5α cells and grown on LB agar plates with X-Gal and IPTG to allow for blue/white colony picking. White colonies containing the PFK DNA insert were grown up and the plasmid was extracted using a miniprep kit. PCR validation using the same primers for *T. congolense* and *T. vivax* PFK amplification confirmed the presence of the insert. The PCR validation of 8 colonies containing the *T. congolense* PFK insert is given in **figure 3.2.** A full description of *T. congolense* and *T. vivax* cloning is given in **section 2.1.1**.

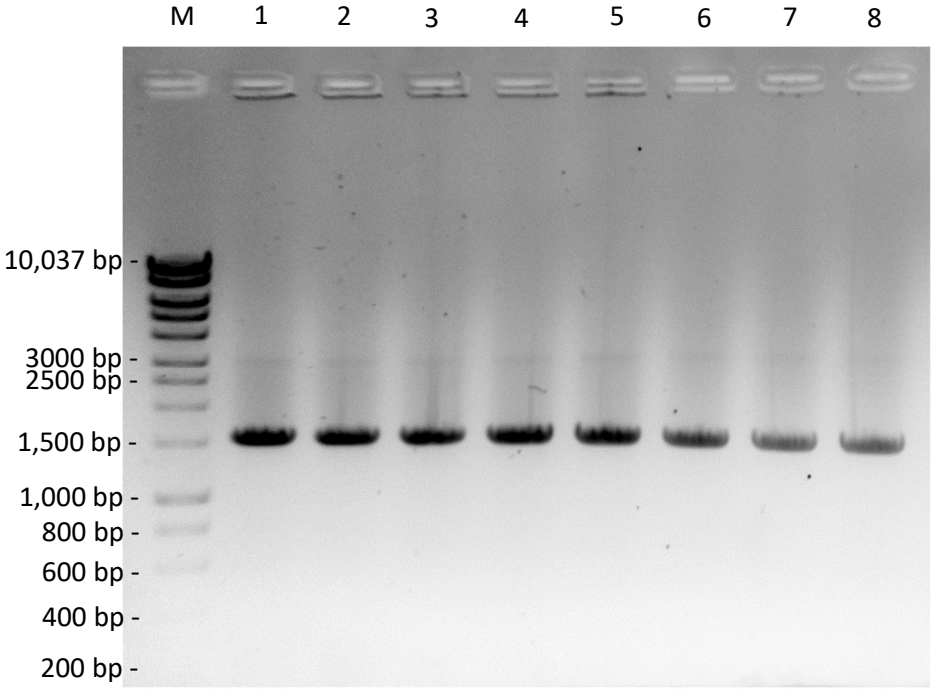

Figure 3.2: Agarose gel electrophoresis of T. congolense PFK T-vector PCR product.

1% w/v agarose gel stained with 'safeview' DNA stain. M = Hyperladder 1Kb MW marker. ***1-4*** *= individual colonies from 3:1 insert:plasmid ligation reaction.* ***5-8*** *= individual colonies from 5:1 ligation reaction. T. congolense PFK DNA sequence = 1515 bp.*

An overnight culture of a single colony of pGEM®-*T. congolense/T. vivax* PFK was pelleted and plasmid DNA was digested with HindIII and XbaI restriction enzymes. The destination vector (pET28a) was digested with the same restriction enzymes. **Figure 3.3** shows the resulting digest products for *T. congolense* PFK.

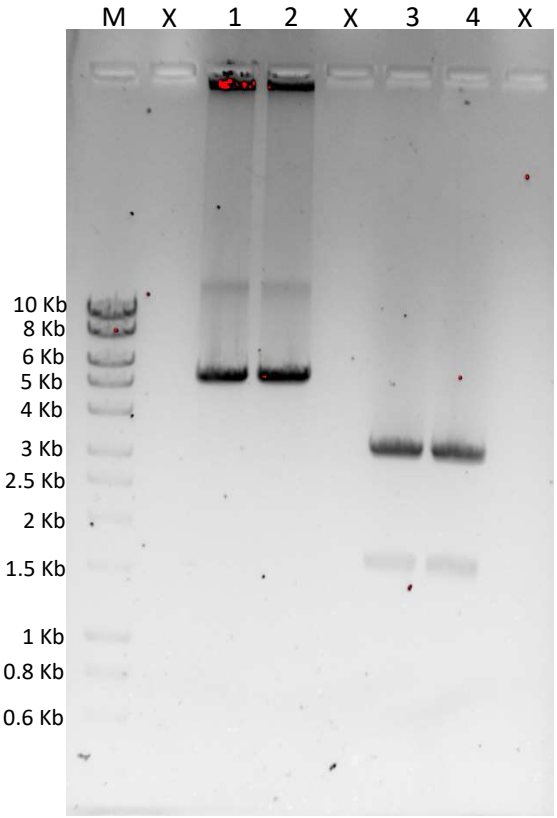

Figure 3.3: Agarose gel electrophoresis of T. congolense PFK T-gEM colony and pET28a vector.

1% w/v agarose gel stained with 'safeview' DNA stain. Digest of T-gEM/T.congolense PFK vector and pET28a vector by HindIII and XbaI restriction enzymes. pET28a vector (cut) = 5,207 bp. T.congolense PFK insert = 1,515 bp. ***M****= Hyperladder 1Kb MW marker.* ***1-2*** *= pET28a digest.* ***3-4*** *= T-gEM/T.congolense PFK digest. 'X' = empty lane.*

Digested pET28a and *T. congolense/T. vivax* PFK DNA was gel extracted and purified to an A260/A280 ratio of 1.8 – 2.0. Ligation ratios of 2:1, 3:1 and 5:1 were used, in both 100 and 50 ng ligation reactions in 10 µl volumes using T4 ligase. Transformation into DH5α cells and growth on LB agar with 34 µM kanamycin was unsuccessful. C41, BL21 and 'E.cloni' (Lucigen) competent cells were also used in transformations but none yielded colonies on the LB agar/kanamycin plates. A full protocol for ligation and transformation attempts is given in **section 2.1.1**.

3.4. Expression of trypanosomatid PFKs.

Expression constructs of *T. brucei, T. cruzi* and *L. infantum* were previously designed and cloned by H. Morgan of the Walkinshaw group at the University of Edinburgh. **Table 3.3** summarises all 5 trypanosomatid PFK expression systems used.

Species	**Affinity tag sequence/cleavage**	**Expression plasmid**	**Construct resistance**	**Expression cell line**
T. brucei	MGSSHHHHHHSSG**LVPRGS**H (Thrombin protease)	pET28a	Kanamycin	C41 (DE3)
T. congolense	MGSSHHHHHHSSG**LVPRGS**H (Thrombin protease)	pET28a	Kanamycin	NA
T. cruzi	MGSSHHHHHHSSG**LVPRGS**H (Thrombin protease)	pET28a	Kanamycin	BL21 (DE3)
T. vivax	MGSSHHHHHHSSG**LVPRGS**H (Thrombin protease)	pET28a	Kanamycin	NA
L. infantum	MSYYHHHHHHDYDIPTT**ENLYFQ**G (TEV protease)	pDEST17	Carbenecillin	C41 (DE3)

Table 3.3: Trypanosomatid PFK expression systems.

All three trypanosomatid PFKs were transformed into chemically competent C41 (DE3) (*T. brucei, L. infantum*) or BL21 (DE3) cells (*T. cruzi*) and grown up on lysogeny broth (LB) agar plates with kanamycin. Single colonies were picked and use to inoculate overnight 50 ml cultures in 2xTY media containing 34 µM kanamycin at 37 ^{o}C. These overnight cultures were used for larger volume (0.5 – 1 L) grow-ups of cultures to an OD of 0.8-0.9. Expression of PFK was induced using 100 mM IPTG at 18 ^{o}C overnight. Cells were then pelleted and flash frozen in liquid nitrogen for use in purification later. A full protocol for trypanosomatid PFK transformation, grow-up an expression is given in **section 2.2.1.**

3.5. Purification of trypanosomatid PFKs.

3.5.1 Affinity chromatography

All three trypanosomatid PFKs were purified using a two-step protocol – an affinity chromatography step followed by a size exclusion chromatography or desalting step. Each trypanosomatid PFK was initially purified using a HiTrap IMAC sepharose column with cobalt, binding to the N-terminal His_6-tag of the protein. Cell suspensions were lysed in wash buffer (50mM TEA, 300 mM NaCl, 20 mM imidazole, 10% glycerol, protease inhibitors, pH 8.0) using a high pressure homogeniser and the resulting lysate was loaded onto the IMAC columns. Additional washes of 10 or 20% of a buffer containing 500 mM Imidazole ('Buffer B' - 50mM TEA, 300 mM NaCl, 500 mM imidazole, 10% glycerol, pH 8.0) were carried out to strip weakly bound molecules from the IMAC column. PFK was eluted with 100% buffer B (500 mM imidazole), stripping the His_6-tagged PFK molecules from the Co^{2+} with the higher imidazole concentration. **Figures 3.4A-C** show the affinity purification profiles of *T. brucei*, *T. cruzi* and *L. infantum* PFKs respectively.

A

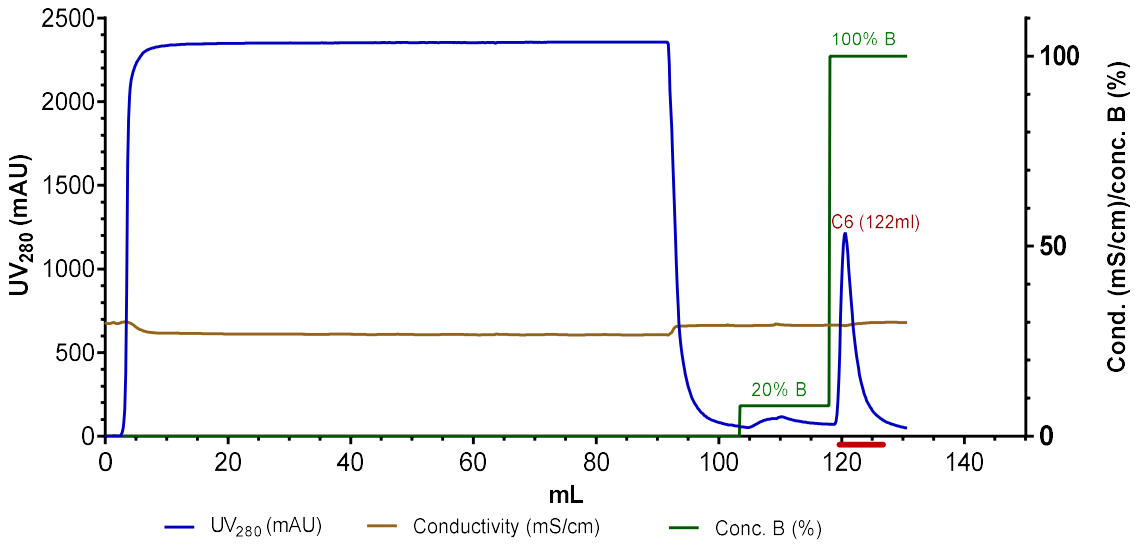
*Tb*PFK affinity chromatography.
2500
2000
1500
1000
500
0
UV280 (mAU)
100% B
C6 (122ml)
20% B
100
50
0
Cond. (mS/cm)/conc. B (%)
0
20
40
60
80
100
120
140
mL
UV280 (mAU)
Conductivity (mS/cm)
Conc. B (%)

B

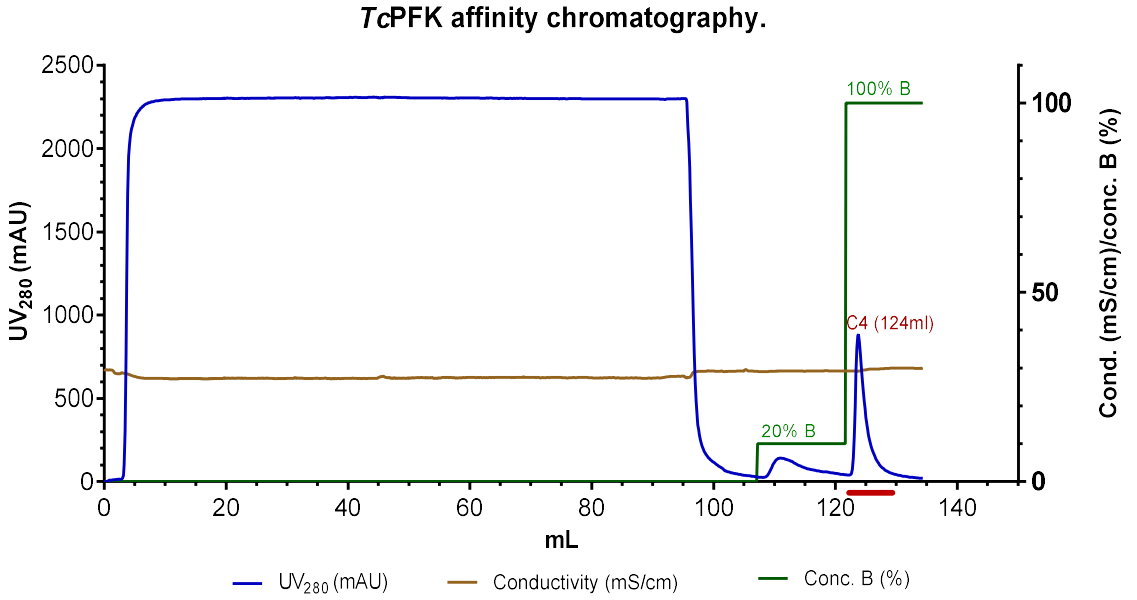
*Tc*PFK affinity chromatography.
2500
2000
1500
1000
500
0
UV280 (mAU)
100% B
C4 (124ml)
20% B
100
50
0
Cond. (mS/cm)/conc. B (%)
0
20
40
60
80
100
120
140
mL
UV280 (mAU)
Conductivity (mS/cm)
Conc. B (%)

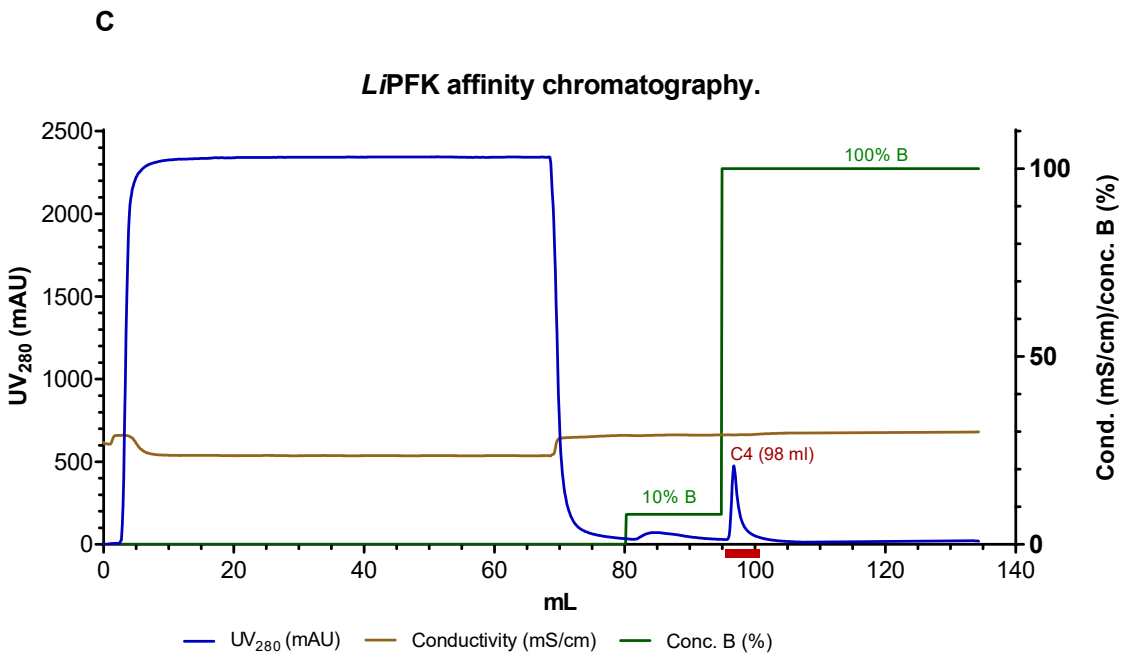

Figure 3.4: IMAC Co^{2+} affinity chromatography of trypanosomatid His_6-PFKs.

*Affinity chromatography of T. brucei (**A**), T. cruzi (**B**) and L. infantum (**C**) PFKs. Cell lysates with N-terminal His_6-PFK washed over Sepharose IMAC column charged with Co^{2+} in wash buffer (50 mM TEA, 300 mM NaCl, 20 mM imidazole, 10% glycerol, pH 8.0). Eluted with 100% 'buffer B' (50 mM TEA, 300 mM NaCl, 500 mM imidazole, 10 glycerol, pH 8.0). Red underline represents pooled fractions. Fraction at highest point of elution peak is labelled in red. All proteins purified from lysate of 1 litre cell pellets. X-axis shows millilitres (mL) of lysate/buffers run over column from the start of the affinity chromatography step.*

3.5.2 Size exclusion purification – *T. brucei* and *T. cruzi* PFKs.

A second purification step was carried out for *T. brucei* and *T. cruzi* PFKs through size exclusion chromatography (SEC) using a GE Healthcare Sephacryl™ S-200 16/60 size exclusion column. 5ml of the concentrated pooled fractions from the affinity chromatography step was filtered using a 0.22 nm filter syringe and loaded onto the column, pre-equilibrated in SEC buffer (20 mM TEA, 5mM $MgCl_2$, 50 mM KCl, pH 7.4). The PFK was eluted by washing with 1.5 column volumes of the above buffer. **Figure 3.5** shows the size exclusion profiles for both *T. brucei* and *T. cruzi* PFKs. Confirmation and quality control of each purification step (IMAC and SEC) was checked by SDS-PAGE gel electrophoresis, shown in **figure 3.6** for *T. brucei* and *T. cruzi* PFKs.

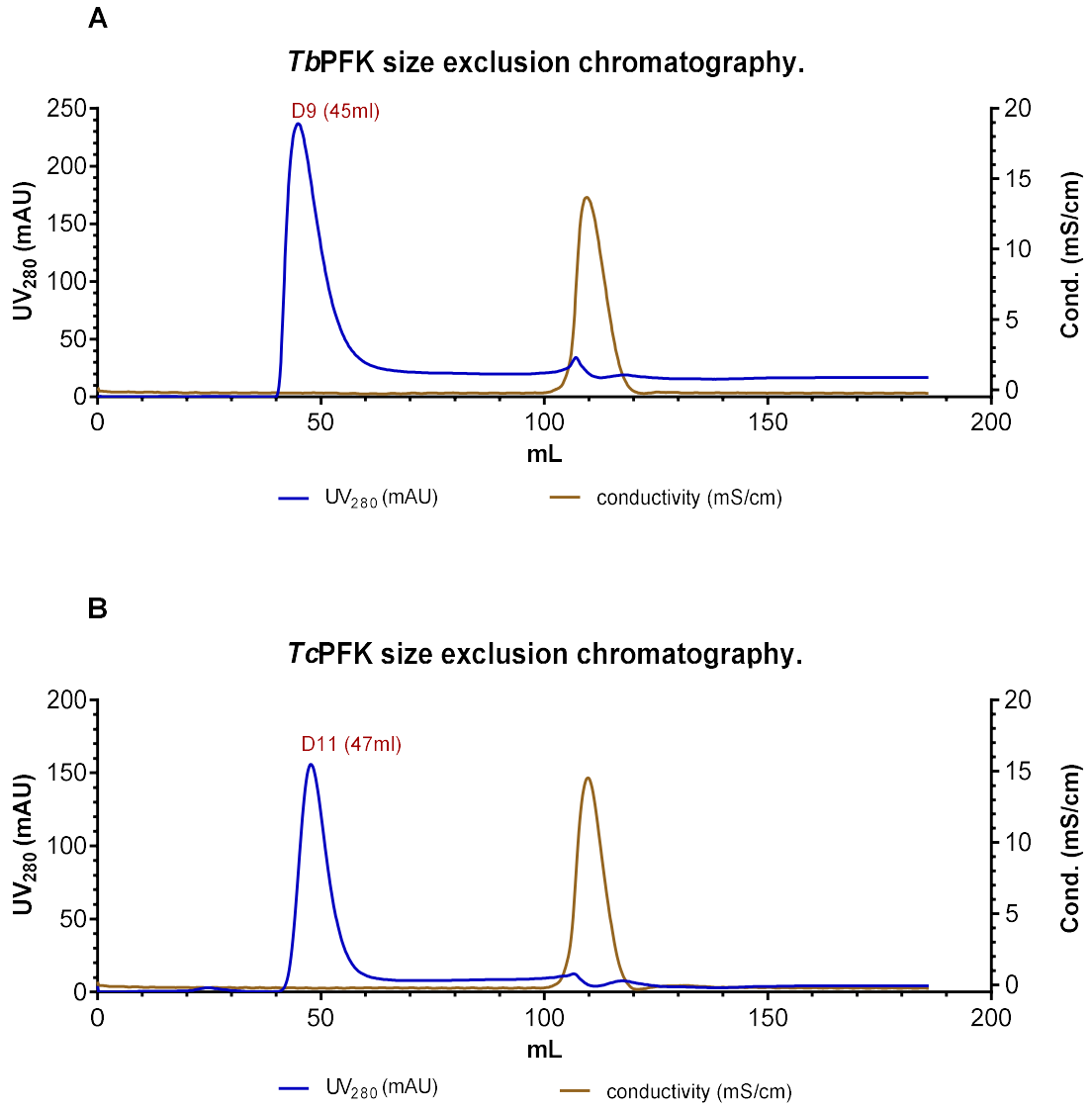

Figure 3.5: Size exclusion chromatography of T. brucei and T. cruzi PFKs.

*Size exclusion chromatography profile of T. brucei (**A**) and T. cruzi (**B**) pooled fractions from IMAC CO^{2+}affinity chromatography. GE Healthcare Sephacryl S-200 16/60 SEC column used, pre-equilibrated with SEC buffer (20 mM TEA, 5mM $MgCl_2$, 50 mM KCl, pH 7.4).*

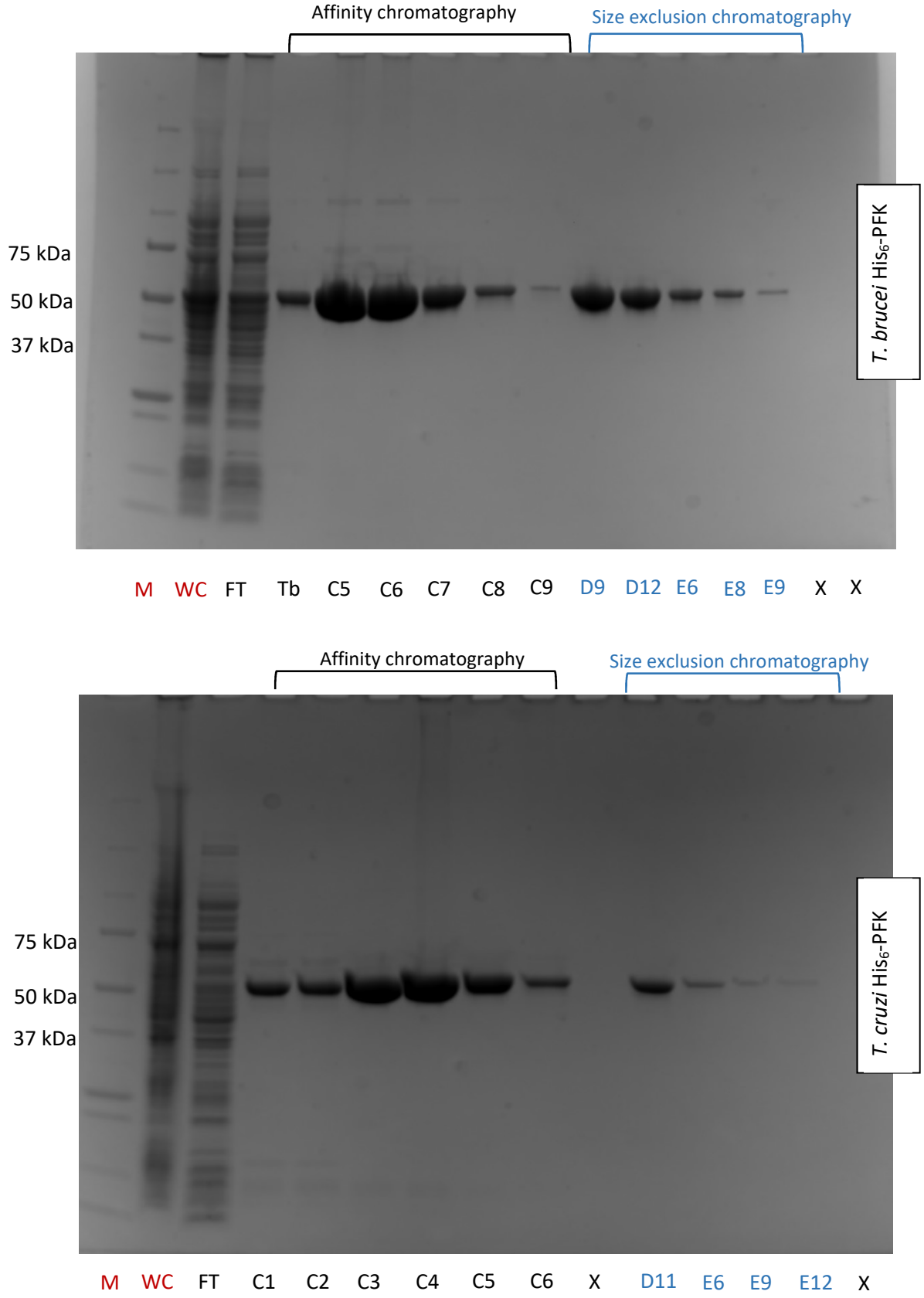

Figure 3.6: SDS-PAGE gel electrophoresis of T. brucei and T. cruzi purification steps.

M= Marker (BioRad Precision Plus Protein™ standards), WC = whole cell lysate, FT = flow through from IMAC column, X = empty well. Fractions for affinity (black) and size exclusion (blue) chromatography are labelled.

3.5.3 Second stage purification of *L. infantum* PFK.

Pooled IMAC elutions of *L. infantum* PFK precipitated on Sephacryl and Sepharose-based size exclusion chromatography columns (data not shown) and so this step could not be used for *L. infantum* PFK. As seen in **figure 3.7B** the IMAC fractions for *L. infantum* PFK *are* reasonably clean – with relatively little contaminating bands. The second stage for *L. infantum* PFK therefore involved a simple desalt size exclusion chromatography step; 5ml of the pooled IMAC fractions were added to a 'HiPrep 26/10 Deslating' column (GE Healthcare) equilibrated with SEC buffer (20 mM TEA, 5mM $MgCl_2$, 50 mM KCl, pH 7.4). The PFK was eluted with 1.5 column volumes of the same buffer. **Figure 3.7A** shows the desalt profile for *L. infantum* PFK. **Figure 3.7B** shows the SDS-PAGE electrophoresis of all purification steps for *Li*PFK (both IMAC and desalt).

3.5.4 Trypanosomatid PFK protein yields.

On average, 1 litre cultures of *E. coli* expressing *T. brucei, T. cruzi* and *L. infantum* PFKs yielded 16, 11 and 3 mg of active, purified protein. For the *T. brucei* and *T. cruzi* purifications, ~20% of protein was lost between the IMAC and SEC steps. It was assumed that this was due to aggregation on the Sephacryl column – a greater amount of protein was lost if this column was not washed with NaOH between purifications.

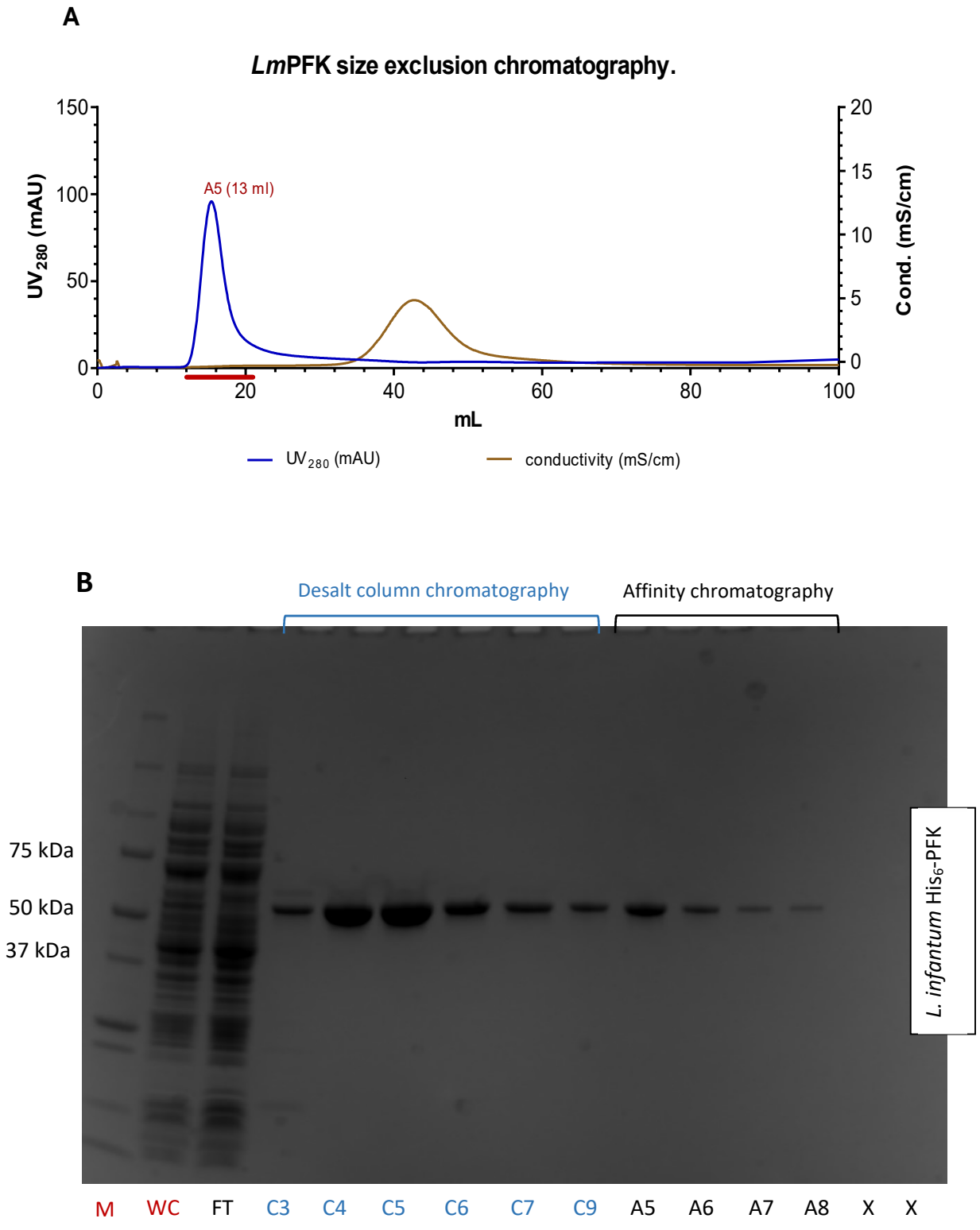

Figure 3.7: Desalt and SDS-PAGE electrophoresis of L. infantum PFK.

M= Marker (BioRad Precision Plus Protein™ standards), WC = whole cell lysate, FT = flow through from IMAC column, X = empty well. Fractions for affinity (black) and desalt column (blue) chromatography are labelled.

3.6. Biophysical characterisation of trypanosomatid PFKs.

3.6.1 Mass spectrometry confirmation of trypanosomatid PFKs.

Purified *Tc*PFK and *Lm*PFK were confirmed using MALDI-TOF mass spectrometry. *Tb*PFK was not tested as the protein from the same expression construct was previously confirmed by mass spectrometry by M. Valdivieso at the UoE (data not shown).

*Tc*PFK and *Lm*PFK gel bands were subjected to a Trypsin digest and spotted onto the MS plate with a CHCA matrix solution containing 0.3% trifluroacetic acid (TFA) to produce positively charged peptide fragments. MS data was collected using a Bruker 'Ultraflex' MALDI-TOF spectrometer at the School of Chemistry, UoE. The MS peptide spectra for *T. cruzi* PFK and *L. infantum* PFK and reuslts of a MASCOT peptide fingerprint search (http://www.matrixscience.com) are shown in **figures 3.8** and **3.9** respectively.

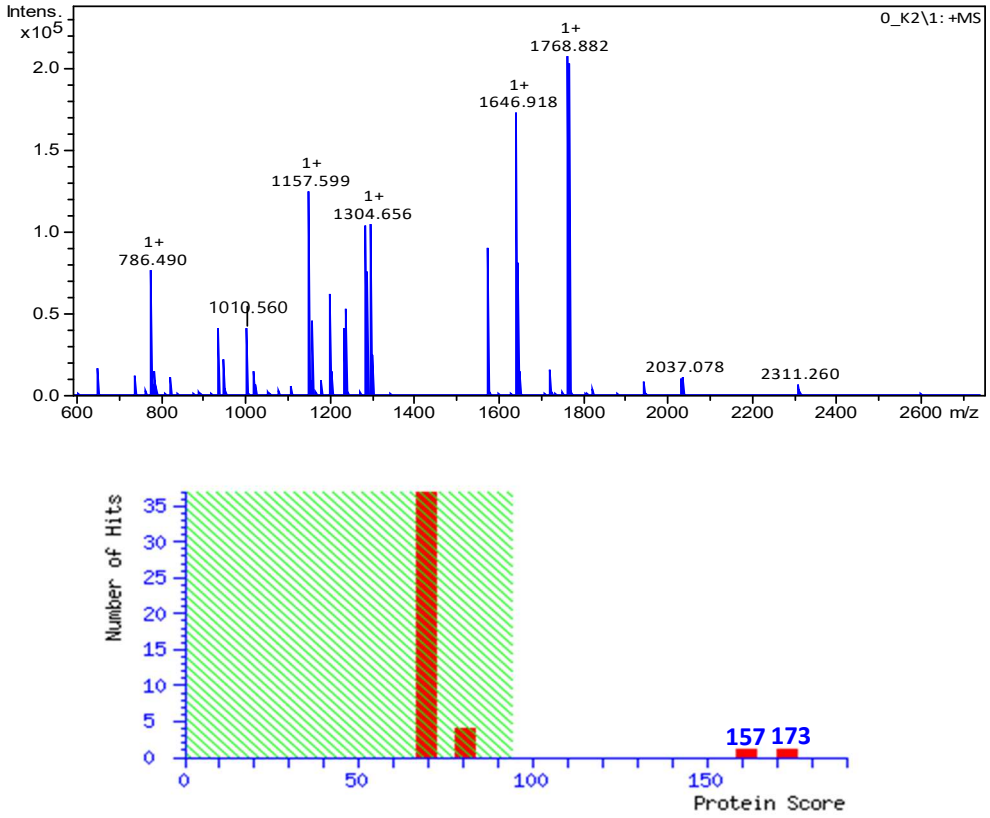

Figure 3.8: T. cruzi PFK MALDI-TOF mass spectrometry confirmation.

*MS peptide fingerprint and MASCOT score histogram shown for LiPFK. MASCOT search results: Score at 173: Mass = 53,988. 6-phospho-1-fructokinase [Trypanosoma cruzi strain CL Brener] Score at 157 : Mass = 53,951 6-phospho-1-fructokinase, putative [Trypanosoma cruzi marinkellei]. T. c. marinkellei and the CL Brener strain have 98.6 % identity – differing by 2 amino acids only. Protein score is -10*Log(P), where P is the probability that the observed match is a random event.*

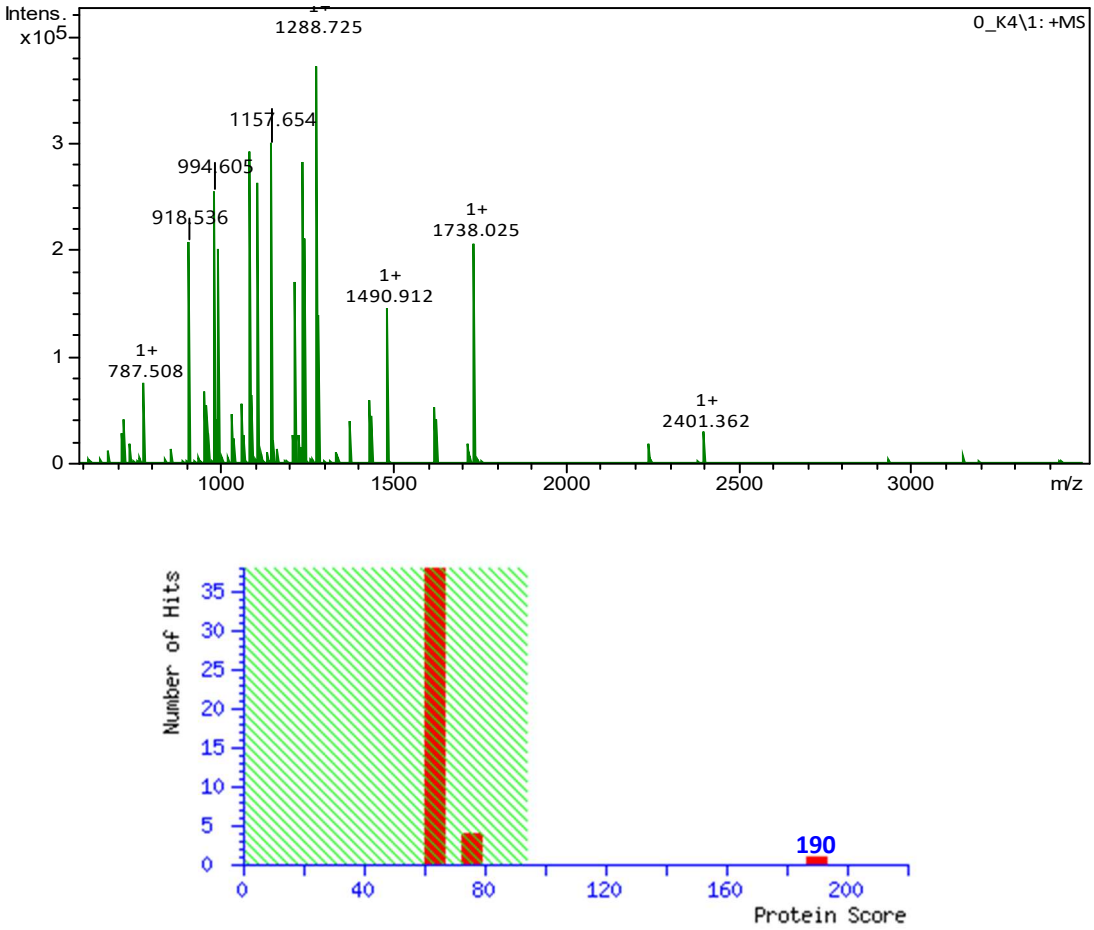

Figure 3.9: L. infantum PFK MALDI-TOF mass spectrometry confirmation.

MS peptide fingerprint and MASCOT score histogram shown for LiPFK. MASCOT search results: Score at 190: Mass = 54,014 Da : ATP-dependent phosphofructokinase [Leishmania infantum JPCM5]. Protein scores greater than 94 are significant (p<0.05).

3.6.2 Purified trypanosomatids were monodisperse when measured using DLS.

Purified stocks of the *T. brucei*, *T. cruzi* and *L. infantum* PFKs were analysed using dynamic light scattering (DLS) to assess the size distribution of protein particles in solution – checking for aggregation and giving an estimate of the size of the molecules in the solution. A full description of the protocol for DLS is given in **section 2.5.1**.

The 3 trypanosomatid PFKs tested in DLS were suspended in TEA buffer (20mM TEA, 10 mM $MgCl_2$, 50 mM KCl, pH 7.4). These concentrations were taken into account when preforming DLS, giving the buffer a viscosity of 1.14 cP (**table 3.4A**). DLS experiments were carried out at 25 ^oC using a Zetasizer APS (Malvern Instruments). Results were analysed using the dedicated Malvern software.

Published crystal structures of *T. brucei* PFK show it to be a homotetramer (PDB: 2HIG, 3F5M) (Martinez-Oyanedel et al., 2007; McNae & Martinez-Oyanedel, 2009). Assuming all three trypanosomatid PFKs form similar homotetramers, the theoretical masses and radii of gyration are given in **table 3.4B**. The radius of gyration was calculated using Pymol 2.0.

A

Material RI	Material absorbance	Buffer RI	Viscosity (cP)
1.45	0.001	1.34	1.14

B

	T. brucei PFK	*T. cruzi* PFK	*L. infantum* PFK
Theoretical tetramer mass (kDa)	223	223	228
Theoretical radius of gyration (nm)	5.6	ND (no crystal structure)	ND (no crystal structure)

Table 3.4: General parameters for DLS of trypanosomatid PFK samples.

*A) Experimental parameters for DLS using TEA buffer (*20mM TEA, 10 mM $MgCl_2$, 50 mM KCl, pH 7.4). *B) Theoretical parameters of trypanosomatid PFKs tested in DLS.*

Both *T. brucei* and *T. cruzi* PFKs gave singular peaks by volume and by intensity – suggesting a singular, monodisperse population of protein (**figures 3.10** and **3.11**). The calculated particle diameters by volume were 12 and 11 nm for *T. brucei* and *T. cruzi* respectively, close to the estimated diameter of *T. brucei* PFK of 11.2 nm (**table 3.4B**). The *L. infantum* PFK sample had a very small contaminating amount of large aggregates (>100 nm in size) – observed by the size distribution profile by intensity (**figure 3.12**). These larger particles however only accounted for ~3% of the population. The size distribution by volume shows the majority of the *L. infantum* protein sample was monodispersed, with an average diameter of 13 nm.

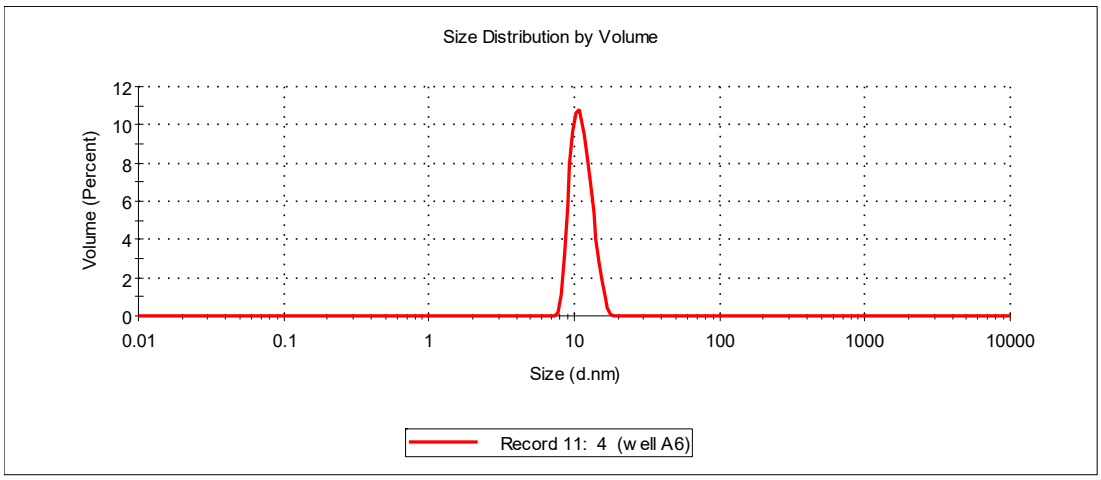

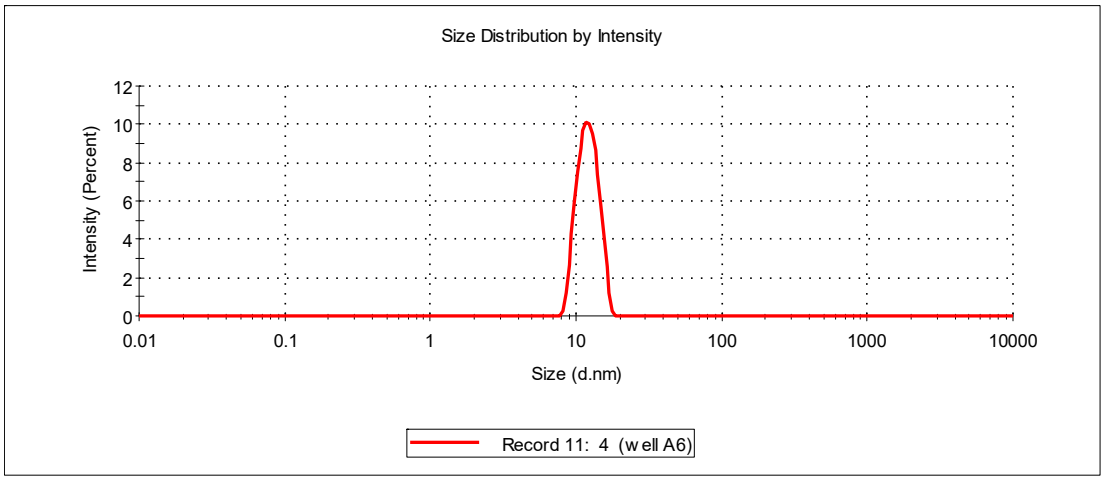

***T. brucei* PFK**	**Count rate (Kcps)**	**Z-average (mean diameter) (nm)**	**Peak1**	**Peak 2**	**Peak 3**
By Intensity	293	11.3	100% 12.2 ± 1.9 nm	N/A	N/A
By Volume	293	12.2	11.3 ± 1.8 nm	N/A	N/A

Figure 3.10: DLS results for T. brucei PFK.

Particle size distribution calculated by intensity and volume. Calculated and measured particle sizes given in table. T. brucei PFK sample appears to be monodisperse and made up of particles of ~11 nm – corresponding to estimated size of TbPFK tetramer.

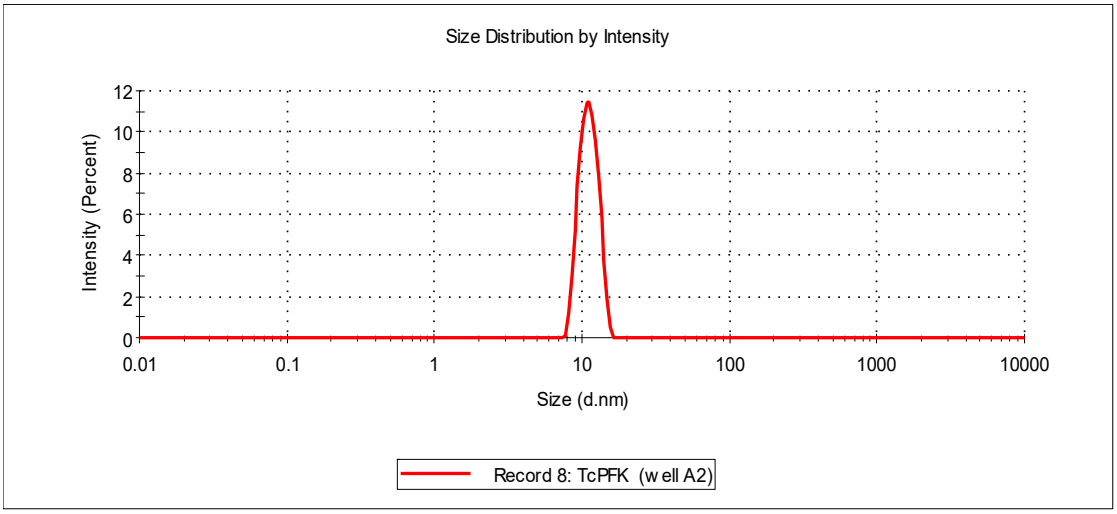

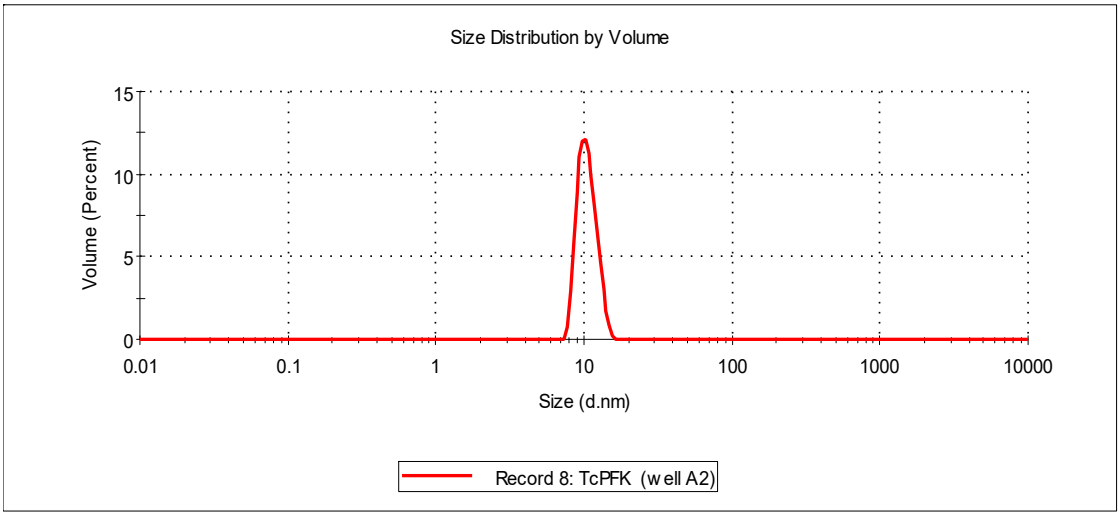

***T. cruzi* PFK**	**Count rate (Kcps)**	**Z-average (mean diameter) (nm)**	**Peak1**	**Peak 2**	**Peak 3**
By Intensity	298	11.2	100% 11.2 ± 1.6 nm	N/A	N/A
By Volume	298	10.5	10.5 ± 1.5 nm	N/A	N/A

Figure 3.11: DLS results for T. cruzi PFK.

Particle size distribution calculated by intensity and volume. Calculated and measured particle sizes given in table. T. cruzi PFK sample appears to be monodisperse and made up of particles of ~11 nm – corresponding to estimated size of TcPFK tetramer.

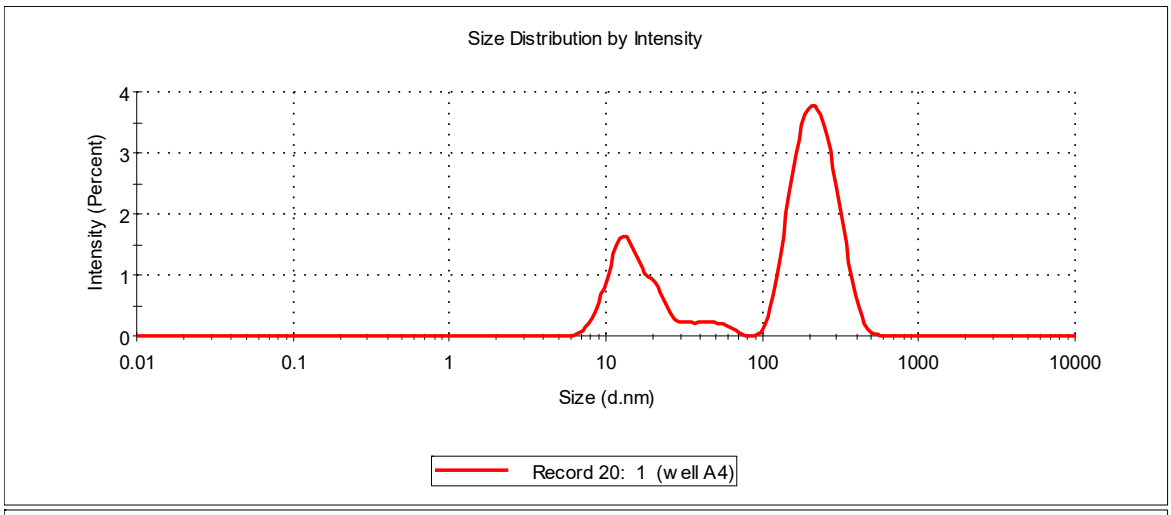

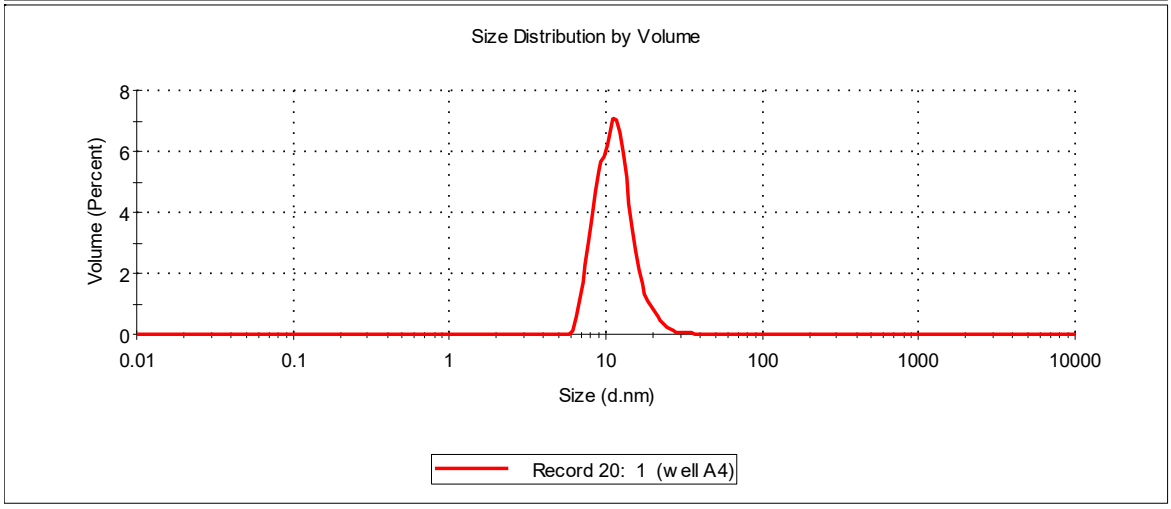

***L. infantum* PFK**	**Count rate (Kcps)**	**Z-average (mean diameter) (nm)**	**Peak1**	**Peak 2**	**Peak 3**
By Intensity	303	45.3	70% 15.3 ± 5 nm	27 % 50 ± 9 nm	3% 225 ± 71 nm
By Volume	303	13.6	99% 11.7 ± 3.8 nm	1% 190 ± 65.4 nm	N/A

Figure 3.12: DLS results for L. infantum PFK.

Particle size distribution calculated by intensity and volume. Calculated and measured particle sizes given in table. L. infantum PFK sample has low (3%) population of large particles (>100 nm) – possibly due to small amount of aggregation.

3.6.3 Thermal denaturation measurements of trypanosomatid PFK.

Thermal denaturation assays (TDA) were carried out to assess the thermal stability of the trypanosomatid PFKs both with and without a range of substrates. TDA determines the transition melting temperature (Tm) or 'denaturation point' – the temperature at which the tertiary structure of the protein breaks down, exposing hydrophobic regions to a fluorescent dye. A real- time PCR instrument was used (BioRad iQ™5 ICycler) to heat the PFK samples from 20 – 80 ^{o}C in the presence of a fluorescent dye – 'SYPRO Orange' (Sigma). Upon denaturation of the protein, the SYPRO Orange dye binds the newly exposed hydrophobic regions, and the increase in fluorescent signal (ex/em = 485/575 nm) is measured in relative fluorescence units (RFU).

3.6.3.1 Trypanosomatid PFKs have good thermal stability.

The transition melting temperatures of *T. brucei*, *T. cruzi* and *L. infantum* PFKs were calculated in the same TEA-based buffer (10 mM MgCl2, 100 mM KCl, 50 mM TEA, 10% glycerol, 0.005% TWEEN, pH 7.4). 50 µL reactions containing 1.9 µM PFK were heated with 0.5 ^{o}C increments from 4 – 80 ^{o}C in the presence of sypro orange. *T. brucei*, *T. cruzi* and *L. infantum* PFKs had melting temperatures (Tm) of 59 ± 0.2 , 54 ± 0.2 and 39 ± 0.3 ^{o}C respectively. The trypanosomatid PFKs preformed well in TDA with good reproducibility - standard deviations (N=3) of transition melting temperatures (Tm) were between 0.2-0.3 ^{o}C. **Figure 3.13** shows the traces for the 3 trypanosomatid PFKs tested. As seen in **figure 3.13** the protein melts in a single unfolding event.

The enzymes therefore are stable at room temperature (25 ^{o}C) – under which the activity, inhibition and biophysical assays described in this thesis were carried out.

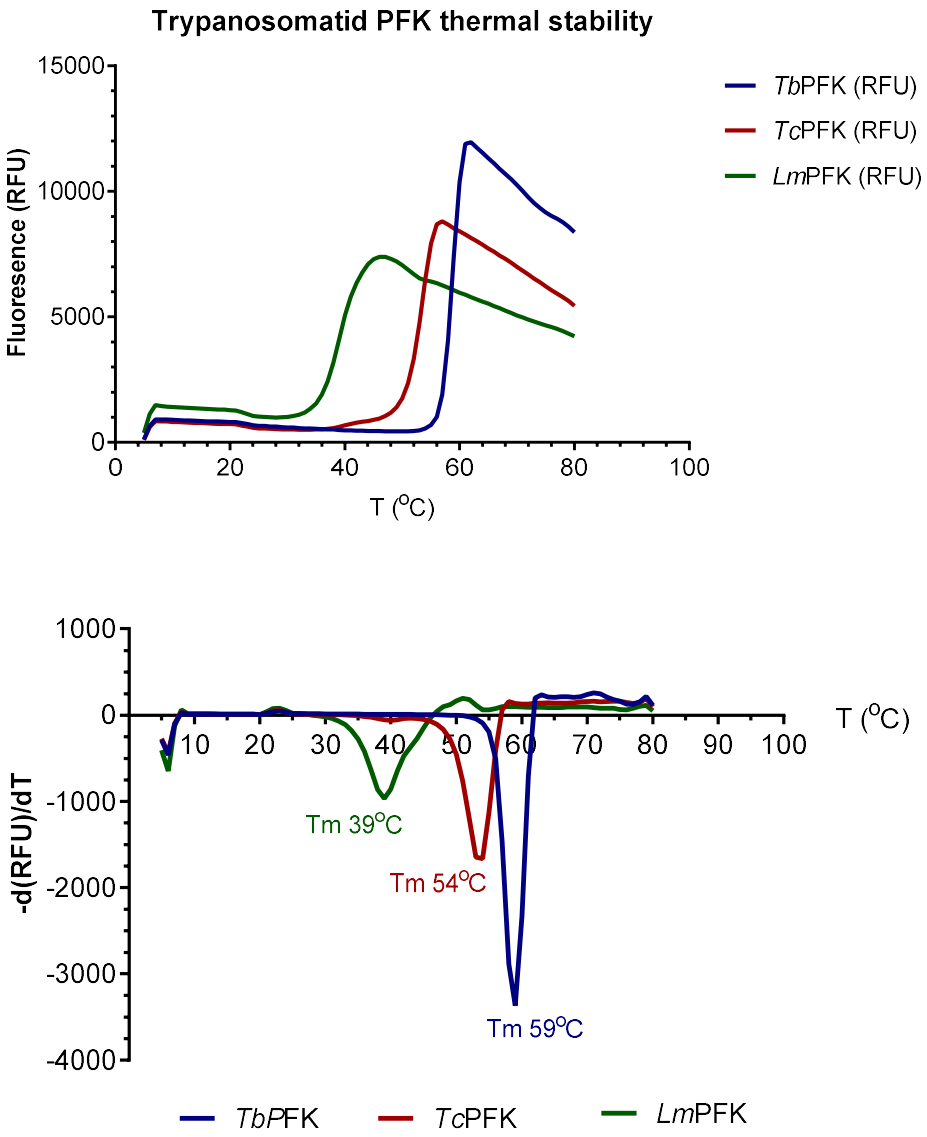

Figure 3.13 : Thermal denaturation assays of trypanosomatid PFKs.

All experiments carried out in triplicate – single experiment trace shown for each PFK. TDA carried out in TEA buffer (10 mM MgCl2, 100 mM KCl, 50 mM TEA, 10% glycerol, 0.005% TWEEN, pH 7.4) with SYPRO orange dye. 1.9 µM PFK in 50 µL reaction. Temperature gradient 20 – 80 °C in 0.5 °C steps, 30 second hold time.

3.6.3.2 : Stability of trypanosomatid PFKs with substrates.

A range of analytes were tested alongside the trypanosomatid PFKs in TDA experiments to test their effect on the thermal stability of the protein. **Figure 3.14** shows the change in melting temperature (ΔTm) for *T. brucei, T. cruzi* and *L. infantum* PFKs in the presence of the allosteric activator AMP, the substrates ATP and F6P and the products ADP and F16BP. AMP, ATP and F16BP all increased the thermal stability of the trypanosomatid PFKS with a positive ΔTm. F6P did not cause a change in the Tm of any of the trypanosomatid PFKs - suggesting that F6P cannot bind in isolation – as previously hypothesised when comparing the apo- and ATP-bound crystal structures of *Tb*PFK (McNae & Martinez-Oyanedel, 2009). Interestingly, ADP reduced the stability in *Tb*PFK and *Tc*PFK and increased *Li*PFK stability by 2-3^{o}C - a small but significant change. This had a cumulative effect when added together with F16BP, suggesting that both products can bind to the PFK enzyme both in isolation and as a pair.

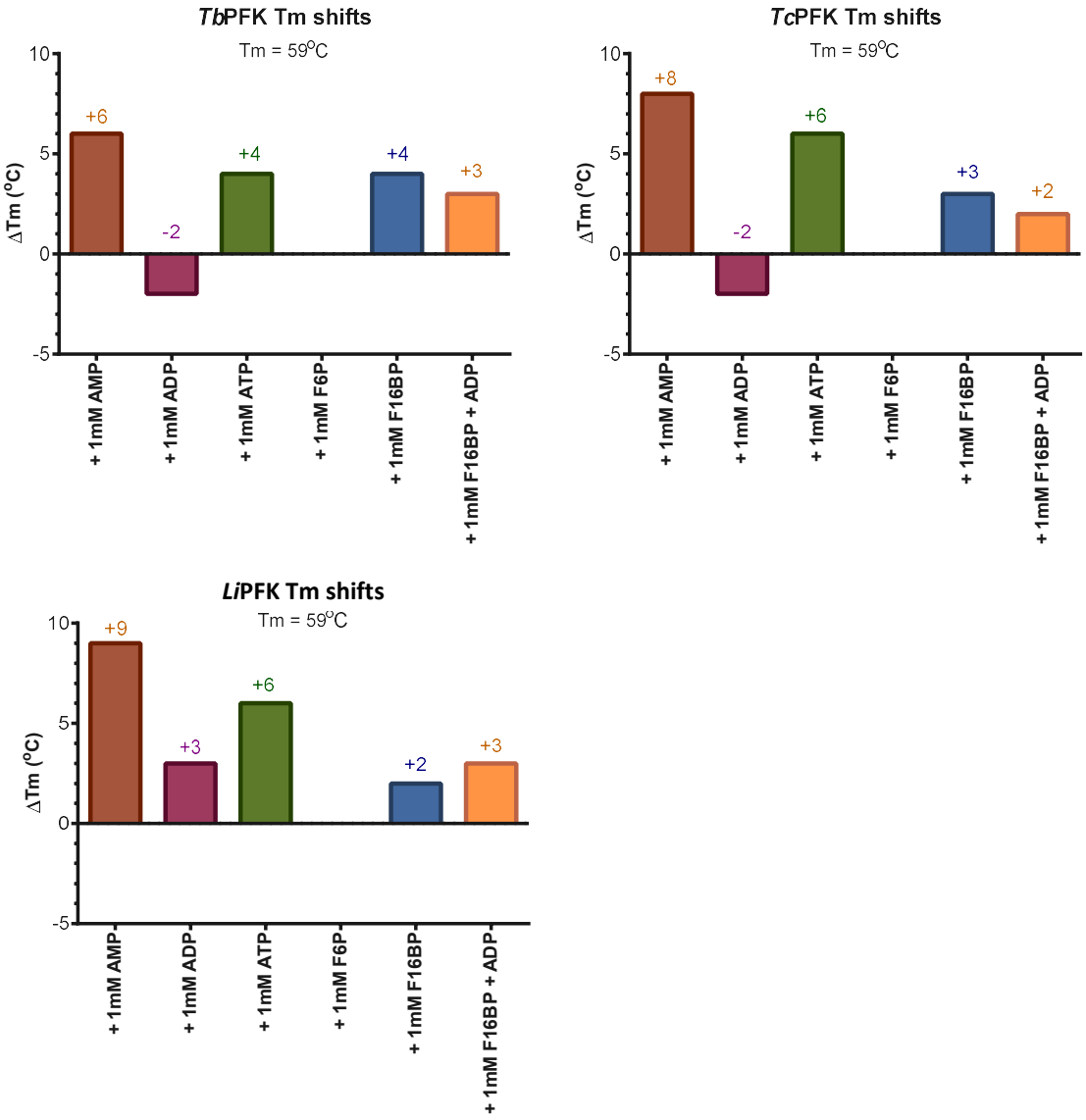

Figure 3.14 : Melting temperature shifts for trypanosomatid PFKs with substrates.

All experiments carried out in triplicate. 2 µM PFK. Carried out with sypro orange dye, 20 – 80 °C temperature range, 0.5 °C increments in TEA buffer (10 mM MgCl2, 100 mM KCl, 50 mM TEA, 10% glycerol, 0.005% TWEEN, pH 7.4). Standard deviation = 0.1-0.3 °C, error bars not shown. 'Lm' = Leishmania infantum.

3.7. Trypanosomatid PFK activity and quality control.

A full description and comparison of the enzyme activity of the three Trypanosomatd PFKs discussed in this thesis is available in **Chapter 4 : PFK enzyme kinetics**.

3.7.1 *T. brucei* PFK was consistent in activity between purification batches.

The SDD project required the testing of a large number of compounds (>600) tested against the *T. brucei* PFK enzyme. From a 1L pellet of C41 cells, the average PFK yield after purification was 15.7 mg. The activity of each batch of enzyme was tested for activity under saturating substrate conditions (5 mM ATP, 10 mM F6P) using a linked enzyme assay (PYK/LDH assay). This assay measures PFK activity by linking the production of ADP by the enzyme to two downstream enzymes – pyruvate kinase (PYK) and lactate dehydrogenase (LDH). The activity is measured by recording the change in absorbance of NADH at 340 nm as it is oxidised to NAD+ using a photospectrometer (**figure 3.15**). A full protocol for this assay is given in **section 2.3.1**.

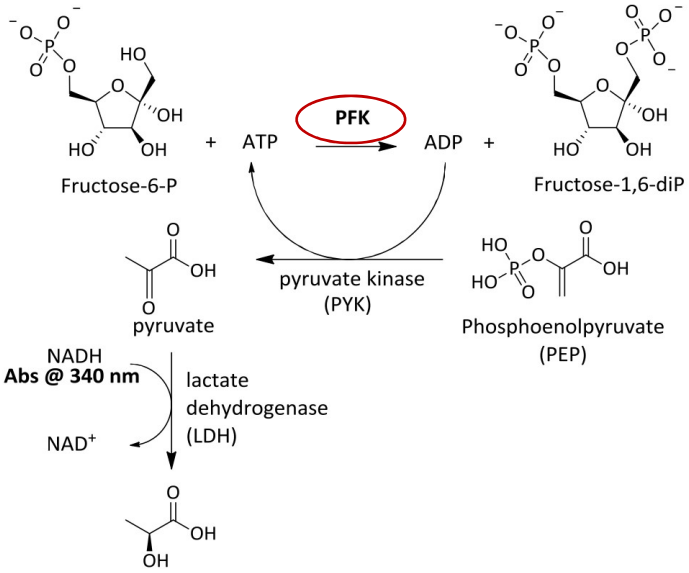

Figure 3.15: Reaction schematic of PYK/LDH assay for measuring PFK activity.

Specific activity was measured firstly by taking the gradient of the raw absorbance trace over time at the linear section of the curve. Each absorbance value was converted to concentration of NADH using the Beer-Lambert law ($A = \varepsilon cl$) assuming an extinction coefficient of 6.22 $mM.cm^{-1}$. Rate of NADH oxidation was converted to specific activity (µmoles NADH converted per minute per milligram of protein). **Figure 3.16** Shows the specific activity of the *T. brucei* PFK batches expressed and purified over a 2-year period. *T. brucei* PFK had relatively consistent batch-to-batch activity.

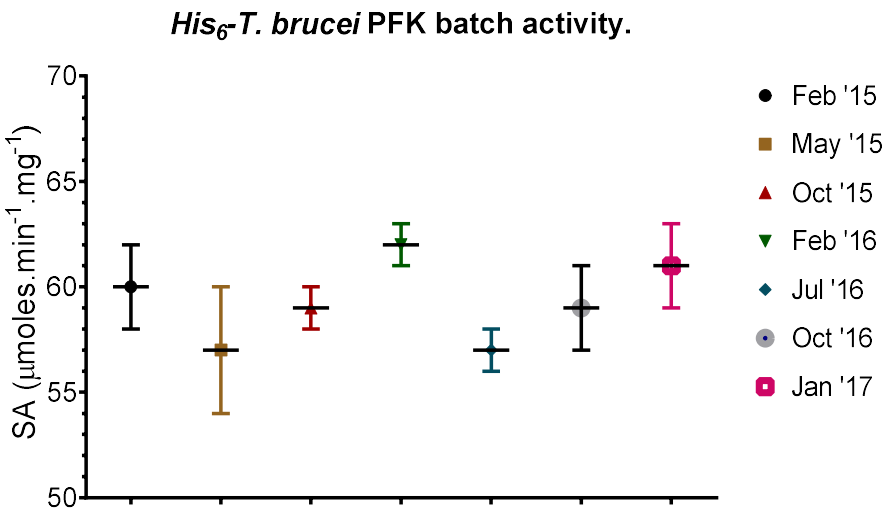

Figure 3.16: T. brucei PFK batches were consistent in activity.

Specific activity of purified recombinant His_6-tagged T. brucei PFK batches over a 2-year period. Activity was tested at 25 °C in TEA buffer (10 mM MgCl2, 100 mM KCl, 50 mM TEA, 10% glycerol, 0.005% TWEEN, pH 7.4) using the PYK/LDH assay. 5mM ATP, 10 mM F6P used. All experiments carried out in triplicate, error bars denote standard deviation.

3.7.2 DMSO inhibits T. brucei PFK activity.

To test the organic inhibitor compounds against trypanosomatid PFK, a solvent is required to dissolve and make up the powdered compound stocks, and to attempt to keep the compound soluble when testing in aqueous buffer. The solvent used for this was dimethyl sulphoxide (DMSO). The activity of *T. brucei* PFK in the presence of different concentrations of DMSO was analysed using the PYK/LDH linked enzyme assay. The effect of DMSO on the downstream auxiliary enzymes (pyruvate kinase and lactate dehydrogenase) was first assessed by providing the assay with 0.5 mM ADP in the absence of PFK – to fuel the downstream reactions (see **figure 3.15**). DMSO had relatively no effect on the auxiliary enzymes up to 10 % (v/v) DMSO (**figure 3.17**). The solvent was then tested against *T. brucei* PFK in the assay with 5 mM ATP and 0.6 mM F6P provided – the substrate concentrations used in the PYK/LDH assay when testing the inhibitor compounds (see **section 6.2.1, chapter 6**). DMSO inhibited the activity of *T. brucei* PFK as a function of concentration. 1 % DMSO lead to a 16 % decrease in activity, and 10 % (v/v) DMSO inhibited the enzyme by almost 70%. It was decided that 1% DMSO would be used as a final concentration in assays as a balance between enzyme activity and likelihood of compound solubility in aqueous solution.

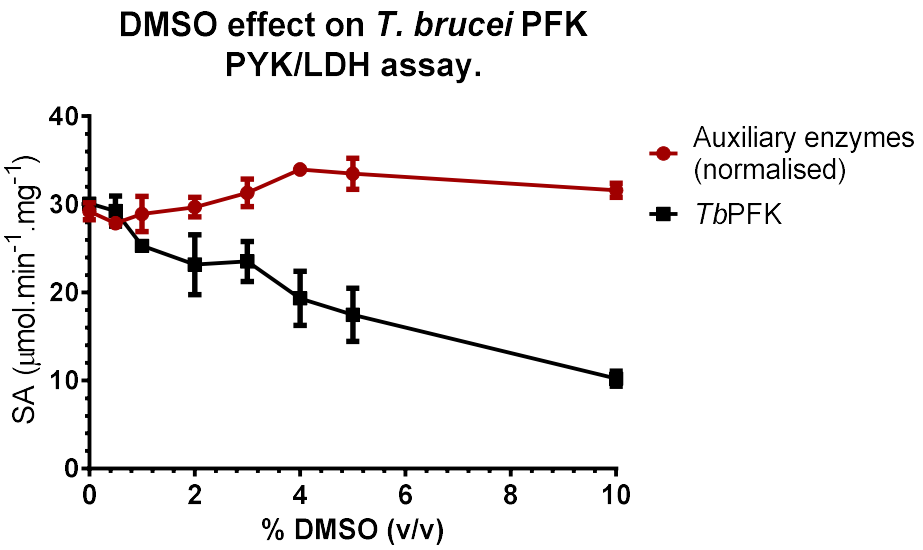

Figure 3.17: DMSO inhibits T. brucei PFK activity.

*Tested using the PYK/LDH linked enzyme assay. 4 µg/ml PFK, 5 mM ATP and 0.6 mM F6P was used when testing against T. brucei PFK (**black**). 0.5 mM ADP was provided when testing against auxiliary enzymes only (**red**)(data normalised to TbPFK activity data). All experiments carried out in triplicate at 25 °C, error bars denote standard deviation.*

3.8. Structural characterisation of T. brucei PFK (X-ray crystallography).

Table 3.5 summarises the available crystal structures of a range of eukaryotic PFKs. As can be seen in the table, the only eukaryotic PFK to be solved with F6P bound is S. cerevisiae PFK (PDB code 3O8O) (Banaszak et. al, 2011). Evans et al. carried out pioneering work on the bacterial PFK structural and mechanism by obtaining a crystal structure of a chimeric bacterial PFK – made up of the ATP binding region of *B. stearothermophilus* PFK grafted onto the *E. coli* PFK enzyme (Evans, 1992). Apo- and ATP-bound structures of *T. brucei* PFK revealed that upon ATP binding, a conformational change in 3 loops surrounding the active site opened up space for F6P to be accommodated (McNae et. al, 2009). As ATP is required as a precursor to F6P binding, it is difficult to produce conditions where either only F6P or ATP and F6P would be bound, without the enzyme turning the substrates over. Protocols for all crystallography experiments can be found in **section 2.6, chapter 2**.

Author	**Organism**	**Ligand**	**PBD code**	**Protein stoichiometry**
Martinez-oyandel et. al. 2007	*T. brucei*	Apo	2HIG	Homo 4-mer (A_4)
McNae et. al. 2009	*T. brucei*	MgATP	3F5M	Homo 4-mer (A_4)
Banaszak et. al. 2011	S. cerevisiae	F6P, F26BP	3O8O	Hetero 4-mr A_2B_2
Benjamin, 2007	*S. pombe*	F6P/ATP	NA	Homo-octamer
Banaszak et. al. 2011	Rabbit - muscle	ADP/ADP,ATP	308N/308L	Monomer
Strater et. al. 2010	*P. pastoris*	ATP, SO_4^{2-}	3OPY	Hetero 12-mer ($A_4B_4C_4$)
Kloos et. al 2015	*H. sapiens* – platelet	Apo/ADP	4RH3/4U1R	Homo 4-mer (A_4)
Webb et. al. 2015	*H. sapiens* – platelet	ATP/ADP	4XYJ/4XYK	Home 4-mer (A_4)

Table 3.5: Summary of published eukaryotic PFK crystal structures.

3.8.1 Two strategies for obtaining a fructose-bound structure of *Tb*PFK.

To obtain a *T. brucei* PFK structure with the F6P substrate bound, two strategies were adopted to 'trap' the enzyme in an inactive form; Either by using non-hydrolysable ATP to obtain a ATP-

F6P bound structure, or trapping the enzyme in an intermediate form – using aluminium trifluoride to obtain an ADP-AlF_3-F6P bound structure in a mimicked transition state.

3.8.2 Crystallography using non-hydrolysable ATP with TbPFK.

A non-hydrolysable ATP analog (Adenosine 5'-(β,γ-imido)triphosphate) was added to an equimolar concentration of F6P (0.5mM) with 4.0 mg/ml *Tb*PFK. This mixture was made up in standard enzyme assay buffer (10 mM MgCl2, 100 mM KCl, 50 mM TEA, 10% glycerol, 0.005% TWEEN, 1% DMSO, pH 7.4) and incubated at 25 °C for 20 minutes before being used in automated crystallography screens using an Art Robbins 'Gryphon' nano-litre pipetting robot. A JCSG-Plus (Molecular Dimensions) 96 condition plate was used to screen for crystal conditions. Rod-like crystals similar to those shown in **figure 3.18A** were found under 2 buffer conditions: (0.1M Tris, 0.2 M $MgCl_2$, 10 % Peg 8K, pH 7.0) and (0.2M Magnesium formate, 20% Peg 3.35K, pH 7.0). Crystals from these conditions were vortexed to produce microseeding material which was used to streak additional Limbro plates with the same conditions but with a pH range from 6.1 -7.1. No crystals large enough to be picked were obtained. Additionally, some larger diamond-like crystals were identified from the screen (0.1 M Bicine, 10 % PEG 6K, pH 9.0)(**figure 3.18B**). These crystals were large enough to pick but diffracted poorly, with the best resolution estimated at >10 Å.

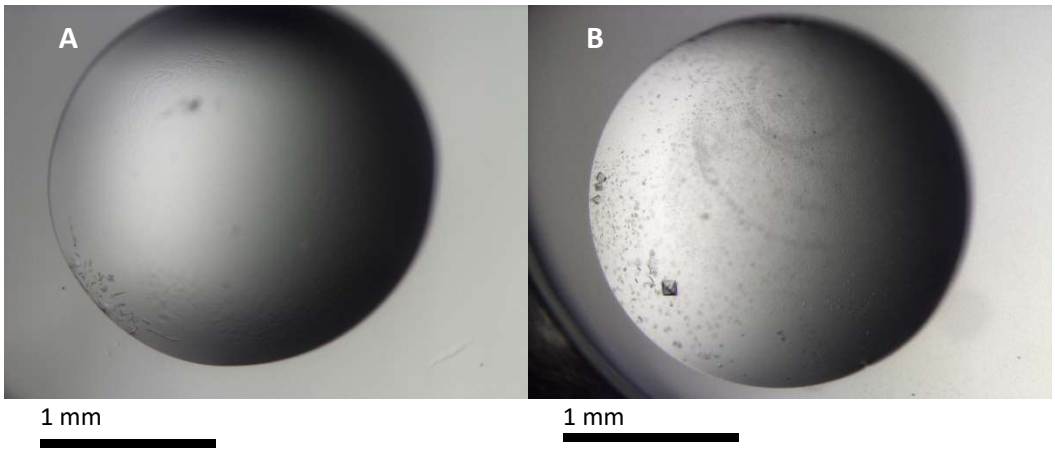

Figure 3.18: Non-hydrolysable ATP with TbPFK produces rod-like and diamond-like crystals.

Plated using Art Robbins 'Gryphon' nano-litre pipetting robot (1µl drop). A) TbPFK with 0.5 mM ATP_{NH}, 0.5 mM F6P.1M Tris, 0.2 M $MgCl_2$, 10 % Peg 8K, pH 7.0 grown at 16 °C over 3 days. B) 0.1 M Bicine, 10 % PEG 6K, pH 9.0.

3.8.3 Attempting the ADP-AlF3-F6P transition state.

To capture the *Tb*PFK enzyme in a 'transition state-like' crystal conformation, aluminium trifluoride was used (AlF_3). The transition state of the phosphotransfer of the γ-phosphate on ATP to F6P is represented in **figure 3.19A**. The free phosphate $[PO_4]^{3-}$ when bound transiently by both ATP and F6P forms a trigonal bipyramid structure. Aluminium trifluoride is also able to form a trigonal bipyramid structure in solution by forming aluminium tetrafluoride – a square planar structure but when transiently coordinated to two additional oxygens forms a trigonal biplanar structure closely mimicking a phospho-transfer transition state (Wittinghofer, 1997)(**figure 3.19B**).

A

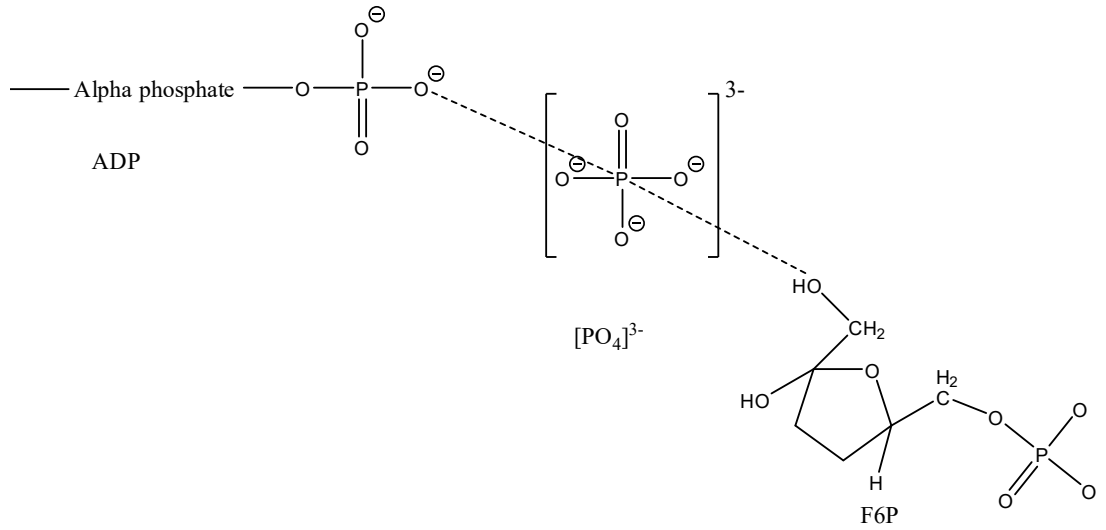

B

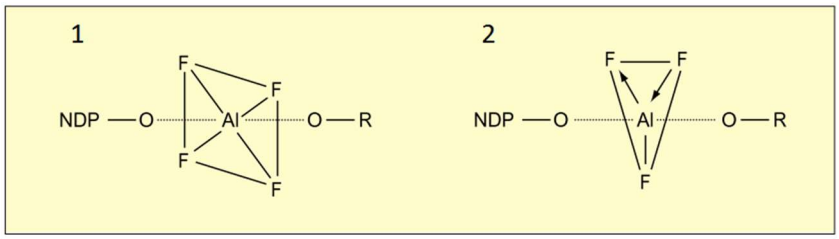

Figure 3.19: Aluminium trifluoride mimics the transition state phosphate in a kinase reaction.

A) Schematic representation of phosphotransfer from ATP to F6P. In its transition state, the phosphate $[PO_4]^{3-}$ adopts a trigonal biplanar structure.

B) Phosphotransfer intermediate can be mimicked by either aluminium tetrafluoride (1) or aluminium trifluoride (2) in solution. NDP = nucleotide diphosphate. R = nucleophile. Adapted from (Wittinghofer, 1997).

3.8.4 AlF_3 in the presence of ADP and F6P increases *Tb*PFK thermal stability.

As a source of aluminium trifluoride was immediately available, it was decided to dissolve a solution in standard enzyme buffer (10 mM MgCl2, 100 mM KCl, 50 mM TEA, 10% glycerol, 0.005% TWEEN, 1% DMSO, pH 7.4) and to pre-incubate the solution with different combinations with *Tb*PFK. TDA was then carried out to observe any effect of the thermal stability of the protein in the presence of the F6P/ADP/AlF_3 mixture. A full protocol can be seen in section **2.5.2.2**. **Table 3.6** shows the change in transition melting temperature (ΔT_m) for *Tb*PFK tested against the various components of the transition state. The F6P/ADP/AlF_3 complex increased the stability of *Tb*PFK by 12 ^oC, with no signs of aggregation by the complex (**figure 3.20**). Alone, AFP, F6P and AlF_3 produced little or no increases in the thermal stability of *Tb*PFK.

Component	ADP	AlF_3	F6P	F6P/ADP	F16BP	ADP/AlF_3	F6P/ADP/AlF_3
ΔT_m	-2	0	0	+1	+2	+1	+12

Table 3.6: The F6P/ADP/AlF3 complex significantly increases the thermal stability of TbPFK.

Thermal Denaturation Assay (TDA) results for TbPFK tested against a range of analytes (1mM) at 2 µM PFK. T_m for TbPFK was observed to be 59.0 ^oC in the absence of analyte.

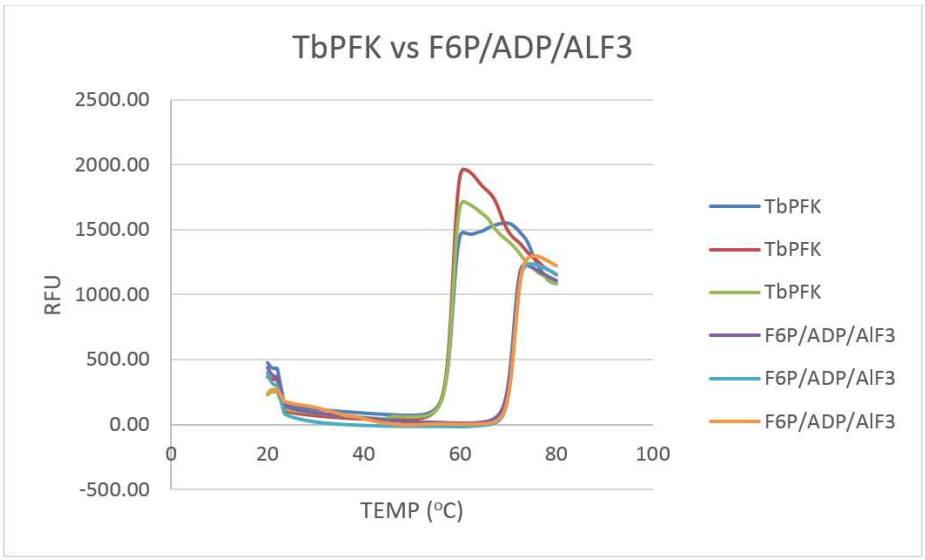

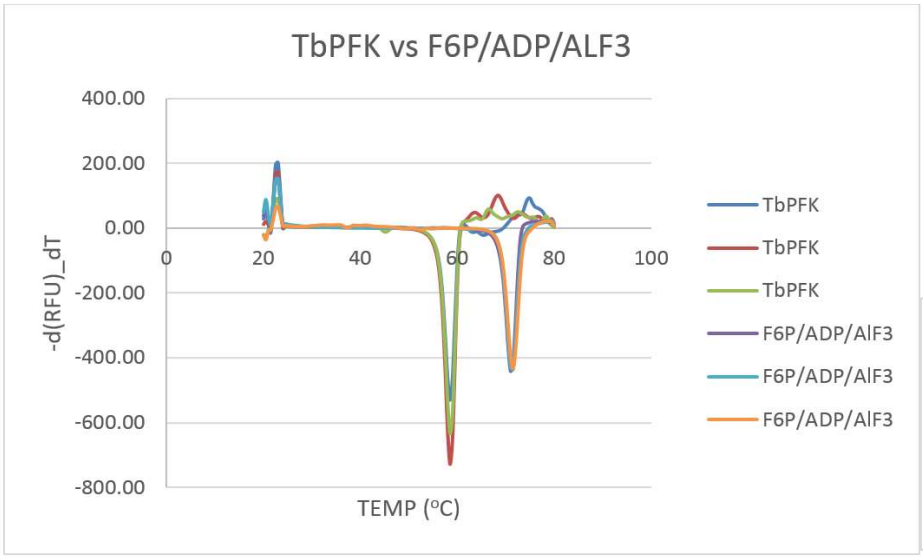

TbPFK Tm = 59.0 °C

TbPFK + F6P/ADP/AlF$_3$ T_m = 71 °C

Figure 3.20: The F6P/ADP/AlF3 complex significantly increases the thermal stability of TbPFK.

A) Raw fluorescence trace for TbPFK with and without the F6P/ADP/AlF$_3$ mixture (1mM). 2 µM PFK, 0.5 °C increments from 20 – 81 °C using Spyro Orange fluorescence dye. Each condition carried out in triplicate. B) Plot showing change in fluorescence over time (d(RFU)/dT).

It was clear from TDA measurements that when all three elements of the F6P/ADP/AlF$_3$ complex were mixed together in the presence of *Tb*PFK, some form of stabilising complex is present. This experiment was repeated to ensure no aggregated AlF$_3$ was being formed and similar results were produced – suggesting the ADP-AlF$_3$-F6P intermediate complex was being formed with *Tb*PFK. Controls containing the F6P/ADP /AlF$_3$ alone without protein showed no significant fluorescent response (data not shown).

3.8.5 Obtaining crystals of TbPFK with the F6P/ADP/AlF_3 complex.

To recreate the conditions used when the F6P/ADP/AlF_3 complex was tested against *Tb*PFK in TDA, an equimolar (1mM) solution of F6P, ADP and AlF_3 was made up in the standard enzyme buffer (50 mM TEA, 10 mM $MgCl_2$, 100 mM KCl, 10% glycerol, 0.005% $TWEEN_{20}$, pH 7.4), in the presence of 3 – 4 mg/ml His_6-*Tb*PFK. The mixture was pre-incubated with the protein for 15 minutes at room temperature before being used. The mixture was plated out using the hanging drop method with 2 drops on each cover slide for each well condition – a 2 µl drop (1:1 protein : well solution) and 3 µl drop (2:1 protein : well solution). Well solutions were buffered from pH 6.1 – 7.1 across the plate using 2-(N-morpholino) ethanesulfonic acid (MES) and imidazole as buffering agents. Polyethelene glycol (PEG) 4K was used at 12 – 18% down the plate. A full protocol can be seen in section **2.6.2.**

After an average of 4 days small rod-like crystals similar to those found in the robot screen with ATP_{NH} were observed as shown in **figure 3.21.**

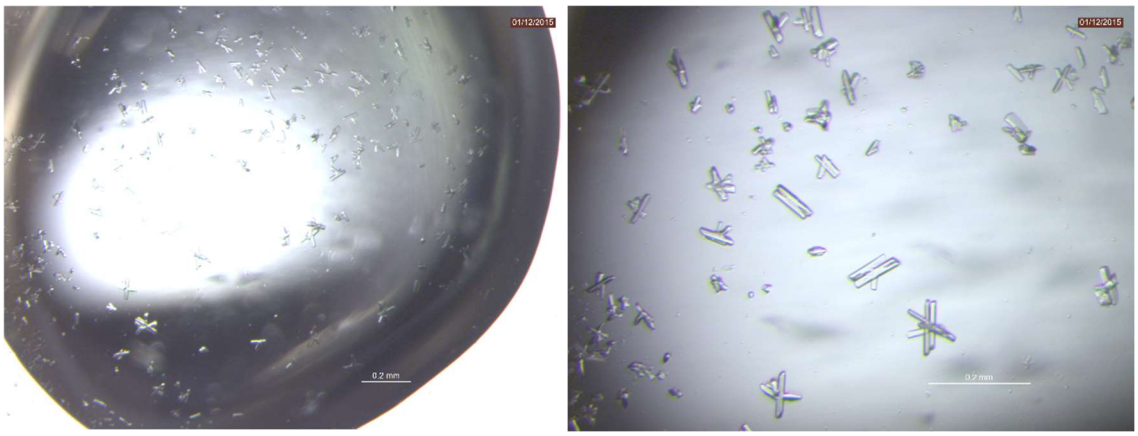

16% PEG 4K, pH 7.1

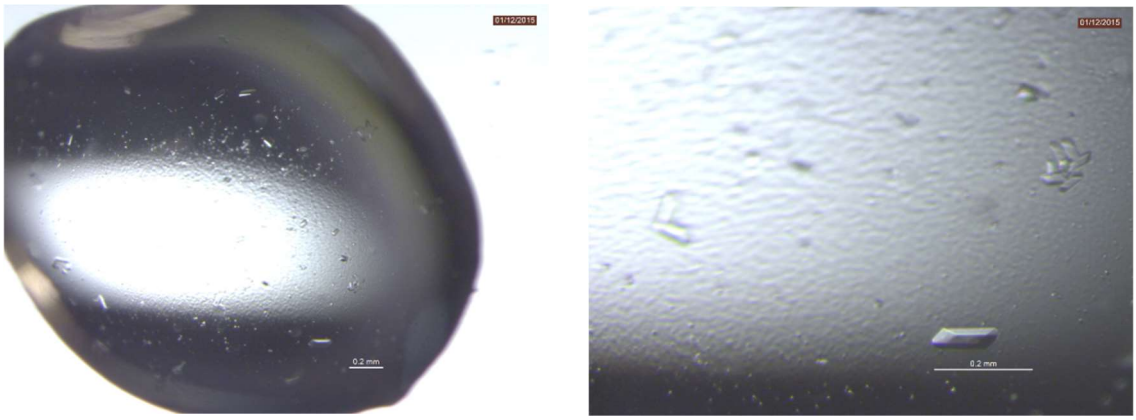

18% PEG 4K, pH 6.9.

Figure 3.21: Rod-like crystals of TbPFK in complex with F6P/ADP/AlF_3.

Different PEG types, micro seeding using existing crystals, streak plating and repeats of previous conditions were all used in an attempt to improve the crystal yield. None produced any significant advances in the size of the rod-like crystals. After a week of rod-like crystal growth it was observed that larger, diamond-like crystals started to grow, such as those shown in **figure 3.22.**

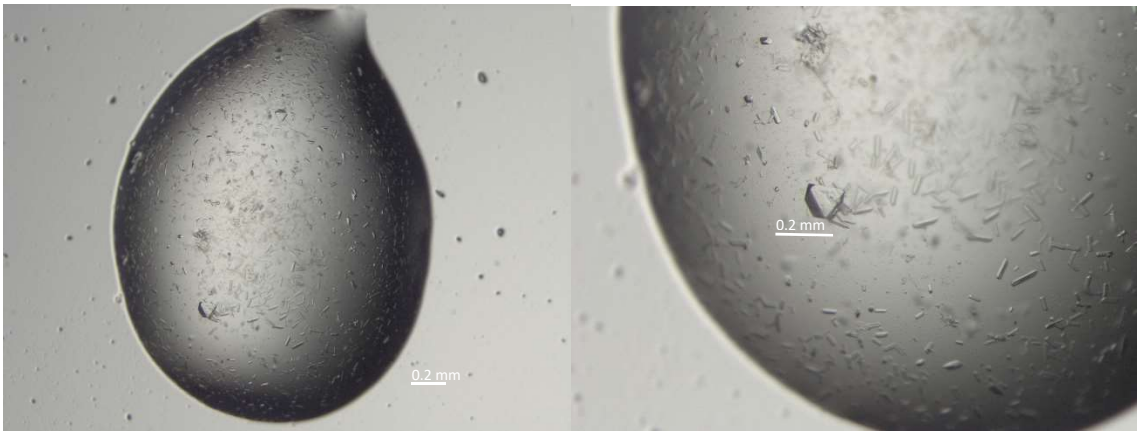

Figure 3.22: Larger diamond-like crystals of TbPFK in complex with F6P/ADP/AlF3 grow after 1 week.

3.5 mg/ml TbPFK + 1mM F6P/ADP/AlF_3. 16% PEG 4K, pH 6.9.

Despite obtaining larger crystals no usable diffraction data below ~8 Å was able to be collected, despite the crystals diffracting as protein. No further attempts at the F6P/ADP/AlF_3 transition state with *Tb*PFK were made before the time of writing.

Chapter 4: Enzyme kinetics and regulatory properties of phosphofructokinase.

4.1. Introduction to phosphofructokinase-1.

Phosphofructokinase-1 catalyses the conversion of fructose 6-phosphate to fructose 1,6-bisphosphate by using either ATP ('ATP-kinase') or PPi ('PPi-kinase) as a phospho donor. The enzyme exists in a wide range of organisms and cells, can be compartmentalised, and can operate as different isozymes and under different metabolic cell stress conditions. As such, the enzymatic activity and regulation of phosphofructokinase is remarkably diverse. Gene duplication and fusion events from a bacterial-like ancestral PFK have resulted in diversity in the structure and regulation of PFK-1 across species (**Chapter 1, section 1.4.1**). Despite this variation in structure, function and regulation, the active site of ATP-kinases is strikingly conserved amongst organisms (**figure 3.1, section 3.2.1**). Compartmentalisation of trypanosomatid PFKs as well as unique structural features and a reversion from PPi to ATP-dependency is likely to be key to their unique enzymatic profile. *T. brucei* PFK has been found to be more evolutionarily comparable to PPi-dependant PFK rather than ATP-PFK, and has been described as a 'chimera' of ATP and PPi-PFKs (Michels et al., 1997). What consequences does this PPi-kinase lineage have on the enzymatic activity of trypanosomatid PFK, and does this separate it from other eukaryotic PFKs? The majorly regulated enzyme in the glycolytic pathway of trypanosomes is the cytosolic enzyme pyruvate kinase (PYK) (Claustre et al., 2002). The only known effector of *T. brucei* PFK is the allosteric activator AMP (Nwagwu & Opperdoes, 1982).

The aim of this chapter is to characterise the kinetic and regulatory properties of three recombinantly expressed ATP-PFKs from *T. brucei, T, cruzi and L. infantum* parasites, and to compare and contrast and gain a greater insight into the function of these enzymes in different trypanosomatids. This may further our understanding of their role in glycolysis, and as potential therapeutic targets. To achieve this a plate based assay was modified to test the kinetics of each enzyme under different concentrations of substrates, pH conditions, known and unknown metabolic intermediates and effectors. Additionally, substrate affinity measurements were also made using surface plasmon resonance (SPR) and thermal denaturation assays (TDA), to describe the binding interaction with the enzyme.

4.2. Substrate kinetics of PFK measured through a linked enzyme assay.

To test the substrate kinetics of the trypanosomatid PFKs, the PYK/LDH enzyme assay was optimised for use as a 96-well plate based kinetic assay. This enzyme-linked assay measures PFK activity by linking ADP production to two downstream enzymes – pyruvate kinase (PYK) and lactate dehydrogenase (LDH). Activity is measured by reading the change in absorbance at 340 nm as NADH is oxidised to NAD^+ using a spectrophotometer. **Figure 4.1** outlines the reaction scheme for the assay, and a full protocol can be found in **section 2.3.1**.

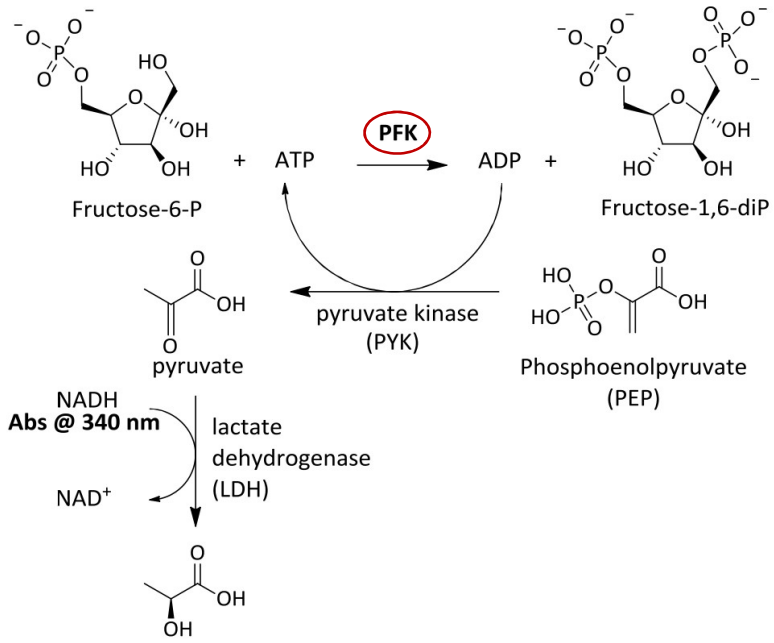

Figure 4.1: PYK/LDH enzyme linked assay used for measuring PFK substrate kinetics.

To measure substrate kinetics against PFK, serial dilutions of ATP and F6P were titrated against a set concentration of PFK and a saturating concentration of F6P or ATP respectively. Absorbance at 340 nm was recorded in 10 second intervals over 10 minutes and converted to concentration using the Beer-lambert law (A = εcl). Initial rates were calculated by taking the slope of absorbance over time then converted to specific activity (µmoles of NADH converted per minute, per milligram of protein). In all experiments an optimised final concentration of 4 µg/ml of PFK enzyme was used. All assays were plated into clear 96-well plates, with a final reaction volume in each well of 100 µl in a TEA-based buffer (10 mM MgCl2, 100 mM KCl, 50 mM TEA, 10% glycerol, 0.005% TWEEN, pH 7.4).

4.2.1 Substrate kinetics of trypanosomatid PFKs.

F6P and ATP titrations were carried out against *T. brucei, T. cruzi* and *L. infantum* PFKs using the PYK/LDH enzyme assay and data was plotted using Graphpad prism. Hyperbolic Michaelis-Menten and 'allosteric sigmoidal' curves were fitted to each dataset and the best fit was assessed by the R^2 value. Details of the Michaelis-Menten and Allosteric Sigmoidal fit models can be found in **section 2.3.1.3**. K_m, K_{half}, k_{cat}, V_{max} and Hill coefficient values were taken from these plots using Graphpad Prism ver. 6. **Figure 4.2** shows an example plot for the titration of ATP against *T. brucei* PFK.

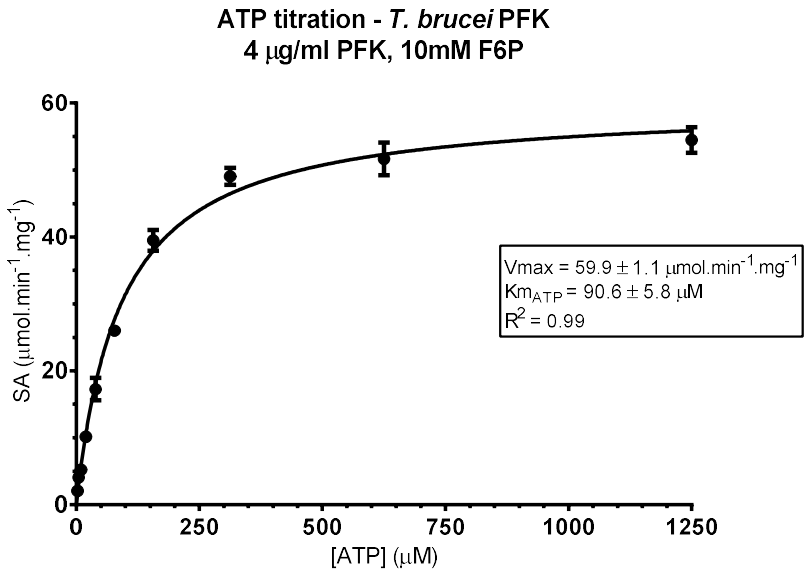

Figure 4.2: Michaelis-Menten plot of ATP titration against T. brucei PFK (PYK/LDH assay).

2-fold serial dilution of 5 mM – 2.4 µM ATP against 4µg/ml PFK and 10 mM F6P. Data points for the highest two concentrations have been omitted for clarity of fit for lower concentrations. Michaelis-Menten fit has been applied. All experiments were carried out at 25 °C in triplicate, error bars denote standard deviation.

All three enzymes showed hyperbolic responses with respect to ATP, and fitted Michaelis-Menten curve models well ($R^2 \geq 0.99$). F6P titrations however revealed sigmoidal binding responses at lower concentrations (data shown in section **4.2.3**), and were fitted with the 'allosteric sigmoidal' curve model. **Table 4.1** shows the calculated kinetic parameters for all three enzymes. Kinetic constants are given as Michaelis constants (Km) for ATP titrations, and half maximal constants (Khalf) for F6P titrations. Both represent affinity for the substrate and are a measure of the concentration of substrate required for half of the maximal activity of the enzyme.

	K_{half}^{F6P} (µM)	Hill coefficient (*h*) (F6P)	K_m^{ATP} (µM)	Hill coefficient (*h*) (ATP)	Specific Activity ($\mu mol^{-1}.min^{-1}.mg^{-1}$)	Kcat (s^{-1})
***TbP*FK**	803 ± 48	2.1 ± 0.2	83 ± 5	1.2 ± 0.2	60 ± 1	54 ± 1
***Tc*PFK**	469 ± 26	1.9 ± 0.2	79 ± 6	1.1 ± 0.1	59 ± 1	53 ± 1
***Li*PFK**	2391 ± 99	2.2 ± 0.1	24 ± 0.4	1.1 ± 0.3	26 ± 1	23 ± 1

Table 4.1: T. brucei and T. cruzi PFKs show comparable substrate kinetics.

Data measured using the PYK/LDH linked enzyme assay. ATP titrations: 12 dilutions 5 mM – 2.4 µM. F6P titrations: 12 dilutions 20 mM – 9.8 µM. All experiments were carried out at 25 °C in triplicate, standard deviations for each parameter are given.

T. brucei and *T. cruzi* PFK had comparable enzyme activities and affinities for F6P and ATP. Interestingly, *L. infantum* PFK, while having the strongest affinity for ATP (Km_{ATP} 24 µM), had a relatively low affinity for F6P (K_{half}^{F6P} >2 mM) and slower maximum activity compared to the other trypanosomatid PFKs at saturating concentrations of (F6P V_{max} = 26 $\mu mol^{-1}.min^{-1}.mg^{-1}$).

4.2.2 Trypanosomatid PFKs show a hyperbolic response to ATP.

ATP titrations against *T. brucei*, *T. cruzi* and *L. infantum* PFKS are shown in **figure 4.3**. Hill plots of the ATP titrations (data not shown) showed no evidence of binding cooperativity with regards to ATP for any of the enzymes tested (Hill coefficient '*h*' = ~1). The trypanosomatid enzymes were not inhibited by ATP at concentrations up to 5mM, unlike mammalian PFKs which are inhibited at ATP concentrations above 2 mM (per. comm. P Fernandes). ATP binds to PFK by forming a complex with Mg^{2+} ions. A sufficient ratio of Mg^{2+} and ATP is therefore required for maximum activity. Only when ATP exceeds Mg^{2+} concentration, is ATP inhibitory against *Tb*PFK (Nwagwu & Opperdoes, 1982). ATP and Mg^{2+} must therefore bind as a pair (MgATP) – when ATP exceeds the Mg^{2+} concentration a high population of individual ATP molecules bind without Mg^{2+} (which is required in co-ordinating the phospho-transfer) and inhibit the enzymes activity.

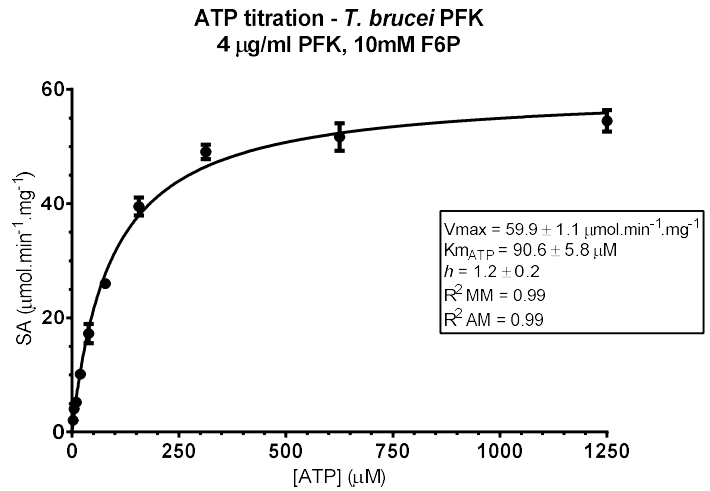

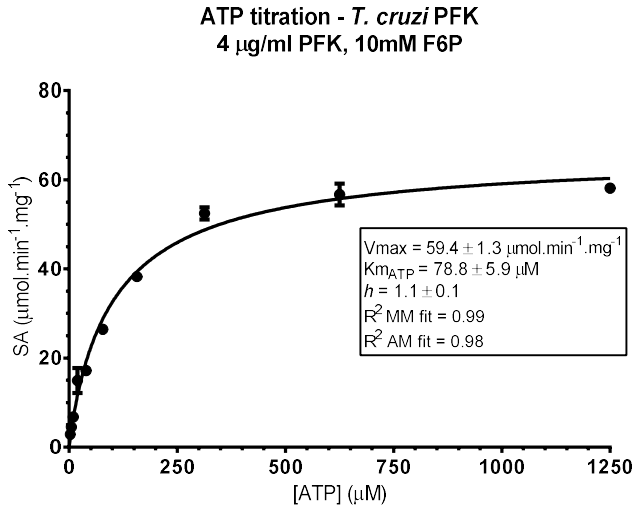

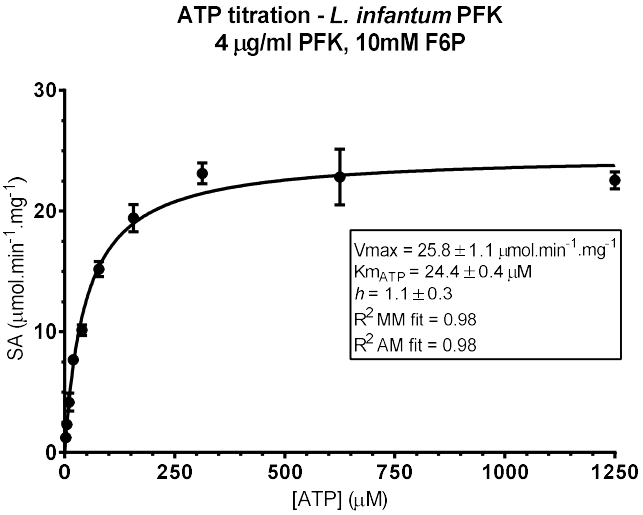

Figure 4.3: ATP titrations against Tc, Tb and LiPFKs.

2-fold serial dilution of 5 mM – 2.4 µM ATP against 4µg/ml PFK and 10 mM F6P. Highest two dilutions have been omitted for clarity of fit. Experiments carried out at 25 °C in triplicate, error bars denote standard deviation. 'AM' = allosteric sigmoidal fit. 'MM' = Michaelis-Menten fit.

4.2.3 Trypanosomatid PFKs show cooperativity in F6P binding.

F6P titrations against all three trypanosomatid PFK enzymes gave Hill coefficient (*h*) values of >1, as shown in **table 4.1**. Furthermore, the plots fitted non-hyperbolic, sigmoidal curve better than a traditional Michaelis-Menten curve fit, and a noticeable sigmoidal tail can be observed at the lower concentrations of F6P for all three enzymes (**figure 4.4**) This sigmoidal binding response and Hill coefficient values of *h* >1 suggest co-operative binding; That the binding of one F6P molecule to one subunit within the PFK tetramer induces a change in a neighbouring subunit to more readily accommodate the next F6P molecule.

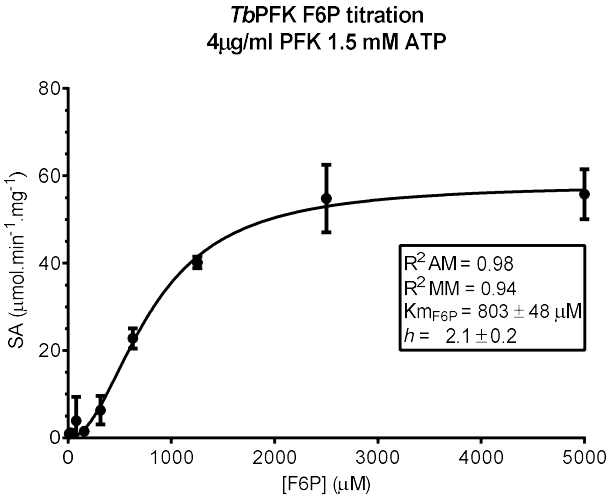

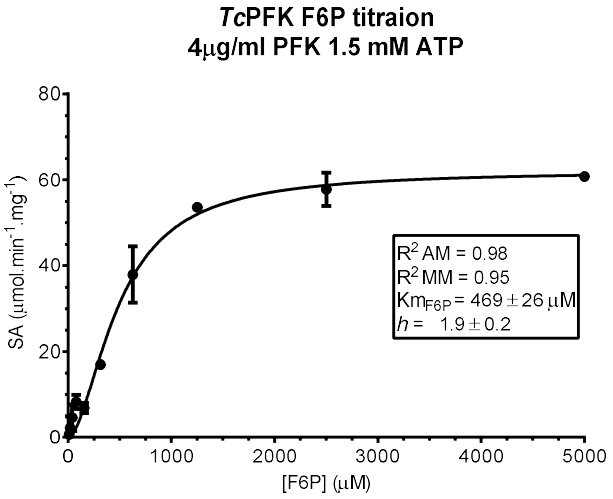

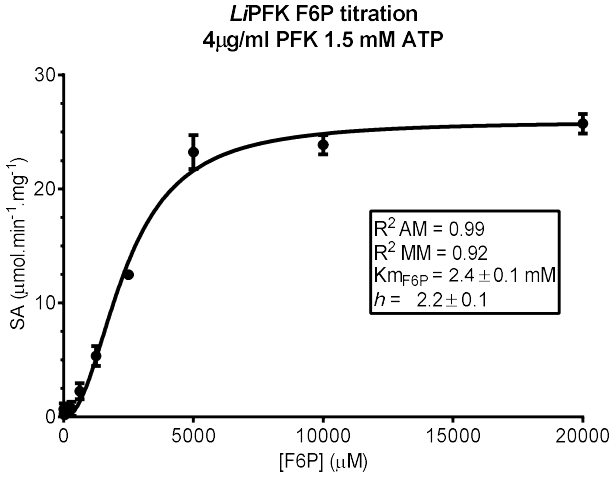

Figure 4.4: F6P titrations against Tc, Tb and LiPFKs.

2-fold serial dilution of 20 mM – 9.8 μM F6P against 4μg/ml PFK and 1.5 mM ATP. Highest two dilutions have been omitted for clarity of fit for T. brucei and T. cruzi plots. Experiments carried out in triplicate at 25°C, error bars denote standard deviation. 'AM' = allosteric sigmoidal fit. 'MM' = Micahelis-Menten fit.

4.2.4 Reaction order matters when measuring PFK kinetics.

A series of F6P and ATP titrations were carried out against PFK in the PYK/LDH assay with different reaction orders;

- 'PFK/ATP + F6P': ATP is incubated with the PFK protein for 15 minutes (RT). Reaction is started by adding F6P.
- 'PFK + F6P/ATP' : A premade mixture of F6P and ATP is added to the PFK to start the reaction (no PFK pre-incubation).
- 'PFK/F6P + ATP' : F6P is incubated with the PFK protein for 15 minutes. Reaction is started by adding ATP.

The dose-response plots for F6P titrations against *T. brucei* PFK using these different reaction order combinations is shown in **figure 4.5**.

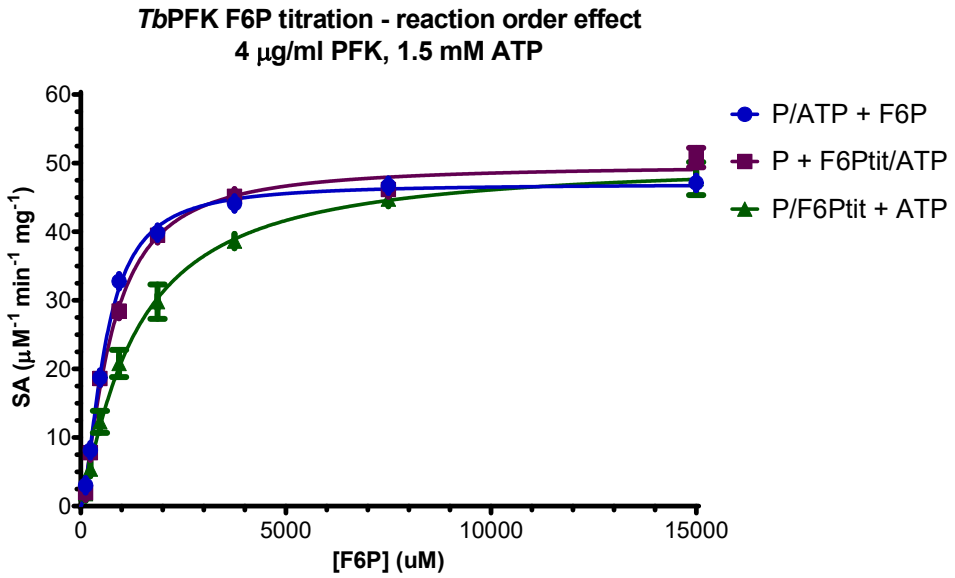

	P/ATP + F6Ptit	P + F6Ptit/ATP	P/F6Ptit + ATP
Vmax (µmol^{-1}.min^{-1}.mg^{-1})	48 ± 0.8	50 ± 0.9	50 ± 1.3
K_{half}^{F6P} (µM)	596 ± 19	736 ± 37	1220 ± 97
Hill coefficient (*h*)	1.7 ± 0.1	1.4 ± 0.1	1.2 ± 0.1

Figure 4.5: Reaction order effects the measured kinetics of T. brucei PFK with regards to F6P.

Allosteric sigmoidal plots of F6P titrations. All experiments carried out at 25°C in triplicate, error bars denote standard deviation. F6P concentrations ranged from 15 mM to 117 µM. 'tit' = titration. Assay buffer contained Mg^{2+} (10 mM MgCl2, 100 mM KCl, 50 mM TEA, 10% glycerol, 0.005% TWEEN, pH 7.4).

From the plots in **figure 4.5** it is evident that when incubated with F6P only, the *Tb*PFK has a lower overall measured affinity for F6P (K_{half}^{F6P} = 1.2 mM). The strongest affinity for F6P is observed when the enzyme is pre-incubated with ATP (K_{half}^{F6P} = 0.6 mM). The overall velocity of the enzyme is unaffected by the reaction order, remaining at ~50 $\mu mol^{-1}.min^{-1}.mg^{-1}$ for each condition.

The effect shown may therefore be observed due to the proportion of the PFK population that is in an ATP bound state when the reaction is started; Comparison of apo enzyme and ATP-bound crystal structures of *T. brucei* PFK reveal that upon ATP binding, a conformational change opens up the active site to more readily accommodate F6P (McNae & Martinez-Oyanedel, 2009)(**Section 1.4.4, figure 1.14**). Pre-incubation with ATP is likely to force the enzyme population into an active state that has greater affinity for F6P. Conversely, incubation with F6P may allow weak binding of F6P initially, perhaps forcing the enzyme into a conformation with lower affinity for the substrate. However, reaction order had little effect on ATP affinities (data not shown), suggesting either;

- F6P cannot bind without ATP
- F6P binds weakly to PFK in the absence of ATP. Weak binding is then overcome by high concentrations and greater affinity for ATP when added.

Cooperativity in F6P binding, measured through the Hill Coefficient (*h*) for each plot was strongest also when ATP was pre-incubated with PFK. The conformational state of *Tb*PFK with ATP bound must allow for co-operative binding of F6P.

4.3. Alternative substrates used by trypanosomatid PFKs.

Phosphofructokinases can be grouped into one of two families; PPi-dependant PFKs and ATP-dependant PFKs. The three trypanosomatid PFKs described in this chapter are ATP-dependant PFKs, but have a PPi-dependant ancestral lineage. To examine if alternative phospho donors could be used, guanosine triphosphate (GTP) and pyrophosphate (PPi) were titrated against PFK with a set concentration of F6P (10 mM final). Again, all PFK enzymes were tested at concentrations of 4 μg/ml.

4.3.1 Trypanosomatid PFKs can no longer use PPi as a phospho donor.

PPi titrations against *T. brucei, T. cruzi* and *L. infantum* PFKs with a set concentration of F6P tested in the Aldolase/TIM linked enzyme assay (described in **section 2.3.2**) yielded no observable activity (data not shown). PPi titrations against PFK could not be tested in the orthogonal PYK/LDH assay as this assay relies on the creation of ADP for the downstream enzymes to work (see **section 2.3.1, chapter 2**). No PPi binding was observed against any of the enzyme surfaces tested in SPR, up to a final concentration of 10 mM.

4.3.2 GTP is an alternative phospho donor for trypanosomatid PFKs.

GTP titrations against PFK and a set concentration of F6P showed hyperbolic responses (h = 1.2 ± 0.1) in the PYK/LDH assay, suggesting GTP could be bound and turned over by the PFK enzyme in place of ATP. Furthermore, it was found that AMP had the same activating effect on the enzyme in relation to GTP as it does when used in ATP titrations - reducing the Vmax but significantly increasing the affinity of PFK for the nucleotide phospho donor (discussed in **section 4.5**). **Figure 4.6** shows the effect of AMP on a GTP titration against *T. brucei* PFK.

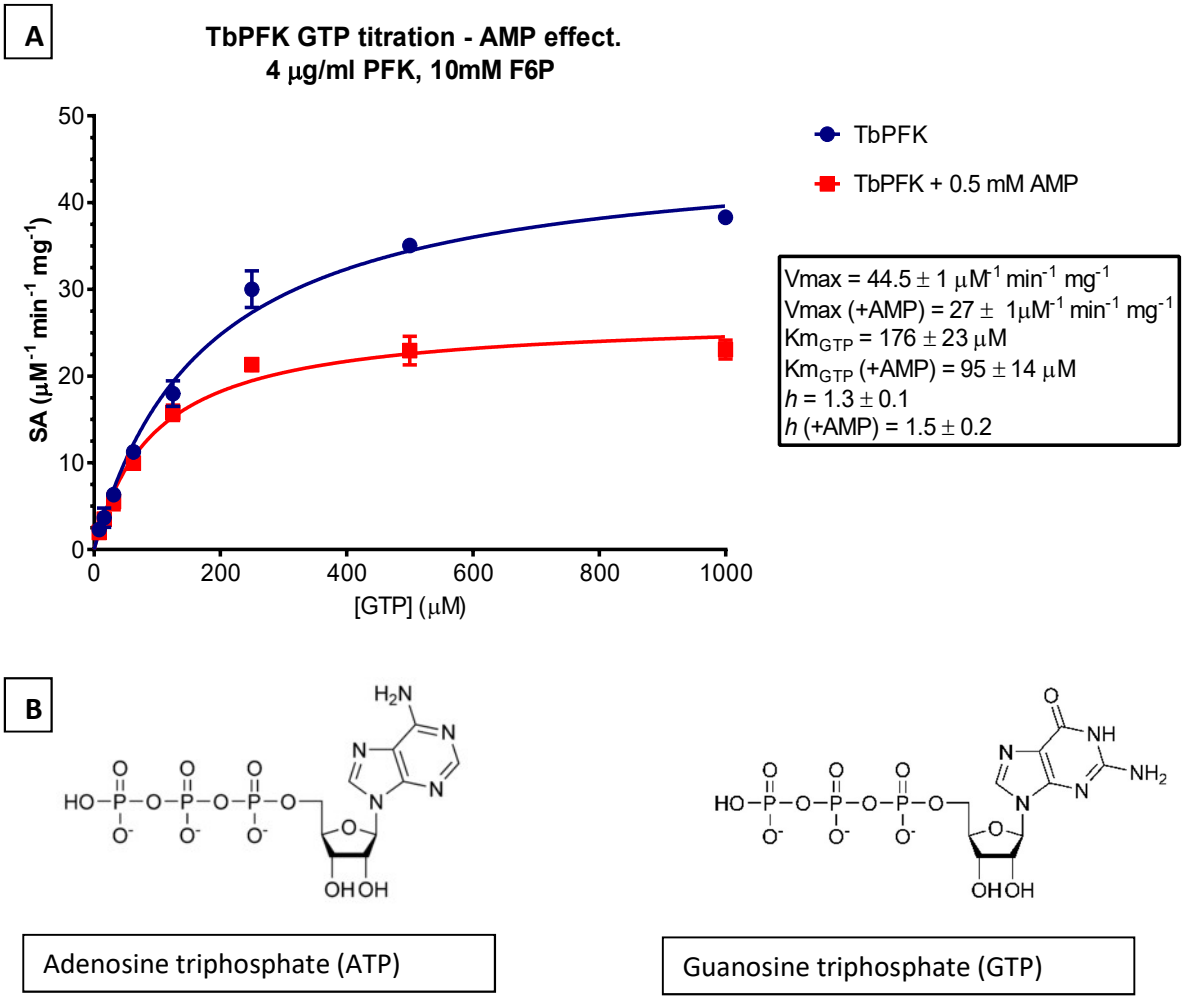

Figure 4.6: AMP increases GTP affinity in T. brucei PFK.

***A**) GTP titration against T. brucei PFK with and without 0.5 mM AMP. All experiments carried out at 25°C in triplicate, error bars denote standard deviation. TbPFK tested at 4 µg/ml final concentration. **B**) Structures of ATP and GTP.*

ATP and GTP differ only by an amino group on the C_6 position of ATP being replaced by a carbonyl group in GTP (**figure 4.6B**). Clearly this does not perturb important interactions with the molecule completely, but moderately reduces affinities for GTP when compared to ATP; Kinetic parameters for ATP and GTP binding for the trypanosomatid PFKs are compared in **table 4.2**.

	Vmax ($\mu mol^{-1}.min^{-1}.mg^{-1}$)	**$K_m^{nucleotide}$ (μM)**	**k_{cat} (s^{-1})**	**k_{cat}/k_m ($s^{-1}.\mu M^{-1}$)**	**Hill coefficient (*h*)**
T. brucei (ATP)	44.5 ± 1.4	50.4 ± 1.8	41 ± 1	0.81	1.3 ± 0.1
T. brucei (GTP)	38.8 ± 0.8	176 ± 23	36 ± 1	0.20	1.4 ± 0.1
T. cruzi (ATP)	68.4 ± 1.0	94.6 ± 4.9	64 ± 1	0.68	1.2 ± 0.1
T. cruzi (GTP)	62.9 ± 1.8	194.8 ± 14.2	59 ± 2	0.30	1.4 ± 0.1
L. infantum (ATP)	7.9 ± 0.1	93.2 ± 5.7	8 ± 1	0.09	1.3 ± 0.1
L. infantum (GTP)	9.9 ± 0.8	331 ± 47.5	10 ± 1	0.03	1.3 ± 0.1

Table 4.2: GTP can be used by trypanosomatid PFKs, but is bound with a lesser affinity than ATP.

All experiments carried out at 25°C in triplicate, standard deviation is given. All PFKs tested at a final concentration of 4 µg/ml.

As seen by the k_{cat}/k_m values, each trypanosomatid enzyme has greater efficiency (higher k_{cat}/k_m) when using ATP over GTP, showing that it is the preferred phospho donor. Despite the increased affinity for ATP, Michaels constants (k_m) for ATP and GTP are comparable. This suggests that the binding of the nucleotide by the trypanosomatid PFKs is focused mainly on the triphosphate group.

4.4. Substrate affinity measurements using SPR.

SPR assays measure the change in the angle of a wave of excited electrons known as a surface plasmon resonance (SPR) as polarised light is focused and refracted off a gold surface onto which a population of protein has been immobilised. The SPR wave is sensitive to the amount of material on the gold surface – the refractive index. The binding of an analyte to this protein surface causes a change in the refractive index due to the build-up of material, and this changes the angle of the plasmon resonance. This change in angle is recorded in real time as resonance units (RU) on a 'sensorgram' (Wear, Blackburn, & Nowicki, 2009). **Figure 4.7** shows an example sensorgram. As binding response is measured in real time, steady state kinetics, on and off rates can be determined. Association (k_{on}) and dissociation (k_{off}) rate constants can be measured from these sensorgram traces in real time, as well as steady state equilibrium constants (K_d). Please see **section 2.5.3** for a detailed explanation of SPR, and the experimental procedures for the results shown in this section. All SPR experiments were carried out on a GE Healthcare Biacore™ T200 instrument.

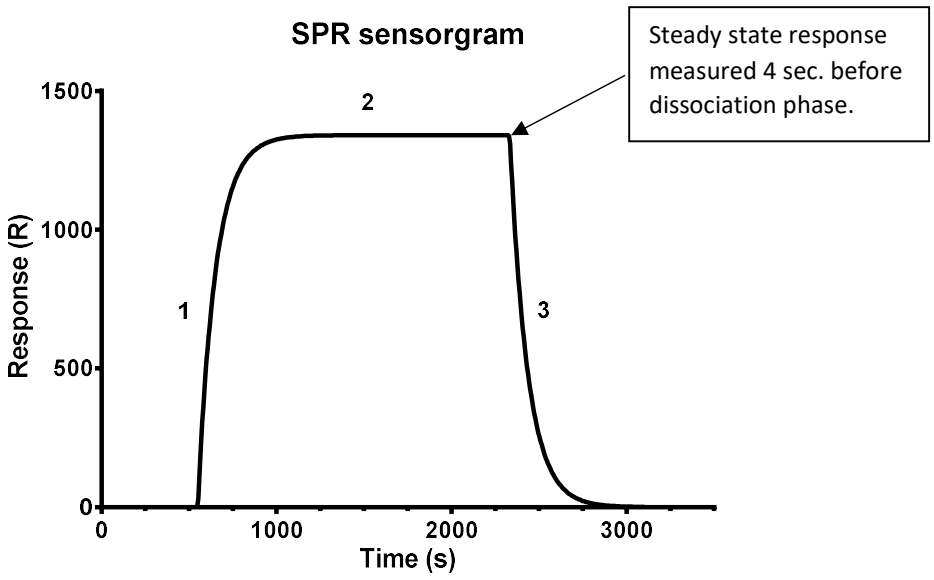

Figure 4.7: example SPR sensorgram.

1) ***Association phase:*** *analyte is washed over the immobilised ligand surface. Rate of association for the ligand-analyte complex is measured (k_{on}) as mass binds to the surface.*
2) ***Steady state phase:*** *analyte is still washed over surface but the formation of [Ligand][Analyte] complex is now at equilibrium; rates of complex formation and complex dissociation are balanced and Equilibrium dissociation constants can be calculated (K_d).*

3) ***Dissociation phase:*** *buffer without analyte is washed over surface. Analyte is removed from the system and the association phase of the reaction is essentially eliminated. Dissociation rate constants (k_{off}) can now be measured.*

4.4.1 SPR surface preparation for testing trypanosomatid PFK substrate binding

A detailed protocol for surface preparation is given in **section 2.5.3.1**. 20 nM stocks of N-terminally His_6-tagged *T. brucei, T. cruzi* and *L. infantum* PFKs were used to create low density surfaces of ~3000 RU using a modified amine capture method (Wear & Walkinshaw, 2006 and Wear et al., 2017). A Ni^{2+}-nitrilotriacetic acid (NTA) chip consisting of 4 flow cells was used – flow cell 1 ('Fc1') which contained no bound ligand and acted as a reference, 'Fc2' had a His_6-*Tc*PFK surface, 'Fc3' His_6-*Tb*PFK and 'Fc4' His_6-*Li*PFK. Surface activity was tested using a 1 mM ATP control. The maximum response (RUmax) of a ligand surface in SPR can be defined as:

$$RUmax = \frac{MW\ analyte}{MW\ ligand} * RU\ of\ immobilised\ ligand * n$$

Where n = stoichiometry of interaction.

Assuming the interaction to have a stoichiometry of 1 and using the 1mM ATP control, the *T. brucei* and *T. cruzi* PFK surfaces both had similar maximum responses (RU_{max}) of ~28 RU. Ligand interactions giving a response above the RU_{max} of the surface suggest multivalent binding. The *L. infantum* surface had a lower RU_{max} of ~8 RU. The use of the Ni^{2+} NTA chip allowed orientation of the PFK enzymes away from the sensor surface, via the N-terminal His_6 tags (Wear et al., 2017).

4.4.2 Substrates and other analytes tested against trypanosomatid PFKs in SPR.

A range of substrates, known and unknown PFK effectors and other metabolites were tested for binding responses against all three trypanosomatid PFK surfaces. 2.5-fold serial dilutions of analytes were made up in running buffer (10mM HEPES, 150 mM NaCl, 10 mM $MgCl_2$, 0.05 % P20, pH 7.4). All analytes to be tested were made up in this buffer and stocks were buffered to pH 7.4 before use. Each concentration of analyte was run over each of the flow cells in parallel at a constant rate of 30 µl.min^{-1}. Analytes had 30 seconds contact time with the surface before being washed off with running buffer for 30 seconds. Steady state affinities (K_d) were calculated by plotting the equilibrium response value (RU) at the equilibrium phase of each sensorgram trace against concentration of analyte. This is measured as the average response over a 4 second period prior to the end of the injection phase (see **figure 4.7**). To measure the association and

dissociation rates of each analyte a ‘1:1 binding’ model was fitted to each sensorgram trace using the dedicated Biacore T200 evaluation software. Analyte binding responses are summarised in **table 4.3**. The summary data in **table 4.3** holds for all three trypanosomatid PFKs tested.

Substrates/ effectors							
Analyte	ATP	ATP +AMP	AMP	AMP +ATP	F6P	F6P + AMP	F6P + ATP
Binding response?	✓	✓	✓	✓	×	×	✓
Specific binding*?	✓	✓	✓	×	×	×	×
Products							
	ADP	ADP +ATP	ADP +AMP	F16BP	F16BP + AMP	F16BP + ATP	
Binding response?	✓	✓	✓	✓	✓	×	
Specific binding?	✓	✓	✓	✓	✓	×	
Metabolites / other							
	GTP	GDP	Citrate	Citrate + ATP	PPi	PEP	F26BP
Binding response?	✓	✓	×	✓	×	×	×
Specific binding?	✓	✓	×	×	×	×	×

Table 4.3: SPR binding responses of analytes tested against T. brucei, T. cruzi and L. infantum PFKs.

Analytes are designated according to whether they firstly showed a binding response on the protein surface then if that response could be read and plotted as being specific binding to the PFK enzyme. Analyte concentration ranges tested were : AMP‡, ADP, ATP‡, GTP, GDP, F6P, F16BP, F26BP – 10 mM – 7.8 µM. Citrate, PPi, Phosphoenolpyruvate (PEP) – 20 mM – 156 µM. ‡1 mM when tested alongside another analyte.*

** 'Specific binding' was considered to be a response approaching saturation close to the theoretical maximum response (RU_{max}) of the PFK surface (RUmax TbPFK and TcPFK = ~28 RU, LiPFK = 8 RU).*

4.4.3 Trypanosomatid PFKs bind ATP with strong affinity.

MgATP bound specifically to all three trypanosomatid PFK surfaces, and with comparable affinities for the three enzymes. **Figure 4.8** shows the sensorgram and steady state kinetic plots for ATP titrations against the three PFKs. **Table 4.4** below shows the calculated kinetic parameters from steady state measurements and from the 1:1 fit kinetic model applied to the sensorgrams shown in **figure 4.8**.

ATP								
	Steady state				Kinetic			
	SS K_d (µM)	**SS R_{max} (RU)**	**Chi^2**		**k_{on} (1/Ms)**	**k_{off} (1/s)**	**K_d (µM)**	**Chi^2**
T. brucei	15.8 ± 2.3	25.4 ± 0.9	0.37		25300 ± 1100	3.08 ± 0.03	120 ± 27	0.87
T. cruzi	35.4 ± 5.6	23.5 ± 0.9	0.27		6970 ± 270	0.56 ± 0.01	80.3 ± 37	0.55
L. infantum	16.8 ± 2.1	7.1 ± 0.2	0.04		823 ± 15	1.01 ± 0.01	1227 ± 667	2.19

Table 4.4: ATP binds with high affinity and with comparable levels between PFKs in SPR.

All values calculated from plots shown in figure 4.7. Chi^2 values are for goodness of fit of curve (in steady state plots) and fit of 1:1 model (in sensorgrams). Chi^2 < 2.0 is considered a good fit. Standard errors are given for each parameter.

Measured steady state affinities for ATP were strong for all three trypanosomatid PFKs, and values were within the same order of magnitude to the K_m^{ATP} measurements for all three PFKs (**table 4.1, section 4.2.1**). Affinities measured from the kinetic plots ($K_d = k_{on}/k_{off}$) were mostly in agreement with steady state measurements for *T. brucei* and *T. cruzi* PFK, but not for *L. infantum* PFK; large injection spikes were removed from the start and end of *Li*PFKs sensorgram traces (data not shown). These spikes masked the true association phase response for *Li*PFK and meant the 1:1 binding model fitted poorly. As can be seen in **figure 4.8,** the k_{on} rates fitted by the 1:1 model are inaccurate and much too fast – resulting in a high K_d value for ATP against *Li*PFK. These injection spikes may have resulted from slight buffer mismatch between the running buffer and ATP titrations. The same batch of buffer was used as running buffer and to make up the ATP dilutions. ATP stocks were also buffered to pH 7.4 in the same running buffer before use.

Dissociation rate (k_{off}) values gained from the 1:1 binding fit on the sensorgrams however are more reliable when looking at the fit of the 1:1 binding model with the recorded sensorgram traces and give a good indication of the time of dissociation for ATP for each of the surfaces – ranging from 0.31 s^{-1} for *T. brucei* PFK to 1.78 s^{-1} for *T. cruzi* PFK. The measured affinities for ATP calculated by steady state measurements are marginally lower, but comparable with those values found using the PYK/LDH enzyme linked assay (section **4.2.1**, **table 4.1**). Considering the homology in ATP binding residues between the three enzymes, the steady state measurements are more feasible – it is expected that each enzymes affinity for ATP would be in the same order of magnitude.

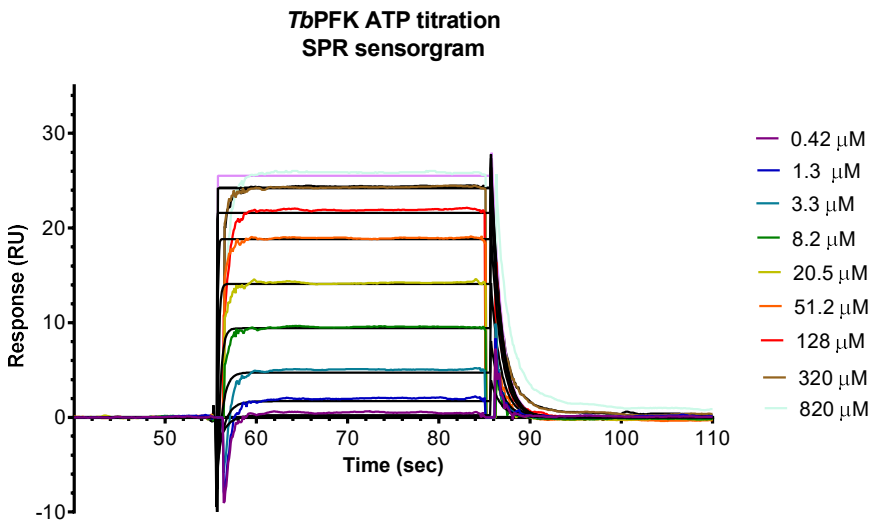

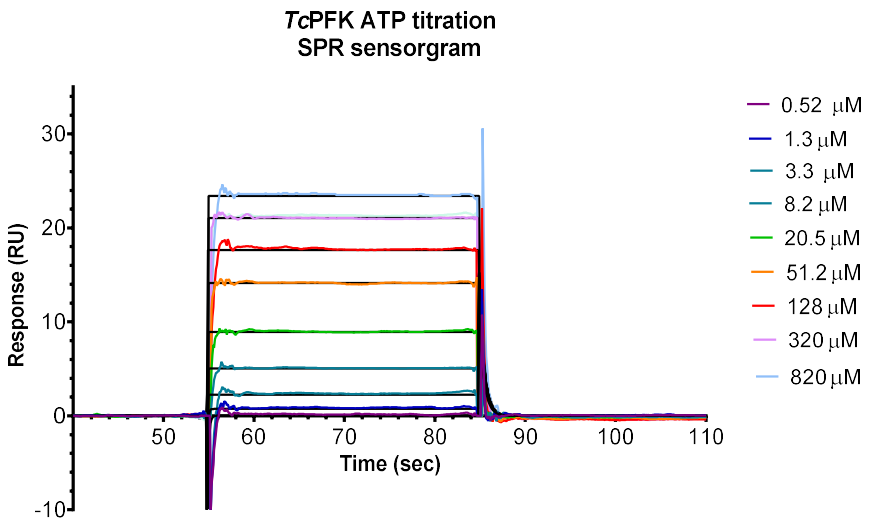

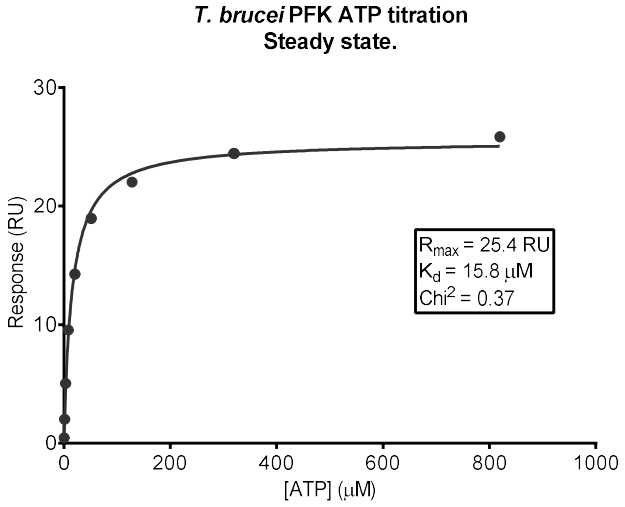

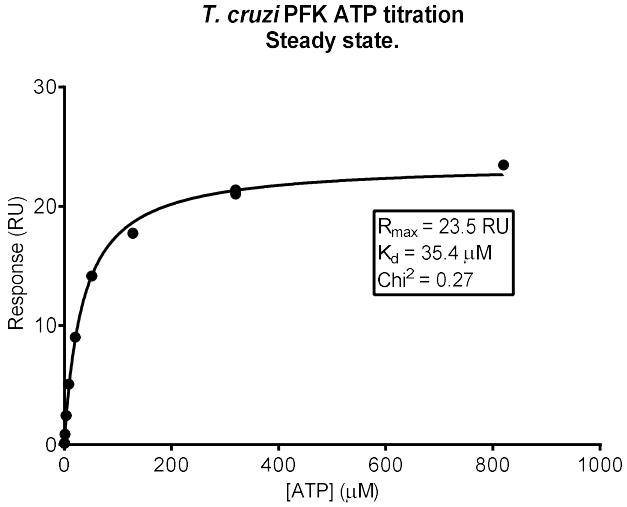

Figure 4.8: SPR sensorgrams show tight, specific binding of ATP against trypanosomatid PFKs.

Continued overleaf.

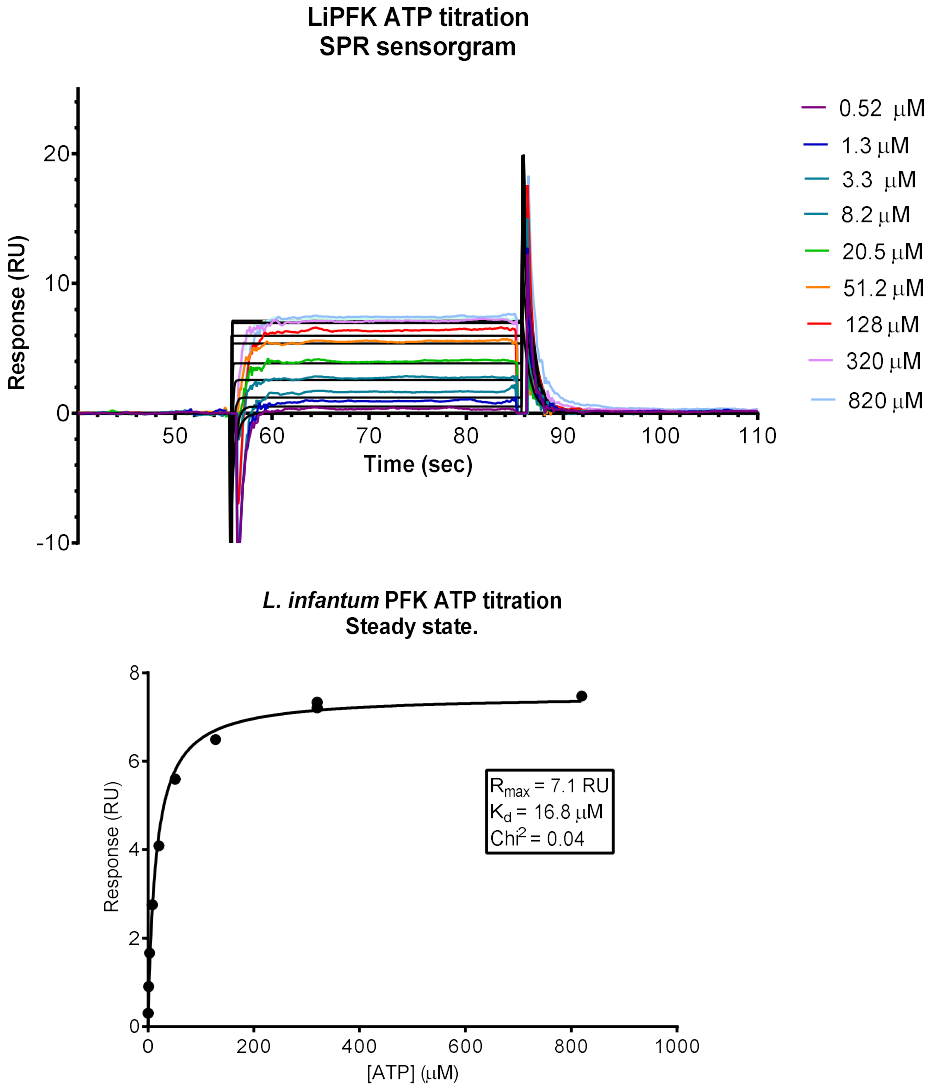

Figure 4.8: SPR sensorgrams show tight, specific binding of ATP against trypanosomatid PFKs.

Continued from previous page.

4.4.4 F6P cannot bind to PFK in isolation in SPR.

No binding response was observed against any of the trypanosomatid PFK surfaces with regards to F6P, up to a top concentration of 10 mM (data not shown). From crystal structures of *T.* brucei PFK it is known that ATP binding induces a conformation change to open up the active site and accommodate F6P more readily. To test for F6P binding in the presence of MgATP, ATP was added to the running buffer (10mM HEPES, 150 mM NaCl, 10 mM $MgCl_2$, 0.05 % P20, pH 7.4) at a concentration of 1mM. F6P series dilutions were made in the same 1mM ATP running buffer and tested against all three PFK surfaces. Under these conditions a F6P binding response was observed for all 3 enzymes, however it did not reach saturation at the highest concentrations (up to 10 mM) (**figure 4.9**).

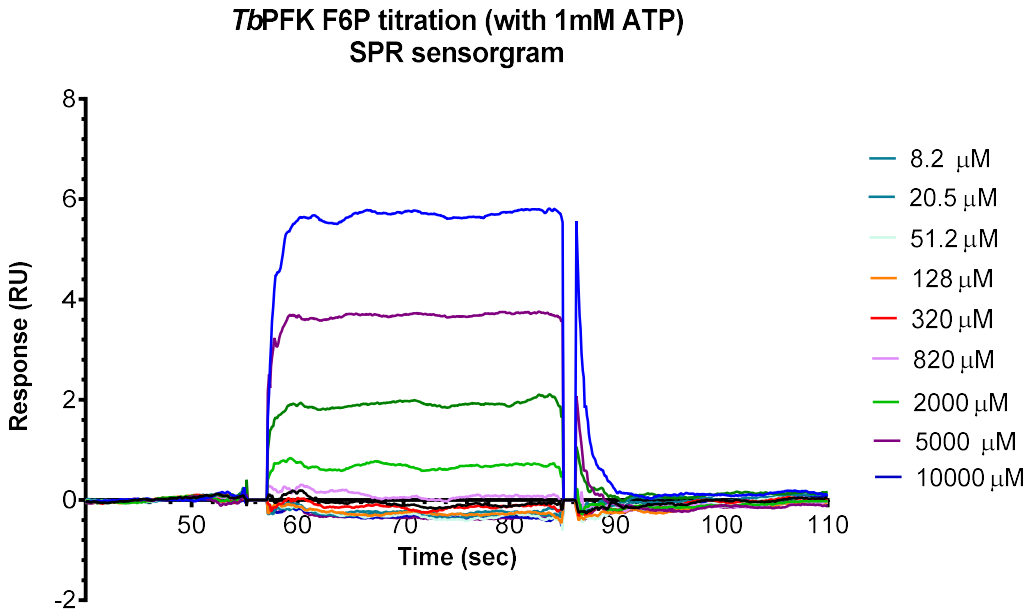

Figure 4.9: In F6P shows weak binding in the presence of ATP, but does not reach saturation.

F6P titration against TbPFK surface (3,000 RU) using SPR at 25°C. RU_{max} of TbPFK surface with ATP control = 26 RU. RU_{max} F6P = 19.5 RU.

As can be seen in **figure 4.9**, at concentrations of F6P approaching 10mM, the response does not appear to reach saturation, and the R_{max} (5.8 RU) remains ~4X lower than the maximum binding response for the *T. brucei* surface (~19.5 RU). F6P is therefore binding very weakly or promiscuously to the protein even in the presence of ATP. It is also possible that the enzyme is turning over F6P in the presence of ATP. Tethering of PFK to a surface may also be interfering with the dynamic changes that are required for F6P to be accommodated in the active site. The presence of ATP however must have induced a change in the enzyme to allow at least weak binding of F6P, compared to when F6P is titrated against the trypanosomatid PFKs alone – where

no response was observed. This SPR data adds evidence to the hypothesis that ATP must be bound first in the reaction scheme to accommodate F6P.

4.5. Molecular regulation of trypanosomatid PFKs.

Table 4.5 shows the range of known effectors of bacterial, trypanosomatid, mammalian and other eukaryotic PFKs. The aim of this section of work was to measure and describe the kinetics of known effectors of trypanosomatid and mammalian PFKs, to further understand the reaction mechanism and regulation of the trypanosomatid PFK enzymes *in vitro.*

	Bacteria	**Yeasts**	**Trypanosomatids**	**Mammals**	**Protists**	**Plants**
Organism	*E.coli*	*S. cerevisiae*	*T. brucei*	*H. sapiens*	*B. burgdorferi*	*S. tuberosum* (potato)
PFK family	ATP-dependant	ATP-dependant	ATP-dependant	ATP-dependant	PPi-dependant	PPi-dependant
Allosteric activators	ADP	AMP ADP F26BP NH_4^+ Pi	AMP	AMP ADP F26BP	Non-allosteric	F26BP
Allosteric inhibitors	PEP	ATP Citrate F16BP	CTCB compounds	ATP PEP Citrate F16BP	Non-allosteric	-

Table 4.5 : Known effectors of bacterial and eukaryotic PFKs.

Known effectors of various bacterial and eukaryotic PFK enzymes. Information summarised from (McNae & Martinez-Oyanedel, 2009).

4.5.1 AMP is the only known effector of trypanosomatid PFK.

The putative AMP binding site in the *T. brucei* PFK structure is located in a pocket under the base of the C-terminal reaching arms, as seen in **figure 4.10** below.

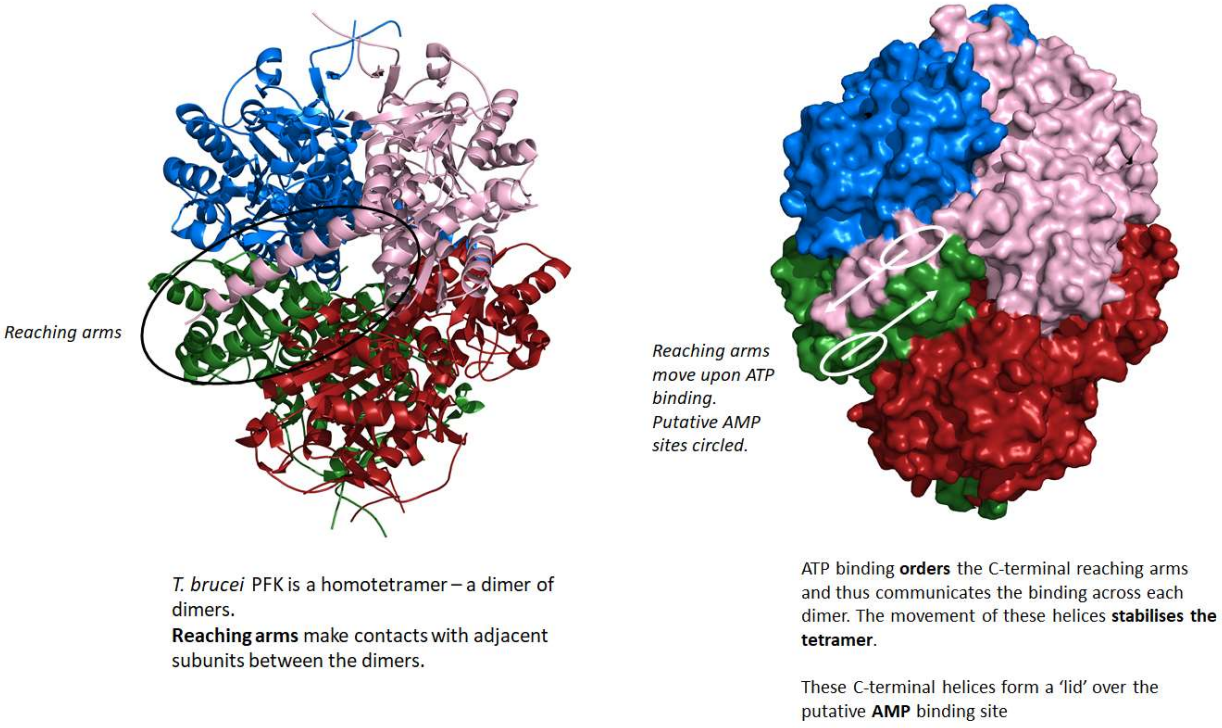

Figure 4.10: The putative Amp binding site in T. brucei PFK is located under the C-terminal 'reaching arms'.

Figure made using ATP-bound TbPFK structure (PDB code 3F5M) (McNae & Martinez-Oyanedel, 2009).

AMP is a known allosteric effector of trypanosomatid PFK: from the ATP-bound structure solved by McNae et al (**figure 4.10**), it has been shown that upon ATP binding, order is brought to the C-terminal reaching arms, and a pocket with a lid forms the putative AMP binding site (McNae & Martinez-Oyanedel, 2009). An unpublished structure of *T. brucei* PFK with AMP bound (Montserrat Valdiviesso, UoE) shows the C-terminal reaching arms forming a lid over the AMP binding site with AMP bound. It is suggested that these C-terminal reaching arms communicate AMP binding across the PFK tetramer, as they form intra-dimer links between adjacent subunits. The activating effect of AMP on *T. brucei* PFK has been reported previously (Nwagwu & Opperdoes, 1982).

4.5.2 AMP stimulates trypanosomatid PFK activity.

The effect of AMP on the substrate kinetics for the three trypanosomatid PFKs was tested using the PYK/LDH linked enzyme assay (see **section 2.3.1.4** for full details). AMP was incubated with each PFK enzyme in the presence of either a set concentration or series dilution of ATP for 10 minutes at room temperature. The reaction was started by adding either a series dilution or set concentration of F6P. AMP was used at a final concentration of 0.5 mM. This AMP concentration had no significant effect on the activity of the downstream enzymes (PYK and LDH) in the assay (data not shown). **Figure 4.11** shows the effect of AMP on F6P and ATP titrations against *T. brucei* PFK.

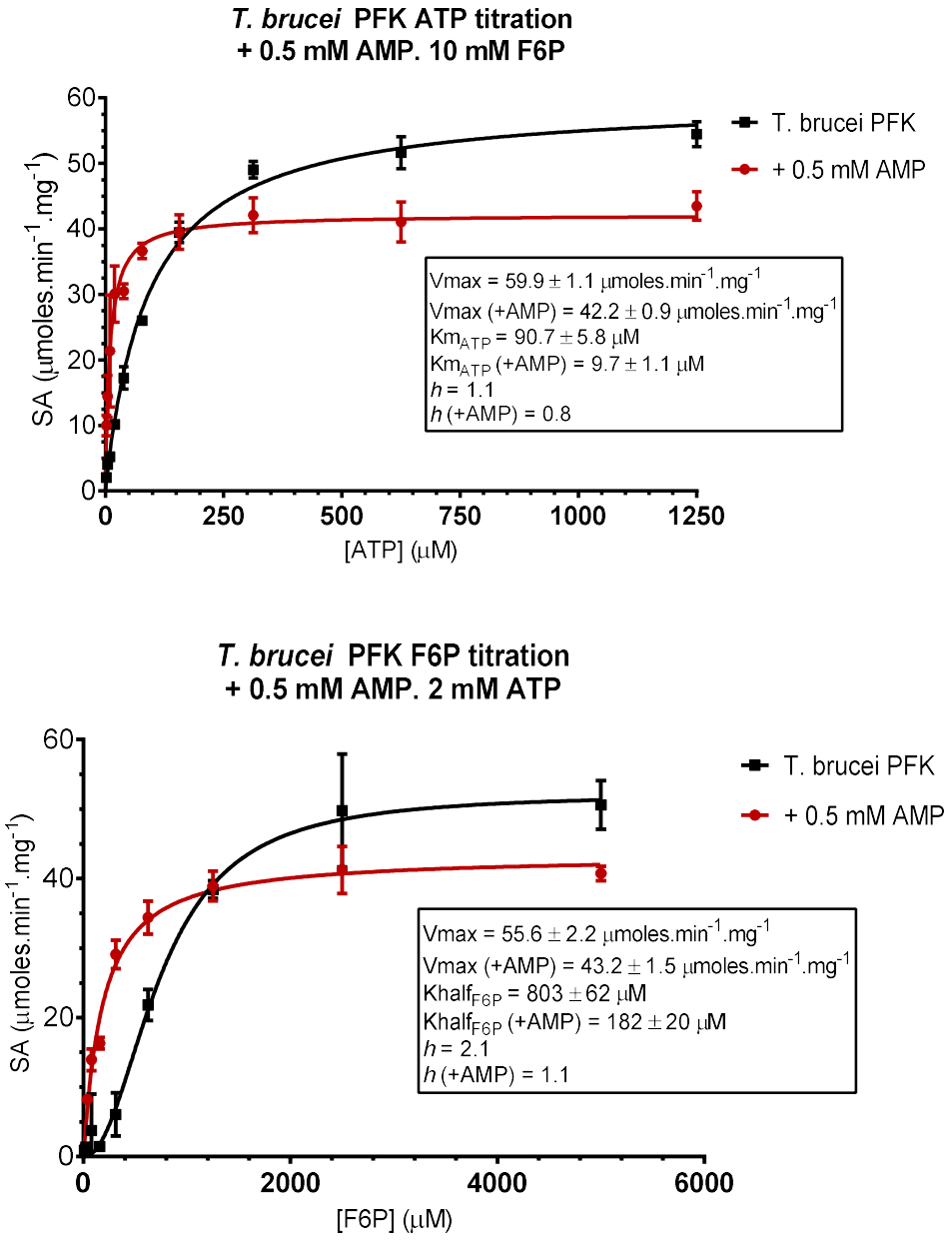

Figure 4.11: AMP strongly increases affinity for both ATP and F6P in T. brucei PFK.

Experiments carried out at 25°C in triplicate, error bars denote standard deviation. Measured using PYK/LDH linked assay. ATP titrations have Michaelis-Menten curve fit, F6P plots have allosteric sigmoidal curve fitted using GraphPad Prism ver. 6. All PFKs tested at 4 µg/ml final concentration. ATP titration = 5 mM – 2.5 µM, top 2 concentrations omitted for clarity. F6P titration = 10 mM – 9.8 µM, top 2 concentrations omitted for clarity.

Kinetic parameters in the presence and absence of AMP for each of the trypanosomatid enzymes are given in **table 4.6**.

AMP significantly increases the affinity of the trypanosomatid PFKs for both ATP and F6P. AMP also removes the observed cooperativity in F6P binding – reducing the Hill coefficient from *h* = 2.1 to *h* = 1.1 for *T. brucei* PFK. This observed effect on cooperativity must result from one of two possibilities;

a) AMP induces a change in the enzyme structure such that previous cooperativity in F6P binding is now not possible. For example from a re-ordering of the C-terminal reaching arms that may communicate change between adjacent subunits.
b) Co-operative binding in the presence of AMP is beyond the resolution of the PYK/LDH assay. As the K_{half} for F6P becomes significantly lower in the presence of AMP, the dose-response curve becomes tighter. As cooperativity is most visible at the lower concentrations of substrate, the plots generated from the data may not have the resolution show any co-operative behaviour.

A structure with *both* ATP and AMP bound may help answer this question. No significant structural changes to the C-terminal helices are observed in the unpublished AMP-*Tb*PFK structure by M. Valdiviesso, UoE.

0.5 mM AMP also results in a lowering of the Vmax by ~20 % with both ATP and F6P titrations. Despite this, the efficiency of the enzyme is increased in the presence of AMP due to increased affinity for substrate; In *T. brucei* for example the Kcat/Km increases from 0.07 to 0.21 $\mu M^{-1}.s^{-1}$ for F6P in the presence of 0.5 mM AMP. (**Table 4.6**).

	K_{half}^{F6P} (μM)	Hill coefficient (h) (F6P)	K_m^{ATP} (μM)	Hill coefficient (h) (ATP)	K_{cat}/K_m ($s^{-1}.\mu M^{-1}$) (F6P)	K_{cat}/K_m ($s^{-1}.\mu M^{-1}$) (ATP)
***Tb*PFK**	803 ± 48	2.1 ± 0.2	90.7 ± 6	1.2 ± 0.2	0.07	0.60
+ AMP	*182 ± 20*	*1.1 ± 0.1*	*9.7 ± 1*	*0.8 ± 0.1*	*0.21*	*3.90*
***Tc*PFK**	469 ± 26	1.9 ± 0.2	79 ± 6	1.1 ± 0.1	0.11	0.67
+ AMP	*58 ± 14*	*0.9 ± 0.1*	*12 ± 2*	*0.9 ± 0.2*	*0.68*	*3.30*
***Li*PFK**	2391 ± 99	2.2 ± 0.1	99 ± 2	1.1 ± 0.3	0.01	0.24
+ AMP	*134 ± 48*	*0.9 ± 0.1*	*74 ± 3*	*0.7 ± 0.2*	*0.15*	*0.28*

Table 4.6: AMP improves the catalytic efficiency of the three trypanosomatid PFKs.

Data measured using PYK/LDH linked enzyme assay. All experiments carried out in triplicate, standard deviation of each kinetic parameter is given.

For each of the *T. brucei*, *T. cruzi* and *L. infantum* enzymes, AMP increases the affinity for substrates (↓K_m^{ATP} or K_{half}^{F6P}) while also decreasing the maximum velocity of the enzyme (↓Vmax). For all three enzymes this results in an increase in catalytic efficiency (↑ K_{cat}/K_m) and we can say that AMP is an activator of the PFK enzyme. This is divergent from the traditional description of allosteric activation where the affinity for substrates is increased, without an effect on the Vmax of the enzyme.

It may be possible that AMP induces an enzyme state where the overall velocity of substrate turnover is lower, but increased interactions allow for much greater affinity for substrate binding, allowing rapid binding of relatively low concentrations of substrate. A further possibility is that AMP is competing with ATP in the active site, and this is resulting in a slower overall velocity of the enzyme. Indeed, previous studies on *T. brucei* PFK have shown that 0.25 – 0.75 mM AMP demonstrates uncompetitive inhibition with ATP (Claustre et al., 2002)

L. infantum had the greatest response to AMP activation – with a 15-fold increase in the catalytic efficiency for F6P in the presence of AMP. Interestingly, this activating effect from AMP places the affinity of *L. infantum* PFK for F6P on par with the other trypanosomatid PFKs (**table 4.6**).

4.5.3 Reaction order dictates if AMPs activating effect on TbPFK is observed.

As described in section **4.2.4**, the order that components are added has an effect on the observed kinetics for PFK when tested in the PYK/LDH assay. Combinations of reaction incubations were carried out again, to test the effect this had on AMP eliciting its activating effect on the enzyme;

- PFK/AMP + ATP + F6P : PFK incubated with AMP for 15 minutes. ATP added. Reaction started with F6P.
- PFK/ATP + AMP + F6P : PFK incubated with ATP for 15 minutes. AMP added. Reaction started with F6P.
- PFK/F6P + AMP + ATP: PFK incubated with F6P for 15 minutes. AMP added. Reaction started with ATP.

Figure 4.12 shows the effect of differing reaction orders on AMP-induced activation of *Tb*PFK with respect to F6P.

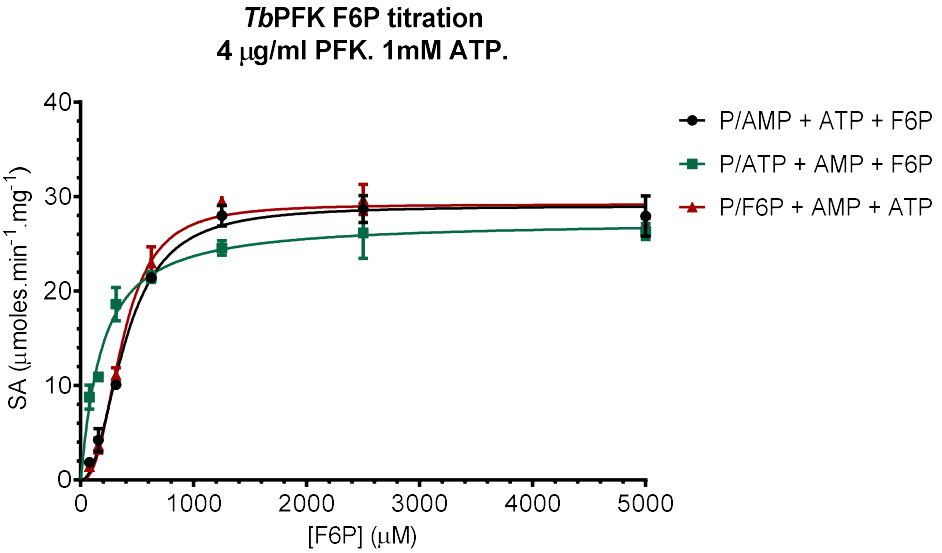

	K_{half}^{F6P} (μM)	V_{max} (mmoles^{-1}.min^{-1}.mg^{-1})	Hill coefficient (*h*)
P/AMP + ATP + F6P	394 ± 19	29.1 ± 0.5	2.2 ± 0.2
P/ATP + AMP + F6P	178 ± 17	27.1 ± 0.7	1.1 ± 0.1
P/F6P + AMP + ATP	369 ± 19	29.2 ± 0.6	2.5 ± 0.3

Figure 4.12: TbPFK activation by AMP is only observed when pre-incubated with ATP.

F6P titration (5 mM – 78 μM) against His_6-TbPFK in LDH/PYK assay. P = PFK protein. '/' represents incubation at room temperature for 15 minutes. AMP was used at a final concentration of 0.5 mM. All experiments carried out at 25 °C in triplicate, error bars denote standard deviation. 'P' = PFK.

The effects of AMP on stimulating activity was seen only when PFK was pre-incubated with ATP, suggesting again that ATP must be bound first for AMP to bind or elicit its effect on the enzyme. Again, we see that when AMP does elicit an effect on the PFK enzyme, it removes any observed co-operativity in F6P turnover.

4.5.4 AMP binds with varying affinity to Trypanosomatid PFKs

Titrations of AMP were carried out against all three trypanosomatid PFK surfaces in SPR assays, and against *Tb*PFK and *Tc*PFK in thermal denaturation assays (TDA). The steady state affinity plots from SPR measurements (ss K_d) for AMP titrations against the three trypanosomatid enzymes are shown in **figure 4.13**.

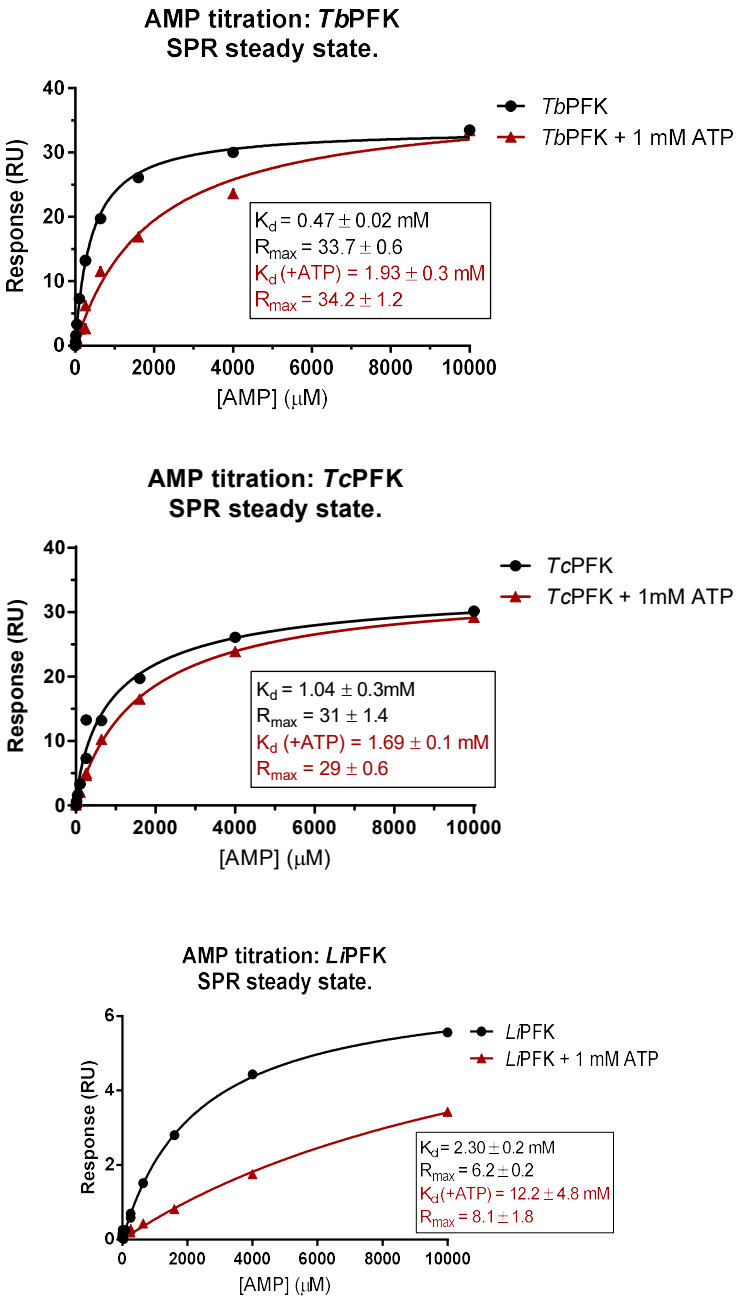

Figure 4.13: AMP affinity measurements against TbPFK, TcPFK and LiPFK at steady state – SPR.

Density of TbPFK, TcPFK and LiPFK surfaces: 3,200, 3,100 and 1,400 RU respectively.

*AMP titration = 10 mM – 0.4 µM. All experiments carried out at 25 °C in running buffer (*10mM HEPES, 150 mM NaCl, 10 mM $MgCl_2$, 0.05 % P_{20}, pH 7.4). Tested against low density (~1,400 – 3,200 RU) surfaces. R_{max} *Tb*PFK and *Tc*PFK = ~28 RU, *Li*PFK = 8 RU.

AMP bound to *T. brucei* PFK with a relatively tight affinity (K_d^{AMP} = 470 µM) measured by steady state kinetics in SPR. *T. cruzi* and *L. infantum* PFK however had weaker measured steady state affinities of > 1 mM (**figure 4.13**). In the presence of ATP, affinities for AMP were weaker for *Tb*PFK and *Li*PFK with ss K_d^{AMP} values of 1.9 and 12 mM respectively in the presence of 1 mM ATP. Interestingly, *Tc*PFK was only moderately effected by ATP, its SS K_d^{AMP} increasing from 1 to 1.7 mM in the presence of ATP.

AMP titrations were also carried out against *Tb*PFK and *Tc*PFK using TDA. AMP was titrated against PFK samples with and without a saturating (0.75 mM) concentration of ATP – protocol can be seen in section **2.5.2.3**. Melting curves for an AMP titration against *Tc*PFK with and without ATP are shown in figure **4.14**. To determine the K_d^{AMP}, thermal melt temperatures were plotted against concentration of AMP and a curve was fitted using the Langmuir isotherm equation (below) for nonlinear regression in Graphpad Prism 6.0, shown in figure **4.15.**

$$Tm = \frac{Tm(AMPmax) * [AMP]}{(Kd + [AMP])} + c$$

Where c = T_m of PFK sample alone.

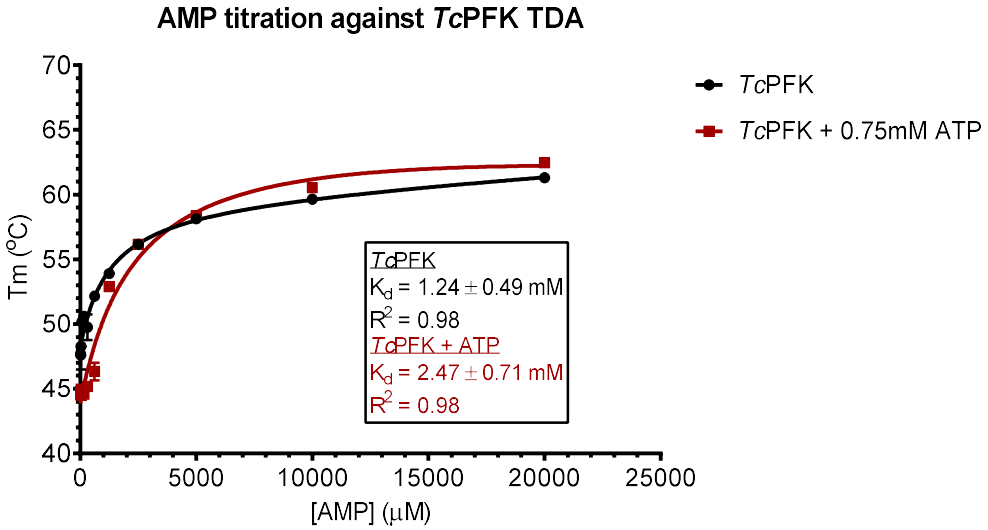

Figure 4.15: AMP titration against T. cruzi PFK carried out using TDA.

TcPFK conc = 2 µM. Temperature range 25 -79 °C. Experiments carried out in triplicate, error bars denote standard deviation. Sypro orange fluorescent dye was used.

Table 4.9 summarises the calculated K_d values for AMP binding with *T. brucei* and *T. cruzi* PFKs in the presence and absence of ATP, as measured in SPR and TDA. *L. infantum* PFK was not tested in TDA.

	***Tb*PFK**	***Tb*PFK + ATP***	***Tc*PFK**	***Tc*PFK + ATP***	***Li*PFK**	***Li*PFK + ATP***
SPR K_d^{AMP} (mM)	0.470 ± 0.02	1.9 ± 0.31	1.04 ± 0.3	1.69 ± 0.10	2.30 ± 0.2	12.2 ± 4.8
TDA K_d^{AMP} (mM)	0.897 ± 0.11	1.59 ± 0.27	1.24 ± 0.49	2.47 ± 0.71	ND	ND

Table 4.9: AMP affinity for T. brucei and T. cruzi PFKs.

** 1 mM ATP in SPR, 0.5 mM AMP in TDA.*

Equilibrium constants for AMP (K_d^{AMP}) are comparable when measured using SPR or TDA. In all cases the presence of ATP lowers the affinity of each trypanosomatid PFK enzyme for AMP.

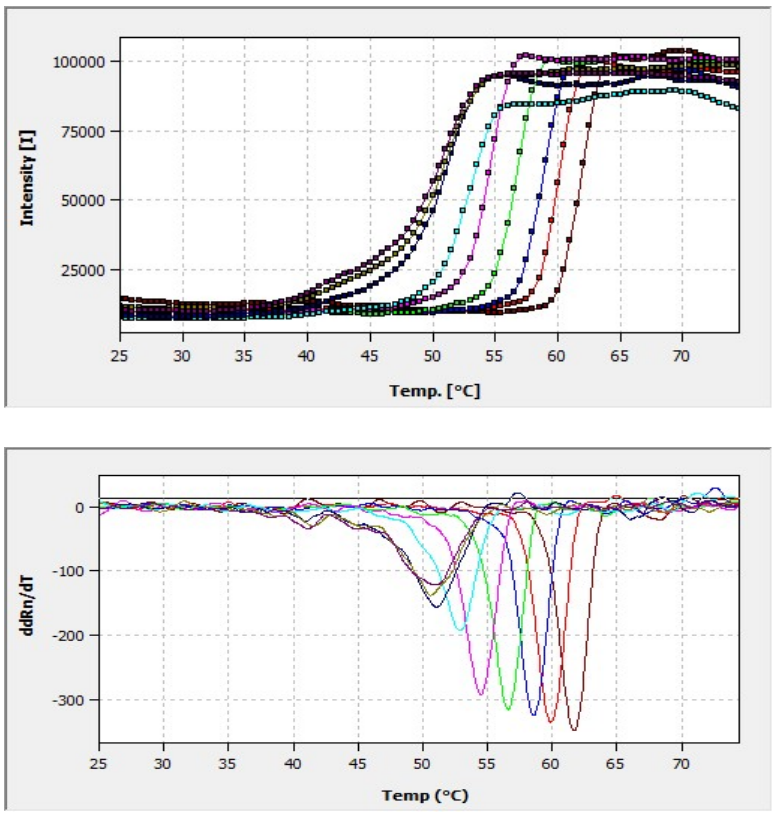

T. cruzi PFK

+ 0 – 20mM AMP

(left to right)

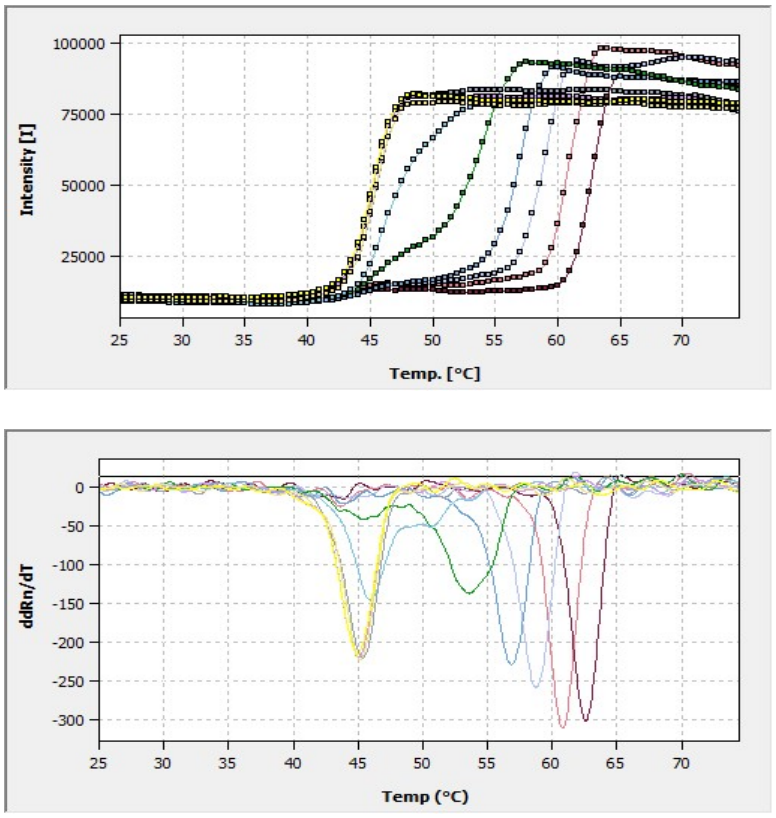

T. cruzi PFK + 0.5mM ATP

+ 0 – 20mM AMP

(left to right)

Figure 4.14: AMP titrated against TcPFK in TDA – thermal melt peaks.

AMP concentration from left to right: 0 , 0.078, 0.156, 0.312, 0.625, 1.25, 2.5, 5, 10 and 20 mM.

4.5.5 AMP did not show activation of trypanosomatid PFKs in SPR experiments.

To test the effect of AMP on analyte binding to immobilised PFK surfaces in SPR, AMP was added to the SPR running buffer (10mM HEPES, 150 mM NaCl, 10 mM $MgCl_2$, 0.05 % P_{20}, 1 mM AMP pH 7.4). Titrations of analytes were made and conducted in the same 1 mM AMP running buffer. AMP did not significantly affect the binding affinity of either ATP or F6P with any of the trypanosomatid PFK surfaces in SPR. Any increase or decrease in K_d was within the margin of error for the experimental values (average standard error in K_d = ± 0.1 mM) (data not shown). Tethering of the enzyme to the SPR chip surface may have hindered either the binding of AMP or a conformational change responsible for carrying out the increase in affinity for ATP or F6P in the presence of AMP.

According to the SPR and TDA data shown in **table 4.9**, there is an interesting range in the binding affinities for AMP between the three enzymes (K_d^{AMP} = 0.47 – 2.3 mM). The *effect* of AMP on enzyme activity when measured in the PYK/LDH assay (*section **4.5.2***) was similar between *T. brucei* and *T. cruzi* at the same concentration of AMP (0.5 mM). This SPR data however suggests that a greater concentration of AMP is required to test the effect, if the SPR affinities shown here are representative of binding to each enzyme. However, no additional activating effect was observed when AMP concentrations >0.5 mM were tested against *T. brucei* or *T. cruzi* PFK (data not shown).

4.5.6 ADP weakly inhibits trypanosomatid PFK activity.

ADP is a known activator of bacterial, mammalian and yeast PFKs (see **table 4.5**). The effect of ADP on the trypanosomatid PFKs was tested. Firstly, ADP affinity measurements were made against *T. brucei*, *T. cruzi* and *L. infantum* PFK surfaces using SPR, as described in section **4.4**. **Figure 4.15** shows the steady state measurements for ADP titrations against the three trypanosomatid PFK surfaces.

ADP bound with reasonably tight affinity to the *T. brucei* and *T. cruzi* PFK surfaces. Interestingly, *L. infantum* PFK had the strongest affinity for ADP (K_d^{ADP} = 0.16 mM). When 1 mM AMP was added to the running buffer, no significant change in the affinity for ADP was observed (data not shown). In the presence of ATP, the affinity (ss K_d) dropped 3-5 – fold for each of the trypanosomatid enzymes (data not shown). This is likely due to competition in the active site and suggests ADP does not bind in an allosteric site, but instead in the ATP binding site.

To test the effect of ADP on the enzyme activity, the TIM/Aldolase assay was used. A 2-fold dilution series of ADP (40 mM – 0.32 µM) was added to 4 µg/ml *Tb*PFK in the presence of saturating ATP (2 mM) and F6P (10 mM). *Tb*PFK was incubated with ATP at room temperature prior to the addition of the ADP titration. Reaction was started by addition of F6P. ADP weakly inhibited the *Tb*PFK activity with an IC_{50}^{ADP} of 7.3 mM (**figure 4.16**). ADP did not have an inhibitory effect on the downstream enzymes (aldolase, TIM or G3PDH) (data not shown).

To test if this inhibition was a competitive effect against ATP or F6P binding, or indeed an allosteric inhibition through binding of ADP elsewhere, set concentrations of ADP were added to ATP and F6P titrations against *Tb*PFK. These experiments are discussed in **supplementary material.**

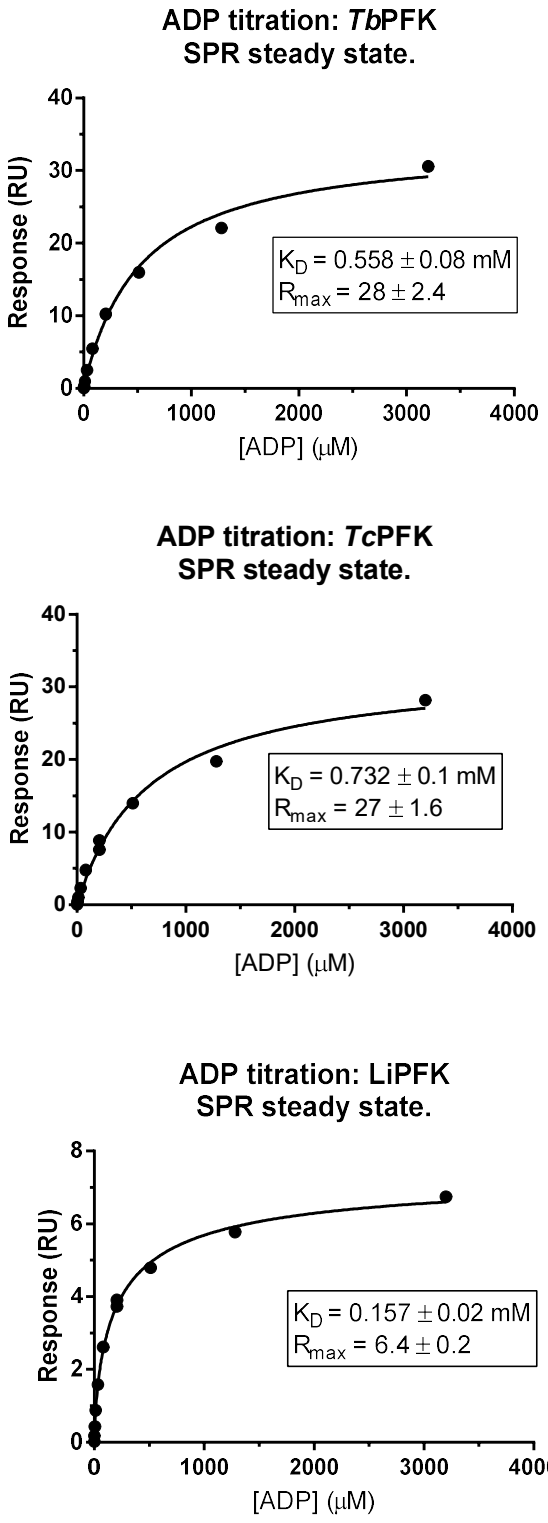

Figure 4.15 : ADP affinity measurements against TbPFK, TcPFK and LiPFK at steady state – SPR.

ADP titration = 3.2 mM – 0.8 µM. All experiments carried out at 25 °C in running buffer (10mM HEPES, 150 mM NaCl, 10 mM $MgCl_2$, 0.05 % P_{20}, pH 7.4). Tested against low density (~1,500 RU) surfaces. R_{max} TbPFK and TcPFK = ~26 RU, LiPFK = 12.1 RU.

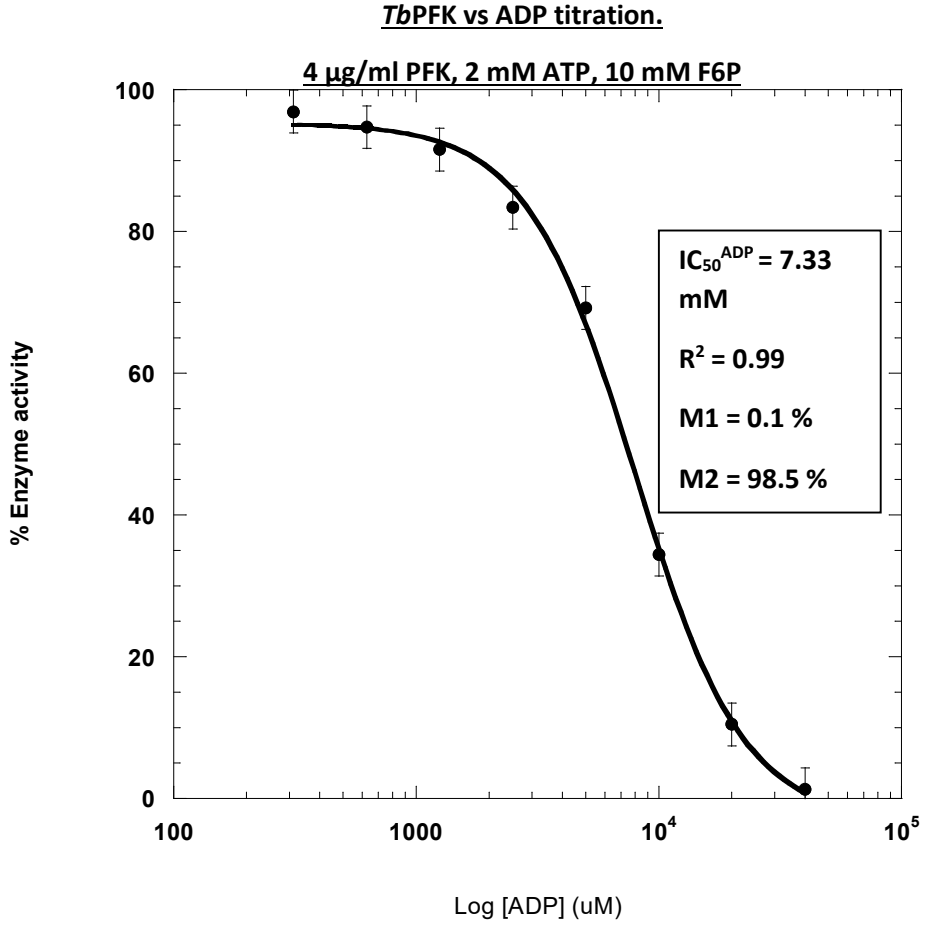

Figure 4.16 : ADP is a weak inhibitor of TbPFK activity.

A) *ADP titration (40 mM – 0.32 µM) against TbPFK measured in the aldolase/TIM assay. 4 µg/ml PFK, 2 mM ATP and 10 mM F6P provided. Carried out in triplicate at 25 °C, error bars denote standard deviation.*

4.5.7 GMP is an alternative activator of trypanosomatid PFK.

Guanosine monophosphate (GMP) had the same activating effect on substrates as AMP on the trypanosomatid PFKs – decreasing the Vmax but increasing the affinity for F6P ($\downarrow K_{half}^{F6P}$)(**figure 4.17**). This results in a significantly increased enzyme efficiency – with k_{cat}/K_m values for *T. brucei* PFK increasing from 0.07 to 0.1 $\mu M^{-1}.s^{-1}$ in the presence of 0.5 mM GMP.

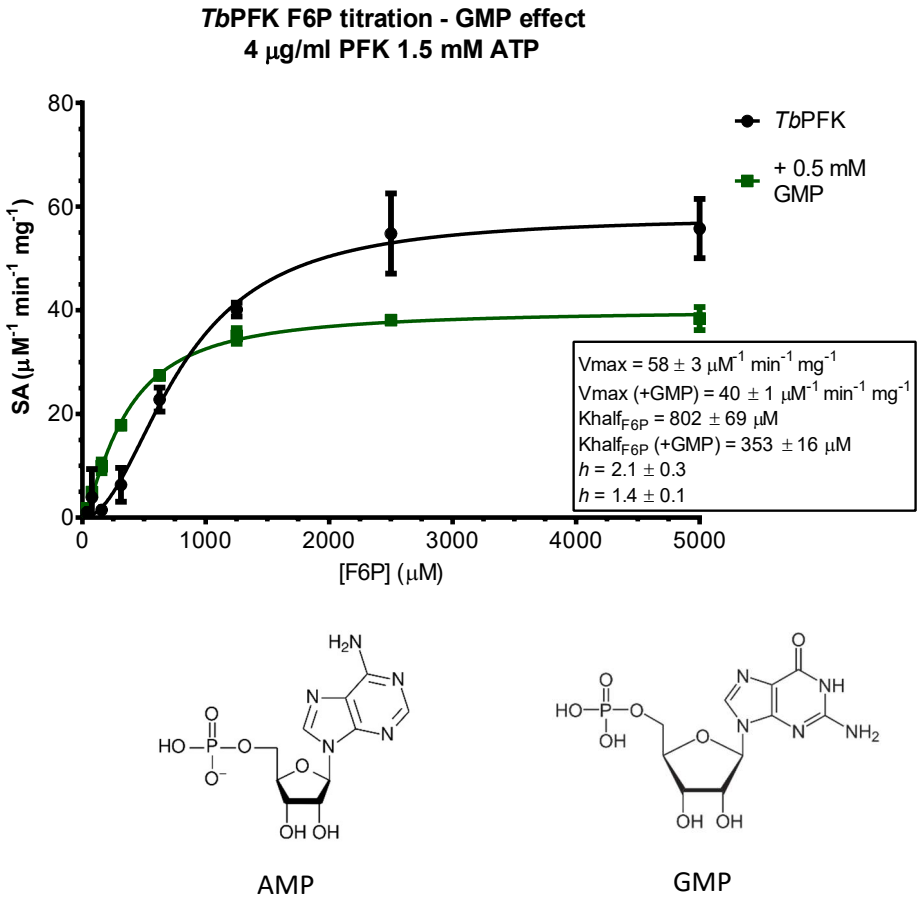

Figure 4.17: GMP is also an activator of T. brucei PFK.

All experiments carried out using the PYK/LDH assay at 25°C in triplicate, error bars denote standard deviation. 5 mM – 9.8 μM F6P titration, 0.5 mM GMP. PFK pre-incubated with 1.5 mM ATP. Tested against 4 μg/ml TbPFK.

Similar to AMP, GMP must be added after the PFK enzyme has been incubated with ATP for the activating effect to be observed. These findings reveal that both GMP and AMP must be accommodated in the same allosteric AMP binding site in *T. brucei* PFK. Unfortunately GMP was not tested in SPR so no comparison in binding affinity for the analyte can be made. **Table 4.7** shows the effect of GMP on substrate binding by PFK in the PYK/LHD linked assay. GMP was not tested against *L. infantum* PFK.

	K_{half}^{F6P} (µM)	Vmax ($\mu mol^{-1}.min^{-1}.mg^{-1}$)	Hill coefficient (*h*)	K_{cat}/K_m ($s^{-1}.\mu M^{-1}$)
T. brucei	802 ± 69	58 ± 3	2.1 ± 0.3	0.07
+ GMP	353 ± 16	40 ± 1	1.4 ± 0.1	0.10
T. cruzi	498 ± 35	62 ± 2	2.2 ± 0.1	0.09
+ GMP	163 ± 17	53 ± 2	1.2 ± 0.2	0.12

Table 4.7: GMP is an activator of T. brucei and T. cruzi PFKs.

Experiments carried out at 25°C in triplicate, standard deviations are given.

4.5.8 Mammalian PFK activators and other metabolites did not affect trypanosomatid PFK activity.

To date, only AMP has been described as an effector of trypanosomatid PFKs. A range of mammalian effectors and metabolic intermediates were tested at a single concentration against the trypanosomatid PFKs using either the LDH/PYK or TIM/Aldolase assays using the standard assay buffer (50 mM TEA, 100 mM KCl, 10 mM $MgCl_2$, 10% glycerol, pH 7.2). To test for an effect on the enzyme, the assays were carried out with substrate (F6P and ATP) concentrations between the K_m^{ATP}/K_{half}^{F6P} and saturating concentrations – i.e. concentrations used were ~$K_{0.75}$. For *Tb*PFK and *Tc*PFK this equated to a concentration of 600 µM F6P, 300 µM ATP and for LiPFK 700 µM F6P, 170 µM ATP (see section **4.2.1, table 4.1** for K_m/K_{half} values). Data was normalised by taking the ratio of enzyme activity *with* effector against *without* effector (control) for each enzyme. A value of 1.0 therefore represents no change in 'normal' activity for each enzyme. This work was carried out in collaboration with Dr P. Fernandes (UoE). None of the tested metabolites had a significant effect on *T. brucei, T. cruzi* and *L. infantum* PFKs (**Figure 4.18**). Both ADP and G6P showed a slight drop in activity for *Li*PFK, however this is likely due to competition with ATP and F6P respectively rather than an allosteric effect on the enzyme.

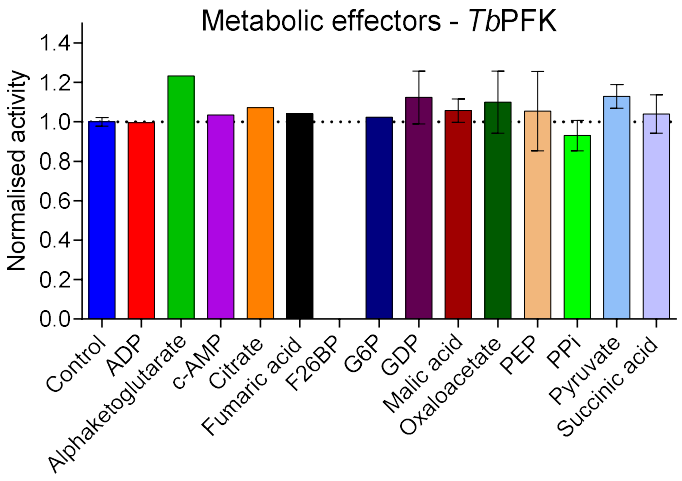

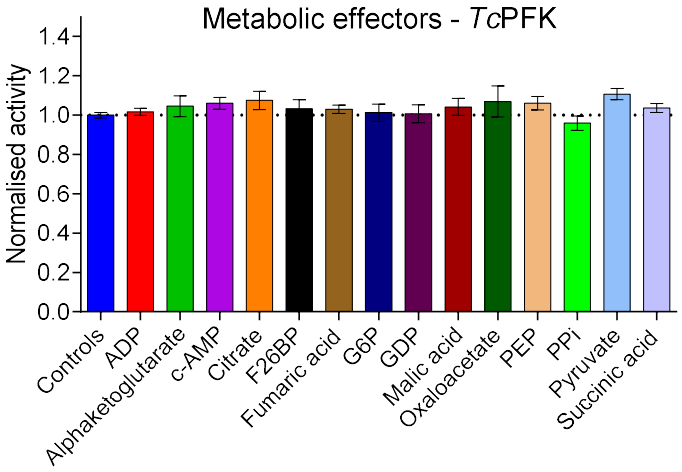

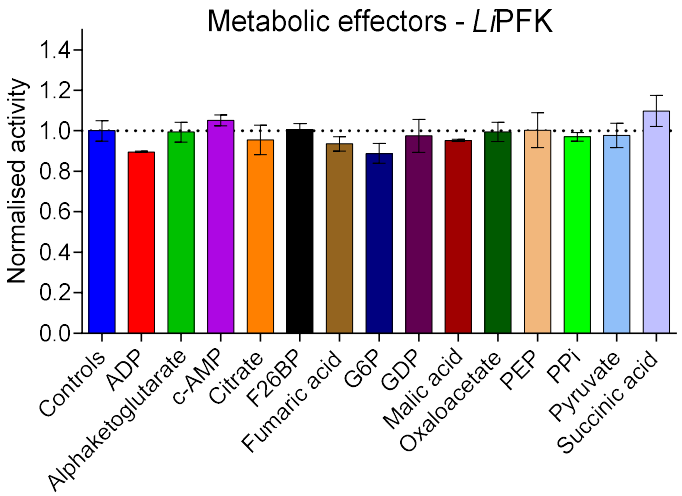

Figure 4.18: Metabolic intermediates had no effect on trypanosomatid PFK activity.

Data measured using the PYKILDH and Aldolase/TIM assays. All experiments carried out at 25°C in triplicate, error bars denote standard deviation.

4.5.9 AMP reduces potency of CTCB compounds.

A range of inhibitor compounds were tested against *Tb*PFK with and without 0.5 mM (final) AMP. In the presence of AMP the IC_{50} values were higher for most compounds (a range of compounds is shown in **table 4.8)**, suggesting weaker interaction and/or an altered mechanism of inhibition between the compound and *Tb*PFK.

As discussed in **section 4.5.1**, AMP induces a 2nd enzymatic state following ATP binding, likely a conformational change in the active site to increase affinity for F6P. The putative AMP binding site is located ~40Å from the active site and CTCB binding pocket so direct competition with the compound is unlikely. We also discuss later **Chapter 6** how CTCB inhibitor compounds are not competitive with either ATP or F6P. The conformational change upon AMP binding must therefore alter either interactions with the CTCB compound or the inhibitory mechanism outside the CTCB binding pocket. This is discussed further in **chapter 6, section 6.7**.

	***Tb*PFK IC_{50} (µM)**	***Tb*PFK IC_{50} (µM) + 0.5 mM AMP**
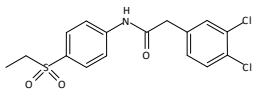 ***CTCB 002***	3.11 ± 0.41	4.45 ± 0.98
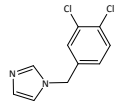 ***CTCB 012***	0.98 ± 0.2	1.14 ± 0.30
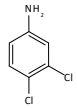 ***CTCB 097***	1.97 ± 0.56	3.90 ± 0.70
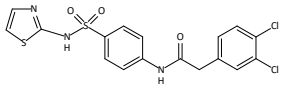 ***CTCB 123***	0.08 ± 0.06	0.10 ± 0.02
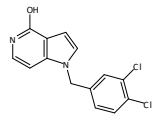 ***CTCB 360***	0.11 ± 0.08	0.11 ± 0.02
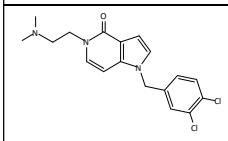 ***CTCB 405***	0.17 ± 0.08	0.21 ± 0.05
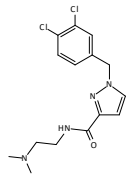 ***CTCB 370***	0.63 ± 0.2	3.82 ± 0.3
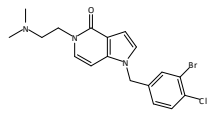 ***CTCB 470***	0.30 ± 0.1	1.29 ± 0.2
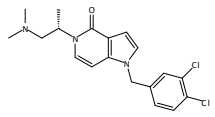 ***CTCB 540***	0.32 ± 0.1	1.71 ± 0.2

Table 4.8 : CTCB compounds are less potent in the presence of AMP.

IC_{50} values calculated using LDH/PYK assay. All experiments carried out in triplicate, standard deviation given.

4.6. Conclusions.

Trypanosomatid enzyme activity.

Affinities for ATP and F6P match well with published data for *T. brucei* and *T. cruzi* PFKs from recombinantly expressed PFK preparations (**table 4.9**).

	Literature	**PFK preparation**	**V_{max} (µmol.min^{-1}.mg^{-1}) /+ AMP***	**K_m^{ATP} (µM) /+ AMP**	**K_m^{F6P} (µM) /+ AMP**
T. brucei	This study	Recombinant. E.coli expression.	60	83 / 9.7	803 / 182
	(Claustre et al., 2002)	Recombinant. E.coli expression.	46 / >46 (extrapolated)	144	1150 / 850
	(Cronin & Tipton, 1987)	Parasite. Purified lysate.	29.6 (extrapolated)	65	999
T. cruzi	This study	Recombinant. E.coli expression.	59	79 / 12	469 / 58
	(Rodríguez et al., 2009)	Recombinant. E.coli expression.	38 (extrapolated)	13	300
	(Aguilar & Urbina, 1986)	Parasite. Purified lysate.	7200	25	2800
Leishmania spp.	This study	Recombinant. E.coli expression.	26	99 / 74	2391 / 134
	(López et al., 2002) (*L. donovani)*	Recombinant. E.coli expression.	ND	ND	3600 / 0.157
	(Berens, R. Marr, 1977) (*L. donovani*)	Parasite. Part purified lysate.	0.29 / 0.43	80	10000 / 500
	(Berens, R. Marr, 1977) (*L. braziliensis*)	Parasite. Part purified lysate.	0.16 / 0.28	60	1400 / 500

Table 4.9 : Comparison of trypanosomatid PFK kinetic parameters with published work.

** AMP was used at a concentration of 0.5 mM in this study. In all other studies here (+AMP) values are given, a concentration of 1.5 mM AMP was used.*

Cooperativity in F6P binding.

Sigmoidal binding responses with relation to F6P have been reported for bacterial PFK (Evans, 1992; Evans, Farrants, Hudson, & Britton, 1981), trypanosomatid PFKs (Cronin & Tipton, 1987)(Nwagwu & Opperdoes, 1982)(Claustre et al., 2002) and mammalian PFK-1 (Moreno-Sanchez et al., 2012). Cooperativity confers the metabolic advantage of amplifying the sensitivity of a signal (Koshland & Hamadani, 2002). PFK can therefore maintain high efficiency in substrate turnover during times of low F6P concentrations.

We have shown in this chapter that F6P appears to bind with positive cooperativity to the trypanosomatid PFKs. F6P titrations produced Hill coefficients of $h > 1$ and a clear sigmoidal behaviour could be observed in dose-response curves. We showed that the reaction order is key to this cooperative behaviour – only when ATP was pre-incubated with the trypanosomatid enzymes did F6P titrations show positive cooperativity. Furthermore, affinity for F6P was greater when PFK was pre-incubated with ATP. This suggests upon ATP binding, the enzyme adopts a conformational state with greater affinity for F6P. This is re-enforced by comparing apo enzyme and ATP-bound *Tb*PFK structures by McNae et. al, where ATP bound forms show an conformational change in 3 active site loops, opening up the active site to more easily accommodate F6P (Martinez-Oyanedel et al., 2007; McNae & Martinez-Oyanedel, 2009). We also observed that co-operative binding of F6P was negated in the presence of the allosteric activator AMP, as previously observed for *Leishmania donovani* PFK (López et al., 2002). In the presence of AMP the sigmoidal responses to F6P titrations changed to more hyperbolic responses with $h \leq 1.0$.

The next question was to address is how ATP binding is communicated across the PFK tetramer, to lead to cooperativity in F6P binding. Again referring to structures by McNae et. al, ATP-binding brings order to C-terminal helices known as 'reaching arms'. These span across adjacent monomers between the dimer of dimers and are likely to the structures responsible for allosterically communicating conformational change across the tetramer as a whole. Provided ATP is bound first, these structural features may be responsible for communicating the signal of F6P binding to the next subunit, promoting a conformational change to a state with higher affinity for F6P.

Two well known models for describing cooperativity in enzymes are the Monod-Wyman-Changeux (MWC) model and the opposing Koshland-Nemethy-Filmer (KNF) or 'sequential' model. **Section 1.4.6, chapter 1** describes these two models of cooperativity.

As we have no evidence of an R and T state with trypanosomatid PFKs without ligand bound, the MWC (symmetry) model cannot be considered. The KNF (sequential) model however fits our observations regarding F6P binding better; The binding of F6P to one subunit confers a conformational change to an adjacent subunit -perhaps through the 'reaching arms' to allow the binding of another F6P molecule more readily. This would be assuming that ATP is bound to all subunits prior to F6P binding. As we observed, ATP must be bound before F6P can be accommodated, and sigmoidal F6P binding responses are only seen when the enzyme is pre-incubated with ATP. One may argue that the PFK apo enzyme may be the low affinity 'T' state in the MWC model, with the ATP-bound enzyme being the high affinity 'R' state. This does not fit however as F6P would have to bind both the low and high affinity states, and we have shown that ATP binding is required before F6P can be accommodated.

F6P binding must induce a second conformational change that is communicated across the tetramer, to allow a more rapid binding of the next F6P molecule. A model for co-operativity is discussed further in **Chapter 7, section 7.2**.

AMP effect and other allosteric effectors.

We have shown in this chapter that trypanosomatid PFKs are not inhibited by ATP at concentrations up to 5mM, and that AMP allosterically activates trypanosomatid PFKs - increasing the catalytic efficiency of the enzyme. Of all of the potential effectors tested, only AMP showed a significant effect on the trypanosomatid PFKs. ADP showed weak inhibition (IC_{50}^{ADP} = >7 mM) of *Tb*PFK activity – likely due to competition with ATP rather than an allosteric effect.

While the increase in affinity for F6P in the presence of AMP correlated well with literature on trypanosomatid PFKs (**table 4.9**), our observed effect of AMP on the PFK enzyme kinetics is novel; We found that trypanosomatid enzyme efficiency was increased in the presence of AMP, through an increase in affinity for ATP and F6P. This was coupled to a slight (~20%) drop in activity (V_{max}). Previous literature has only reported an increase in F6P affinity, coupled with an *increase* in V_{max} (Claustre et al., 2002). These are more traditional characteristics of an allosteric activator. We have shown however that trypanosomatid PFKs response to AMP *in vitro* is dependant on reaction order – the AMP effect was only observed when PFK was pre-incubated with ATP. In some of the published literature, this pre- incubation step was not carried out, or it is unclear what the reaction order was. Under no reaction conditions did we observe a significant increase in V_{max} for any of the trypanosomatid enzymes in the presence of AMP. Our data

however is in agreement that AMP increases the efficiency of the trypanosomatid PFKs; AMP remains the signal for low energy stores in trypanosomatids - its binding to PFK increases the enzymes affinity for the substrates ATP and F6P, allowing rapid binding at low concentrations. Of each of the trypanosomatid PFKs tested *L. infantum* PFK showed the greatest sensitivity to AMP – with an 18-fold increase in the affinity for F6P. This is in agreement with published data for *Leishmania spp.* PFKs (**table 4.9**), including a reported 20-fold increase in the affinity for F6P when *L. donovani* PFK is in the presence of AMP (Berens, R. Marr, 1977). This information may add to our understanding of the physiological control of the glycolytic enzymes in the environment in which *Leishmania spp.* survive in the human infective stage, as discussed further in **chapter 7, section 7.2**.

We outlined evidence of a possible reaction scheme; showing that AMP can only activate the enzyme if ATP is already bound. AMP changed the sigmoidal binding behaviour of F6P to a more hyperbolic response with each of the trypanosomatid PFKs. This effect was also observed in previous studies on *T. brucei* PFK – the addition of AMP caused the enzyme to exhibit hyperbolic behaviour for F6P binding (Claustre et al., 2002). Claustre et. al. also found that the binding of ATP dramatically increased the affinity of the enzyme for F6P binding. Comparisons of apo and ATP-bound *Tb*PFK reveal the AMP binding site is formed upon ATP binding, and the ordering of the C-terminal reaching arms forms a lid over the allosteric site (McNae & Martinez-Oyanedel, 2009). A description of the proposed binding mechanism of F6P cooperativity and AMP activation of trypanosomatid PFK is given in **chapter 7, section 7.2**.

Chapter 5: Phosphofructokinase in reverse.

5.1. Introduction – PFK in reverse.

Phosphofructokinase-1 is considered an irreversible enzyme. It plays a regulatory role in glycolysis because of this feature; committing the cell to glycolysis. The enzyme fructose 1,6-bisphosphatase converts F16BP to F6P in gluconeogenesis, and so PFK need not run in reverse. In trypanosomatids, an additional FBPase enzyme (FBPase-2) facilitates the conversion of F26BP back to F6P (see **section 1.4.2, chapter 1)**. PFK-1 therefore is not required to run in the reverse reaction in the cell. Phosphofructokinases can be grouped into one of two major families according to whether they use ATP (ATP-kinases)(E.C. 2.7.1.11) or pyrophosphate (PPi-kinases)(E.C. 2.7.1.90). Both are high-energy phosphodonors;

$$\Delta G^{o} (PPi + F6P \rightarrow F16BP + Pi) = -2.1 \text{ Kcal/mol}$$

$$\Delta G^{o} (ATP + F6P \rightarrow F16BP + ADP) = -4.4 \text{ Kcal/mol.}$$

Many PPi-Kinases, such as those found in higher plants, are known to run in reverse (Mertens, 1991). T. brucei PFK evolved from an ancestral PPi-PFK to an ATP-dependant enzyme and has retained a number of structural features from this divergence (Martinez-Oyanedel et al., 2007). The ability to run in reverse however, is not considered to be one of these inherited traits (P. a Michels et al., 1997). Three of the four ATP-consuming steps in glycolysis are considered to be 'irreversible' – the reactions carried out by hexokinase, phosphofructokinase and pyruvate kinase. To run these reactions in reverse a high thermodynamic cost must be paid to drive the equilibrium in the reverse direction. It is difficult to imagine therefore how or why one of these enzymes would run in reverse. This chapter aims to investigate how efficiently the PFK enzyme can run in reverse, what the conditions required are and whether these conditions are physiologically relevant. Orthogonal enzyme assays were used to test conditions where the kinetics of the reverse reaction could be measured. A schematic of the reverse PFK reaction is shown in **figure 5.1** below.

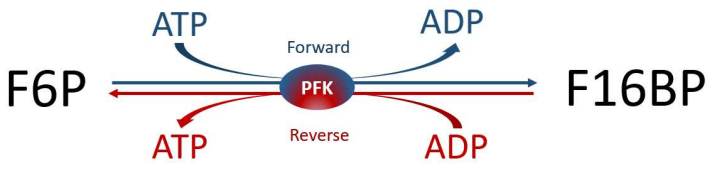

Figure 5.1 : Reaction scheme for forward and reverse PFK activity.

5.2. Substrate kinetics of PFK in reverse.

5.2.1 Reverse PFK activity observed using the kinase-Glo assay.

The Promega 'Kinase-Glo®' kit is an end point assay that measures ATP production or consumption in a kinase reaction by quenching the reaction and measuring the resulting ATP concentration - linking it to the luciferin/luciferase reaction. For the forward reaction (where ATP is consumed) a decrease in luminescence suggests kinase activity. For the reverse reaction, an increase in luminescence (ATP production) suggests reverse kinase activity when ADP is provided. This is summarised in **figure 5.2** below.

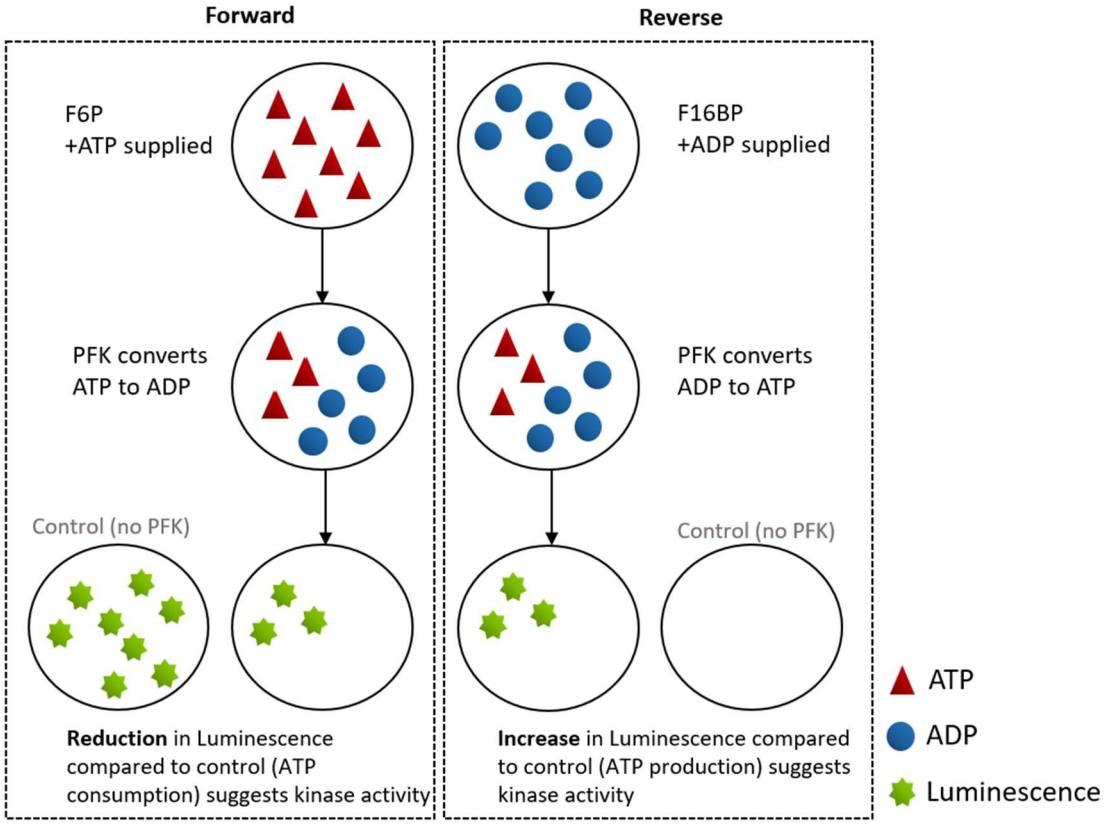

Figure 5.2 – Kinase-glo® scheme used for measuring reverse PFK activity.

Showing how Kinase-glo® assay can be used to measure forward and reverse PFK activity.

An initial test was carried out using 2 µg/ml T. brucei PFK pre-incubated with 5 mM ADP for 10 minutes at 25°C. The reaction was then started with 5mM F16BP. The 'reverse' kinase reaction was allowed to run for 30 minutes at 25°C in reaction buffer (50 mM TEA, 10 mM MgCl2, 5 mM KCl, 0.1% w/v bovine serum albumin (BSA), 0.005% $Tween_{20}$, pH 7.4). A comprehensive protocol for this assay can be found in **section 2.3.5.2**.

As **figure 5.3** shows below, the luminescence for the wells containing *T. brucei* PFK with ADP and F16BP increased relative to the well containing *Tb*PFK and ADP only (which shows a low level of background luminescence signal). This suggests that the PFK present is turning over ADP to produce ATP only when F16BP is also present. Additional controls containing PFK and F16BP only (no ADP) did not show a significant increase in luminescence relative to buffer only and PFK only controls (data not shown). ADP only controls did not result in significant increases in luminescence, ruling out the possibility of spontaneous formation of ATP. Promega 'Ultrapure' ADP stocks were used (>99% purity) to ensure background noise was kept to a minimum.

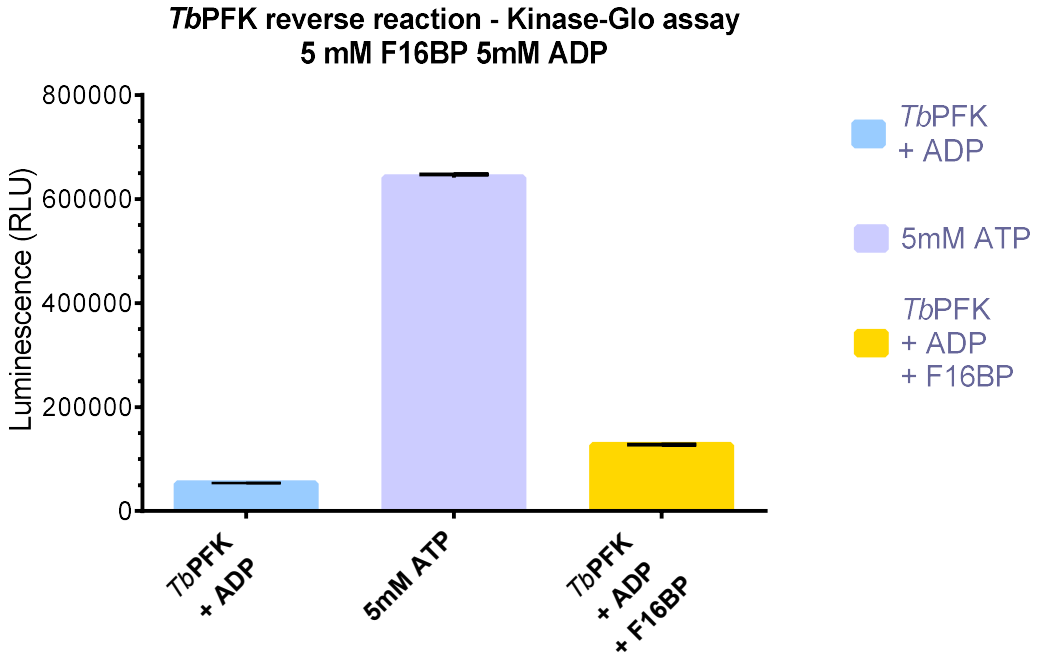

Figure 5.3 : Evidence of the T. brucei PFK reverse reaction in Kinase-Glo assay.

All conditions carried out in triplicate at 25 °C, error bars denote standard deviation. ADP, F16BP and ATP were used where stated at a final concentration of 5 mM each.

With evidence of T. brucei PFK producing ATP in the presence of ADP and F16BP, two additional trypanosomatid PFK enzymes were tested: *T. cruzi* and *L. infantum* PFKs, along with a crude preparation of one of the human PFK isoforms – PFK-M (muscle isoform PFK).

Again, 2 µg/ml of PFK was used and pre-incubated with 5 mM ADP. The reaction was started with 5mM F16BP and allowed to run for 30 mins at 25°C. The resulting luminescence values were converted to ATP concentrations using an ATP standard calibration curve (see **figure 5.4A**) to give the concentration of ATP produced for each PFK enzyme (**figure 5.4B**).

The three trypanosomatid PFKs had comparable activities – each converting ADP to ATP at a rate of ~2 – 2.35 µmol.min^{-1}.mg^{-1}. The rates were calculated based on the concentration of ATP produced (µM) over the time the kinase reaction was allowed to run (30 mins). The final concentration of the crude PFK-M preparation was not able to be determined at the time, but this enzyme also showed ATP production from ADP, at a rate of ~8.2 µM.min^{-1}. These crude rates are estimations only – the limitation of the Kinase-Glo assay is that it is an end point assay and steady state rates cannot be measured. It also only measures ATP production – no F6P production resulting from the reverse reaction can be measured. An orthogonal assay was therefore required to check if the apparent reverse activity observed was an enzymatic turnover of F16BP to F6P or simply a condition-specific spontaneous production of ATP from the ADP in solution.

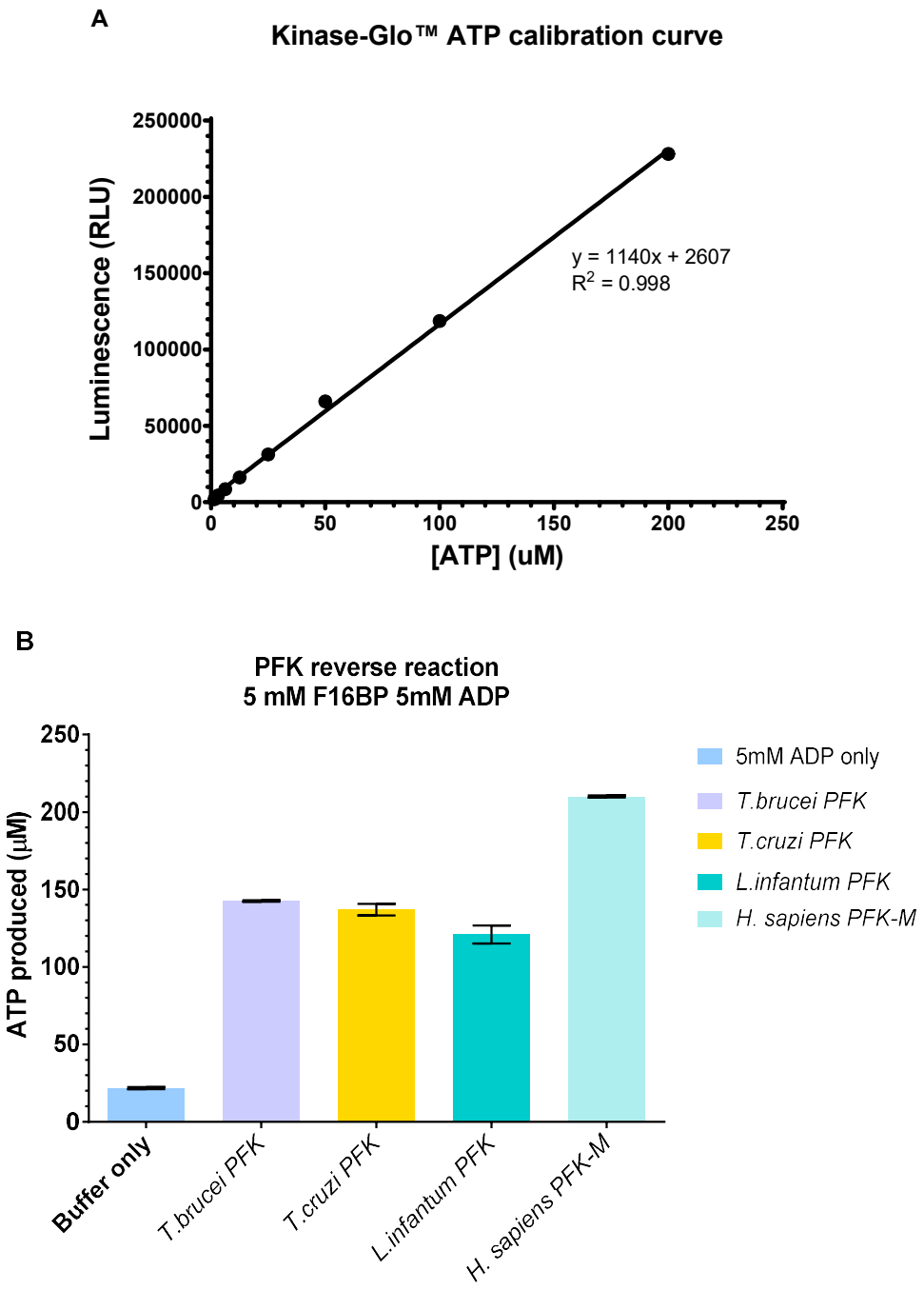

Figure 5.4: ATP produced by reverse PFK reaction using Kinase-Glo™ assay.

A) Calibration curve showing luminescence (RLU) of a standard ATP concentration range in assay buffer. B) ATP produced by PFKs in reverse reaction shown in µM. Luminescence values from Kinase-Glo™ assay were converted to ATP concentration using above calibration curve. Each condition tested in duplicate at 25 °C, error bars show standard error. ADP and F16BP were added to a final concentration of 5 mM.

5.2.2 Optimisation of PGI/G6PDH reverse PFK assay.

To measure the reverse PFK activity in a kinetic-based assay an established protocol for an FBPase activity assay was altered. The reaction scheme for the final assay is shown below in **figure 5.5**. The assay was optimised for measuring reverse PFK activity at 25 °C in reaction buffer (10 mM MgCl2, 50 mM TEA, 100 mM KCl, 10 % glycerol, 0.005 % Tween20, pH 7.4). The assay links the production of F6P by PFK to the downstream enzyme phosphoglucose isomerase (PGI) and glucose-6-phosphate dehydrogenase (G6PDH). The reduction of NAD^+ to NADH provided a measurement of activity by measuring absorbance at 340 nm using a spectrophotometer. A detailed explanation of the assay can be found in **section 2.4.1**.

4

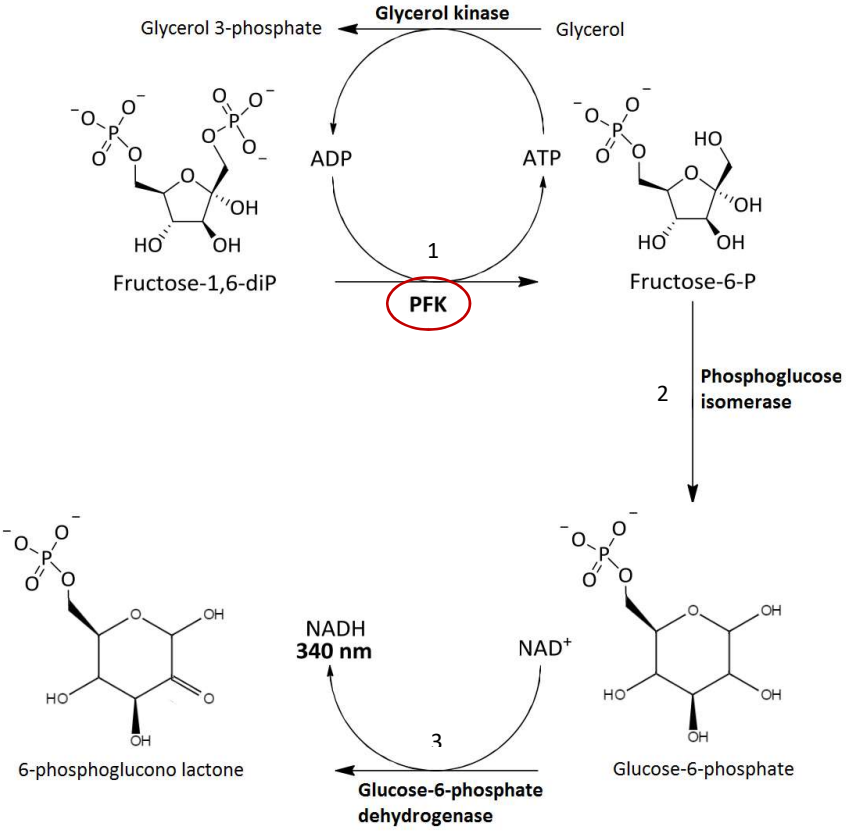

Figure 5.5: PGI/G6PDH linked enzyme assay reaction scheme for measuring reverse PFK activity.

F6P production by PFK working in reverse (1) is measured through the linked enzymes phosphoglucose isomerase (PGI)(2) and glucose 6-phosphate dehydrogenase (G6PDH)(3) via measuring the reduction of NAD+ to NADH which can be measured on a spectrophotometer at 340 nm. Glycerol kinase was added as an ATP sink (4).

An ATP-sink was added to the assay to remove the build-up of ATP that could inhibit the PFK being tested and/or skew the equilibrium of the reverse reaction (**figure 5.5**). A luciferin/luciferase reaction was initially considered but after checking absorption spectra it was observed that the absorption maximum for D-luciferin was 330 nm – preventing an accurate reading of NADH at 340 nm. Next, glycerol kinase was considered however the commercially available form of the enzyme from Bacillus stearothermophilus (Sigma G0774) Glycerol kinase in *E.coli* is known to be inhibited by F16BP as a feedback loop (Zwaig & Lin, 1966). Despite this an available stock was tested to examine its effect on the assay.

To optimise the concentration of glycerokinase a titration of the enzyme was carried out under super-saturating downstream conditions (all other downstream enzymes and glycerol in excess – see **section 2.4.1** for protocol). **Figure 5.6** shows the effect of this glycerol kinase titration on the measured TbPFK activity. The addition of glycerol kinase to the assay increased the overall measured TbPFK rate by ~25%, despite being inhibited by F16BP. ATP is possibly bound to the glycerol kinase enzyme without being hydrolysed, and thus the enzyme is still acting as a sink for free ATP molecules. With free ATP removed from solution, the equilibrium shifts in favour of the reverse reaction.

A final glycerokinase concentration of 5 U/ml in each 100 µl assay well (0.5 U/well) was used. 1 Unit of glycerokinase converts 1 µmol. Of ATP at 25°C. At its maximum rate, with glycerokinase included, *Tb*PFK converts ADP to ATP at a rate of ~12 $\mu M.min^{-1}$ (**figure 5.6**). The reverse assays were run at 25°C for a maximum of 15 minutes. This means that at 15 minutes a maximum of 0.018 µmol of ATP will be produced in the well (12 $\mu M.min^{-1}$ for 15 min. in a 100 µL reaction volume = 0.018 µmol ATP produced). Since the concentration of glycerokinase used (0.5 U/well) can convert 0.5 µmol ATP to ADP, this should act as a sufficient ATP sink in the assay.

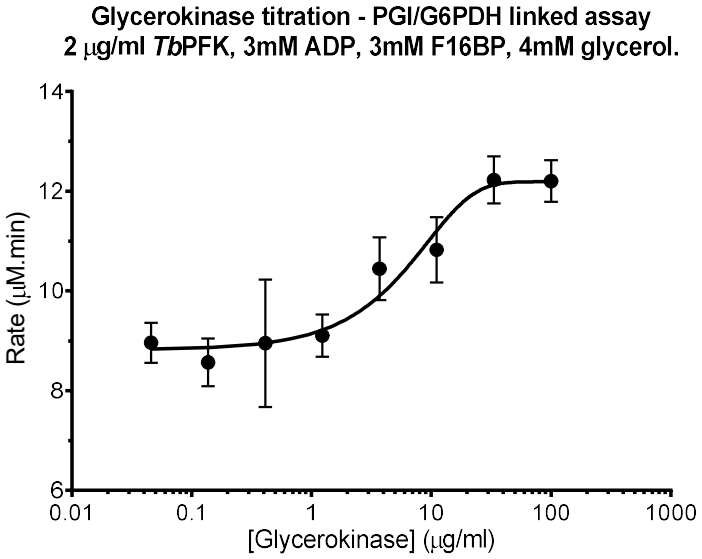

Figure 5.6: Effect of glycerol kinase titration of PGI/G6PDH reverse assay.

Effect of glycerol kinase on the initial rate of PGI/G6PDH reverse PFK activity assay. Each experiment was tested in duplicate at 25°C, error bars show standard error. Sigmoidal curve applied using GraphPad Prism 6.0. Glycerol kinase concentration is shown in Log_{10} scale on the X-axis.

5.2.3 Substrate kinetics for trypanosomatid PFK in reverse.

The optimised PGI/G6PDH assay allowed for real-time measurements of reverse PFK enzyme activity. Titrations of the substrates of the reverse reaction (F16BP and ADP) were carried out to calculate the Michaelis constant (Km) for each, when PFK is running in reverse. An optimised concentration of 2 μg/ml of PFK was used and all experiments were carried out in triplicate at 25°C. No significant drop in NADH absorbance at 340 nm was observed in negative controls containing no PFK enzyme (data not shown). Rate calculations were made by taking the gradient of at least 6 points in the linear section of the raw absorbance trace and converting absorbance values to micro molar NADH concentrations using the Beer-Lambert law (A = Ɛcl). Velocity was calculated as micromoles NADH converted per minute ($\mu M.min^{-1}$) and converted to specific activity ($\mu mol.min^{-1}.mg^{-1}$).

Figure 5.7 shows substrate-velocity plots for ADP and F16BP titrations against *T. brucei* PFK in the PGI/G6PDH assay. Contrary to the forward reaction, both ADP and F16BP fitted a hyperbolic curve fit for TbPFK. However with regard to *Tc*PFK and *Li*PFKs, F16BP titrations fitted allosteric sigmoidal curves better, suggesting cooperativity in F16BP binding with these species. Hill coefficient values for *Tc*PFK and LiPFK also suggested cooperativity in F16BP binding (**table 5.1**).

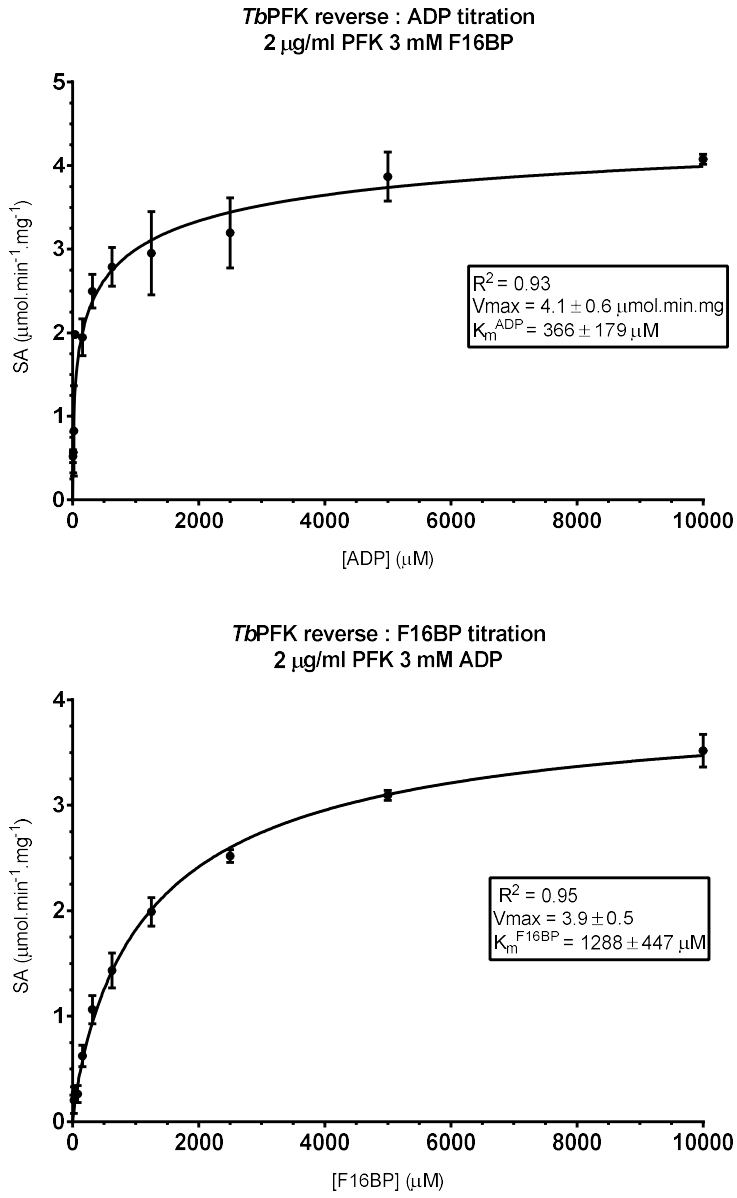

Figure 5.7: Michaelis-Menten plots for ADP and F16BP titrations in the PGI/G6PDH reverse PFK assay.

A) MM plot of ADP titration against TbPFK and a set concentration (3 mM) of F16BP. All reactions preformed in triplicate, error bars denote standard deviation.

B) MM plot of F16BP titration against TbPFK and set concentration (3 mM) ADP. All reactions in triplicate, error bars denote standard deviation.

Table 5.1 shows the gathered kinetic parameters obtained for each enzyme tested in the reverse.

	$K_m^{F16BP/F6P}$ (μM)	Hill coefficient (*h*) *	$K_m^{ADP/ATP}$ (μM)	V_{max} (μmol.min^{-1}.mg^{-1})	k_{cat} (s^{-1})
Reverse					
*Tb*PFK	601 ± 78	1.2 ± 0.3	685 ± 233	4.1 ± 0.3	15 ± 1
*Tc*PFK	1295 ± 98	2.3 ± 0.4	265 ± 48	4.5 ± 0.4	9 ± 1
*Li*PFK	4891 ± 958	1.9 ± 0.2	2636 ± 720	3.8 ± 0.5	7 ± 1
Forward					
*Tb*PFK	803 ± 48	2.1 ± 0.2	83 ± 5	60 ± 1	54 ± 1
*Tc*PFK	469 ± 26	1.9 ± 0.2	79 ± 1	59 ± 1	53 ± 1
*Li*PFK	2391 ± 99	2.2 ± 0.1	24 ± 0.4	26 ± 1	23 ± 1

**F16BP or F6P titrations only.*

Table 5.1: kinetic parameters for Trypanosomatid PFKS run in reverse.

All values taken from plots of initial velocity versus substrate concentration. All plots fitted with either a hyperbolic or allosteric sigmoidal curve using GraphPad Prism 6.0. All experiments were carried out in triplicate at 25 °C, standard deviation is given.

Both *T. brucei* and *T. cruzi* PFK enzymes have similar kinetic parameters with respect to substrate affinity and maximum velocity in the reverse reaction. Reverse substrate Michaelis constants (K_m) are within a similar range as those for the forward substrates (ATP and F6P)(**table 5.1**). *L. infantum* PFK however, similar to the forward reaction with regards to F6P, had a significantly reduced affinity for F16BP and ADP, and a lower overall enzyme activity (demonstrated by the k_{cat}) compared to *Tb*PFK and *Tc*PFK in the reverse reaction. All three parasitic PFKs however appear to be acting enzymatically in reverse: all have enzyme turnover (k_{cat}) values within a sensible range for a working enzyme (~ 10 – 10^6 s^{-1}) and all could be fitted to substrate dose-response curves with hyperbolic or allosteric sigmoidal curves.

5.2.4 *L. infantum* and *T. cruzi* PFK show co-operatively in F16BP binding.

Similar to F6P titrations in the forward reaction, the F16BP titrations against *T. cruzi* and *L. infantum* PFK did not obey Michaelis-Menten kinetics at concentrations below 10mM. Allosteric sigmoidal curves fitted better to F16BP titrations for *Tc*PFK and *Li*PFK, and significant cooperativity was observed; Hill coefficient values for *Tc*PFK and *Li*PFK shown in **table 5.1** above

suggested cooperativity in F16BP binding (h = 1.9 – 2.3 ± 0.2) for F16BP alone. Interestingly, no cooperative binding response was observed for *Tb*PFK with regards to F16BP. The trypanosomatid PFK enzymes were each tested in triplicate on at least three separate occasions. While *Tc*PFK and *Li*PFK were consistent in showing a cooperative response to F16BP titrations, only hyperbolic responses were observed with *Tb*PFK.

5.3. Allosteric regulation of PFK in reverse.

As described in the study of the forward PFK reaction (**Chapter 4, section 4.4**), trypanosomatid PFKs are allosterically activated by AMP. In the presence of AMP they showed a slight drop in Vmax coupled with a significant drop in the Km for both ATP and F6P. As discussed in the aforementioned section, AMP is likely to alter the structure of the PFK active site to more readily accommodate the F6P and ATP substrates. We also found that reaction order dictates this response – AMPs activating effect was only observed when the PFK enzyme was pre-incubated with ATP. The logical question is what effect, if any, AMP would have on the reverse reaction. Without an AMP/ATP-bound structure it is hard to speculate with confidence, but two theoretical models are possible;

I. AMP inhibits the reverse reaction by forcing the enzyme into a state that favours the binding of the forward reaction substrate F6P only.
II. AMP activates the reverse reaction by forming state that accommodates ADP and F16BP in the same manner as it accommodates ATP and F6P with increased affinity.

Figure 5.8 summarises these two possibilities as a reaction schematic for PFK working in the forward and reverse directions.

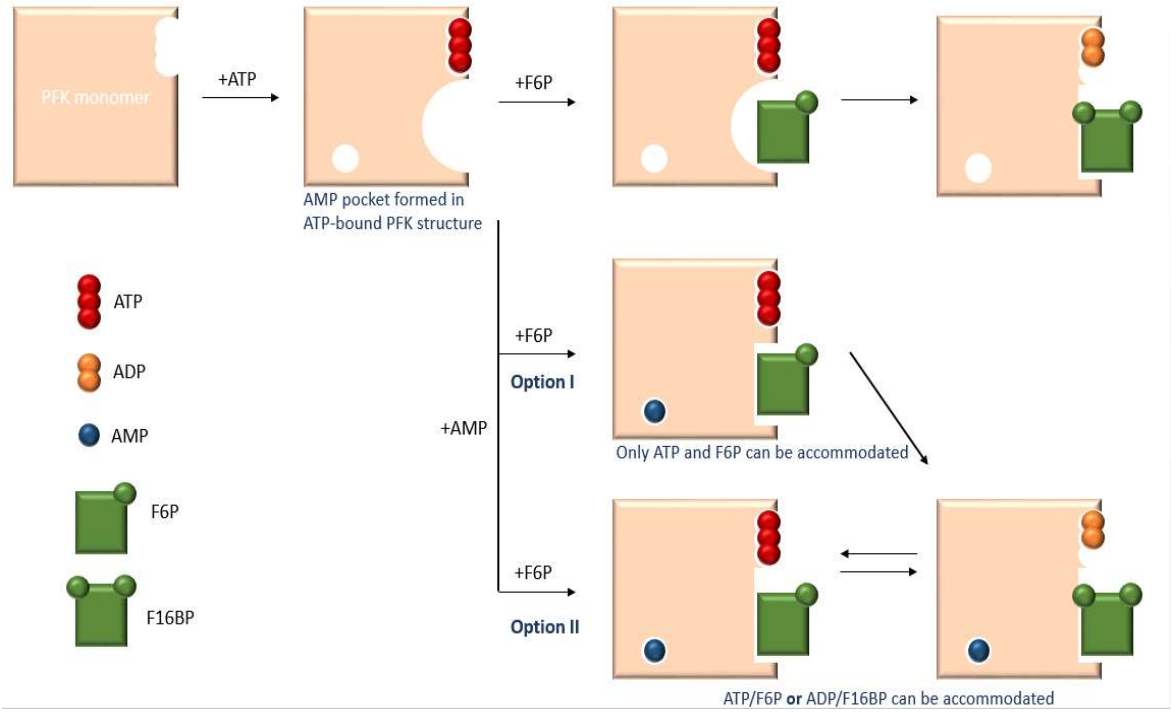

Figure 5.8: Theoretical models for AMP-induced conformational states of PFK monomer.

ATP binds first in the trypanosomatid reaction scheme. AMP and/or F6P cannot bind until ATP is bound. 2 options for AMP-induced fit models for F6P/F16BP binding are shown.

5.3.1 AMP allosterically activates trypanosomatid PFK reverse reaction.

Substrate dose-response curves for the reverse PFK reaction were carried out as stated in **5.2.3**, in the presence and absence of AMP. AMP was added to a final concentration of 0.5 mM after PFK incubation with ADP. The mixture was incubated at 25 ^{o}C for 10 minutes and the reaction was started with the addition of F16BP at 25 ^{o}C in the PGI/G6PDH assay.

T. cruzi, T. brucei and *L. infantum* PFKs were all activated by AMP in the reverse reaction with regards to F16BP titrations. In contrast to the activation of the forward reaction by AMP, T. brucei PFK responded in a more 'textbook' manner for allosteric activation; the K_{half} for F16BP dropped while Vmax remained relatively constant, as shown for the F16BP titrations with and without AMP (**figure 5.10A**). AMP increased the affinity for F16BP with *Tc*PFK and *Li*PFK, coupled with an increase in the Vmax of the enzymes. Similar to the forward reaction with regards to F6P, AMP removed the observed cooperativity in F16BP binding in the reverse reaction. This can be observed in the loss of the sigmoidal tail in F16BP dose response curves (*Tc*PFK and *Li*PFK, **figure 5.10B, 5.10C**) and the Hill coefficient values (**table 5.2**).

AMP increases the affinity for ADP too in the reverse reaction. With respect to ADP titrations against *Tb*PFK and *Tc*PFK, the presence of AMP slightly increased the affinity for ADP (~2-fold decrease in K_m^{ADP}) (**table 5.2**), and results in a slight reduction (~20-25% reduction) in the Vmax (**figure 5.9A, 5.9B**).

Again, *Li*PFK was more affected by AMP with regards to both F16BP and ADP titrations in the reverse reaction. The affinity for both substrates was dramatically increased in the presence of AMP (8-fold increase for ADP, 4-fold increase for F16BP) as well as the Vmax for the enzyme (**figure 5.10C, 5.9C**). Activation by AMP resulted in a 5-fold and 8-fold increase in catalytic efficiency (k_{cat}/K_m) for F16BP and ADP respectively. **Table 5.2** shows the kinetic parameters for each PFK enzyme tested in reverse, with and without AMP. Experimental procedures were as described for the F16BP titrations mentioned above.

ADP titrations – PGI/G6PDH reverse assay.

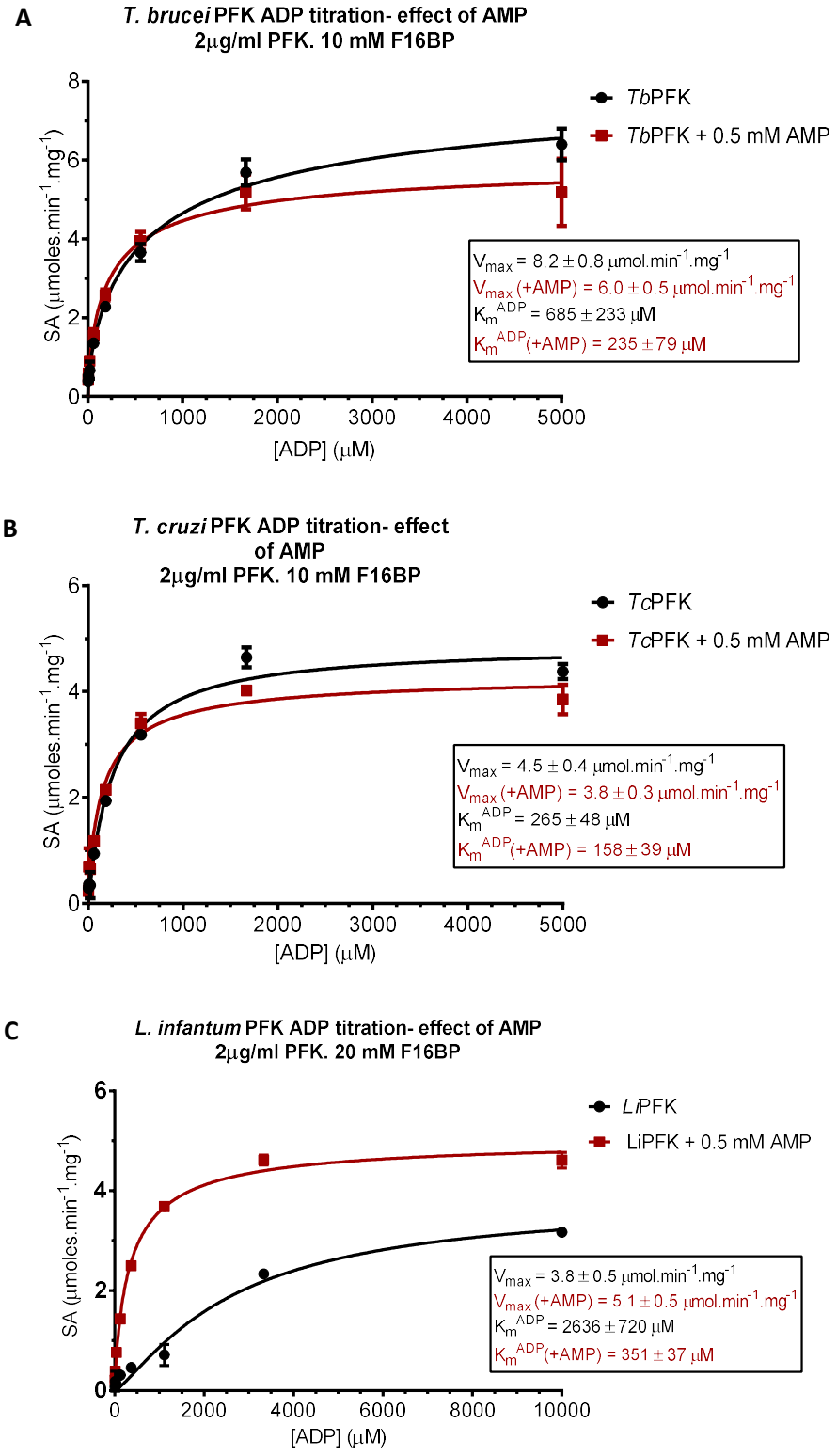

Figure 5.9: AMP activation of T. brucei and T. cruzi PFK in reverse.

Dose-response plots of ADP titrations with (red) and without (black) 0.5 mM AMP for trypanosomatid PFKs. Michaelis-Menten curve fitted (GraphPad Prism 6.0) All conditions carried out at 25 °C in triplicate, error bars denote standard deviation.

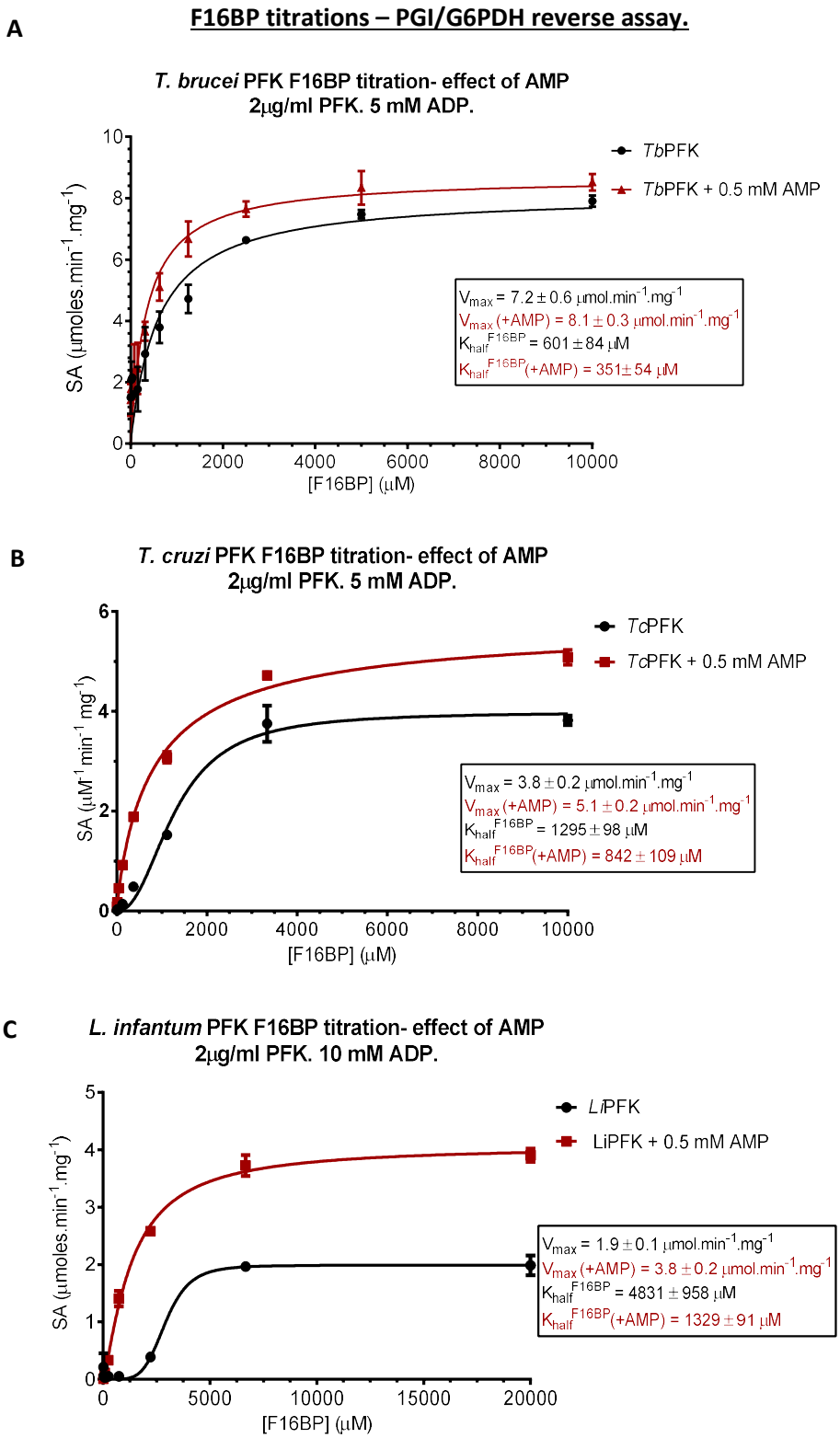

Figure 5.10: AMP activation of T. brucei and T. cruzi PFK in reverse.

Dose-response plots of F16BP titrations with (red) and without (black) 0.5 mM AMP for trypanosomatid PFKs. Allosteric sigmoidal curve fitted (GraphPad Prism 6.0) All conditions carried out at 25 °C in triplicate, error bars denote standard deviation.

		K_{half}^{F16BP} (µM)	V_{max}^{F16BP} (µmol.min^{-1}.mg^{-1})	K_{cat}^{F16BP} (s-1)	K_{cat}/K_{half}^{F16BP} ($s^{-1}.\mu M^{-1}$)	Hill coefficient (*h*)
***T. brucei* PFK**		601 ± 84	7.2	13	0.022	1.2 ± 0.2
	+ AMP	351 ± 54	8.1 ± 0.3	14	0.039	0.9 ± 0.2
***T. cruzi* PFK**		1295 ± 98	3.8 ± 0.2	7	0.005	2.3 ± 0.4
	+ AMP	842 ± 109	5.1 ± 0.2	9	0.011	1.0 ± 0.2
***L. infantum* PFK**		4831 ± 958	1.9 ± 0.1	4	0.001	1.9 ± 0.2
	+ AMP	1329 ± 91	3.8 ± 0.2	7	0.005	1.3 ± 0.1
		K_m^{ADP} (µM)	V_{max}^{ADP} (µmol.min^{-1}.mg^{-1})	K_{cat}^{ADP} (s^{-1})	K_{cat}/K_m^{ADP} ($s^{-1}.\mu M^{-1}$)	Hill coefficient (*h*)
***T. brucei* PFK**		685 ± 233	8.2 ± 0.8	15	0.022	0.7 ± 0.1
	+ AMP	235 ± 79	6.0 ± 0.5	11	0.046	0.7 ± 0.1
***T. cruzi* PFK**		265 ± 48	4.5 ± 0.4	8	0.030	1.1 ± 0.1
	+ AMP	158 ± 39	3.8 ± 0.3	7	0.044	0.8 ± 0.1
***L. infantum* PFK**		2636 ± 720	3.8 ± 0.5	7	0.003	1.3 ± 0.2
	+ AMP	351 ± 37	5.1 ± 0.1	9	0.026	0.8 ± 0.1

Table 5.2: Kinetic parameters for AMP-activation of trypanosomatid PFK reverse activity.

All experiments were carried out in PGI/G6PDH reverse assay at 25oC. All parameters are calculated from substrate-vs-initial rate plots with either Michaelis-Menten plots fitted (TbPFK and TcPFK) or allosteric-sigmoidal plots fitted (LiPFK). All experiments were carried out in triplicate.

The apparent stimulatory effect of AMP appears to be more complicated in the reverse reaction, with multiple responses observed. The Vmax for each enzyme either increased or remained the same in the presence of AMP with respect to F16BP titrations. The Vmax of all enzymes bar *Li*PFK was slightly reduced in the presence of AMP with respect to ADP titrations. This may be a competitive effect of AMP binding weakly in the ADP/ATP site, or a result of the AMP-PFK bound complex adopting a conformation that has little effect on ADP binding. It is clear however that increased F16BP binding is accommodated for with the addition of AMP, and improves the efficiency of PFK working in reverse – demonstrated by increases in the k_{cat}/K_{half}^{F16BP} (**table 5.2**).

The effect of reaction order was not as clear in the reverse reaction ; When added after the incubation of PFK with ADP, AMP had a consistent activating effect with respect to F16BP titrations. When added prior to ADP, AMP produced mixed effects on the enzymes – either showing activation through an increased Kcat/Km or not showing any effect (data not shown). Responses in the presence of AMP were more consistent when AMP was added after ADP, suggesting that prior binding of ADP is necessary for AMP binding or at least the observation of its activating effect on the enzyme in reverse.

5.3.2 F26BP is not a regulator of the reverse PFK reaction.

Fructose 2,6-bisphosphate (F26BP) was tested up to a concentration of 1 mM against the trypanosomatid PFKs in the PGI/G6PDH reverse activity assay. No significant effect of F26BP on PFK activity was observed (data not shown). Many PPi-dependant PFKs ('PPi-PFKs) that are known to run in the reverse direction are regulated by F26BP. PPi-PFKs found in higher plants that also possess ATP-PFK and FBPase enzymes are stimulated by F26BP. Yeast and mammalian ATP-PFKs are activated by F26BP. As discussed in **Chapter 4**, the trypanosomatid PFKs were not affected by F26BP, likely due to a separate evolutionary branching from yeast, plant and mammalian PFKs which developed an allosteric site for F26BP binding from an ancestral active site (**section 1.4.1, Chapter 1**). This is likely the same reason for why no regulation of the reverse PFK reaction by F26BP was observed.

5.4. Inhibition of the reverse PFK reaction.

We have so far shown that trypanosomatid PFKs are able to run in the reverse direction; turning over ADP to produce ATP and behaving enzymatically under titrations of the reverse substrates ADP and F16BP. We have also established that the allosteric activator of the forward PFK reaction (AMP) is also an effector of the reverse reaction.

The 'CTCB' inhibitors described in **Chapter 6** inhibit trypanosomatid PFK by binding to a unique allosteric pocket and blocking the movement of a catalytically important loop ('Asp229 loop') that co-ordinates the transfer of a phosphate from ATP to F6P. If trypanosomatid PFKs are able to act in reverse and facilitate transfer a phosphate from F16BP to ADP, it is logical to assume that by blocking the mechanism responsible for this phosphotransfer we will also inhibit the reverse reaction.

5.4.1 CTCB compounds inhibit trypanosomatid PFK running in reverse.

Using the PGI/G6PDH linked assay, several CTCB compounds were titrated against the *T. brucei* PFK enzyme running in reverse to test for inhibition. The concentration that resulted in inhibition of 50% of the enzyme activity was measured. This is known as an 'IC_{50}'. IC_{50} values for CTCB compounds against *Tb*PFK were measured using the LDH/PYK linked enzyme assay, as described in **Chapter 6, section 6.1**. Enzyme concentrations were optimised previously for the PGI/G6PDH assay, and were comparable with concentrations used in the forward reaction assay for measuring PFK inhibition (2 µg/ml in PYK/LDH assay and 4 µg/ml in LDH/PYK assay). Equimolar concentrations (3mM) of F16BP and ADP were used in the assay. The reaction was carried out at 25 ^{o}C in reaction buffer (10 mM MgCl2, 50 mM TEA, 100 mM KCl, 10 glycerol, 0.005 % Tween20, 1% DMSO, pH 7.4). A full protocol can be seen in **section 2.4.1.2**. **Figure 5.11** shows the dose-response curves for three CTCB compounds tested against *T. brucei* PFK.

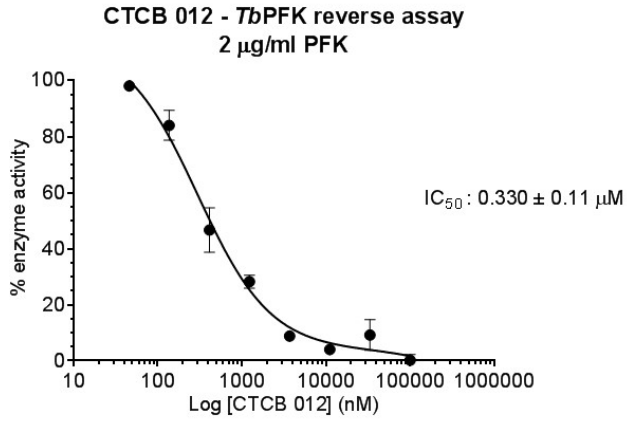

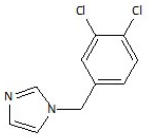

CTCB 012

PFK reaction	IC_{50} (µM)
Forward	0.83
reverse	0.33

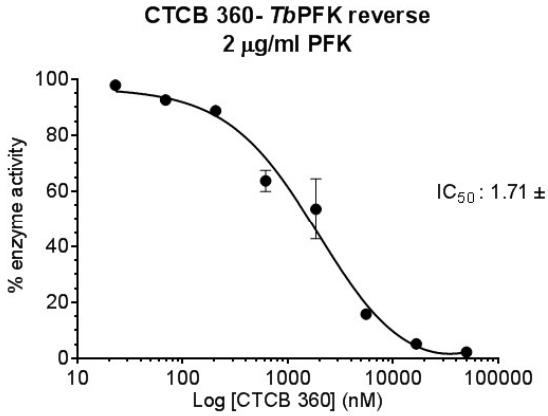

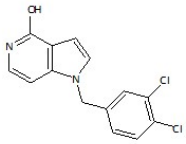

CTCB 360

Reaction	IC_{50} (µM)
Forward	0.11
reverse	1.71

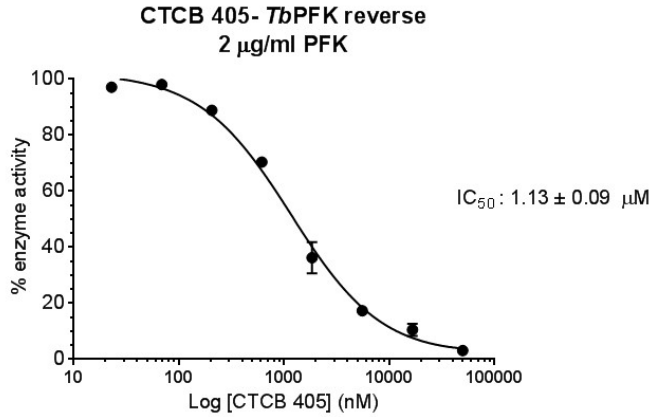

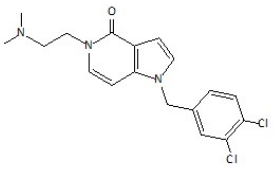

CTCB 405

Reaction	IC_{50} (µM)
Forward	0.25
reverse	1.13

Figure 5.11 : Inhibition curves for CTCB compounds tested against T. brucei PFK in the reverse assay.

CTCB compounds were titrated against TbPFK running in reverse in the PGI/G6PDH assay at 25 °C. Compound concentrations are given in Log values on the X axis and enzyme activity on the Y axis – calculated as a percentage of the uninhibited enzyme activity using negative controls containing DMSO in place of compound. Error bars represent standard deviation (n=3). IC_{50} values for each compound in the forward reaction (PYK/LDH assay) and reverse reaction (PGI/G6PDH assay) are given.

The compounds tested show that the reverse *Tb*PFK reaction can be inhibited, with IC_{50} values in the same order of magnitude as the forward reaction. IC_{50} values are not directly matching and it is difficult to pinpoint the reason; compounds were tested against the downstream enzymes in the reverse assay however no significant inhibition was observed. This does not rule out weak promiscuous binding to the downstream components however. This is investigated as a potential cause for similar discrepancies in IC_{50} values in two orthogonal assays and is discussed further in **Chapter 6, section 6.2.3**. The same buffer conditions, 'non-binding' 96 well plates and pipette tips were used compared to the forward assay (PYK/LDH assay).

It is clear however that the movement of the Asp229 loop is crucial for *Tb*PFK to function in both directions. In the Apo-*Tb*PFK crystal structure (2HIG), a leucine on the Asp229 loop docks into the site into which the CTCB compounds bind. Preventing the docking of this loop inhibits the enzyme as described in **chapter 6, section 6.6**. Furthermore, this is further evidence that the enzyme is carrying out the reverse phosphotransfer – from F16BP to ADP to produce ATP and F16BP, and that it is not simply spontaneous ATP or F6P formation that is responsible for the apparent reverse reaction signal.

Since we showed that F16BP but not F6P can bind in isolation, it is possible that the Asp229 loop has affinity for F16BP and in the ADP/F16BP bound enzyme form, this may force the loop into the 'closed' apo-enzyme form with the leucine residue docked into the CTCB binding pocket (**section 1.4.5, chapter 1**). If this is the preferred conformation when ADP and F16BP are bound, it explains why the IC_{50} values for compounds inhibiting in the reverse direction are higher.

5.5. Conclusions – trypanosomatid phosphofructokinase in reverse.

In this chapter we investigated whether PFK could run in reverse, and if so what the conditions required are to run the enzyme in this direction. We present data showing that trypanosomatid PFKs can run in reverse in two orthogonal assays, and that the substrate kinetics for F16BP and ADP can be measured. We showed that trypanosomatid PFK behaved enzymatically in reverse, adhering to Michaelis-Menten kinetics and in some cases demonstrating cooperativity in F16BP binding. It was shown that AMP was an allosteric effector of the reverse reaction that improved the catalytic efficiency of the reverse reaction in trypanosomatid PFKs.

Additionally, we showed that PFK could be inhibited in the reverse direction by inhibitors designed to allosterically block the catalytic activity of the forward enzyme.

Trypanosomatid PFK appears to run in reverse under conditions that are arguably close to theoretical physiological values; **Table 5.3** shows published ADP, ATP, F6P and F16BP concentrations within cells from various organisms.

Organism	**[ATP]**	**[ADP]**	**[F6P]**	**[F16BP]**
E.coli	1.35 mM[1]	0.82 µM[2]	0.95 mM[3]	15 mM[6]
Leishmania spp.	ND	ND	>1mM[4]	>1 mM4 (check)
H. sapiens	1.3 – 1.8 mM[5] (cytoplasmic)	150 -390 µM[5] (cytoplasmic)	ND	4 – 12 µM[5] (cytoplasmic)

(Yaginuma et al., 2015) *2.* (Albe, Butler, & Wright, 1990) *3.*(Danchin, Dondon, & Daniel, 1984) *4.* (Akpunarlieva et al., 2017) *5.* (Nakayama, Kinoshita, & Tomita, 2005) *6.* (Bennett, Kimball, & Gao, 2009).

Table 5.3 : literature values for measured cellular concentrations of PFK metabolites.

In *E. coli* cells, where PFK is located in the cytosol, ADP and F16BP concentrations have been reported as 0.56 – 0.82 mM and 15 mM respectively in growing cell populations (Bennett et al., 2009; Lowry, Carter, Ward, & Glaser, 1971). In trypanosomes PFK is compartmentalised into the glycosome, and so it is possible that these concentrations are even higher. F16BP concentrations in *Leishmania* promastigotes have been reported to be greater than 1 mM (Akpunarlieva et al., 2017), and is arguably a similar concentration in *T. brucei* and *T. cruzi* cells under the same

conditions. The trypanosomatid PFK enzymes tested here can therefore run in reverse under conditions close to physiological concentrations. A question remains; If the concentrations of ADP and F16BP required for trypanosomatid PFK to run in reverse are achievable *in vivo*, is there evidence of trypanosomatids using PFK in reverse?

To address this question it is necessary to look at a number of examples of PFK being able to run in reverse in vivo; E. coli cells possess two ATP-dependant PFKs (PFK-1 and PFK-2), and an FBPase enzyme. It has been shown that in E.coli cells with depleted ATP-kinases and FBPase enzymes, a recombinant PPi-kinase enzyme can replace the function of both ATP-kinases in glycolysis and run in reverse to perform the function of FBPase in gluconeogenesis (Kemp & Tripathi, 1993). The *E. coli* PFK enzyme has been shown to run in reverse *in vitro* in a pH-dependant manner (Auzat & Garel, 1992).

Labelled hexose sugars derived from C^{13}-labelled F16BP have been found via LC-MS of *T. brucei* cells (in which the FBPase is thought to be inactive), suggesting the reverse activity of *T. brucei* PFK in cells (Creek et al., 2015). The Lab of Dr Frédéric Bringaud at the University of Bordeaux, France has also recently shown that FBPase-null mutants of procyclic T. brucei parasites are capable of producing hexose 6-phosphates (in the absence of glucose) from amino acids, by gluconeogenesis (unpublished – Per. Comm. Dr P. Michaels). This suggests that PFK can fulfil the role of FBPase in the gluconeogenesis pathway by carrying out the conversion of F16BP to F6P. A sample of one of our CTCB compounds has been sent for use in this study to inhibit PFK and confirm its role in this reversed pathway (results pending at time of writing).

Chapter 6 : Inhibition of trypanosomatid PFK.

The work in this chapter focuses on the Wellcome Trust funded 'Seeding Drug discovery' (SDD) project carried out by the Walkinshaw Lab at the University of Edinburgh in collaboration with the medicinal chemistry company Selcia Ltd based in Ongar, Essex. The aim of the SDD project was to design, synthesise and test small molecule inhibitors of *Trypanosoma brucei* PFK. The desired outcome being the development of new orally administered drug compounds against Human African Trypanosomiasis (HAT). **Section 1.4.8, chapter 1** details why PFK was chosen as a target for anti-trypanosomatid drugs. The aim of the work reported in this chapter is to rank and characterise the inhibition of trypanosomatid (*T. brucei* and others) PFK by novel organic small molecules.

6.1 Developing drug-like compounds against Human African Trypanosomiasis.

An initial screening project of 340, 000 small molecules against *T. brucei* PFK enzyme activity was carried out in collaboration between the Walkinshaw lab and the National Institute for health (NIH)(Brimacombe et al., 2014). This study identified >1,000 small molecule inhibitors of *T. brucei* PFK. From here, the Walkinshaw lab undertook a structure-based design approach to developing compounds from these chemical series as part of the Wellcome-funded SDD project. Existing crystal structures of apo- and ATP-bound *T. brucei* PFK by Iain McNae allowed the identification of the unique pocket into which the initial inhibitors bound. This pocket will be referred to as the 'CTCB compound binding site'.

6.1.1 SDD project workflow.

A structure-based design approach to drug discovery requires a constant feedback loop of compound design, testing, characterisation and crystallographic confirmation of binding in order to improve upon compound classes and chemical groups that enhance or hinder binding to the target protein. These characteristics must be in balance with optimising the pharmacokinetic properties of the compound to increase its bioavailability (entry through the blood-brain barrier, trypanosome and glycosome as well as potential metabolism and clearance by the host organisms) and specificity against the target organism. Division of labour and specialisation is therefore essential to ensure this information is generated in a timely manner. A summary of the workflow of the SDD project is given in **figure 6.1**.

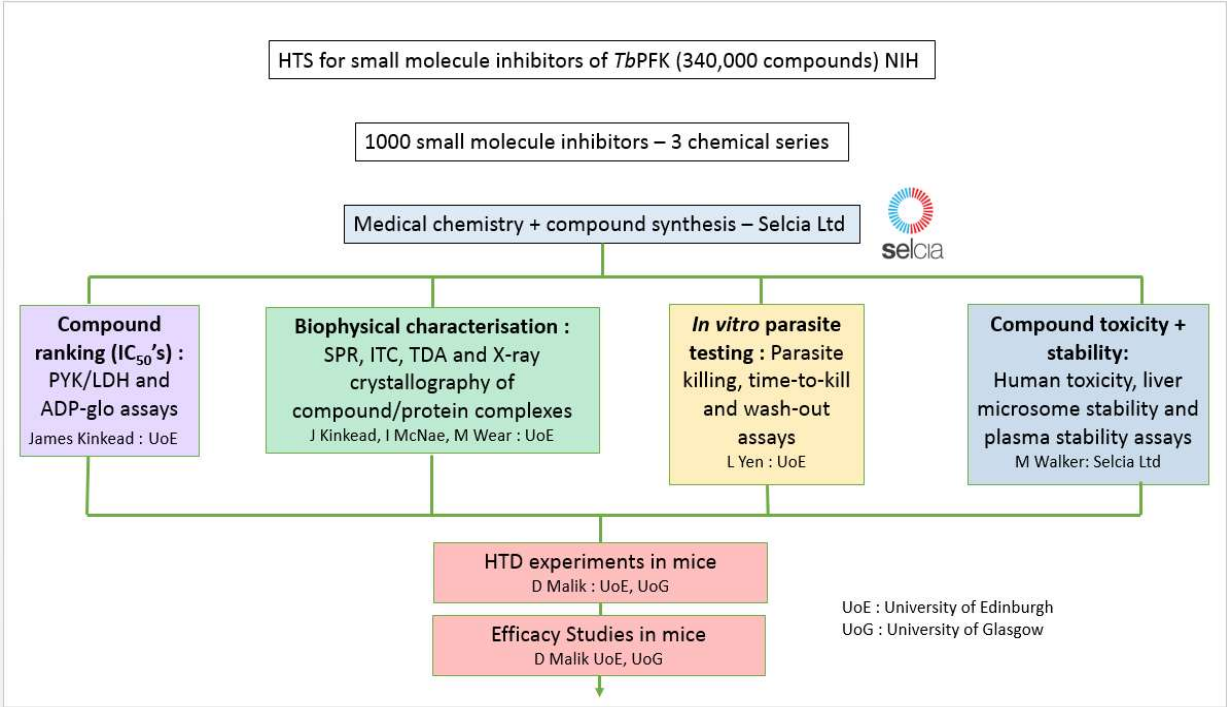

Figure 6.1: Workflow schematic for University of Edinburgh SDD programme.

Initial compound series were based on the sulphonamide chemical class that was identified in the NIH screen. Later development resulted in sulphone, benzamidizole and pyrazole chemical classes. The best inhibitors from these were refined into the 3rd generation chemical scaffolds of azaindoles and amido-pyrazoles. A summary of this chemical class development is given in **figure 6.2**.

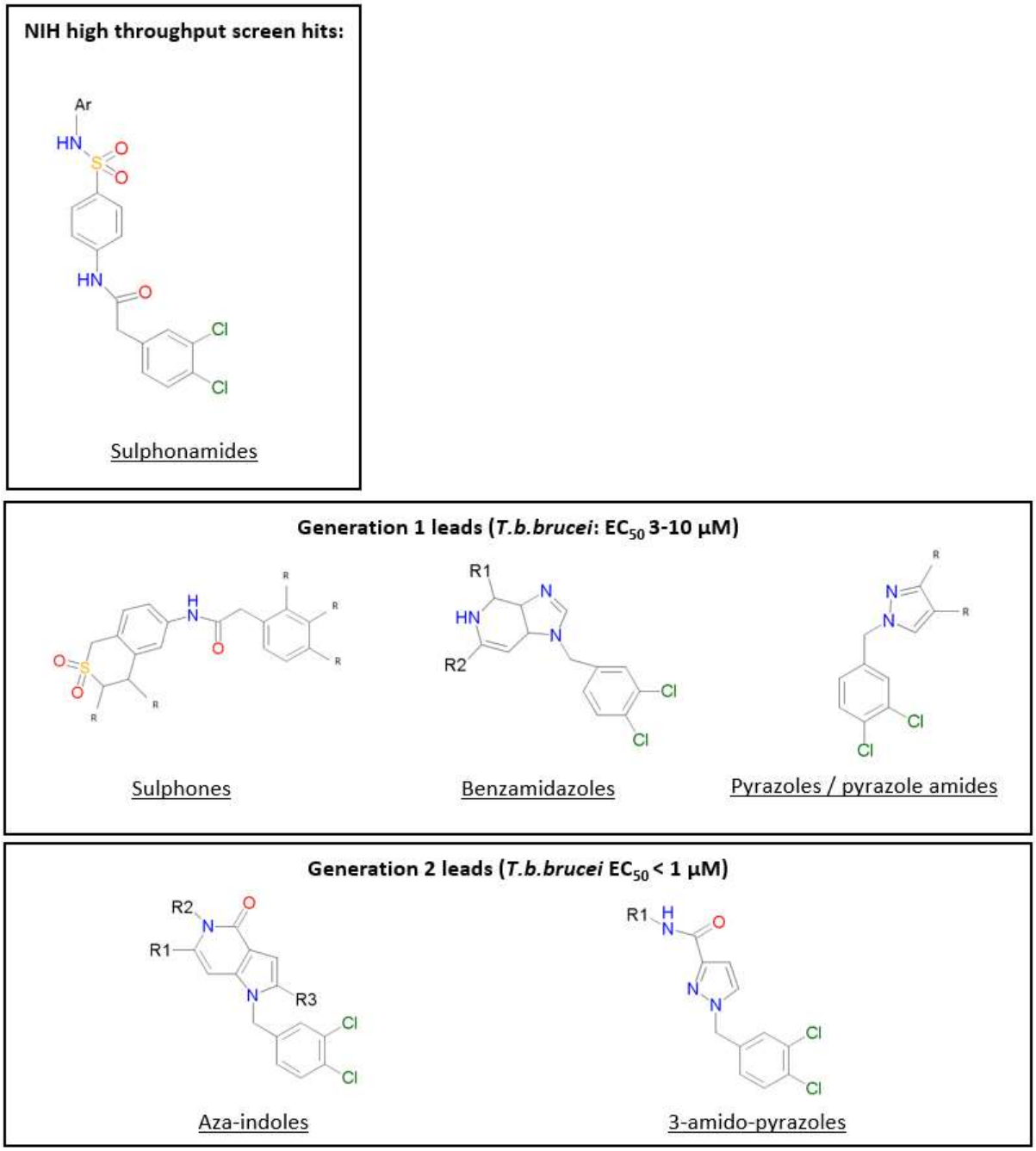

Figure 6.2: Evolution of CTCB compound chemical classes.

Evolution of chemical scaffolds of CTCB compounds throughout the Wellcome Trust SDD project. EC_{50} relates to the concentration of compound required for 50% death of in vitro cultured T.b. brucei parasites.

6.1.2 Assays used in compound ranking and enzymatic characterisation.

Compound testing and characterisation was carried out initially by ranking compounds according to their potency against the enzyme. This was quantified by measuring the IC_{50} of each compound – the concentration of compound at which the enzyme is at half maximal activity. These were measured for each compound in 2 orthogonal enzyme assays – the ADP-Glo™ assay and the PYK/LDH linked enzyme assay. Compounds were also ranked according to their binding response at single concentrations against a *T. brucei* PFK surface in SPR.

Compounds with strong potency against the *T. brucei* PFK enzyme (IC_{50} < 20 µM) were selected for further characterisation: affinity measurements using SPR, characterisation of binding stoichiometry and binding thermodynamics in Isothermal Titration Calorimetry (ITC), specificity testing against human PFK isoforms and characterisation of competition with F6P and ATP. This workflow is summarised in **figure 6.3.** 636 'CTCB' compounds (named after the Centre for Translational and Chemical Biology at the UoE) in total were tested at least twice in each orthogonal assay.

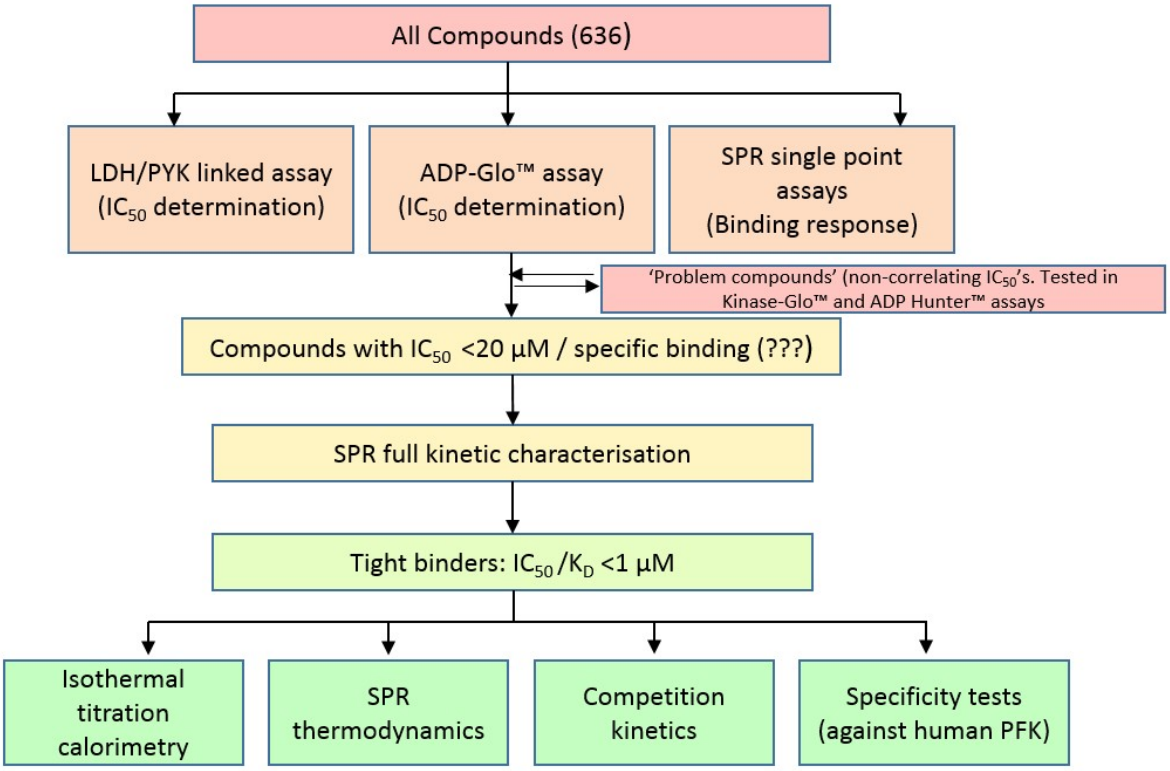

Figure 6.3: CTCB compound testing flow diagram.

Compounds tested in the 2 primary assays were tested in parallel against cultured GVR35 *T. brucei brucei* parasites and ranked by their EC_{50} (concentration at which half the trypanosome population is killed). A close comparison of potency against the enzyme and against the trypanosomes was required to ensure compound development was targeted.

6.1.3 CTCB compound ranking against T. brucei PFK by orthogonal assays.

CTCB compounds were primarily ranked based on IC_{50} measurements against *T. brucei* PFK in the PYK/LDH and ADP-Glo™ orthogonal assays (see **section 2.3.1** and **2.3.4** respectively for protocols). The spread of potencies against *Tb*PFK of the 636 compounds tested over the SDD project is represented in **figure 6.4.** Inhibitor potency ranged from 22 nM to >150 µM, with 13 compounds having an IC_{50} of less than 100 nM.

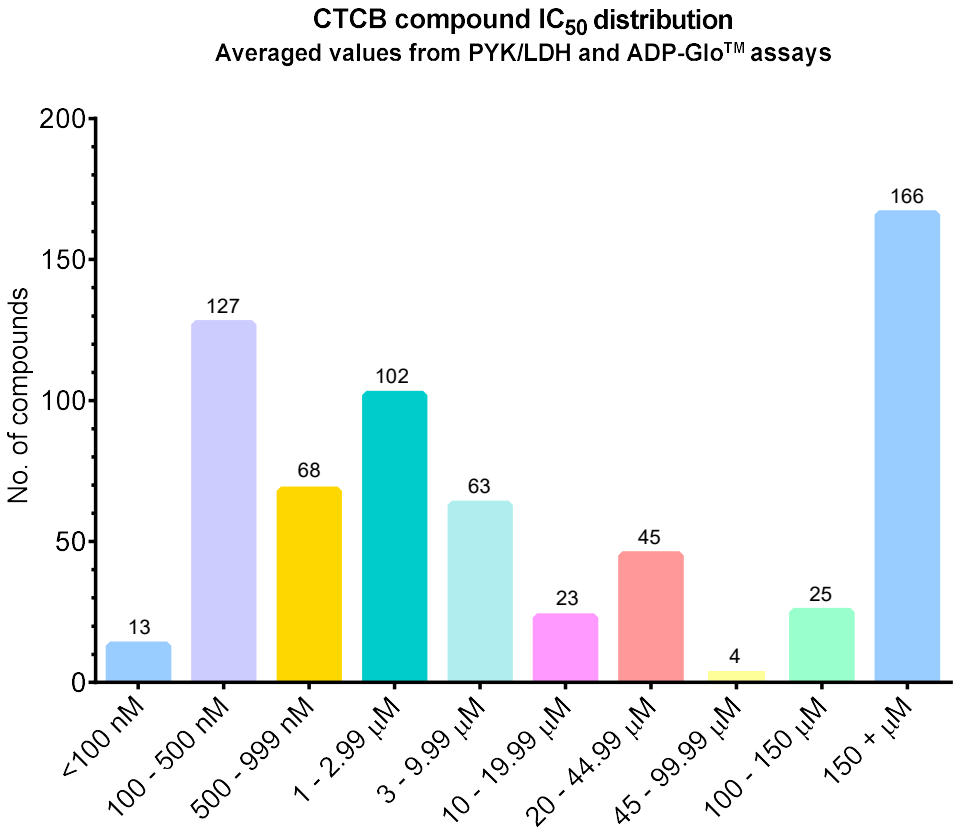

Figure 6.4: Distribution of CTCB compound potency against T. brucei PFK.

Distribution of averaged IC_{50} values (µM) measured in PYK/LDH and ADP-Glo™ assays for inhibition of T. brucei PFK at 25 °C.

6.2. Primary compound ranking by LDH/PYK and ADP-Glo™ assays.

6.2.1 Ranking by PYK/LDH assay.

The PYK/LDH enzyme-linked assay measures *T. brucei* PFK activity by linking the production of ADP to the downstream enzymes pyruvate kinase (PYK) and lactate dehydrogenase (LDH), as seen in **figure 6.5**. Activity is observed by reading the change in absorbance of NADH at 340 nM over time.

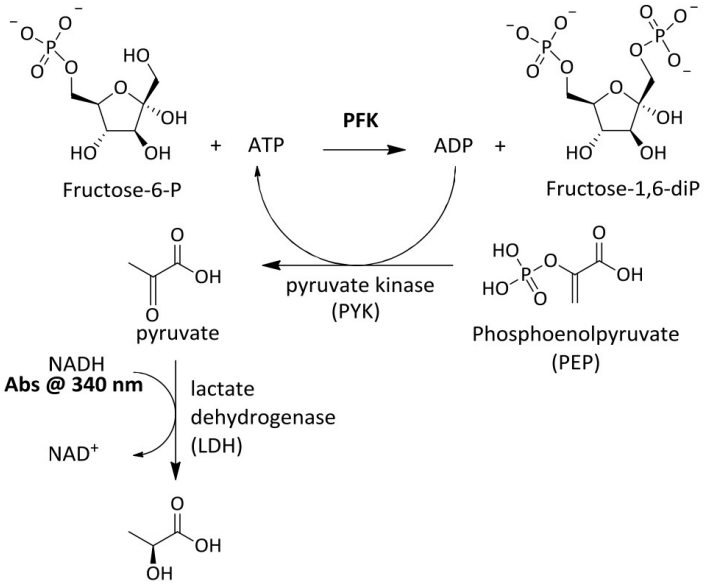

Figure 6.5: PYK/LDH linked assay reaction scheme.

Compounds were titrated against a fixed concentration of PFK (4 µg/ml) and supplied with a fixed concentration of ATP (5 mM). Compound titrations were mixed with the PFK enzyme in the presence of ATP and incubated for 30 minutes before the reaction was started with a sub-saturating concentration of F6P (0.6 mM). Reactions were carried out at 25 °C. For a full protocol please see **section 2.3.1**. Compound titration ranges were decided upon according to limits of solubility and/or predicted potency. The PYK/LDH assay allowed measurements to be taken in real-time – recording the absorbance at 20 second intervals over 12 minutes. The absorbance values were converted to NADH concentration using the Beer-Lambert law (A = Ɛcl). The initial velocity of the PFK reaction (µM NADH oxidised per minute) for each concentration of inhibitor was then taken and plotted as a function of the compound concentration in a dose-response curve as exemplified in **figure 6.6.** A sigmoidal curve was plotted using the positive control (5 µM CTCB 001 or CTCB 405) as the minimum constraint (M1) and the negative control (DMSO) as the maximum constraint in curve fitting. Details of curve fitting can be found in **section 2.3.1.3**.

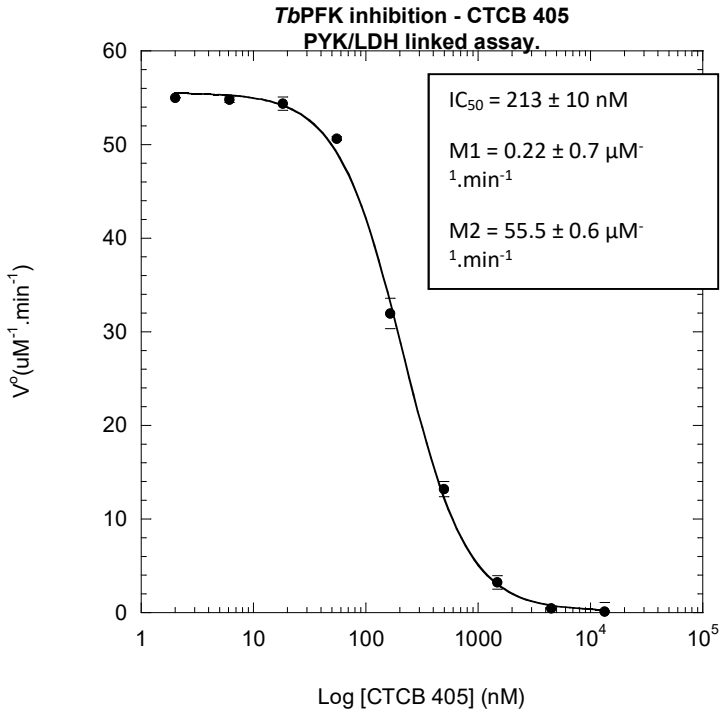

Figure 6.6: Dose-response curve for CTCB 405 inhibition of TbPFK – measured using PYK/LDH assay.

CTCB 405 series dilution of 13.3 µM – 6.1 nM. TbPFK concentration was 4 µg/ml final. F6P = 0.6 mM, ATP = 5 mM final. 'M1' and 'M2' are the upper and lower constraints of the sigmoidal curve, representing the positive control (CTCB 001 - 100% inhibition) and negative control (DMSO – 0% inhibition). Experiments carried out in triplicate at 25 °C, error bars denote standard deviation.

6.2.2 Ranking by ADP-Glo™ assay.

The ADP-Glo™ assay produced by Promega was used as the orthogonal assay in CTCB compound ranking. The ADP-Glo™ assay is an end-point assay that measures the ADP produced in a kinase reaction after a set amount of time. This is achieved by first removing any unused ATP. Any ADP produced is converted back to ATP to be used in the luciferin/luciferase reaction, giving a luminescent output. A full protocol can be seen in **section 2.3.4**.

Serial dilutions of CTCB compounds were incubated with an optimised concentration of PFK (0.5 µg/ml final) and a set concentration of ATP (0.1 mM final) in reaction buffer (50 mM TEA, 10 mM $MgCl_2$, 5 mM KCl, 0.1% w/v bovine serum albumin (BSA), 0.005% $Tween_{20}$, 1% DMSO, pH 7.4). The reaction was started with a 5X ATP/F6P mixture (0.1 mM and 0.5 mM final conc. respectively) and allowed to run at 25 °C for 30 minutes. The luminescence was measured and converted to ADP produced using an ADP standard calibration curve as shown in **figure 6.7A.**

Concentrations of ADP produced were plotted as a function of CTCB compound concentration, and a sigmoidal curve was applied as shown in **figure 6.7B.** Curve fitting is explained in **section 2.3.4.2**. Positive controls (5 µM CTCB 001 or ‘405) were used for the lower constraint (m1) and negative controls (DMSO) for the upper constraint (m2) when plotting the sigmoidal curve.

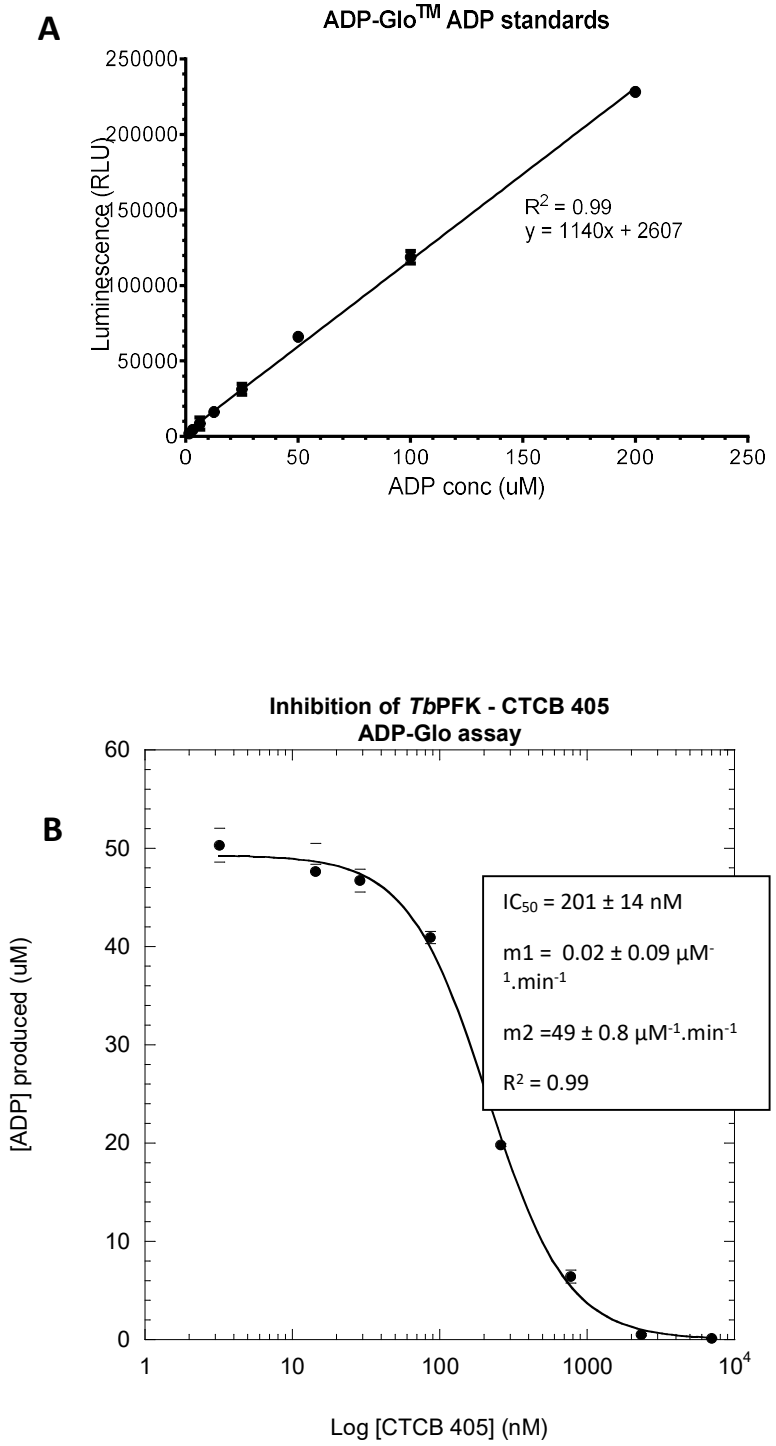

Figure 6.7: Dose-response curve for inhibition of TbPFK by CTCB 405 – as measured by ADP-Glo assay.

***A**) ADP standard calibration curve for converting ADP-Glo kit Luminescence (RLU) to concentration of ADP produced (µM). ADP produced from the kinase reaction is converted to ATP and used in the luciferin/luciferase reaction by the ADP Glo kit. **B**) Dose-response curve for CTCB 405 against TbPFK. CTCB 405 serial dilution from 7 µM – 3.2 nM. TbPFK concentration was 0.5 µg/ml. 0.1 mM ATP, 0.5 mM F6P. Experiment carried out at 25oC in triplicate. Error bars denote standard deviation.*

6.2.3 Calculating Z-prime of primary assays.

The 'Z-factor' coefficient is a measurement of the quality of high throughput assays. It represents both the dynamic range of the assay signal and the variation in the measurement of those signals (Zhang, Chung, & Oldenburg, 1999). The Z-prime of the PYK/LDH and ADP-Glo™ assays were calculated using the positive and negative controls. When using positive and negative controls, the Z-factor is defined by;

$$Z' = 1 - \frac{(3\sigma c_+ + 3\sigma c_-)}{|\mu c_+ - \mu c_-|}$$

Where μ = mean, σ = standard deviation, c_+ = positive control (max. signal) and c_- = negative control (min. signal). (Zhang et al., 1999)

Z-factor	Interpretation
1.0	Ideal assay. Z-factor cannot be greater than 1.
1 > Z ≥ 0.5	An excellent assay.
0.5 > Z ≥ 0	A marginal assay.
<0	There is too much overlap between the positive and negative controls for the assay to be useful.

PYK/LDH assay Z-factor:

Positive control (maximum signal) = DMSO in place of CTCB compound (0% PFK inhibition – maximum abs/min).

Negative control (minimum signal) = 5 µM CTCB 405 (100% PFK inhibition). N = 73. Raw assay data were used – the gradient of the linear part of the plot of NADH absorbance over time (Abs/min).

$$Z' = 1 - \frac{(3 * 0.185 + 3 * 0.009)}{|1.137 - 0.0110|}$$

$$Z' = 1 - \frac{(0.586)}{|1.356|}$$

$$Z' = 0.57$$

ADP-Glo™ assay Z-factor:

Positive control (maximum signal) = DMSO in place of CTCB compound (0% PFK inhibition – maximum RLU).

Negative control (minimum signal) = 5 µM CTCB 405 (100% PFK inhibition). N = 74. Raw assay data was used – the luminescent signal produced (RLU).

$$Z' = 1 - \frac{(3 * 2708 + 3 * 244)}{|25254 - 1565|}$$

$$Z' = 1 - \frac{(8856)}{|23689|}$$

$$Z' = 0.63$$

Both assays have a Z-factor values of >0.5, and so both are excellent, reproducible assays for using in high throughput screening (Zhang et al., 1999).

6.2.4 CTCB compound correlation between primary assays

Correlation between the primary assays was measured using a Spearman nonparametric correlation test for non-normal data, In a correlation plot of 311 compounds with IC_{50} < 50 µM, data correlated reasonably well – giving a positive correlation coefficient of rs = 0.69 (**figure 6.8A**). When only compounds with IC_{50} < 1 µM were included however, the correlation was weaker - with rs = 0.46 (**figure 6.8B)**.

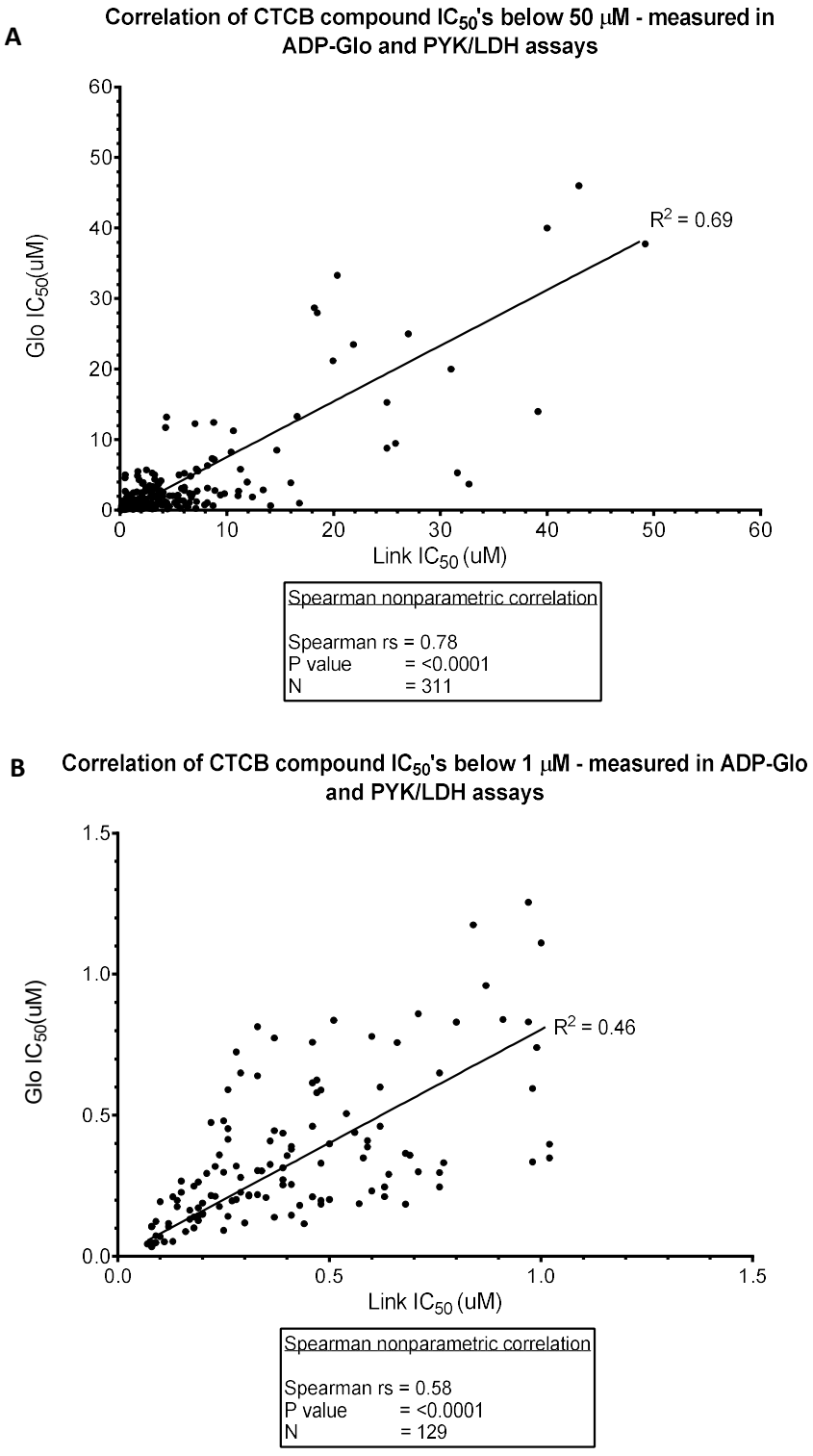

Figure 6.8: Correlation of CTCB compound potency against T. brucei PFK as measured by PYK/LDH and ADP-Glo™ assays.

A) Correlation of IC50 values < 50 μM B) Correlation of IC50 values < 1 μM. Data was tested for normality using the D'Agostino-Pearson omnibus normality test and was found to be non-normal (P<0.0001). Correlation was therefore tested using a spearman nonparametric correlation test for data not following a Gaussian distribution using Graphpad Prism. R^2 value for a line of best fit is given.

6.2.4.1 Discrepancies in IC50 values between primary assays.

The IC_{50} values for CTCB compounds measured in the ADP-Glo™ assay were on average 2.7X lower than the PYK/LDH assay measured values (based on compounds with IC_{50} <50 µM. N = 311). A number of compounds however showed significantly higher IC_{50} values when measured in the PYK/LDH assay. A selection of these 'problem compounds' is shown in **table 6.1**.

The discrepancies in IC_{50} values between each assay did not appear to be attributed to a certain chemical class; While many of the 'problem compounds' belonged to the sulphonamide chemical class, the compounds in the azaindole chemical class had a range of discrepancies – from 1.4 - 10.7 X higher values in the PYK/LDH assay (**table 6.1**). The ADP-Glo™ and PYK/LDH experiments are orthogonal assays, and measurements are taken at different stages of the PFK reaction; In the PYK/LDH assay measurements are taken when the enzyme is at a constant rate (Abs/time taken at linear part of activity curve). The ADP-Glo™ assay was optimised so that the end-point measurements were taken when ~50% of the provided ATP was hydrolysed (**figure 6.7B**). Some slight variation in the absolute IC_{50} values for compounds may therefore be expected, but not to the extent of some of the compounds listed in **table 6.1**. Other factors must be responsible for the discrepancies.

Compound	PYK/LDH assay IC_{50} (µM)	PYK/LDH assay N	ADP-Glo™ assay IC_{50} (µM)	ADP-Glo™ assay N	Difference (fold)
	Azaindoles				
CTCB 405 (Ctrl) 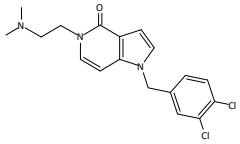	0.27 ± 0.08	55	0.197 ± 0.07	56	1.4 X
CTCB 339 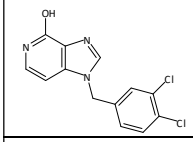	0.91 ± 0.25	5	0.24 ± 0.16	5	3.8 X
CTCB 338 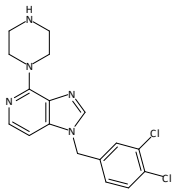	8.71 ± 0.53	3	0.65 ± 0.2	3	13.4 X
CTCB 293 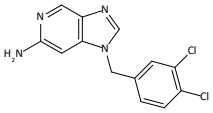	2.71 ± 0.88	6	0.47 ± 0.14	5	5.8 X
CTCB 325 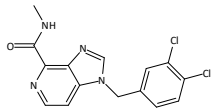	2.88 ± 0.55	3	0.27 ± 0.08	3	10.7 X
	Sulphonamides				
CTCB 002 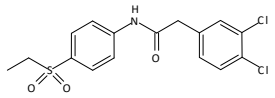	3.48 ± 0.41	3	0.98 ± 0.3	3	3.6 X
CTCB 298 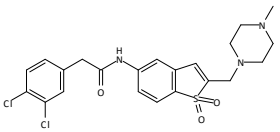	6.36 ± 1.12	3	0.47 ± 0.14	3	13.5 X
CTCB 308 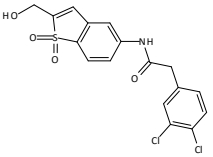	6.13 ± 0.40	3	0.66 ± 0.23	3	9.3 X

Table 6.1: CTCB compounds with varying degrees of difference in IC50 values between primary assays.

'Difference' refers to the factor by which PYK/LDH assay values differ from ADP-Glo™ assay. IC_{50} values measured using the PYK/LDH and ADP-Glo™ assays. Standard deviations are given.

6.2.4.2. IC50 discrepancy troubleshooting: changing buffer and assay components in PYK/LDH assay.

To examine further why some compounds had significantly higher IC_{50}'s in the PYK/LDH assay, differences between the assay conditions were identified. **Table 6.2A** compares the running conditions between the two primary assays. These differences were the inclusion of bovine serum albumin (BSA), protein, KCl and substrate concentrations. To assess the impact of these differences, the running conditions of the PYK/LDH assay were altered to match the ADP-Glo™ assay. The compounds were tested again, and the effect on the IC_{50} compared to the previous assay conditions was measured – as shown in **table 6.2B**.

A

Component	PYK/LDH assay	ADP-Glo™ assay
Buffer		
$MgCl_2$	10 mM	10 mM
T.E.A (triethanolamine)	50 mM	10 mM
KCl	100 mM	20 mM
Glycerol	10%	-
Bovine serum albumin (BSA)	-	0.1 % (w/v)
$Tween_{20}$	0.005%	0.005%
Protein		
*Tb*PFK	4 µg/ml	0.5 µg/ml
Substrates		
F6P	0.6 mM	0.5 mM
ATP	5 mM	0.1 mM

B

Compound	Lower F6P (0.1 mM F6P)	Lower ATP (0.5 mM ATP)	Buffer: - glycerol	Buffer : + BSA	Buffer: - glycerol, + BSA
CTCB 405	-	-	-	-	-
CTCB 339	-	-	-	-	-
CTCB 338	-	3.5 X	3 X	2 X	2 X
CTCB 293	6 X	-	3 X	3 X	1.5 X
CTCB 325	-	-	-	-	-
CTCB 002	-	2 X	2X	2X	-
CTCB 298	-	2 X	2 X	-	1.5 X
CTCB 308	6 X	2 X	2 X	-	2 X

Table 6.2: Altering buffer and assay components in PYK/LDH assay does not fully correct discrepancies.

***A**) Summary and comparison of buffer and assay components in PYK/LDH and ADP-Glo™ assays. Differing conditions between the assays are highlighted. **B**) Results of changes in IC50 values for compounds in the PYK/LDH assay under different buffer and assay conditions. Values represent drop in IC_{50} value compared to previous value measured in PYK/LDH assay.*

As seen in **table 6.2B**, no single change in the PYK/LDH assay conditions was responsible for the IC_{50} discrepancies for the 'problem' compounds tested. Lowering the concentration of F6P from 0.6 mM to 0.1 mM had a large effect on CTCB 293 and CTCB 308, dropping the discrepancy in IC_{50} values 6-fold. This would suggest perhaps a degree of competition between F6P and these compounds, but as will be shown later in **section 6.7.1**, no CTCB compounds were found to be competitive with F6P.

Including BSA and removing glycerol had a small effect on most compounds, but this effect was not cumulative. A change in the optimised PFK concentration had little effect on IC_{50} discrepancies, and caused greater deviation in IC_{50} values in repeats of the same compound in the PYK/LDH assay – as this resulted in a poor signal: noise ratio (data not shown).

With chemical classes and assay conditions being ruled out as the causative agents of the 'problem compounds', it was decided to look at the chemical properties of the functional groups belonging to the compounds; **Figure 6.9** shows the correlation between the basicity of a range of CTCB compounds (pKb) and the discrepancy in their IC_{50} values between assays.

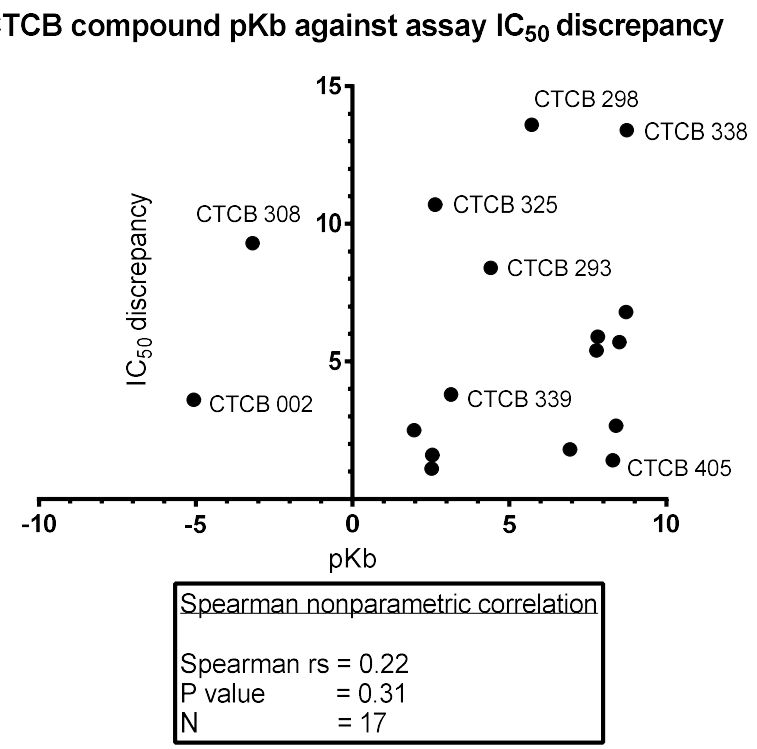

Figure 6.9: Of the 'problem compounds', the less basic compounds have a higher IC50 discrepancy.

Computed pKb values for a range of 'problem' CTCB compounds plotted against factor of difference between IC_{50} values generated by the PYL/LDH and ADP-Glo™ assays. CTCB numbers have been annotated to the right hand side of each data point.

Figure 6.9 shows indeed that there is a relatively weak correlation (rs = 0.22) between the less basic compounds, and higher discrepancy in IC_{50} values. There are some exceptions to the rule however; CTCB 405 and CTCB 338, despite having the same pKb value, have significantly different IC_{50} discrepancies between assays. The varying basicity of the compounds will affect how they interact with other components in the assay such as BSA or downstream enzymes, which of course are different in each assay. While controls showed that no CTCB compound affected the downstream activity of the assays, it does not rule out the possibility of promiscuous binding to other assay components, effectively reducing the free inhibitor concentration in the assay.

No single uniting factor appears to be responsible for the 'problem compounds' between assays. A combination of uncontrollable factors such as compound basicity and variable factors such as the concentration of F6P and inclusion of BSA contribute generally but not equally for each of the compounds. These variables cannot be altered without jeopardising the reproducibility within the optimised assays. This problem therefore highlights the need for orthogonal assays

in high throughput screening, to minimise on false positives or negatives throughout the process.

6.2.5 Inhibition of PFK corresponds to parasite killing.

For a structure-based drug design to be successful, any gains in potency against the enzyme must also be matched by increases in potency against the target organism**. Figure 6.10** shows a good correlation between IC50 values for the CTCB compounds and the EC50 (concentration of compound at which 50% parasite killing is achieved) of the same compounds against cultured *T. brucei brucei* trypanosomes. Inhibition of the essential PFK enzyme is targeted by the CTCB compounds; Inhibition of PFK is clearly translating to effective cell death of BSF *T. brucei* trypanosomes.

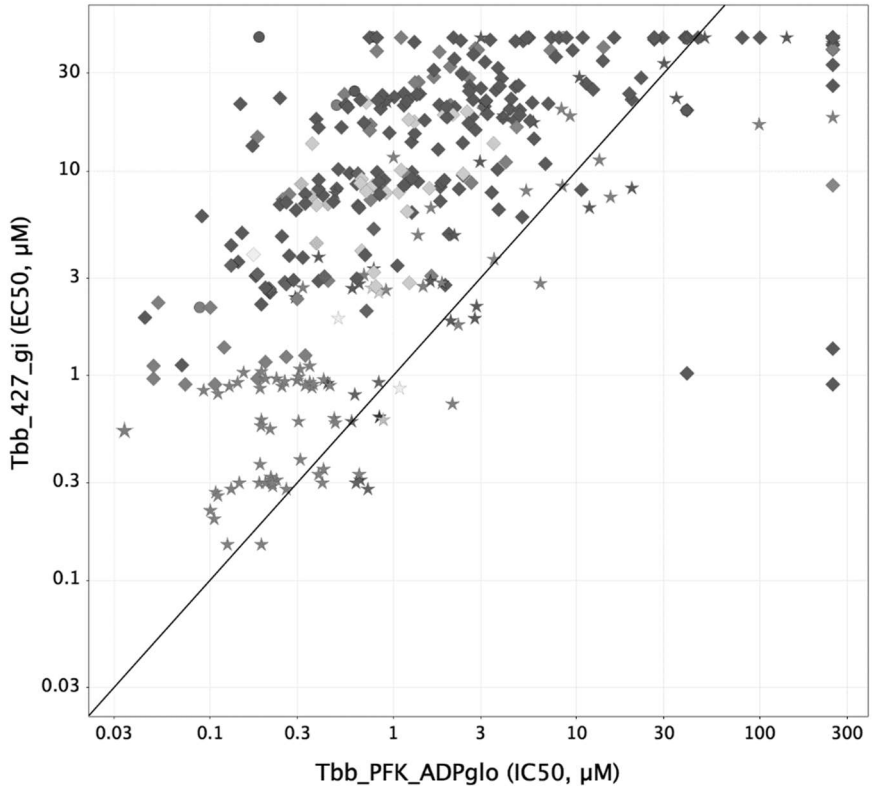

Figure 6.10: Inhibition of PFK by CTCB compounds correlates with killing of trypanosome cultures.

Correlation plot – CTCB compound inhibition of T. brucei PFK (IC_{50}) (X-axis) against killing of cultured T. brucei brucei '427' strain trypanosomes (EC_{50})(Y-axis). Basic compounds are labelled with stars (★), compounds with neutral or acidic groups labelled as diamonds (♦). IC_{50} values were measured using the ADP-Glo™ assay. Image generated by C. Swain, Cambridge MedChem Consulting.

A grouping of basic compounds (labelled★) can be seen in **figure 6.10** as the most potent compounds against both the enzyme and parasite. Basic compounds may allow greater penetration into the hydrophobic parasite cell and glycosome membranes - resulting in more potent killing of trypanosome.

6.2.6 Compound ranking using SPR.

The ADP-Glo™ and PYK/LDH assays were used primarily for ranking of potency against the enzyme on a week-by-week basis. Single point ranking through SPR was also carried out on a less regular basis, testing batches of ~30-60 compounds at a time. The single point screening by SPR was used to identify compounds for further characterisation by SPR – only compounds that showed potent, specific binding to the PFK surface at single point were chosen for further analysis. All PFK surfaces described in this chapter were made using the his_6-tag capture and couple technique described in **section 2.5.3.1**.

6.2.6.1 CTCB 405 is an excellent control for ranking in SPR.

Single point screening in SPR involves measuring the response (in resonance units - 'RU') of each compound at a single concentration against the PFK surface. In order to rank compounds in single point using SPR, a control compound must be used as a reference. This control compound needs to bind tightly and specifically to the PFK surface, in a 1:1 stoichiometry and must be reproducible in its response and not interfere or bind promiscuously to the protein surface or SPR chip matrix. The lead compound identified from the NIH screen – 'CTCB 001' was used initially as a control for all assays as it was the original compound scaffold and was known to inhibit *Tb*PFK with high potency (ADP-Glo™ IC_{50} = 220 nM) .

Later however, CTCB 405 was identified as a much better candidate as a standard for all CTCB compounds. It has a similar potency against *T. brucei* PFK (ADP-Glo™ IC_{50} = 197 nM) but had 'cleaner' binding profiles (flat equilibrium responses) and better reproducibility in SPR compared to CTCB 001. As shown in **figure 6.11A** CTCB 405 binds very cleanly to the *T. brucei* PFK surface in SPR; The sensorgram shows fast on rates and slow off rates, with the response reaching equilibrium at the higher concentrations. Also, the compound completely dissociates back to baseline. Furthermore, CTCB 405 gives excellent steady state plots such as that shown in **figure 6.11B**. Its binding response has excellent reproducibility with an average standard deviation for SS K_d of 11 nM (based on an average SS KD of 91 nM, N = 5. On a *T. brucei* PFK surface of 3,000 RU).

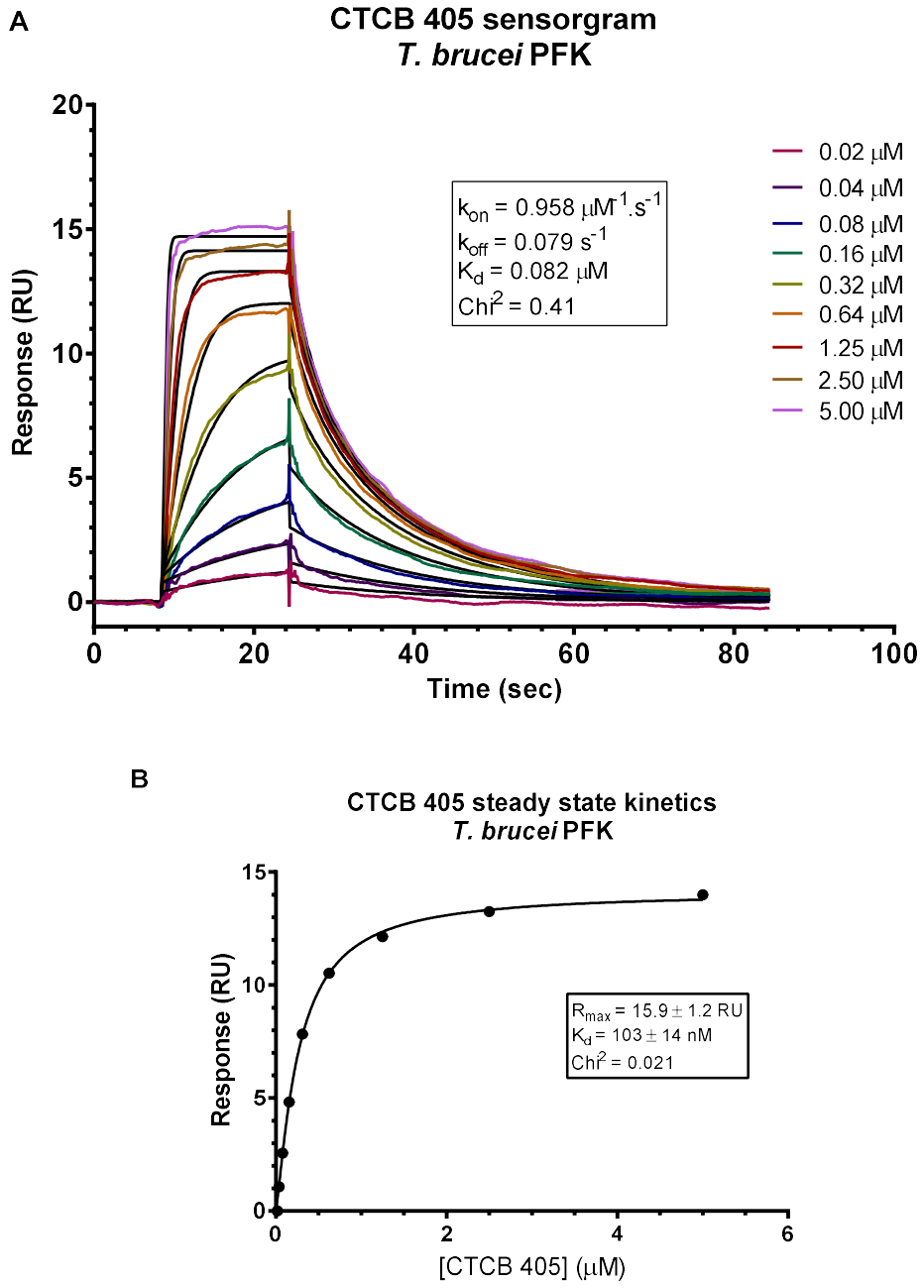

Figure 6.11: CTCB 405 is an excellent control compound for measuring binding against TbPFK in SPR.

***A**) SPR sensorgram for CTCB 405 titration against T. brucei PFK surface (Density = 1500 RU). 1:1 binding model has been fitted to each sensorgram trace (black). Tested at 25 °C. **B**) Steady state dose-response plot for CTCB 405 against TbPFK. Standard error values are given.*

6.2.6.2 Single point ranking by compound 'binding response' and 'stability'.

Single point ranking of CTCB compounds using SPR was carried out by measuring both the compound 'binding response' and 'binding stability' against a *T. brucei* PFK surface. All measured responses were reference subtracted and corrected for molecular weight. An explanation of SPR binding response measurements is given in **section 2.5.3**. Single concentrations of CTCB compounds were tested at 50 µM and later 10 µM as increasingly more potent compounds were developed.

'Binding response' measurements look at the overall binding response (RU) of the compound, measured by the response at the 'equilibrium' phase of the sensorgram – measured 4 seconds before the end of the injection phase (**figure 6.12)**. The concentration of the complex is proportional to the corrected response.

'Binding stability' measures the binding response (RU) 5 seconds after the end of the injection phase, when the compound is dissociating from the PFK surface (**figure 6.12**). The binding stability and response of each compound was ranked against the response of the standard - CTCB 405. CTCB 405 was repeated 4 times in each assay, to assess the reproducibility of the PFK surface.

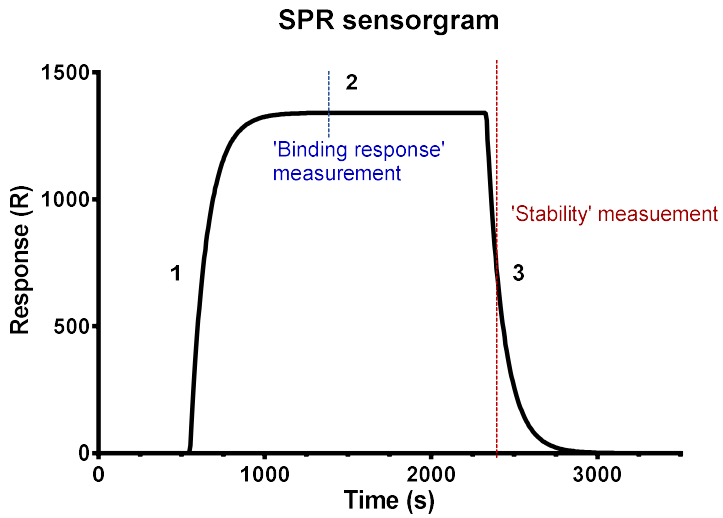

Figure 6.12: Binding 'response' and 'stability' measurements taken in SPR single point compound ranking.

*Example sensorgram trace for a single concentration of compound. **1**) Association phase – compound washed onto surface and binds as a function of concentration of compound. **2**) Equilibrium phase – compound association and dissociation in equilibrium. 'Binding response' measurements taken during this phase. **3**) Dissociation phase – compound no longer injected, washed off with running buffer. 'Stability' measurement taken 5 seconds after equilibrium phase.*

The single point binding responses and stability measurements for a batch of 96 compounds against a low density *Tb*PFK surface (1,500 RU) is shown in **figure 6.14**. The responses were grouped into 3 sections – 'high', 'medium' and 'low', relative to the repeats of the CTCB 405 standard, shown in red. Generally, compounds within the 'medium' binding range were picked for further analysis. Compounds with responses much higher than CTCB 405 were assessed further; Very high binding responses suggest promiscuity in binding to the PFK surface. The maximum binding response 'R_{max}' value relates to the binding capacity of the ligand surface – ie the response measured at saturation of the PFK surface. For a small molecule interaction with an immobilised protein the recommended R_{max} is ~ 25 RU (GE Healthcare, n.d.). RU_{max} can be calculated by;

$$RUmax = \frac{MWanalyte}{MWligand} * RU\ of\ immobilised\ ligand * n$$

For CTCB 405 (MW = 364 Da) tested against a *T. brucei* PFK surface (monomer MW = 54 KDa) of 1500 RU the RU_{max} is the following:

$$RUmax = \frac{364}{54000} * 1500 = 10\ RU$$

This theoretical response is accurate to the actual saturating response measured for CTCB 405, as seen in **figure 6.14A.** As an example, the compounds CTCB 501 and '552 have responses that deviate greatly from the theoretical RU_{max} for the compounds. According to the above equation, CTCB 501 and '552 (MW = 378 and 404 Da respectively) have a theoretical RU_{max} of 10 and 11 RU. The actual measured responses of these compounds was much higher (**figure 6.14A**), suggesting either a >1:1 stoichiometry or promiscuous binding to the PFK surface. Other factors such as 'carryover' can also be assessed when single point responses demonstrate this behaviour. SPR single point binding measurements are a quick method of flagging 'sticky' or promiscuous binders of the target ligand. Both binding and stability responses are equally important to measure – an increase in stability relative to CTCB 405 suggests the PFK/inhibitor complex is more stable as a result of favourable binding interactions with the enzyme. The importance in measuring both parameters in single point screening is exemplified by the varying responses for compound CTCB 482 shown in **figure 6.14**. CTCB 482 had a strong binding response against *Tb*PFK (**figure 6.14A**), but a poor stability score (**figure 6.14B**). CTCB 482 is a potent inhibitor of *Tb*PFK – with an IC_{50} of 44 nM (ADP-Glo™ assay). Poor stability does not confer poor chemical interactions between the compound and protein. It may also result from

unfavourable changes in hydration upon compound binding, a lack of conformational freedom in the compound or from tethering of PFK to a surface effecting the binding.

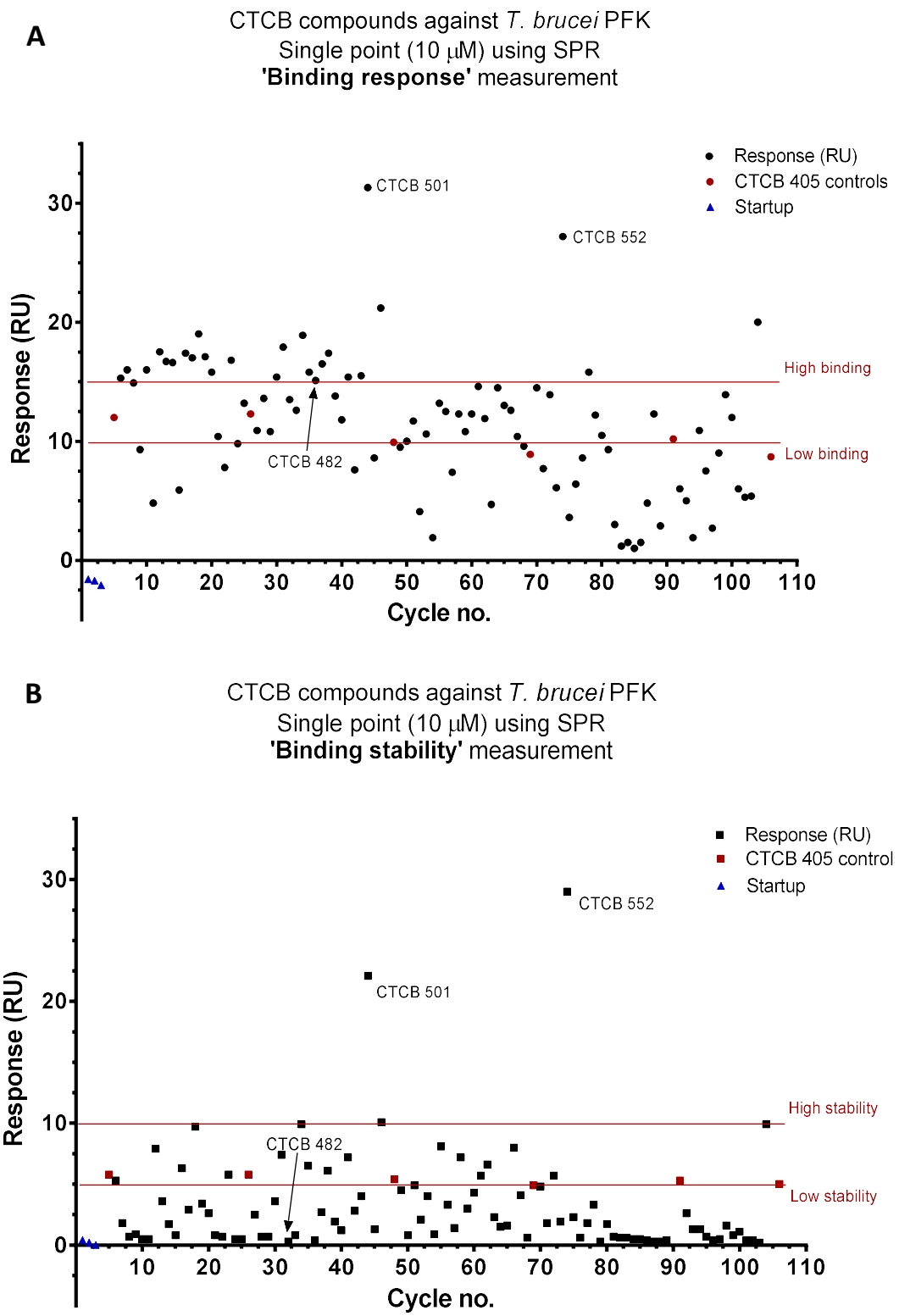

Figure 6.14: CTCB compound single point ranking in SPR.

Batch of 93 CTCB compounds tested at a single concentration (10 µM) against low density (1,500 RU) T. brucei PFK surface using SPR. CTCB 405 was used as a control at a concentration of 10 µM. ***A****) Shows molecular weight-corrected binding responses.* ***B****) Shows the binding 'stability' measurement for the same compounds.*

6.3. Discussion : Ranking CTCB compounds using primary assays and SPR.

We have described the development and use of two excellent primary assays for compound ranking against *Tb*PFK. Both the PYK/LDH and ADP-Glo™ assays had excellent Z-prime values (0.57 and 0.63 respectively) resulting from reproducibility in IC_{50} measurements, reliable controls and good signal-to-noise ratios. Compound IC_{50} values correlated well with both PFK binding affinity (through SPR measurements) and parasite death (EC_{50} values), confirming that binding and inhibition of *T. brucei* PFK translated to effective parasite killing. Observed discrepancies in IC_{50} values between the orthogonal assays for some compounds did not result from a single controllable factor. Correlation between assays however was acceptable for the majority of compounds, and only a minority of compounds had significant discrepancies. Changing the protocol to account for potential discrepancies was unfeasible, considering there was not one unifying variable that was responsible for the discrepancies seen. The need for at least 2 orthogonal assays in inhibitor ranking is therefore important. Coupled with cross-checking with other methods such as SPR, false positives or negatives can be avoided. This is paramount in a structure based approached to drug design, as information from initial testing of compounds against the target directly influences the next step in design of the compound. Single point ranking of compounds by both binding response and stability measurements is a quick and effective method of compound ranking provided a reliable ligand surface can be immobilised. As will be discussed in **section 6.4.3**, single point stability measurements can be used to estimate off rates. SPR therefore is an invaluable tool in the ranking and initial characterisation of binding for small molecules against a target. It allows large batches of compounds to be tested simultaneously. For smaller scale, week-to-week compound testing and ranking, the two primary assays described in this section are quick and reliable.

6.4. Biophysical Characterisation of CTCB inhibitor compounds.

Following ranking by potency against the enzyme and cultured parasites, biophysical characterisation of CTCB compound binding to *T. brucei* PFK was carried out. This work had 3 main aims; To assess the kinetics of CTCB binding with PFK, determine the specificity of binding, and describe the mechanism of binding and inhibition.

6.4.1 Compounds bind T. brucei PFK with high affinity in SPR experiments.

SPR was used as the primary assay for measuring the binding kinetics of CTCB compounds to PFK. The following results were achieved by measuring compound binding against low density (~1500 – 3000 RU) surfaces of *T. brucei* and *T. cruzi* PFKs with N-terminal His_6-tags. Initial SPR experiments were carried out with medium density surfaces (~12000 RU). It was found later however that with the low density surfaces, compound binding sensorgrams were significantly cleaner, fitted 1:1 binding models better, and fewer compounds showed 'multiphasic' binding behaviour. Higher density surfaces have a greater proportion of heterogeneous binding orientations. The binding response of these populations can add artefacts to the sensorgram, giving false evidence of multiphasic binding, affecting the fit of 1:1 models to the data.

To measure the kinetic parameters in SPR, eight 2-fold serial dilutions of the compounds (12.5 µM – 6 nM) were carried out in running buffer (10 mM HEPES, 150 mM NaCl, 0.05 % P20, 1 % DMSO, pH 7.4). Each concentration was run against a *T. brucei* His_6-tagged PFK surface of 1500 - 3,100 RU and a *T. cruzi* PFK surface of 1500 RU. Compounds were washed over the surface at 30 $\mu l.min^{-1}$ with a 15 second contact time before being washed off for 60 seconds with running buffer. **Figure 6.15** shows a typical sensorgram trace with 1:1 binding model applied for CTCB 531 against *T. brucei.* The Chi^2 value gives an estimation of the goodness of fit of the 1:1 binding model to the measured sensorgram data. A Chi^2 value below 2.0 is considered an acceptable fit.

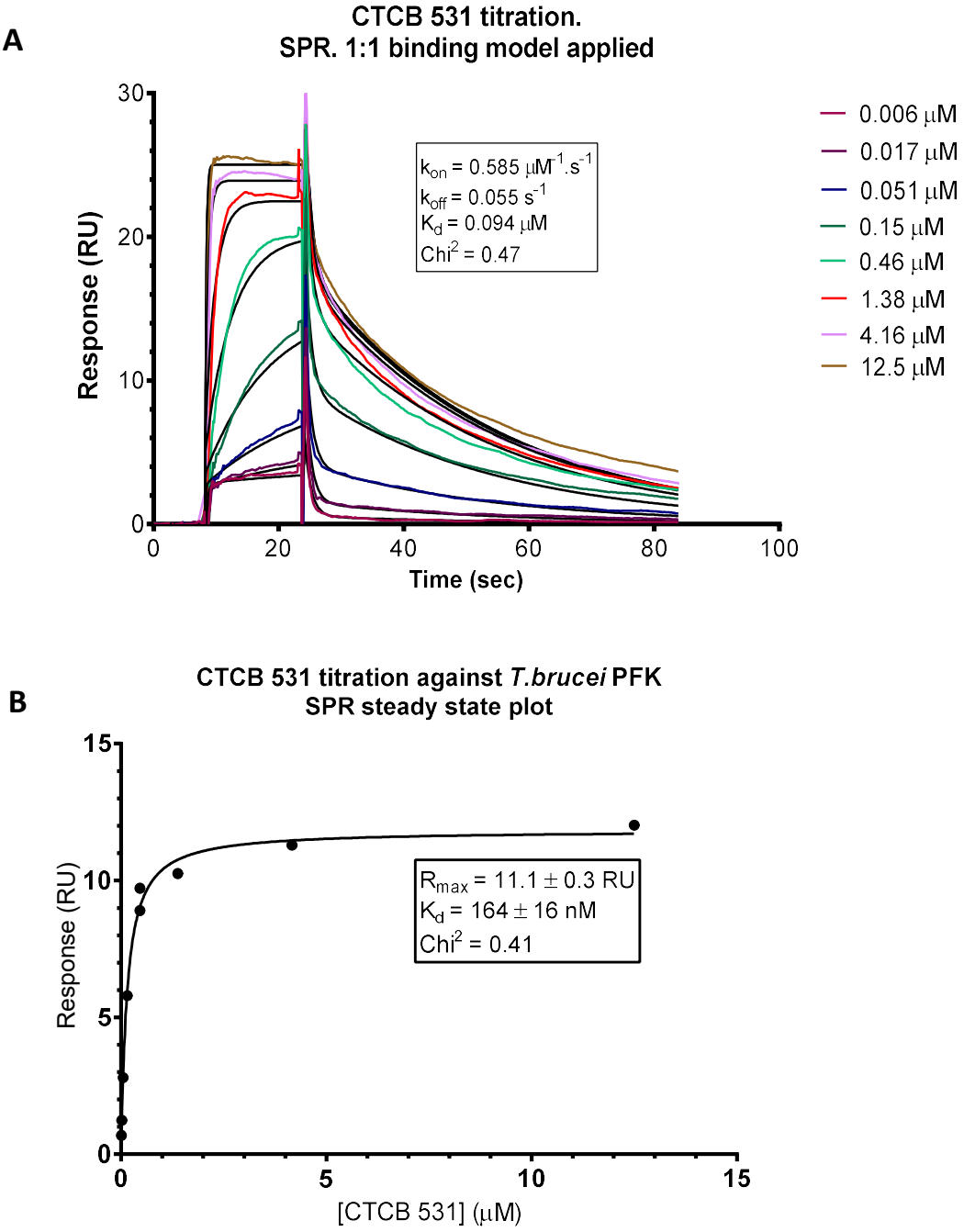

Figure 6.15: CTCB 531 is a tight binder of PFK - as measured in SPR.

CTCB 531 titration (12.5 µM – 6 nM) against a low density (~1500 RU) T. brucei PFK surface measured in SPR. ***A****) Sensorgram for CTCB 531 titration with 1:1 binding model applied (black).* ***B****) Plot of steady state responses of CTCB 531 titration against T. brucei PFK surface. 0.46 µM concentration was repeated as control to test reproducibility surface response. Standard errors are given.*

The calculated binding parameters for a range of tight binding CTCB compounds against a low density (3100 RU) *T. brucei* PFK surface are given in **table 6.3.** Both steady state (SS) and kinetic K_d values from 1:1 binding fits have been given. IC_{50} values as measured by the ADP-Glo™ assay are also given. While not directly comparable, the affinities (K_d) of the compounds as measured by SPR closely match the IC_{50} values of the compounds. There are of course some exceptions; CTCB 486 for example is a potent inhibitor of *T. brucei* PFK (IC_{50} = 92 nM). It had a proportionally poor affinity (874 nM or 470 nM) as measured from either kinetic or steady state plots in SPR. This may be a result of comparing the inhibition of PFK in free solution against when it is covalently tethered to the SPR chip surface. However, as can be seen in **table 6.3** each of the reported compounds are structurally similar, with only slight differences in the side chains, and each binds in a similar orientation (per. comm. Iain McNae UoE). *Tb*PFK was uniformly orientated to the N-terminal his_6-tag during surface generation. Despite a uniformity in PFK orientation on the SPR chip surface, dynamic loops that may be sterically hindered or interrupted from tethering the PFK tetramer to the surface and thus may result in lower affinity when measured. CTCB 486 has the longest side chain of the compounds shown in **table 6.3** - increasing the chance of interactions with these dynamic loops that form a lid over the CTCB binding pocket. This may explain the discrepancy between SPR-measured K_d and IC_{50} values for compounds such as CTCB 486. Again the importance of a number of measures of inhibition and binding when selecting compounds is of high importance in high throughput screening, to avoid false negatives or positives.

		SS		Kinetic			
Compound	**ADP-Glo™ IC_{50} (µM)**	**K_d (µM)**	**Chi^2**	**K_d (µM)**	**k_{on} ($µM^{-1}.s^{-1}$)**	**k_{off} (s^{-1})**	**Chi^2**
CTCB 405 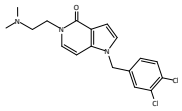	**0.197**	**0.093**	0.05	**0.082**	0.958	0.079	0.41
CTCB 531 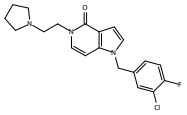	**0.139**	**0.164**	0.17	**0.094**	0.585	0.055	0.47
CTCB 470 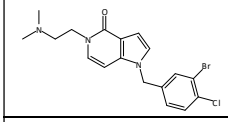	**0.216**	**0.203**	2.84	**0.173**	0.156	0.027	1.34
CTCB 540 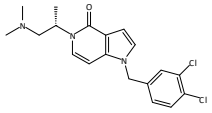	**0.650**	**0.311**	2.01	**0.120**	0.217	0.026	1.22
CTCB 480 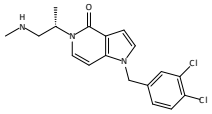	**0.199**	**0.217**	1.07	**0.154**	0.265	0.041	1.63
CTCB 460 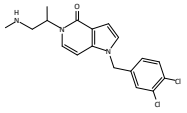	**0.105**	**0.237**	1.16	**0.165**	0.381	0.063	1.63
CTCB 461 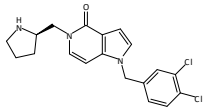	**0.319**	**0.330**	1.80	**0.301**	0.595	0.179	1.48
CTCB 486 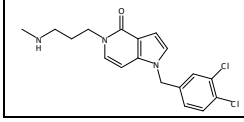	**0.092**	**0.874**	0.69	**1.06**	0.443	0.470	0.30

Table 6.3: Kinetic parameters for a range of CTCB compounds against a T. brucei PFK surface in SPR.

Kinetic values were measured from titrations of CTCB compounds tested against a low density (3,200 RU) T. brucei PFK surface. 'SS' = steady state measurements. Chi^2 relates to goodness of fit of steady state plots ('SS') and the 1:1 binding model to measured data ('kinetic').

6.4.2 CTCB compound affinities are driven by dissociation rates.

The range in affinities (K_d) of the CTCB compounds results from varying dissociation rates (k_{off}). This is shown in **figure 6.16,** where association and dissociation rate constants have been plotted against affinity constants for a batch of CTCB compounds against *T. brucei* PFK as measured using SPR. The association constants of CTCB compounds with a range of affinities stay relatively constant (~0.5 $\mu M^{-1}.s^{-1}$), while the dissociation rate constants drop (dissociation of the PFK/CTCB complex is slower) as the affinity increases. Unlike association constants (k_{on}), dissociation constants are not a function of compound concentration, but of the stability of the compound/protein complex in the absence of free compound. Provided the 1:1 interaction model is a good fit, decreasing kinetic K_{off} measurements from SPR are therefore a good measure of favourable binding interactions with the target, and are important measurements for rational drug design.

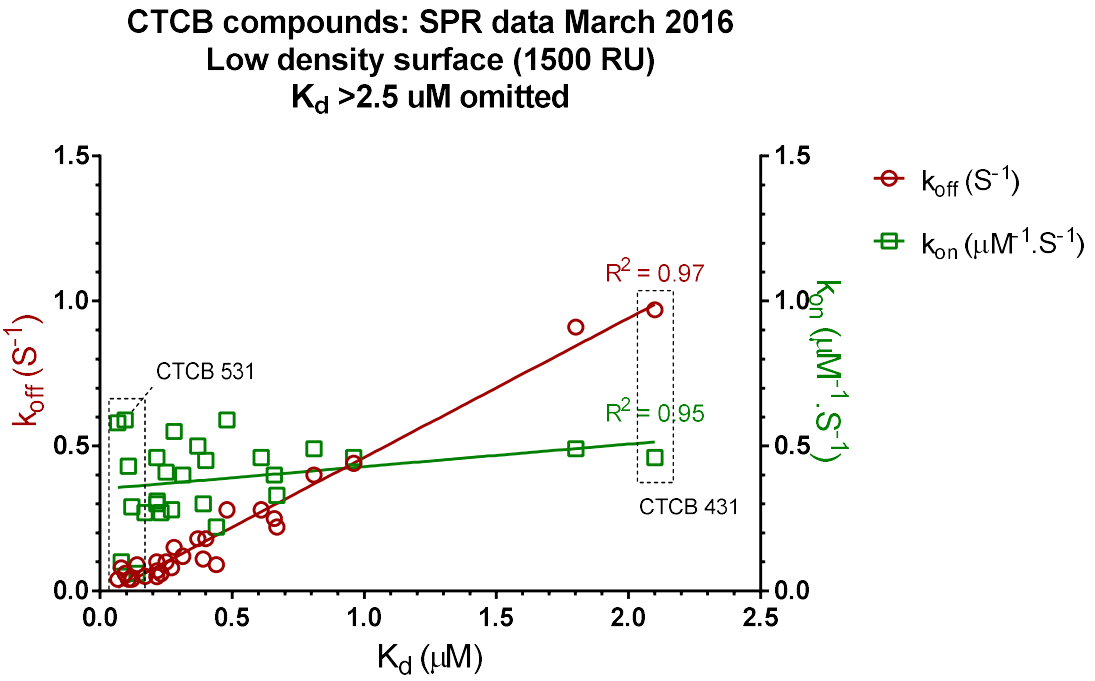

Figure 6.16: CTCB compound affinities are driven by dissociation rates (k_{off}).

Association (k_{on}) and dissociation (k_{off}) rate constants plotted against compound affinities (K_d) for 28 CTCB compounds tested against a low density (3100 RU) T. brucei PFK surface using SPR. A line of best fit has been applied to both the association constant and dissociation constant data sets. CTCB 431 and '531 have been boxed and labelled.

6.4.2.1 Properties determining slow and fast dissociation rates.

No correlation was observed when SPR-derived dissociation rates (k_{off}) were plotted against compound molecular weight, pKa or pKb (data not shown). An interesting observation was made however when comparing two compounds at opposite ends of the spectrum of dissociation rates shown in **figure 6.16**; CTCB 531 (k_{off} = 0.055 s^{-1}) and CTCB 431 (k_{off} = 0.971 s^{-1}) differ only by the replacement if a chlorine atom with a fluorine on the dihalo-benzyl ring (**table 6.4**).

	k_{on} ($\mu M^{-1}.s^{-1}$)	k_{off} (s^{-1})	K_d (μM)
CTCB 431 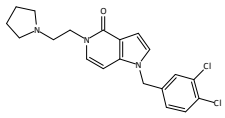	0.460	**0.971**	2.110
CTCB 531 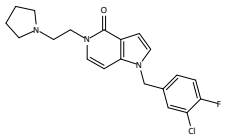	0.585	**0.055**	0.094
CTCB 589 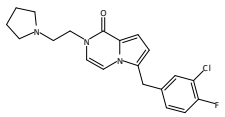	0.490	**0.052**	0.106

Table 6.4: Could the dilaho-benzyl ring define compound dissociation rates?

Both CTCB 589 and CTCB 531 with the chloro-fluoro- group in place of chloro-chloro have significantly slower dissociation rates over CTCB 431. While chemically the chlorine and fluorine atoms will bind with similar Van der Waals interactions in the pocket, changes to the hydration shell in the pocket and/or the rotational degrees of freedom of the compound in the pocket may contribute to the differing dissociation rates due to the difference in atomic size. No other comparisons could be made due to insufficient SPR data to compare more than a pair of compounds with differences in the dihalo-benzyl ring.

6.4.3 Dissociation constants can be estimated from single point measurements in SPR.

Estimated dissociation constants (k_{off}^{est}) were calculated for CTCB compounds using single point binding stability measurements and the known kinetic data for CTCB 405; Stability measurements are a measure of the response 5 seconds after the compound has started to be washed off the chip, during the dissociation phase. During this phase dissociation of the protein/inhibitor complex is not determined by concentration; k_{off} can be estimated from a single concentration when compared to a known dissociation constant for a similar compound (CTCB 405). The ratio between stability measurements of the control compound CTCB 405 and another compound must be proportional with the ratio of dissociation constants, provided association rates are similar (which they are – see **section 6.4.2**). The estimated dissociation constant for a compound 'X' is therefore given as:

$$koff(est)\ Cmpd\ X\ = \frac{Koff\ CTCB\ 405}{(Stability\ CTCB\ 405 : Stability\ cmpd\ X)}$$

As shown in **figure 6.17**, there is good correlation between estimated and measured dissociation constants for a range of CTCB compounds tested. This is a useful tool for accurately estimating dissociation rate constants for compounds, when time or other resources prevent full kinetic characterisation in SPR.

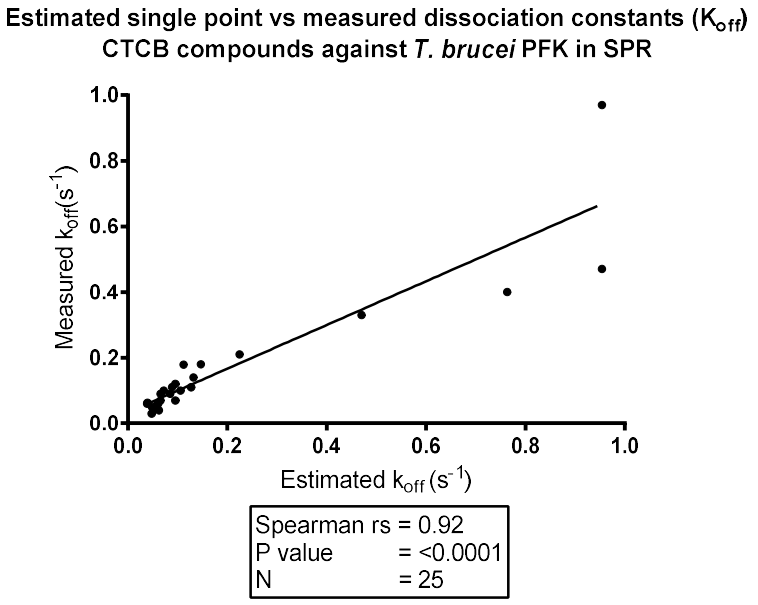

Figure 6.17: Dissociation constants can be accurately estimated from single point measurements.

Correlation plot of dissociation constants estimated from single concentration (10 µM) 'stability' measurements of CTCB compounds, plotted against measured dissociation constants from serial compound titrations. Tested against a low density (3100 RU) TbPFK surface using SPR.

6.4.4 CTCB compounds are not promiscuous binders.

HSA is a monomeric protein with multiple roles involving carrying, holding or transporting toxins, proteins and small biomolecules in the bloodstream (Fasano et al., 2005). HSA has a multitude of clefts, but two main drug binding sites – named 'Sudlow's sites' I and II - bind a number of commonly known drugs such as Warfarin and Ibuprofen, respectively. The abundance and binding abilities of HSA in the blood make it an obvious first hurdle to clear when it comes to effective pharmacokinetic design of drug molecules – promiscuous compounds will be bound by HSA, reducing the bioavailability of the drug in the bloodstream.

To test for general promiscuity in CTCB compound binding, an SPR chip was prepared with a reference cell, a *T. brucei* PFK surface and a surface of human serum albumin (HSA). See **section 2.5.3.4** for a full protocol. A homogenous HSA surface was made using fatty acid and globulin-free human serum albumin, coupled using standard amine coupling methods (GE Healthcare, n.d.). The final HSA surface had a density of 12,600 RU. CTCB compounds were first tested against the HSA surface as single point concentrations (50 µM) in running buffer (10 mM HEPES, 150 mM NaCl, 0.05 % P20, 1 % DMSO, pH 7.4), with CTCB 001 repeated as a standard control. Serial dilutions of selected compounds (titration of 50 - 0.39 µM compound) were then tested against the surface to generate steady state K_d values against the HSA surface. Warfarin was used as a positive control for HSA binding. **Figure 6.18** shows the single point binding responses of 46 CTCB compounds, with steady state K_d values given in brackets as a reference.

The standard compound (CTCB 001) had a surprisingly high affinity for the HSA surface (K_d = 48 µM), however as can be seen in **figure 6.18** the remainder of the CTCB compounds tested had very low affinities (>100 µM) for HSA. The calculated steady state affinity for the positive control Warfarin was 12 ± 3 µM, in agreement with published affinities for HSA (19 – 39 µM) (Wybranowski, Cyrankiewicz, and Ziomkowska, 2008).

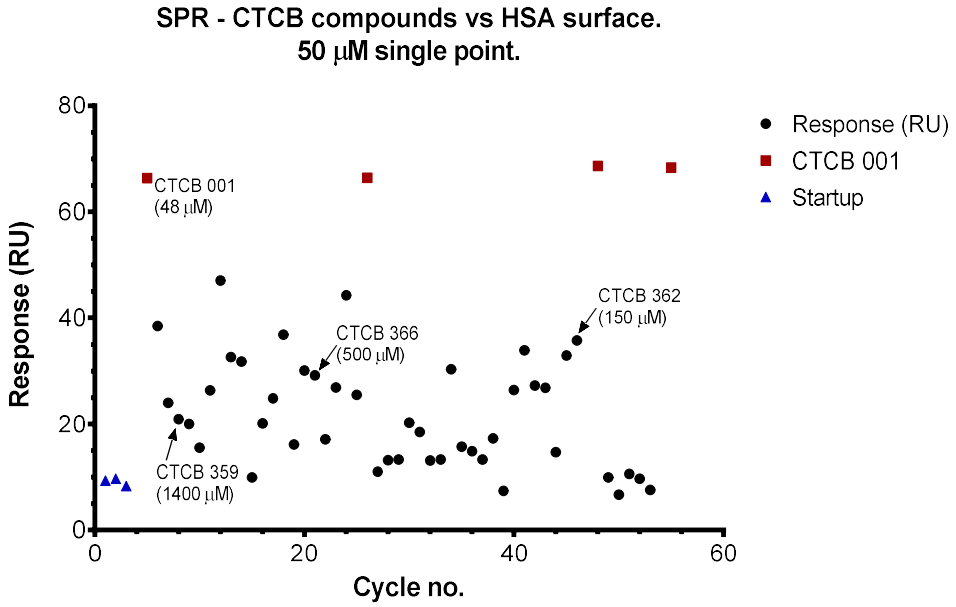

Figure 6.18: CTCB compounds bind very weakly to human serum albumin (HSA).

Molecular weight-corrected responses of CTCB compounds (black dots) tested at 50 μM against human serum albumin surface (12,600 RU). CTCB 001 (red squares) was repeated to test quality of surface. Numbers in brackets correspond to steady-state affinity (K_d) of compound when tested against the same HSA surface as a 2-fold serial dilution.

Measured affinities of CTCB compounds for HSA were plotted against available mouse plasma protein binding data and showed a correlation between affinity for HSA and plasma protein binding (**figure 6.19**).

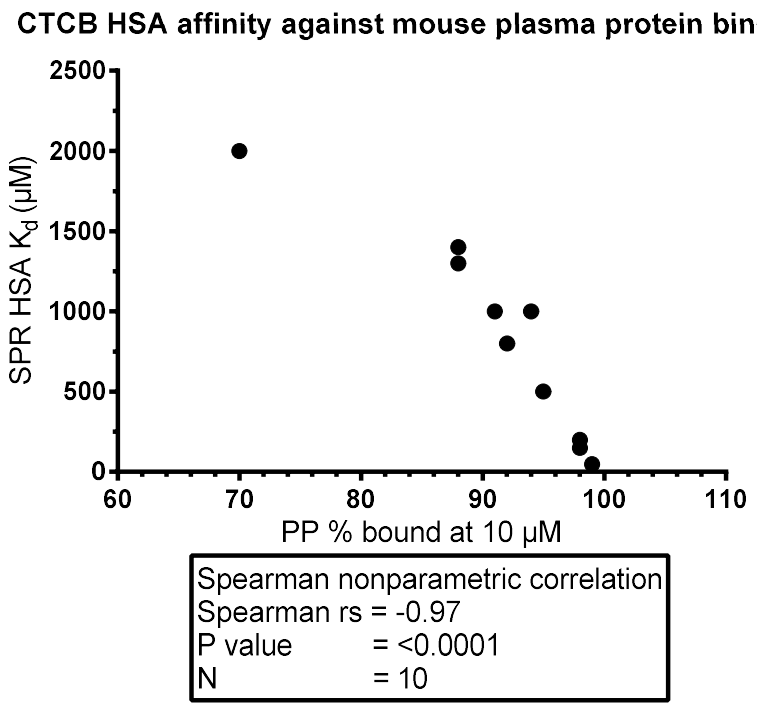

Figure 6.19: CTCB compound affinity for HSA correlates with mouse plasma protein binding.

Steady state affinity (K_d) values measured using SPR against an immobilised surface of human serum albumin (HSA). Corresponding plasma protein binding values measured at a concentration of 10 µM compound in mouse plasma.

6.4.5 Thermodynamics of CTCB compound binding using SPR.

The thermodynamics of binding for three tight binding CTCB compounds was investigated using SPR. This was achieved through titrations of compound against a *T. brucei* PFK surface (3,000 RU) at 13 temperatures ranging from 5 – 41 °C. This was carried out for compounds CTCB 405, '470 and '589. Kinetic K_d values were calculated from 1:1 binding models applied to the sensorgrams at each temperature. **Figure 6.20** shows the data obtained for CTCB 405.

The affinity constants K_d measured at each temperature are related to the enthalpy and entropy changes of the reaction through the equation for Gibbs free energy;

$$\Delta G = -RTInK \text{ and } \Delta G = \Delta H - T\Delta S$$

Where K = K_d , R = gas constant (taken as 8.314 J/mol-K) and T = temperature (Kelvin). The temperature dependence on changes in free energy can described and plotted according to the van't Hoff equation (Perozzo, Folkers, & Scapozza, 2004a):

$$InK_d = \left(\frac{\Delta H^\circ}{RT}\right) - \left(\frac{\Delta S^\circ}{R}\right) \quad \text{van't Hoff equation}$$

Where K_d = equilibrium dissociation constant, R = universal gas constant, T = absolute temperature (K) ΔH° = entropy change and ΔS° = entropy change.

A van't Hoff plot, like that shown for CTCB 405 in **figure 6.20** can then be used to calculate the enthalpic contribution (ΔH°) – by taking the slope of the plot which gives $\Delta H^\circ/R$. The entropic contribution (ΔS°) can be measured by taking the y-axis intercept, which gives $\Delta S^\circ/R$. With these parameters the free energy (ΔG°) can be calculated. The enthalpic, entropic and free energy parameters calculated for CTCB 405, '470 and '589 are shown in **table 6.5**.

A

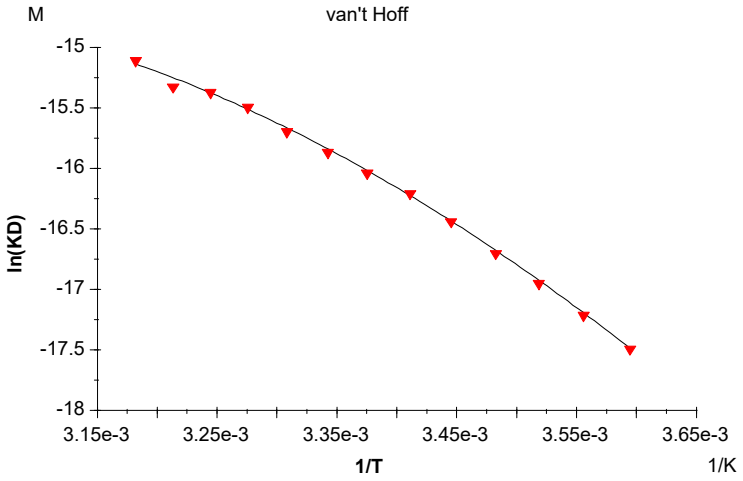

B

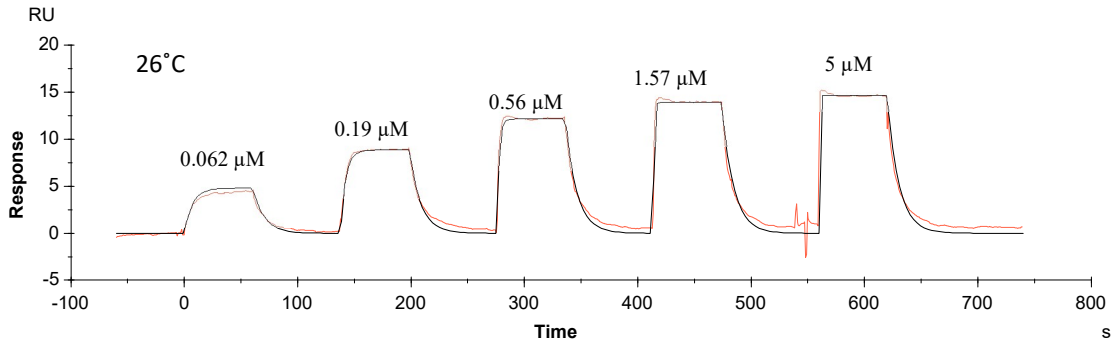

C

Temp. (°C)	5	8	11	14	17	20	23	26	29	32
K_d (nM)	25.5	33.8	43.8	56.4	73.1	92.7	109	131	153	189
K_{on} ($\mu M^{-1}.s^{-1}$)	0.21	0.24	0.31	0.34	0.41	0.50	0.62	0.77	0.89	1.10
K_{off} ($x10^{-3}\ s^{-1}$)	5	8	13.5	19.1	30	46.7	67.8	98.2	136	211

Figure 6.20 Thermodynamics of CTCB compound binding measured by SPR.

Thermodynamic profiling of CTCB 405 binding to T. brucei PFK surface in SPR. ***A****) Van't Hoff thermodynamic plot* ***B****) Sensorgram traces for CTCB 405 (red) measured at 26 °C with 1:1 binding model (black) fitted.* ***C****) Kinetic parameters for CTCB 405 at each temperature tested. Data for 35, 38 and 41 °C have been omitted.*

	K_d (nM)	ΔG° (kcal.mol^{-1})	ΔH° (kcal.mol^{-1})	TΔS° (kcal.mol^{-1})	ΔCp (kcal.K^{-1}.mol^{-1})
CTCB 405	113	-9.48	-10.77	-1.29	0.24
CTCB 470	130	-9.40	-11.24	-1.84	0.26
CTCB 589	106	-9.520	-11.72	-2.20	0.22

Table 6.5: Thermodynamic parameters for CTCB compounds binding to T. brucei PFK in SPR.

Data measured from CTCB compound titrations (5 µM – 62 nM) against low density T. brucei PFK surface (3100 RU) using SPR. Parameters calculated from van't Hoff analysis curves. All parameters relate to thermodynamics of binding at 26 °C.

As expected from a biological system, the ΔG° values for all three compounds are the same (~9.5 Kcal.mol^{-1}), with different enthalpic and entropic contributions. As the CTCB compounds tested have similar affinities and bind in the same pocket, a constant ΔG° value is expected. ΔCp is a measurement of the change in heat capacity for the system – it tells us how much heat is added to the system per unit temperature rise. For the compounds above, ΔCp has a positive value, suggesting that upon binding there is a movement of charged or polar groups. A negative ΔCp value suggests a hydrophobic group has been moved during binding (Perozzo, Folkers, & Scapozza, 2004b). This ΔCp value contributes very little, but is important to include when calculating the ΔG° of the system. Taking ΔCp into consider the equation for calculating free energy becomes:

$$RTInK_d = \Delta H°_{T°} - T\Delta S°_{T°} + \Delta Cp°(T - T_o) - T\Delta Cp°In(\frac{T}{T_o})$$

Where ΔCp° = change in heat capacity and T_o is the reference temperature (298K) (Martin A. Wear et al., 2017). This is the equation used to calculate ΔG° values as shown in **table 6.5**.

6.4.6 CTCB compounds bind T. brucei PFK in a 1:1 stoichiometry.

CTCB compounds tested against *Tb*PFK in SPR fitted 1:1 binding models well, with Chi^2 values for the fit of <2.0. To comprehensively confirm this binding stoichiometry and to characterise the thermodynamics of binding, compounds were also tested using Isothermal Titration Calorimetry (ITC) experiments. ITC measures the change of heat upon the binding of analyte to ligand in a thermally isolated (adiabatic) cell. The apparatus includes two cells: a sample cell containing the macromolecule(PFK) and a reference cell. The ligand (CTCB compound) is held in a syringe and titrated into the sample cell. A constant power is applied to the reference cell and acts as a feedback circuit to the sample cell. This maintains the two cells at the same temperature (ΔT=0). Upon binding of ligand to protein, heat is given out or taken in. This temperature difference between the cells is detected by a calorimeter and the power applied to the sample cell is adjusted accordingly. The power used to maintain ΔT = 0 between the cells is the baseline. The change in reference power upon ligand and analyte interaction is measured as peaks (in endothermic reactions) or troughs (exothermic) showing the change in 'reference power' over time (µcal/sec). The heat evolved or absorbed during binding is quantified by integration of these peaks (**figure 6.21**)(Holdgate, 2001). ITC offers the ability to directly measure the enthalpy change from binding. As well as this ITC can be used to simultaneously measure the molar ratio (stoichiometry), the binding constant (K_d) and entropy change (ΔS°) upon binding of ligand to protein.

To carry out thermodynamic characterisation of CTCB compounds binding to *T. brucei* PFK using ITC, compounds were titrated into a cell containing a solution of PFK (**Figure 6.21**).

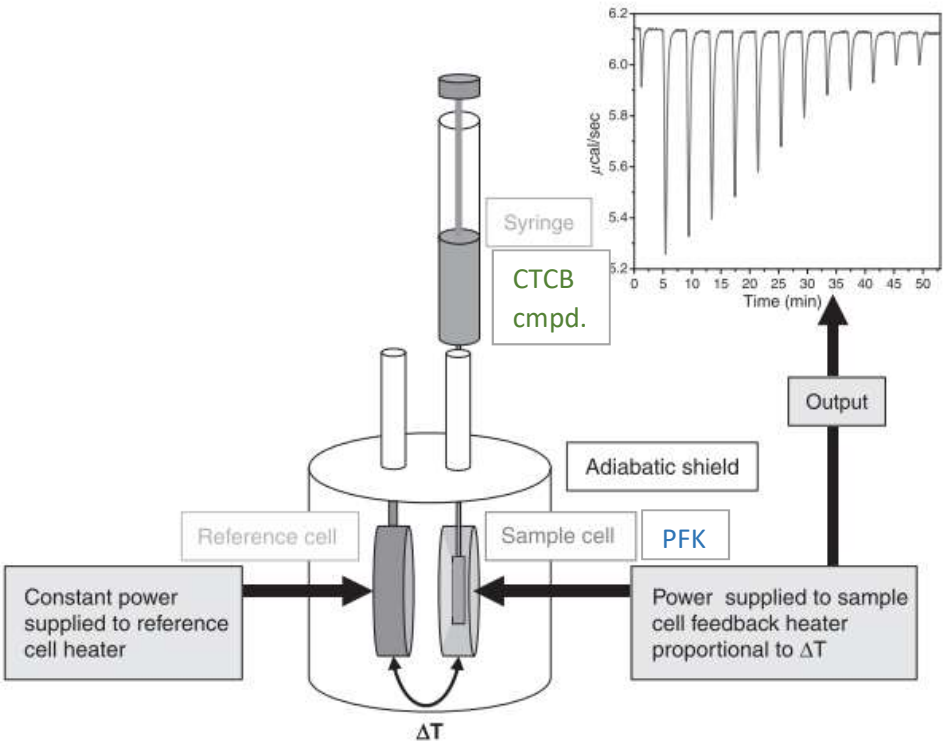

Figure 6.21 : ITC assay schematic.

CTCB compound is titrated into a cell containing PFK. The change in temperature ΔT is accurately measured by measuring the power (µcal/sec) required maintain temperature between the sample and reference cells so that ΔT=0. Image adapted from Freyer & Lewis, 2008.

The following ITC results were carried out in HBS buffer (10 mM HEPES, 150 mM NaCl, 0.005% p20, pH 7.4, 1% DMSO). Proteins stocks were desalted (HiTrap 5ml Desalting column, GE Heathlcare) with the above buffer to ensure minimal buffer mismatch between ligand and analyte when injected. Solubility limits for all compounds were tested in this HBS buffer system prior to ITC experiments. This buffer system matched that used in the SPR experiments. CTCB compound titrations consisted of 16 injections with 180 second delay between injections and 750 rpm stirring at 25 °C. All solutions were degassed prior to use. A full protocol can be seen in **section 2.5.4**. Controls included:

- Injection of each CTCB compound into buffer - to assess heat of dilution of ligand.
- Injection of buffer into protein – measure heat of dilution of analyte (this is generally negligible as protein diluted by < 20%).

- Injection of buffer into buffer – an instrument blank. Generally negligible.

For the data show below the heat of dilution is negligible. Data for the first injection in each experiment was omitted. Data was analysed using a 'one-site' model assuming one binding site (one compound molecule per *Tb*PFK monomer) using the dedicated MicroCal analysis software. Details of ITC data analysis can be found in **section 2.5.4.1.**

The CTCB compounds performed well in ITC. The compound titrations had minimal baseline noise, heat of dilution, no evidence of buffer mismatch and relatively large heat changes for noncovalent binding interactions - greater than the average value of 5 – 10 Kcal mol^{-1} (Perozzo et al., 2004b) . **Figure 6.22** shows an example trace for CTCB 405 titrated against *Tb*PFK.

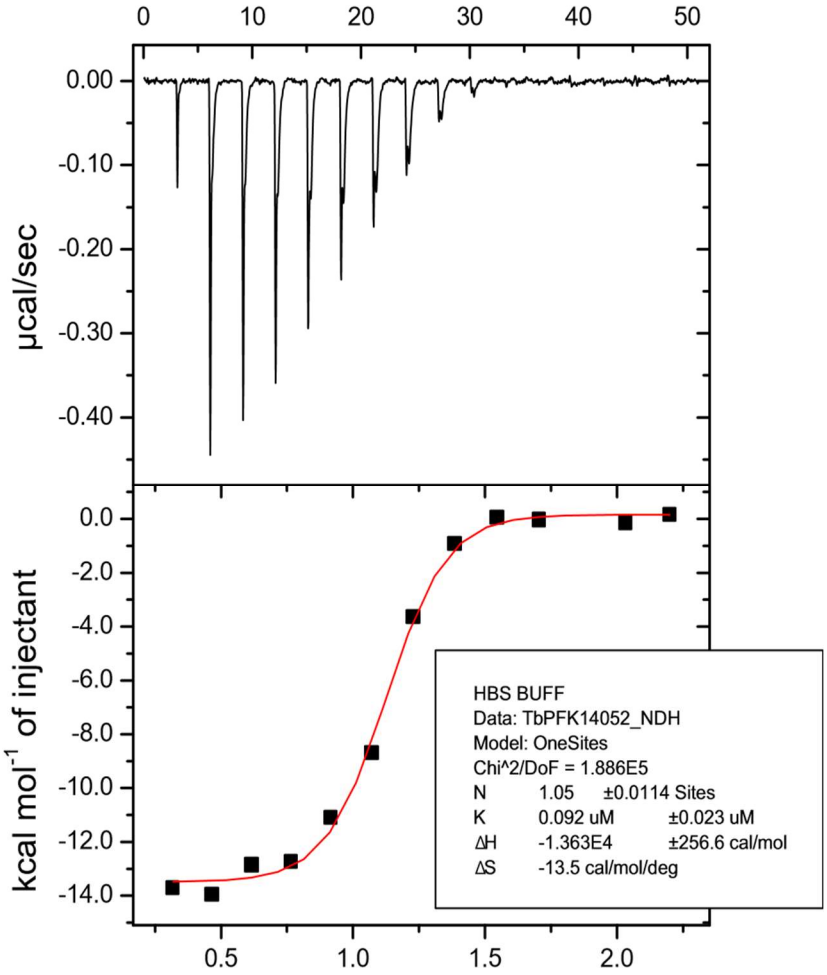

Figure 6.22: CTCB 405 binds PFK in a 1:1 stoichiometry as measured by ITC.

ITC trace of titration of 150 µM CTCB 405 into 12.8 µM T. brucei PFK at 25 °C. Top panel shows raw ITC trace for each injection (thermogram), starting from highest to lowest injections of compound (left to right). Bottom panel shows integrated data of each injection (Kcal/mol) (Y-axis) against the molar ratio (X axis) with non-linear regression (one-site model) fitted.

Binding stoichiometry can be determined from the molar ratio of compound: protein at the equivalence point of the ITC curve. For all of the CTCB compounds where a reliable trace was measured, the compounds bound with an almost perfect 1:1 stoichiometry with *T. brucei* PFK. **Table 6.6** shows the results of all compounds plotted.

Measured K_d values match nicely with those measured in SPR (see **table 6.3, section 6.4.1**). Measured free energy contributions (ΔG°) are also in agreement with those calculated from SPR thermodynamic profiling for CTCB 405, '470 and '589 via van't Hoff analysis (**table 6.5**), and within the typical range for drug-like molecules (-7 to -12 Kcal/mol)(Holdgate, 2001). All compounds tested bound with negative ΔH° and ΔS° contributions – suggesting CTCB compound binding with *Tb*PFK has favourable hydrogen bonding and hydrophobic interactions (Freyer & Lewis, 2008). These also agreed with the average ΔH° and TΔS° values for drug-like molecules of -19 to +20 Kcal/mol and -14 to +10 Kcal/mol respectively (Holdgate, 2001). All of the compounds tested in ITC possessed the azaindole scaffold and thus bind in roughly the same orientation, so the similarity in Gibbs free energy (ΔG°) contributions is to be expected (see **section 6.6.1**).

The thermodynamic parameters for CTCB 480 and 481, which represent the enantiomers of a single compound are similar, highlighting the sensitivity and reliability of the assay.

	Molar ratio (N)	K_d (µM)	ΔH° (kcal.mol^{-1})	TΔS° (Kcal.mol^{-1})	ΔG° (Kcal.mol^{-1})
CTCB 405 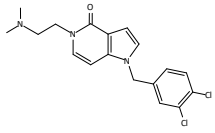	**1.05 ± 0.02**	**0.092 ± 0.002**	**-13.6 ± 0.26**	**-4.03**	**-9.57**
CTCB 421 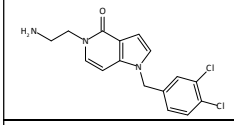	1.12 ± 0.03	0.370 ± 0.43	-2.6 ± 0.17	6.17	-8.77
CTCB 435 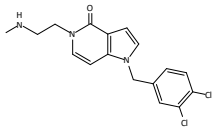	1.01 ± 0.02	0.215 ± 0.09	-14.4 ± 0.13	-6.01	-8.6
CTCB 470 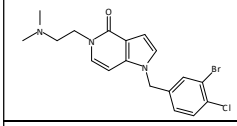	**1.24 ± 0.02**	**0.218 ± 0.06**	**-9.53 ± 0.23**	**-0.44**	**-9.09**
CTCB 480 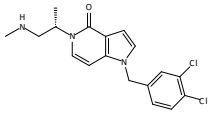	1.04 ± 0.01	0.204 ± 0.08	-14.2 ± 0.18	-5.09	-9.11
CTCB 481 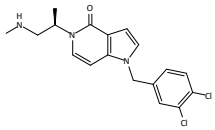	1.02 ± 0.01	0172 ± 0.08	-14.1 ± 0.17	-4.98	-9.12
CTCB 531 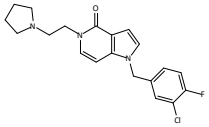	1.28 ± .01	0.158 ± 0.05	-11.5 ± 0.11	-2.24	-9.26
CTCB 589 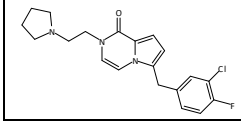	**1.20 ± 0.01**	**0.090 ± 0.02**	**-11.3 ± 0.17**	**-1.66**	**-9.64**

Table 6.6: Thermodynamic parameters of CTCB compounds measured by ITC against T. brucei PFK.

All experiments carried out at 25 °C in HBS buffer (10 mM HEPES, 150 mM NaCl, 0.005% p20, pH 7.4, 1% DMSO). Data calculated from 'one site' binding model plots (MicroCal™ Origin® analysis software). ΔG° values have been calculated using the equation $\Delta G = \Delta H - T\Delta S$, *given T = 298.15 K.*

6.4.6.1 Normalised ITC thermodynamics are more accurate.

To allow for a better comparison between compounds and with SPR-derived thermodynamic values, ΔH°, ΔS° and ΔG° were normalised for a fixed stoichiometry of 1.0. This involved re-plotting the ITC data and adjusting assumed syringe (compound) concentration until a stoichiometry of 1 ± 0.05 was achieved. This assumed that there was no error in *Tb*PFK concentration between assays (likely as the same working stock of protein was used for all assays) but rather an error in the absolute compound concentration. All ITC assays were carried out over a 48 hour period. The normalised thermodynamic parameters for CTCB 405, 470 and 589 binding with *Tb*PFK are given in **table 6.7**. See **table 6.6** for comparison (compounds in bold).

	K_d (μM)	**ΔH° (kcal.mol^{-1})**	**TΔS° (Kcal.mol^{-1})**	**ΔG° (Kcal.mol^{-1})**
CTCB 405	0.092 ± 0.002	-13.5 ± 0.25	-4.03	-9.58
CTCB 470	0.588 ± 0.13	-14.9 ± 0.25	-5.66	-9.24
CTCB 589	0.114 ± 0.02	-13.3 ± 0.20	-3.67	-9.63

Table 6.7 : normalised ITC thermodynamic values for CTCB 405, 470 and 589.

Normalising the ITC fits to achieve a stoichiometry of 1.0 had a significant effect on the ΔH° value for CTCB 470 and 589. The thermodynamic parameters calculated for these two compounds shown in **table 6.6** were calculated with fits showing stoichiometries of 1.24 and 1.20 respectively. PFK monomers cannot have 1.2 binding sites, and so by correcting for potential errors in absolute compound concentration to achieve a fit with N fixed to 1.0, the thermodynamic parameters are more accurate and comparable with the values obtained by SPR.

6.5. Discussion: SPR and ITC as biophysical tools in structure-based design.

SPR proved to be a remarkably information rich method of analysing CTCB compound binding. Alongside the two primary assays, SPR was used in compound ranking, estimation of off-rates, steady state and kinetic affinity measurements, analysis of binding stoichiometry and thermodynamic profiling of the inhibitor compounds. Single point assays in SPR offer a fast and accurate method of affinity ranking large batches of compounds. Estimated off rates (k_{off}^{est}) described in **section 6.4.3** were found to be accurate and reliable when compared to the actual data measured from compound titrations. Thermodynamic profiling was carried out for only 3 CTCB compounds, but produced data on enthalpic and entropic measurements and free energy changes (ΔG°) that agreed with those measured by ITC. Thermodynamic profiling is invaluable in structure-based drug design – giving further insights into compound binding beyond basic affinity measurements.

Comparing CTCB 405 and CTCB 470 as an example, we can make further judgments on the drug candidates; CTCB 405 and '470 differ by a bromine replacing a chlorine on the dichloro-benzene ring, as can be seen in **figure 6.23B**. Looking at the thermodynamic profile of the two compounds (**figure 6.23C**) we can see that despite the free energy of binding (ΔG°) being the same for each compound, there is a significantly more negative enthalpic contribution (ΔH°) for CTCB 470 (>1 Kcal/mol, Std. dev. = 0.25 Kcal/mol). Enthalpic contributions result from the release of water molecules and/or from increased interactions such as hydrogen bonding, Van der Waals interactions or salt bridges. As we can see in **figure 6.23D**, the additional electron shell in the bromine of CTCB 470 gives a much larger density in the X-ray structure of the compound bound to *T. brucei* PFK. The Van der Waals radii of chlorine and bromine are 175 pm (1.75 Å) and 185 pm (1.85 Å) respectively. Increased Van der Waals interactions from the bromine of CTCB 470 compared with the chlorine of CTCB 405 may explain the slightly greater enthalpic contribution to binding for '470 over '405.

Entropic changes can contribute either positively (+TΔS°) or negatively (-TΔS°) to the free energy of binding. Entropic changes can arise from a loss in the degrees of freedom in movement of all the molecules involved in the interaction. The more negative TΔS° value for CTCB 470 may be a result of the larger bromine atom restricting movement compared to CTCB 405 due to steric bulk. Combined with the kinetic information given in **figure 6.23C**, we can make the judgement that CTCB 470 may be the better drug candidate over CTCB 405; Despite being a marginally

weaker binder and inhibitor of *T. brucei* PFK (K_D = 173 nM over 82 nM, IC_{50} = 216 nM over 197 of CTCB 405), it has a much slower off rate (0.027 s^{-1} over 0.079 s^{-1}), and will therefore have a longer half life when bound to the PFK target. Added to the thermodynamic information mentioned above, we can see that CTCB 470 is a marginally better drug candidate, with minimal enthalpic penalties to overcome to allow binding. Coupled with inhibition assays, this example shows the power of SPR in assessing multiple parameters in compound binding.

A

CTCB 405

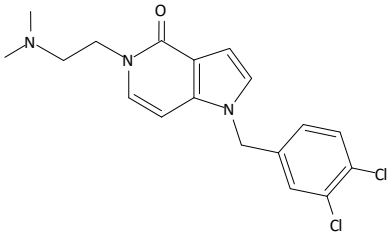

CTCB 470

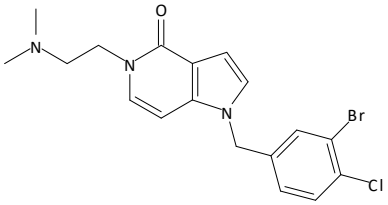

B

SPR thermodynamic profiles:

		ITC/SPR	ITC/SPR	ITC/SPR	
At 26 °C	K_d (nM)	ΔG^o (Kcal.mol^{-1})	ΔH^o (Kcal.mol^{-1})	$T\Delta S^o$ (Kcal.mol^{-1})	ΔC_p (Kcal.mol^{-1})
CTCB 405	113	-9.48 / -9.58	-10.77 / 13.5	-1.29 / -4.03	0.24
CTCB 470	130	-9.40 / -9.24	-11.24 / 14.9	-1.84 / 3.67	0.26

C

SPR / enzyme assay derived affinity and inhibition data:

	k_a ($\mu M^{-1}.s^{-1}$)	k_d (s^{-1})	K_d (μM)	ADP-Glo™ IC_{50} (μM)
CTCB 405	0.958	0.079	0.082	0.197
CTCB 470	0.156	0.027	0.173	0.216

D

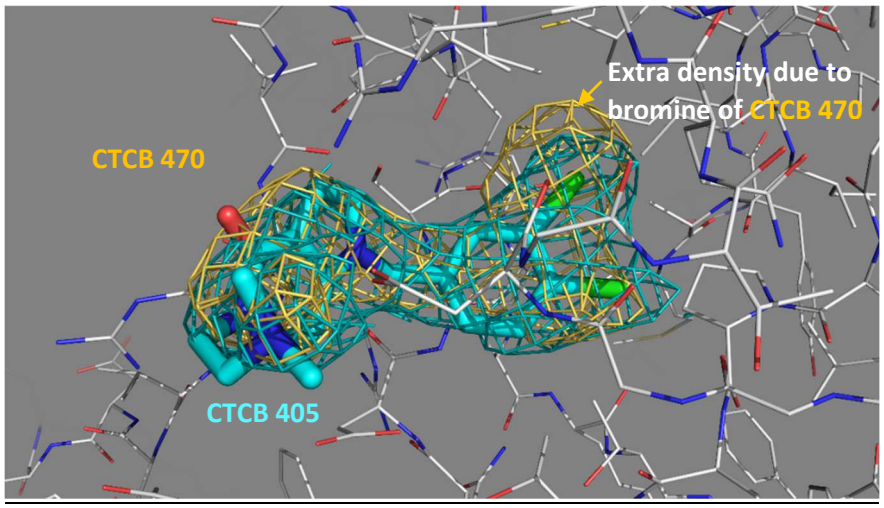

Figure 6.23: Complete analysis of CTCB 405 and '470 compound binding.

A) *Chemical structures of CTCB 405 and '470.* ***B)*** *Thermodynamic parameters from compound binding against TbPFK measured by SPR and ITC.* ***C)*** *Inhibition and kinetic binding data of compounds against TbPFK derived from ADP-Glo™ assay and SPR.* ***D)*** *TbPFK crystal structure (lines) with CTCB 405 bound (Cyan sticks). Density maps for CTCB 405 (cyan mesh) and CTCB 470 (yellow mesh) are also shown.*

6.6. Structural characterisation and mechanism of inhibition.

6.6.1 Binding poses of CTCB compounds.

A number of X-ray structures of *T. brucei* PFK with various CTCB compounds bound have been determined. All structures were solved by Iain McNae of the Walkinshaw Group at the University of Edinburgh. Crystals were obtained by either co-crystallisation or ligand soak methods (Hassell et al., 2006). Diffraction data was collected remotely at the Diamond Light Source synchrotron facility in Oxfordshire.

Fragments

The 3,4-dihalobenze group is fundamental to CTCB compound potency against *T. brucei* PFK. **Figure 6.25** shows the binding position of a fragment – CTCB 012 within the binding pocket of *Tb*PFK. The chlorine on the 4-position of the benzyl ring forms a particularly important 'halogen bond'. Sirimulla et all describe halogen bonds as;

"A short, noncovalent C–X···D–Z interaction, where D is a halogen bond donor, C–X is a carbon-bonded chlorine, bromine, or iodine; D–Z is a carbonyl, hydroxyl, thiol, aromatic ring, charged carboxylate, phosphate group, or amine, and the X···D distance is less than or equal to the sums of the respective van der Waals radii." (Sirimulla, Bailey, Vegesna, & Narayan, 2013).

When covalently bound to a carbon atom, halogens possess a positive nuclear charge as well as a ring of electron density, this allows halogen binding to both an electron *negative* region and a region of *positive* electrostatic potential (Sirimulla et al., 2013). **Figure 6.24** shows the electron density map of a halogen bound to carbon atom.

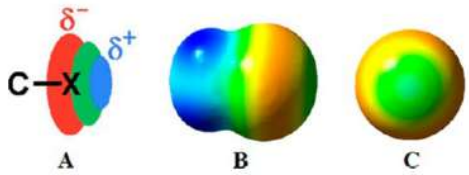

Figure 6.24: When covalently bound, halogen atoms possess electrophilic and electronegative regions.

Image adapted from Sirimulla et. al 2013. A) Representation of electron distribution in bound halogen atom. B+C) Electrostatic potential map of CH_3I molecule. Prepared using 'Gaussian 9' software (Gaussian Inc) by Sirimulla et. al 2013. Blue = positive charge, Red = negative charge.

As a consequence of halogen binding, the chlorine in the 4-position of the benzyl ring of CTCB compounds makes contacts both with the positively charged nitrogen of the backbone of ASP199, and the lone electron pair oxygen on the carbonyl group of GLY197. The chlorine atom in the 3-position of the dichlorbenzyl ring most likely makes purely Van der Waals contacts. Both halogens in the 3- and 4- positions are required and form the basis of CTCB compound binding. The small fragment 3,4-dichloroaniline, when tested against *Tb*PFK had a remarkable IC_{50} of 3.3 µM as measured in the PYK/LDH assay.

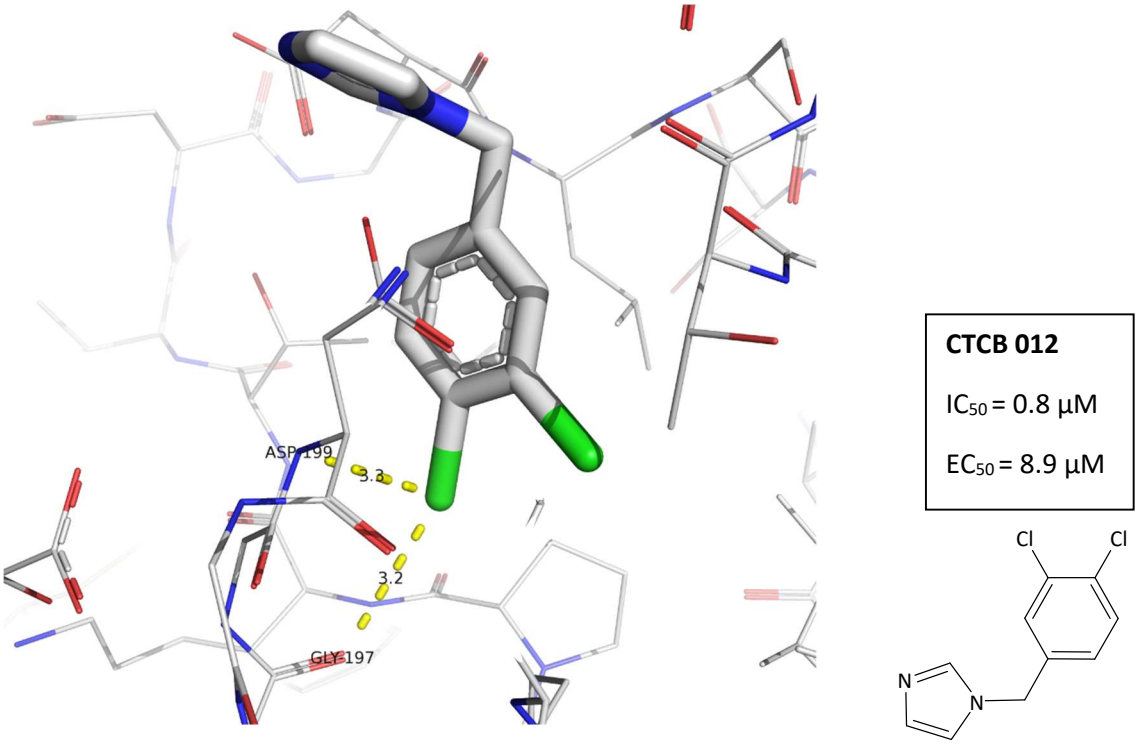

Figure 6.25: Binding of CTCB 012 as example of halogen binding in 3,4-dihalo ring of CTCB compounds.

The chlorine atom in the 3-position of the dichlorbenzyl ring makes halogen bond contacts with ASP199 and GLY197 of TbPFK. Image made using Pymol ver. 2.0. Structure solved by Dr Iain McNae (unpublished at time of writing).

Ligand efficiency (LE) describes the energy of binding per non-hydrogen atom of a ligand (CTCB compound) to a receptor (PFK enzyme)(Kuntz, Chen, Sharp, & Kollman, 1999). It can be calculated from IC_{50} values according to the equation:

$$LE = 1.37(-\log IC50)/N$$

Where N = the number of non-hydrogen atoms in the ligand structure. (Chen, Engkvist, & Kogej, 2015)

Small fragments such as 3,4-dichloroaniline (CTCB 097) (162 Da) or CTCB 012 (227 Da) have extraordinary ligand efficiency – with LE values of 0.85 and 0.61 µM respectively. These are impressive given CTCB 360, one of the most potent CTCB compounds has an LE value of 0.49 (**table 6.8**).

Compound	**MW (Da)**	**IC_{50} (µM)**	**Ligand efficiency**
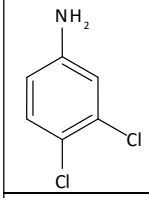 **CTCB 097**	162	3.1	0.85
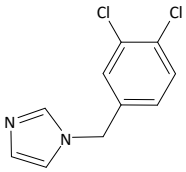 **CTCB 012**	227	0.8	0.61
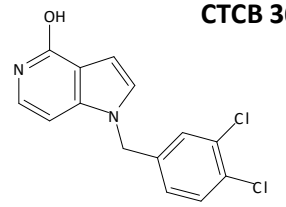 **CTCB 360**	293	0.1	0.49

Table 6.8: CTCB fragments demonstrate high ligand efficiency.

Ligand efficiency calculated as described above. IC_{50} values measured in ADP-Glo assay.

The binding position of the 3,4-dichlorobenzyl ring within *Tb*PFK is sufficient to block the leucine residue that is normally docked in the CTCB binding pocket, as revealed in the apo *Tb*PFK structure 2HIG. **Figure 6.26** shows the position of CTCB 012 in the CTCB binding pocket of *Tb*PFK, with the 2HIG structure overlaid.

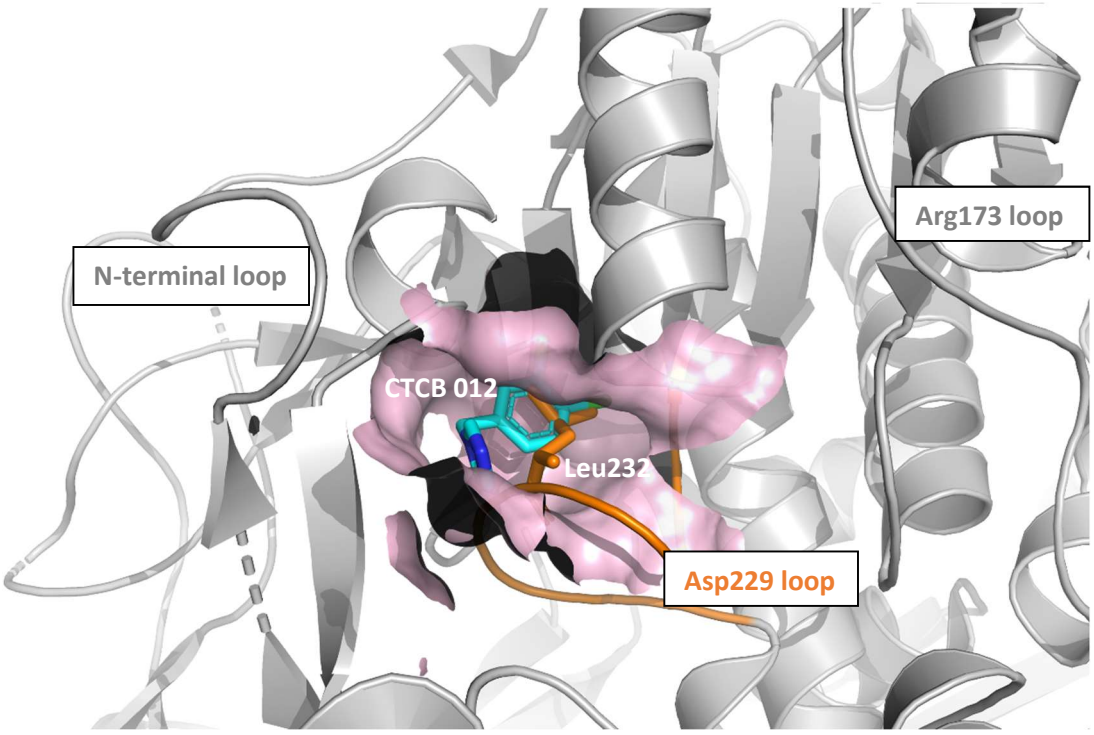

Figure 6.26: Binding of CTCB 012 prevents normal docking position of Leu232.

Apo-TbPFK structure (2HIG) shown in grey cartoon form. Binding position of CTCB 012 (sticks – cyan) in CTCB binding pocket (surface – pink). Asp229 loop of 2HIG structure has been coloured orange, with Leu232 shown (sticks – orange). Alignment of 2HIG to TbPFK-CTCB12 RMS = 0.792 Å. Structure solved by Dr Iain McNae (2HIG)(CTCB 012 structure unpublished at time of writing).

As can be seen in **figure 6.26**, the normal docked position of Leu232 overlaps with the dichlorobenzyl ring of CTCB 012.The binding of smaller CTCB compound fragments such as CTCB 012 effects only the position of the Asp229 loop. In the crystal structures of similar fragments, no significant changes are made to the positions of the Arg173, inserted or N-terminal loops that also surround the active site (data not shown).

Azaindoles.

The azaindole family of compounds are the most numerous of the different scaffold types making up the 636 CTCB compounds designed against *Tb*PFK. As well as the halogen contacts made by the 3,4-dichlorobenzyl ring (**figure 6.25**), the azaindoles make additional hydrogen bond contacts with one of two proximal aspartate residues – Asp199 or Asp275. **Figure 6.27** shows the two observed binding modes of the potent azaindole compound CTCB 360 in *Tb*PFK.

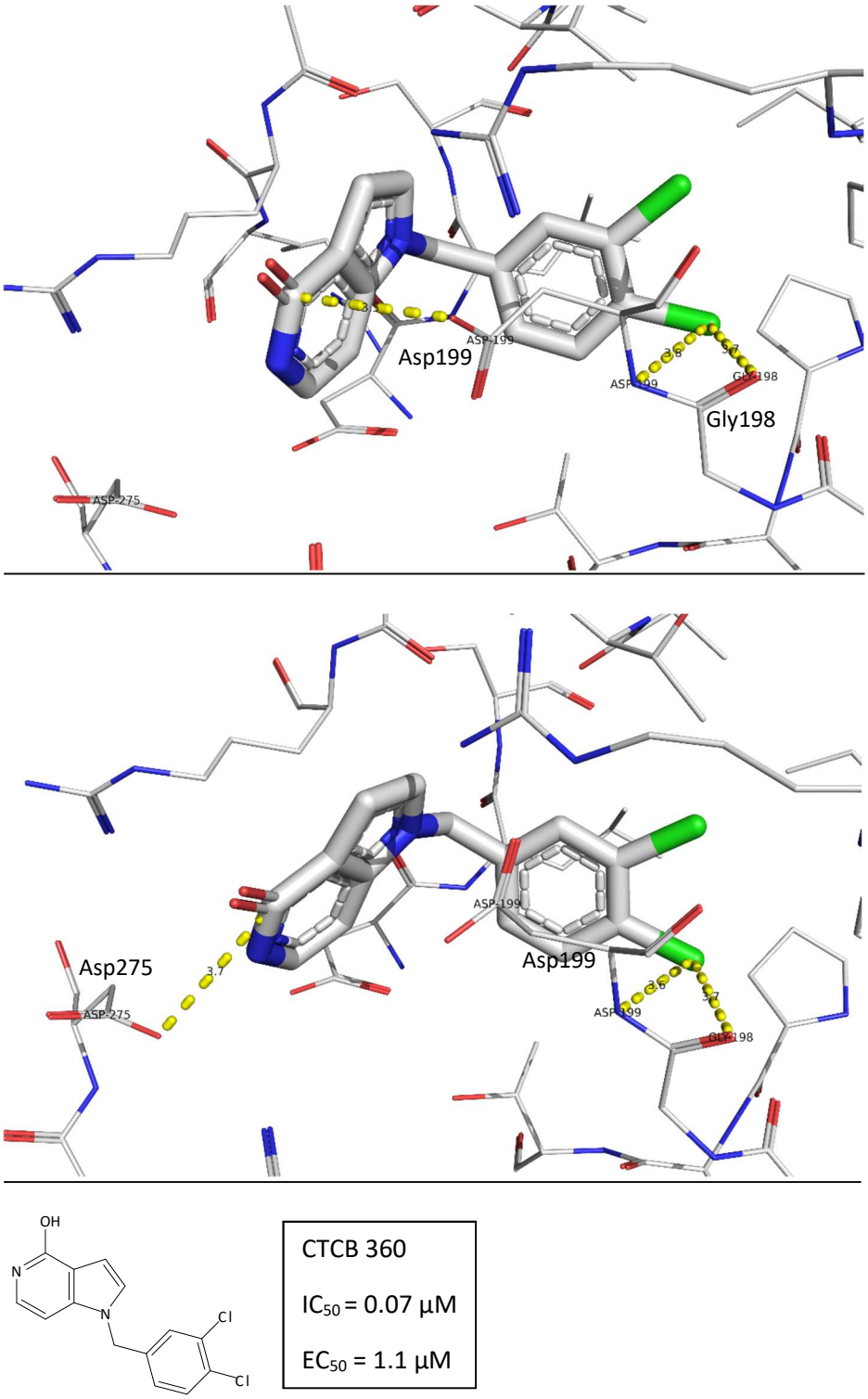

Figure 6.27: The azaindole CTCB 360 adopts 2 binding positions in TbPFK.

A) *Binding orientation 1: CTCB 360 makes hydrogen bond contacts (yellow dashes) with Asp199 in TbPFK.* ***B)*** *Binding orientation 2: CTCB 360 makes hydrogen bond contacts with Asp275 in TbPFK. Structure solved by Dr Iain McNae (unpublished at time of writing).*

To gain potency through additional contacts with *Tb*PFK residues out with the CTCB binding pocket, the next generation of azaindole compounds included groups branching off the azaindole ring. It was found that basic groups enhanced the potency of compounds against cultured *T. b. brucei* 427 strain parasites (data not shown).

Second generation azaindoles.

Second generation azaindoles added various basic groups to the azaindole ring in an attempt to pick up additional interactions outside the CTCB binding pocket. The crystal structure of CTCB 405 bound in *Tb*PFK shown in **figure 6.28** is a good example of the binding pose adopted by the second generation azaindoles; The amine group bends out of the pocket to make an additional hydrogen bond interaction with Asp199 residue (**figure 6.28**). Similar to the smaller fragments, the azaindoles binding pose only interfered with the Asp229 loop, and not any of the additional dynamic loops surrounding the active site.

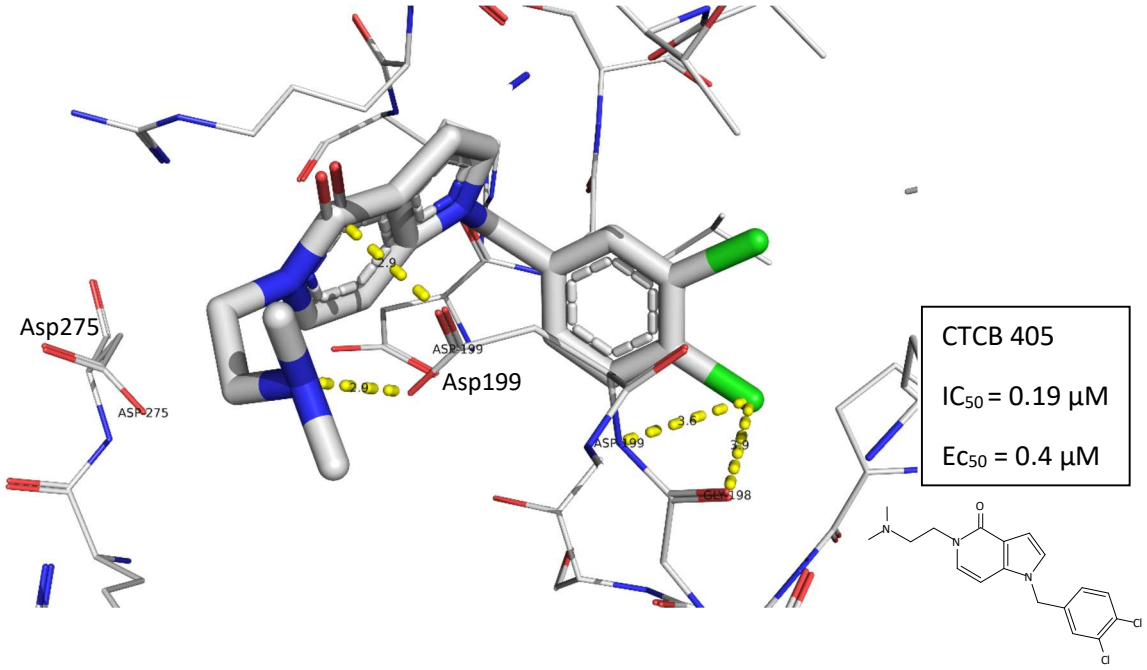

Figure 6.28: Second generation azaindole CTCB 405 makes additional hydrogen bond with Asp199.

Azaindoles, like CTCB 405 shown here make 2 hydrogen bond contacts (yellow dashes) with Asp199. Structure solved by Dr Iain McNae (unpublished at time of writing).

Pyrazoles.

These compounds adopt an orientation that pushes the N-terminal loop out of position. In Apo *Tb*PFK structures, ATP-bound *Tb*PFK structures and structures with the CTCB scaffold types mentioned above, the N-terminal loop forms a lid over the active site. The consequences of this binding orientation, and a more detailed description of the binding mode of pyrazoles in seen in **section 6.4.3**.

6.6.2 CTCB compounds inhibit T. cruzi PFK with increased potency.

To compare and contrast binding affinities of CTCB compounds for *T. brucei* and *T. cruzi* PFKs, high density (~12,000 RU) His_6-*Tb*PFK and His_6-*Tc*PFK surfaces were made and tested using SPR. Full experimental details can be found in section **2.5.3**. As an example, a comparison of the sensorgrams for CTCB 360 titrated against *T. brucei* and *T. cruzi* PFK surfaces is shown in **figure 6.29**.

The differences in binding were striking; Compared to the *Tb*PFK surface CTCB 360 has a much slower off-rate with *Tc*PFK that can be observed from the sensorgram trace alone (**figure 6.29**). The slower off rate for the inhibitor against *T. cruzi* PFK translates to a ten-fold tighter binding constant (kinetic K_d = 7 µM against *T. brucei* PFK compared with 0.2 µM against *T. cruzi* PFK). Increased potency against the *Tc*PFK enzyme activity compared with *Tb*PFK was also observed; CTCB 360 was a stronger inhibitor against *T cruzi* PFK – with an IC_{50} of 22 nM compared with 120 nM against the *T. brucei* enzyme, as tested in the PYK/LDH assay.

Table 6.9 shows collated data comparing inhibition and binding affinity of a selection of CTCB compounds against *T. brucei* and *T. cruzi* PFKs. All SPR data given is from a high-density surface (12,000 RU), and so K_D values are higher than those measured from the low-density surfaces.

		SPR K_d (µM)		Enzyme IC_{50} (µM)	
Compound	*Scaffold type*	*T. brucei*	*T. cruzi*	*T. brucei*	*T. cruzi*
CTCB 001 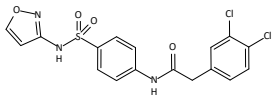	Sulph.	4.9	0.9	0.31 ± 0.1	0.03 ± 0.04
CTCB 012 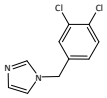	Frag.	ND	ND	0.80 ± 0.1	0.230 ± 0.1

	SPR K_d (µM)			Enzyme IC_{50} (µM)	
CTCB 097 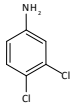	Frag.	ND	ND	1.99 ± 0.25	2.27 ± 0.18
CTCB 189 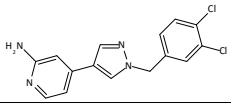	Pyra.	ND	ND	0.34 ± 0.18	0.27 ± 0.11
CTCB 293 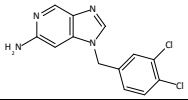	Aza.	42.5	7.6	0.270 ± 0.17	0.05 ± 0.03
CTCB 360 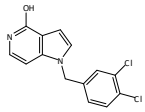	Aza.	7.0	0.2	0.100 ± 0.03	0.020 ± 0.02
CTCB 366 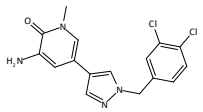	Pyra.	ND	ND	2.59 ± 0.36	2.67 ± 0.22
CTCB 374 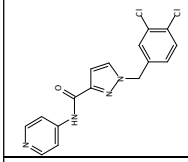	Pyra.	ND	ND	0.29 ± 0.06	0.26 ± 0.03
CTCB 386 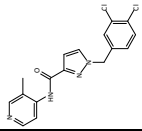	Pyra.	ND	ND	0.41 ± 0.03	0.47 ± 0.03
CTCB 405 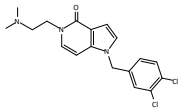	Aza.	ND	ND	0.270	0.05
CTCB 589 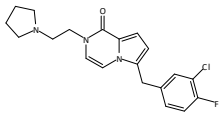	Aza.	ND	ND	0.96 ± 0.06	0.31 ± 0.01

Table 6.9: CTCB compounds have greater potency and bind tighter to TcPFK than TbPFK.

Enzyme IC_{50} values calculated using PYK/LDH assay. SPR-derived K_d values were calculated using high density (~12,000 RU) surfaces. 'Frag.' = fragment, 'Sulph.' = sulphonamide, 'Aza.' = azaindole, 'Pyra.' = pyrazole. 'ND' = no data comparable between TbPFK and TcPFK.

The data in **table 6.9** suggests that the chemical scaffold of the compound dictates the difference in affinities and potency of the CTCB compounds between *Tb*PFK and *Tc*PFK; The azaindole compounds show a much greater difference in affinity for *Tc*PFK over *Tb*PFK than the compounds with a pyazole scaffold.

.

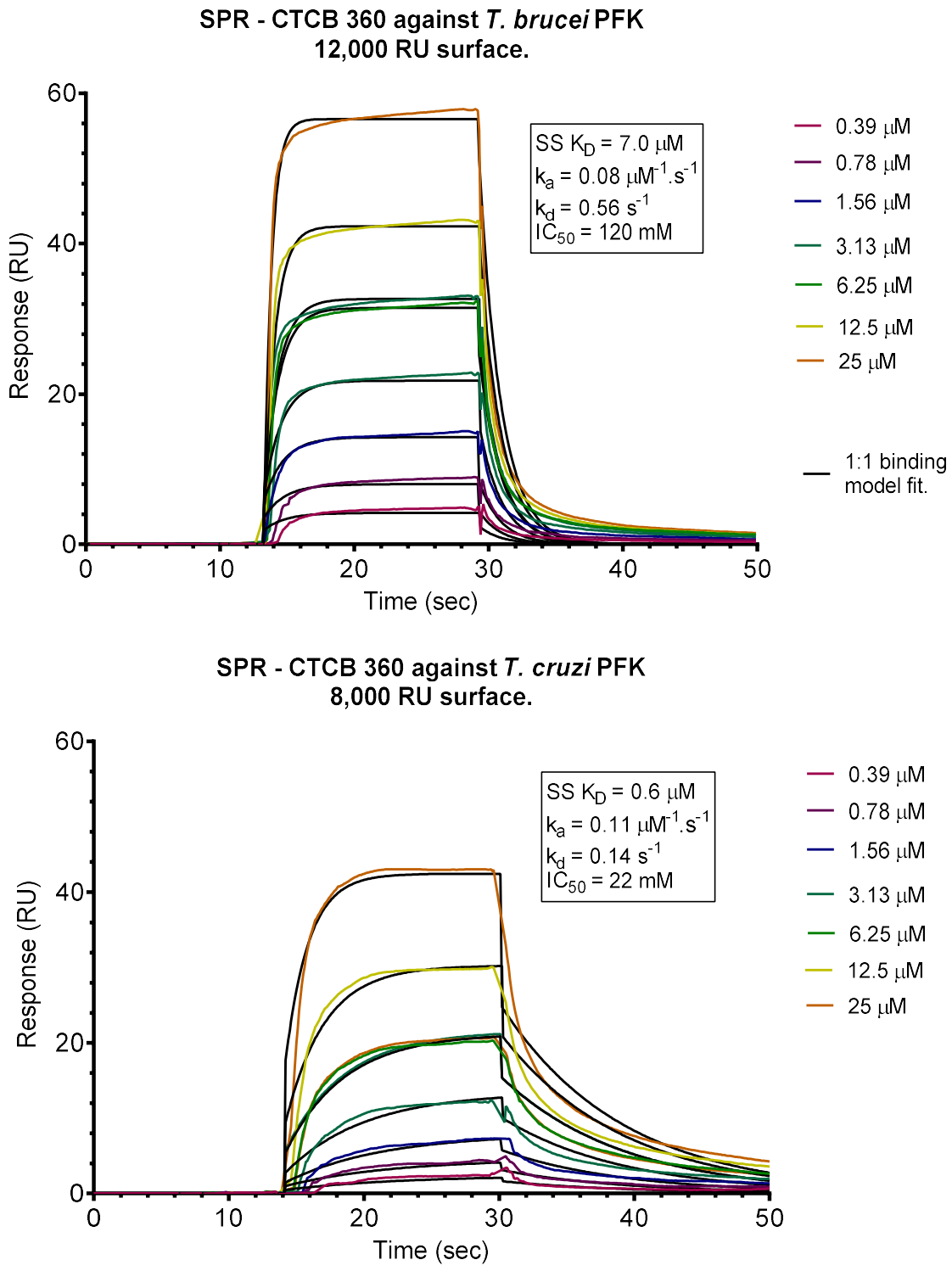

Figure 6.29: CTCB 360 demonstrates a remarkable jump in affinity to T. cruzi PFK over T. brucei PFK in SPR

SPR sensorgram traces for CTCB 360 titrations against T. brucei (12,000 RU) and T. cruzi (8,000 RU) surfaces. 1:1 binding models (black) have been fitted to each sensorgram. IC_{50} values for CTCB 360 against both species given were measured using the PYK/LDH assay.

6.6.3 Increased inhibition of *Tc*PFK may reveal opportunity for compound development.

Data shown in **table 6.9** demonstrates the increase in inhibitor potency and compound affinity for *Tc*PFK over *Tb*PFK. The two enzymes share 77% identity in sequences, and *Li*PFK, *Tb*PFK and *Tc*PFK are homologous in their ATP, F6P and CTCB binding pockets (**section 3.2.1, chapter 3**). Increased CTCB potency against *T. cruzi* PFK therefore must result from interactions outside the CTCB binding pocket.

Four dynamic loops surround the trypanosomatid PFK binding site and CTCB pocket; The Arg 173 loop (res. 170 – 178), Asp 229 loop (res. 225 – 235) and inserted loop (res.329 – 348) surround the active site and contribute to the catalytic activity of the PFK enzyme. An additional loop, the 'N-terminal loop' (res. 15 -23) forms a lid over the CTCB binding pocket and is observed in both the apo and ATP-bound structures of *T. brucei* PFK.

A sequence alignment between *T. brucei* and *T. cruzi* PFK for the dynamic loops surrounding the trypanosomatid active site is shown in **figure 6.30**. The catalytically important Asp 173 loop, Asp 229 loop and inserted loop are homologous between *T. brucei* and *T. cruzi* PFKs, however identity in the N-terminal loop is only 44%.

The data shown in **table 6.9** suggested that there was a greater increase in both affinity and potency against *Tc*PFK for the azaindole compounds compared with the pyrazole type compounds. The binding poses of these two different scaffolds may explain this difference, in particular their interaction with the N-terminal loop; **Figure 6.31** shows the crystal structures of CTCB 189 (pyrazole scaffold) and CTCB 293 (azaindole) bound to *Tb*PFK. The binding orientation of the pyrazole compound (CTCB 189) appears to push the N-terminal loop out of the position it adopts in the ATP-bound PFK structure. In the azaindole (CTCB 293) bound structure the N-terminal loop remains in the 'normal' position. It is possible that the increased affinity observed for CTCB compounds with the azaindole scaffold may be due to interactions with the dynamic N-terminal loop. In contrast the pyrazole scaffold compounds, which push the N-terminal loop out of position have much smaller differences in affinity and potency when comparing *Tb*PFK and *Tc*PFK. As the only difference in the *Tb*PFK and *Tc*PFK sequences was observed in the N-terminal loop, it is reasonable to suggest that increased affinity for azaindole-like CTCB compounds against *Tc*PFK may be due to favourable interactions with the N-terminal loop.

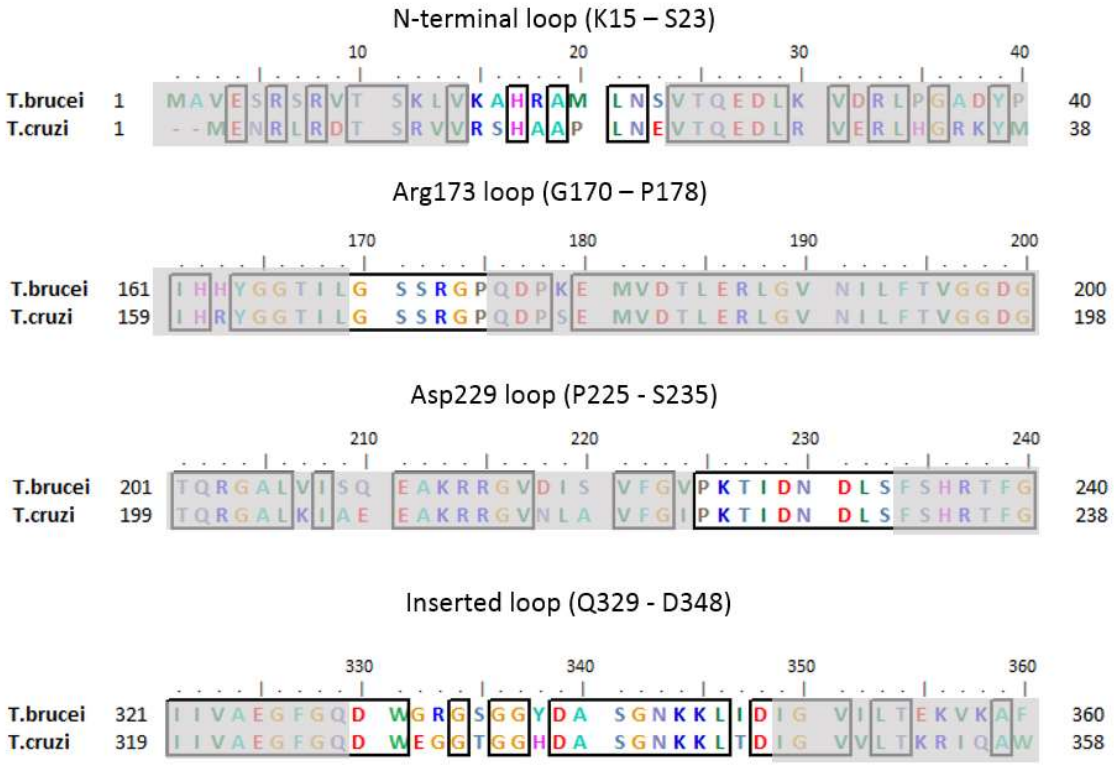

Figure 6.30: The N-terminal loop is not well conserved between T. brucei and T. cruzi PFKs.

Alignment of T. cruzi and T. brucei PFK monomer a.a. sequence. Homologous residues are boxed.

A

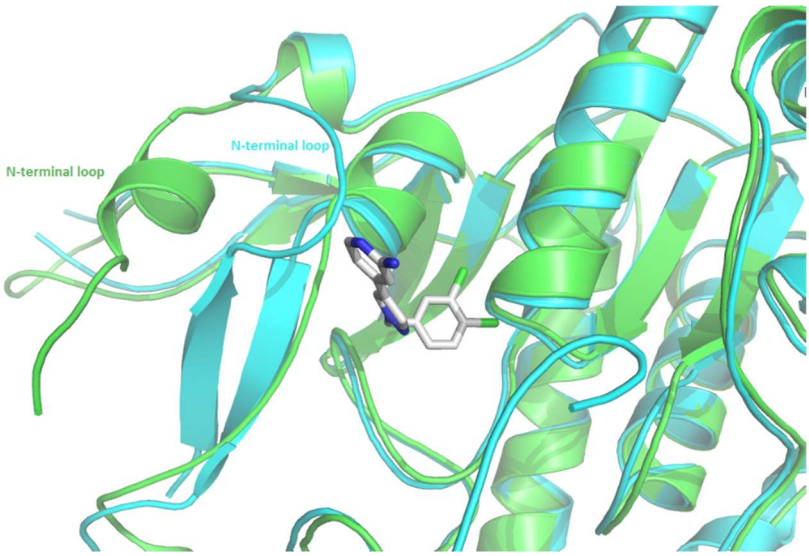

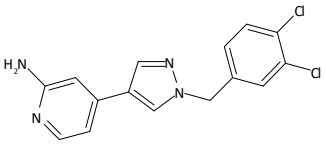

CTCB 189

(Pyrazole)

Cyan = TbPFK ATP bound (3F5M) Green = TbPFK + CTCB 189

B

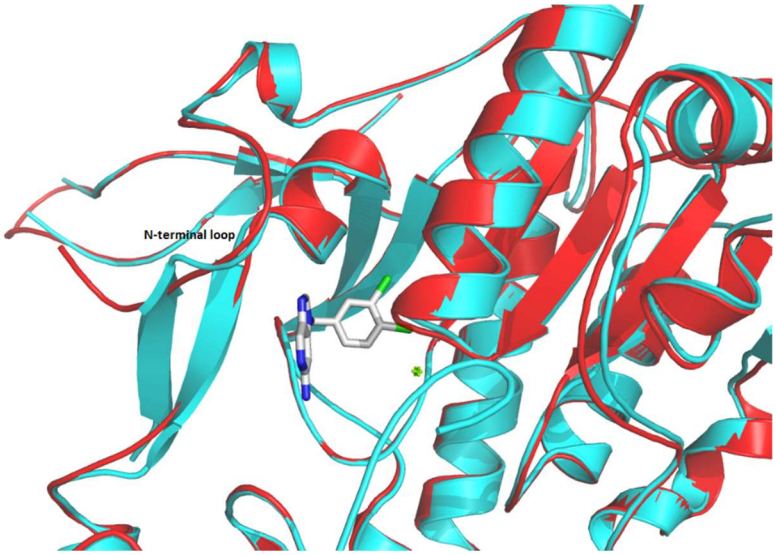

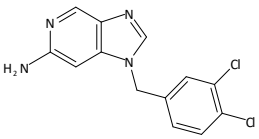

CTCB 293

(azaindole)

Cyan = TbPFK ATP bound (3F5M) Red = TbPFK + CTCB 293

C

	T. brucei IC_{50}	*T. cruzi* IC_{50}
CTCB 189 (pyrazole)	337 nM	267 nM
CTCB 293 (azaindole)	320 nM	52 nM

Figure 6.31: Binding pose of pyrazole compounds effects N-temrinal loop.

A) *Pyrazole compound CTCB 189 bound to TbPFK overlaid on ATP-bound TbPFK structure 3F5M.* ***B)*** *Azaindole compound CTCB 293 bound to TbPFK.* ***C)*** *IC_{50} data for example CTCB 189 and CTCB 293 compounds against TbPFK and TcPFK, measured using ADP-Glo assay. Structures solved by I. McNae (unpublished at time of writing).*

6.7. CTCB compound specificity.

6.7.1 CTCB compounds are not competitive with PFK's substrates.

To investigate if the CTCB compounds inhibited PFK without competing with the enzymes substrates, the PYK/LDH enzyme linked assay was used. ATP and F6P titrations were carried out in the presence of set concentrations (2x, 1x and 0.5x IC_{50}) of inhibitor. As discussed in **section 4.2.1**, the order of reaction is important for PFK – with ATP binding preceding F6P binding. To ensure all possibilities were covered, the competition kinetics experiments were carried out with and without incubation of the CTCB compound and *Tb*PFK. The assays are summarised in **table 6.10**. Full experimental procedures can be found in **section 2.3.1.4.**

	ATP titration	F6P titration
'Pre-incubated' competition assays	**(*Tb*PFK / cmpd. / F6P)** + ATP	**(*Tb*PFK / cmpd. / ATP)** + F6P
Non pre-incubated competition assays	**(*Tb*PFK / F6P)** + (ATP / cmpd.)	**(*Tb*PFK / ATP)** + (cmpd. / F6P)

Table 6.10: Reaction order in compound competition assays.

Brackets denote analytes that were pre-incubated together on ice for 10 minutes, then an additional 5 minutes at 25 °C. 'Cmpd' = CTCB compound.

Competition kinetics experiments were carried out using 5 CTCB compounds; A fragment (CTCB 012), a sulphonamide identified from the original NIH screen (CTCB 123)(Brimacombe et al., 2014) and three of the most potent inhibitors of *T. brucei* PFK (CTCB 360, '405 and 460)(**figure 6.32**). Michaelis-Menten curves of the substrate titrations were used to look for evidence of competition. **Table 6.11** outlines the classical hallmarks of different types of competition on enzyme kinetics. **Figure 6.33** shows the plots for F6P and ATP titrations against *T. brucei* PFK in the presence of CTCB 360.

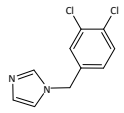

CTCB 012 (fragment)

IC_{50} = 0.8 ± 0.09 µM

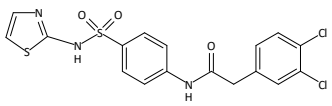

CTCB 123 (sulphonamide)

IC_{50} = 0.13 ± 0.05 µM

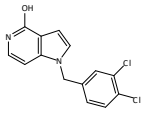

CTCB 360 (azaindole)

IC_{50} = 0.10 ± 0.03 µM

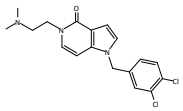

CTCB 405 (azaindole)

IC_{50} = 0.27 ± 0.08 µM

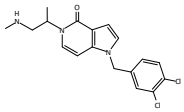

CTCB 460 (azaindole)

IC_{50} = 0.08 ± 0.03 µM

Figure 6.32: CTCB compounds used in PFK competition assays.

IC_{50} values measured in PYK/LDH assay.

Type of competition	**Effect on V_{max}**	**Effect on K_m**
Uncompetitive	↓	↓
Non-competitive	↓	-
Competitive	-	↑

Table 6.11: Kinetic phenotypes of different types of competitive inhibitors.

Information summarised from (Price & Nairn, 2009).

A

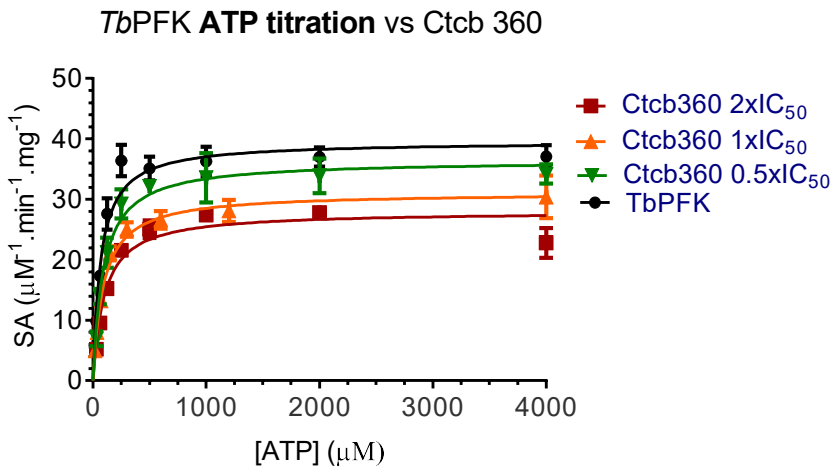

	***Tb*PFK only**	CTCB 360 **0.5X IC_{50}**	CTCB 360 **1X IC_{50}**	CTCB 360 **2X IC_{50}**
Vmax (μmol^{-1} min^{-1} mg^{-1})	39.6 ± 1.6	36.5 ± 1.1	31.1 ± 0.8	27.9 ± 1.5
Km (μM)	137 ± 8.3	181 ± 6.2	181 ± 6.9	199 ± 12.6

B

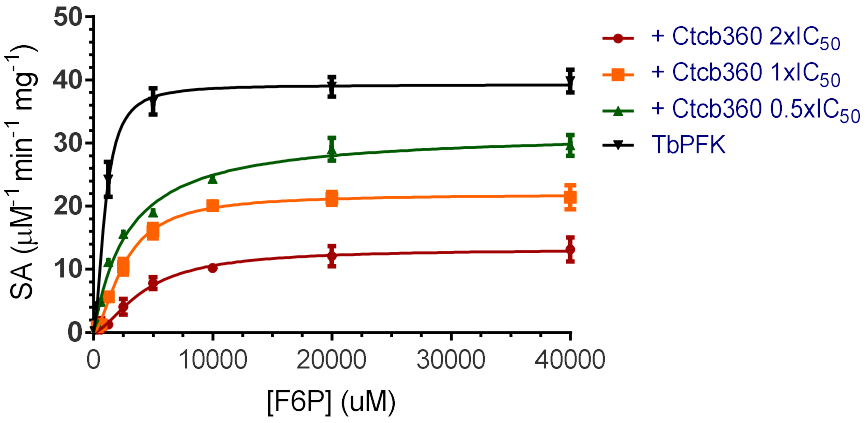

	***Tb*PFK only**	CTCB 360 **0.5X IC_{50}**	CTCB 360 **1X IC_{50}**	CTCB 360 **2X IC_{50}**
Vmax (μmol^{-1} min^{-1} mg^{-1})	39.2 ± 0.5	31.7 ± 0.7	21.9 ± 0.4	13.2 ± 0.4
K_{half} (μM)	965 ± 30	1297 ± 92	2663 ± 151	4240 ± 276

Figure 6.33: CTCB 360 inhibits T. brucei PFK without competing with ATP or F6P.

A) *ATP titrations (4 mM – 31 μM) against T. brucei PFK with set concentrations of CTCB 360 (0.5 X, 1X and 2X IC_{50}) (50, 100 and 200 nM respectively). 10 mM F6P, 4 μg/ml T. brucei PFK* ***B)*** *F6P titrations (40 mM – 310 μM) against T. brucei PFK. Fixed CTCB 360 concentrations as above. 5 mM ATP, 4 μg/ml T. brucei PFK. All experiments carried out in triplicate, error bars denote standard deviation.*

In the case of CTCB 360 shown in **figure 6.33**, mixed inhibition characteristics can be seen with both ATP and F6P; In both substrate titrations the Vmax is reduced and the K_m^{ATP} or K_{half}^{F6P} is increased – showing a mix of the phenotypes outlined in **table 6.11**. The CTCB 360 compound therefore shows no evidence of competition with ATP or F6P. This was the outcome for all the compounds tested in these experiments: either producing 'mixed inhibition' or non-competitive phenotypes (data not shown). Pre-incubation of the compound had no effect on these conclusions. CTCB compounds are not competitive with the substrates of *T. brucei* PFK. The CTCB compounds also had no effect on the cooperative binding response with respect to F6P; The Hill coefficient (*h*) for 0, 0.5X , 1X and 2X CTCB 360 IC_{50} was between 1.7-1.8 ± 0.1 for the F6P titrations shown in **figure 6.33**.

6.7.2 CTCB compound specificity between PFK from different species.

The SDD project took a structure-based design approach to the development of the CTCB inhibitor compounds. The attraction of PFK as a target for trypanocidal drugs over other glycolytic enzymes was the binding pocket identified from crystal structures of *T. brucei* PFK. Crucially, this pocket is not present in the mammalian form of the enzyme – resulting in specificity for the trypanosomatid enzyme over the host. The aim of the work in this section was to investigate if the synthesised CTCB compounds were in fact specific over the mammalian form of the enzyme *in vitro*, and if they had comparable affinity between trypanosomatid PFKs.

6.7.2.1 The most potent CTCB compounds do not inhibit human PFK.

To test for specificity of CTCB compounds for *T. brucei* PFK over mammalian PFK, 8 of the most potent CTCB compounds were tested against the human muscle isoform of PFK (PFK-M) in the aldolase/TIM assay - see **section 2.3.2.2** for experimental details. Human muscle PFK is the most abundant of the three human PFK isoforms PFK-P (platelet), PFK-L (Liver) and PFK-M (Muscle). No inhibition of human PFK-M was observed for any of the compounds tested. A titration of CTCB 405 against human PFK-M and *T. brucei* PFK is shown in **figure 6.34.** CTCB 405 has an IC_{50} of 180 nM against *Tb*PFK in the PYK/LDH assay.

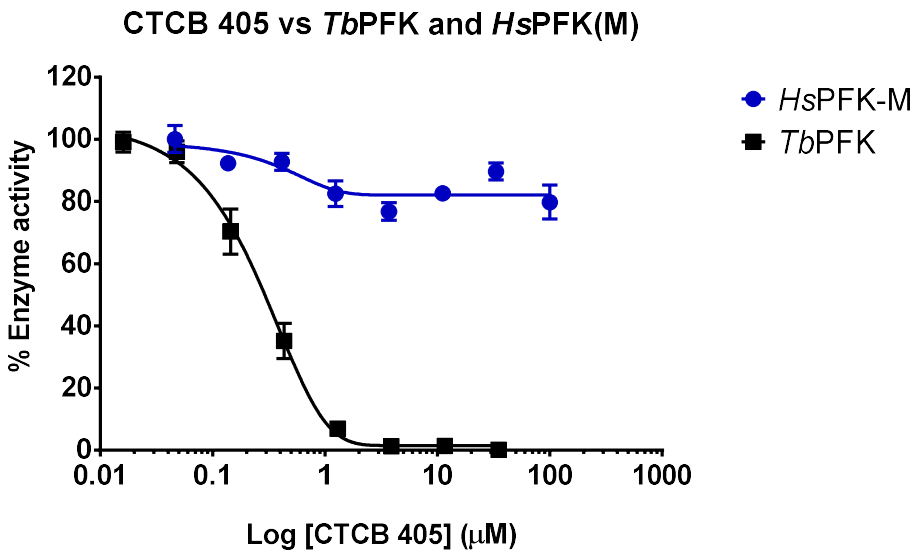

Figure 6.34: CTCB 405 shows no significant inhibition of human PFK-M.

Data measured using the aldolase/TIM linked assay at 25 °C. Experiments carried out in triplicate, error bars denote standard deviation. T. brucei PFK and H. sapiens PFK-M at equimolar concentrations (80 nM). 1mM ATP and 0.6 mM ATP were provided. Sigmoidal curves have been fitted to both enzyme datasets. Top concentration of CTCB 405 = 100 µM.

6.8. Discussion – Mechanism and specificity of CTCB compound binding.

We have shown in this section that the CTCB compounds bind tightly with specific interactions. The binding poses of the CTCB compounds within the 'CTCB binding pocket' of *T. brucei* PFK show how even small fragments can inhibit the normal docking of the catalytically important Asp 299 loop.

We observed a striking increase in potency for the CTCB compounds against *T. cruzi* PFK compared to *T. brucei* PFK. This increased potency revealed further information on the relationship between the CTCB chemical classes and the binding mode; The pyrazole class of compounds destabilised the N-terminal loop, which normally forms a lid over the active site. The azaindole compound class demonstrated remarkable increases in potency against *Tc*PFK, and in crystal structures did not interfere with the N-terminal loop. We showed through sequence alignments that the only significant differences in the active site and CTCB binding pocket between the TbPFK and *Tc*PFK enzymes was within the N-terminal loop. While crystal structures of the CTCB compounds bound within *Tb*PFK do not show interactions with any other dynamic loops within the active site, some evidence was presented for the azaindole class of CTCB compounds making contacts with the 'N-terminal loop'.

We have also shown in this chapter the specificity of the CTCB compounds; firstly we showed that the binding and inhibition by the CTCB compounds was not competitive with PFKs substrates. Mixed inhibition phenotypes were observed when CTCB compounds were tested against titrations of F6P and ATP, showing a lack of direct competition with these compounds. This is an obvious advantage in drug design, as the CTCB compounds will not be competing with high concentrations of substrates within the trypanosomes. F6P concentrations have been found to be >1mM in *Leishmania spp.* for example (Akpunarlieva et al., 2017).

Secondly and perhaps more importantly, we have shown that the CTCB compounds are specific to the trypanosomatid PFK over the Human enzyme. No significant inhibition was observed when CTCB compounds were tested up to a concentration of 100 µM against the human muscle isoform of PFK. The CTCB binding pocket is incomplete in the human PFK structure, as discussed in **section 7.4, chapter 7**. Coupled with the observations described in this chapter that CTCB compounds are not promiscuous binders, we have shown that the CTCB compounds are highly specific and potent inhibitors of the *T. brucei* PFK enzyme, and have the potential as specific inhibitors against other trypanosomatid PFKs.

Chapter 7 : Conclusions.

7.1. Trypanosomatid PFK is an essential, yet simply regulated glycolytic enzyme.

In **chapter 4** we observed that phosphofructokinase from *T. brucei*, *T. cruzi* and *L. infantum* trypanosomatids is regulated by the physiological effector AMP (and the structurally similar GMP). No other physiological effector of other eukaryotic PFKs or metabolic intermediate tested had any significant effect on our enzymes, however other, less obvious regulatory mechanisms may exist. AMP was an activator of the PFK enzyme; increasing the catalytic efficiency of the trypanosomatid PFKs (k_{cat}/K_m) with regards to both substrates ATP and F6P by factors between 1 – 7X and 3 – 15X respectively.

7.1.1 Trypanosomatid PFKs are not sensitive to allosteric ADP or ATP inhibition.

ADP is an activator of the ancestral bacteria-like PFK, yeast PFK and mammalian PFK enzymes (**section 4.5, chapter 4**)**. Section 1.4.1, chapter 1** shows the evolution of eukaryotic PFKs from their bacterial ancestor. Yeast and mammalian PFKs retained an effector site imparting inhibition by PEP and activation by ADP. ADP did not regain its regulatory activity when trypanosomatids changed back to the use of ATP as phosphodonor, later in evolution (Bapteste, Moreira, & Philippe, 2003). We did observe weak inhibition of *Tb*PFK by ADP (IC_{50}^{ADP} = 7.2 mM), though we propose that this may be in competition with ATP in the active site rather than allosteric inhibition. The binding orientation of AMP in an unpublished structure of *T. brucei* PFK with AMP bound (Montserrat Valdivieso and Iain McNae, UoE) suggests that the extra phosphate of the ADP molecule could be accommodated within the AMP binding site (**section 1.4.7, chapter 1**)(per. Comm. I. McNae).

ADP was shown to bind all three enzymes in SPR – giving steady state K_d's of 0.56, 0.73 and 0.16 mM for *Tb*PFK, *Tc*PFK and *Li*PFK respectively. AMP had no effect on the affinity of *Tb*PFK for ADP in SPR, suggesting a lack of competition for the ADP or AMP binding sites. We propose therefore that ADP binds as a product in the active site or as a substrate for the reverse PFK reaction as discussed further in Chapter 5. We have no evidence of ADP binding within the allosteric AMP site, and the weak inhibition of ADP on *Tb*PFKs activity is likely due to competition with ATP in the active site.

We did not observe any binding response or inhibition of any of the three trypanosomatid PFKs with regards to citrate at concentrations up to 10 mM. Citrate inhibits mammalian PFK by

enhancing the ATP inhibition effect on the enzyme. It does this as high citrate (a TCA cycle intermediate) signals that biosynthetic intermediates are readily available, and no further glucose is required to be broken down. The effector site responsible for the sensitivity (as well as ATP sensitivity) of mammalian and yeast PFK resulted from an acquisition of an extension that developed a citrate binding site (G. A. Dunaway, 1983; Heinisch et al., 1989). Therefore whereas a loss in allosteric ADP sensitivity by trypanosomatid PFKs resulted from a loss of an effector site, the lack of ATP/Citrate sensitivity is attributed to the lack of a event resulting in a new effector site (see **section 1.4.1, chapter 1**). The TCA cycle is also repressed in the BSF *T. brucei* parasites, and so regulation by citrate would seem unlikely (Zikova et al., 2017).

Compartmentalisation of trypanosomatid PFK means that the enzyme does not sense the overall cellular (i.e. the cytosolic) ATP concentration; Feedback inhibition through ATP is an important regulatory feature of yeast and mammalian PFK and hexokinase enzymes (those using ATP as a substrate in glycolysis) as they are located in the cytosol. As glycolysis results in the net production of 2 ATP molecules per molecule of glucose consumed, inhibition of the enzyme activity by ATP or hexose phosphates (G6P, F6P and F16BP) is required. Preventing the auto-stimulation of these enzymes by the surplus ATP produced by the process ('turbo-effect') could result in the build-up of intermediates to toxic levels when the catalytic capacity of the first enzymes of the pathway exceeds that of the downstream enzymes (**figure 7.1**). Trypanosomatid PFK and hexokinase, and the other enzymes involved in the first seven steps of glycolysis are compartmentalised within glycosomes, where the ATP:ADP ratio is held constant – there is no net production of ATP within the glycosomes, only in the cytosol where pyruvate kinase (PYK) is localised. The turbo-effect by ATP build up is therefore not possible regarding the enzymes in the glycosomes and sensitivity to ATP is not required (Haanstra et al., 2008). We did not find G6P, F6P or F16BP to be inhibitory against *T. brucei* PFK either. Under the conditions used, trypanosomatid PFK is clearly not effected by negative feedback regulation from its products.

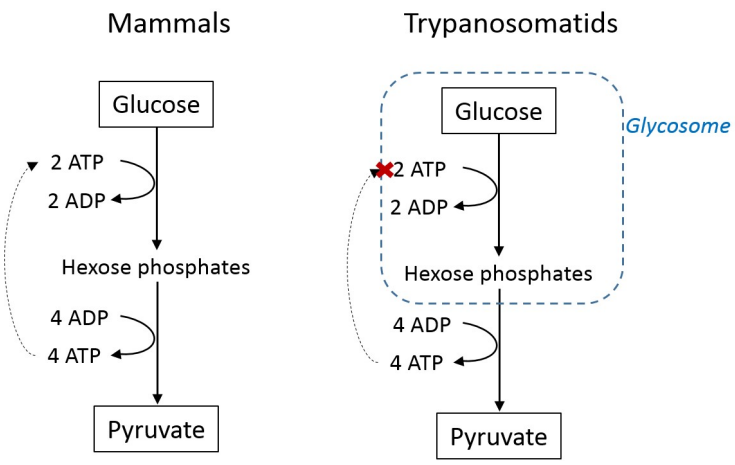

Figure 7.1: Feedback inhibition by ATP in glycolysis.

The net production of ATP in glycolysis (4 x ATP) can act as fuel for the ATP consuming reactions upstream (dotted lines) and lead to build-up of metabolic intermediates of the capacity of the upper part of the pathway exceeds that of the lower part). Most eukaryotic organisms prevent this through negative feedback inhibition of hexokinase by hexose phosphates (G6P, F6P and F16BP) (Haanstra et al., 2008). *In trypanosomatids net production of ATP occurs outside the glycosomal membrane which is impermeable to nucleotides. Several kinases within the glycosomes maintain the balance between ATP consumption and production* (Deramchia et al., 2014).

7.1.2 AMP is the low energy signal and activator of trypanosomatid glycolysis.

In mammalian glycolysis, AMP activates PFK by binding to an allosteric site and reversing the inhibitory effect of high ATP concentrations on the enzyme. When energy supplies are low (i.e. a low ATP:AMP ratio) the enzyme is stimulated and more ATP is produced through glycolysis. ADP is not used as the low energy signal as it can be converted into additional ATP by adenylate kinase (ADP + ADP = ATP + AMP).

This offers a much more resource efficient method of signalling. AMP binds to an allosteric site, and allows more sensitivity as a regulator than ADP – small changes in ATP concentration result in large changes in AMP concentration – the breakdown of 2 ATP molecules results in a net loss of 1 ATP but a gain of 1 AMP molecule (**figure 7.2**). This is a resource-efficient way of recouping an ATP molecule while producing a signal molecule to stimulate glycolysis.

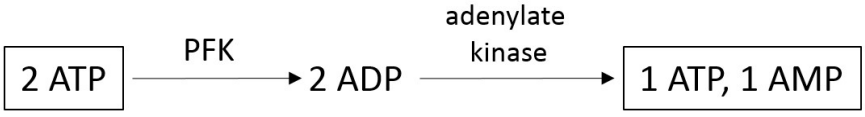

Figure 7.2: AMP is produced from ADP by adenylate kinase.

In contrast to the important regulatory role PFK plays in mammalian glycolysis, we know from flux control analysis that while there is no single rate limiting step of glycolysis, PFK plays a lesser role in the control of glycolysis in trypanosomatids (**section 1.3.5, chapter 1**) (Haanstra et al., 2017). Unlike all other eukaryotic PFKs, trypanosomatid PFKs are not stimulated by F26BP, but instead this activation of the pathway is facilitated via stimulation of pyruvate kinase (PYK) in the cytosol. Nonetheless AMP was an activator of all three of our trypanosomatid PFK enzymes. A glycosomal adenylate kinase produces AMP from ADP in *T. brucei* parasites (Ginger et al., 2005). Similar to activation of PFK in mammals, it is likely that AMP is the low-energy signal in the trypanosomatid glycosomes, activating the PFK enzyme and stimulating glycolysis. PFK in this scenario acts as a 'scavenger' enzyme.

7.2. A mechanism for trypanosomatid PFK enzyme activity.

Various assays and biophysical methods described throughout this thesis have allowed us to accumulate evidence for a more complete understanding of trypanosomatid PFK activity. **Figure 7.3** describes a mechanism for PFK activity and regulation by AMP. The evidence used to build this model is summarised in **table 7.1**.

7.2.1 A model for trypanosomatid PFK activity and regulation.

The model for trypanosomatid PFK activity shown in **figure 7.3** assumes two 'activated' enzyme conformations – the first upon ATP binding and the second upon subsequent AMP binding. In the ATP-bound state a conformational change in the loops surrounding the active site allows for F6P binding. AMP binding to this activated ATP-bound state results in the second 'locked' active state – affinity for both ATP and F6P is increased but the mechanism conferring cooperativity in F6P binding is lost. This AMP-induced loss of cooperativity is perhaps due to a conformational change or locking of the C-terminal reaching arms that span across adjacent subunits, and under which the putative AMP binding pocket lies. A crystal structure with both ATP and AMP bound would help answer this hypothesis, investigating in particular the effect AMP binding has on the conformational state of the C-terminal reaching arms.

In the ATP-bound active conformation, cooperativity in F6P binding can best be described as following the KNF or 'sequential' model for cooperativity (see **section 1.4.6, chapter 1**); Provided ATP has bound to all subunits within the tetramer first, the binding of a molecule of F6P to one of the subunits induces a conformational change in the neighbouring subunit that increases affinity for the binding of another F6P molecule. We cannot consider the MWC 'symmetry' model as the rules governing this model dictate that the change between inactive and active enzyme states is independent of ligand binding. In our model the active state is only formed when ATP binds first. Some features of the MWC symmetry model however can be applied: The binding of F6P was found to be cooperative, but how is this cooperativity signalled across the tetramer? One possibility is the large dynamic 'inserted loop' feature. This large unstructured loop could potentially make contacts with the neighbouring inserted loop upon F6P binding, signalling a conformational change in the neighbouring F6P site to increase affinity for another F6P molecule (**figure 7.4**). With this in mind, the PFK subunits would work in pairs within the tetramer, similar to that described in the MWC symmetry model.

Hypothesis	Evidence
(A) ATP binds to PFK first in the reaction scheme, inducing an active enzyme state.	1. A comparison of apo- and ATP-bound *T. brucei* PFK crystal structures shows ATP binding induces a conformational change to open up the active site and accommodate F6P (**section 1.4.5, chapter 1**). 2. A binding response for F6P against *T. brucei* PFK surface in SPR was only possible when ATP was present (**section 4.4.4, chapter 4**). 3. Pre-incubation of PFK with ATP resulted in greater affinity for F6P (lower K_m^{F6P}) (**section 4.2.4, chapter 4**).
(B) F6P binds PFK in a cooperative manner in the presence of ATP.	1. F6P titrations against trypanosomatid PFKs result in dose-response curves with sigmoidal tails at lower [F6P]. 2. Hill coefficients are >2.0 with regards to F6P titrations against the PFK enzymes (**Section 4.2.3, chapter 4**)
(C) ATP must be bound for AMP to elicit its activating effect.	1. The activating effect of AMP on PFKs activity was only observed when the enzyme was pre-incubated with ATP first (**section 4.5.3, chapter 4**).
(D) AMP binding induces a second conformation. This is a 'locked' active state with high affinity for substrates.	1. The observed activation by AMP results in increased affinity for both ATP and F6P (**section 4.5.2, chapter 4**). 2. Cooperativity in F6P binding is lost when AMP is present (**section 4.5.2, chapter 4**). 3. AMP also activates the reverse reaction, suggesting a second conformational state independent of ATP activation (**section 5.3.1, chapter 5**).

Table 7.1: Evidence used for formation of our trypanosomatid PFK activity model.

*Showing the observations used to develop our PFK mechanism model and the evidence for each of these observations. Annotations A-D are referenced in the model diagram (**Figure 7.3**).*

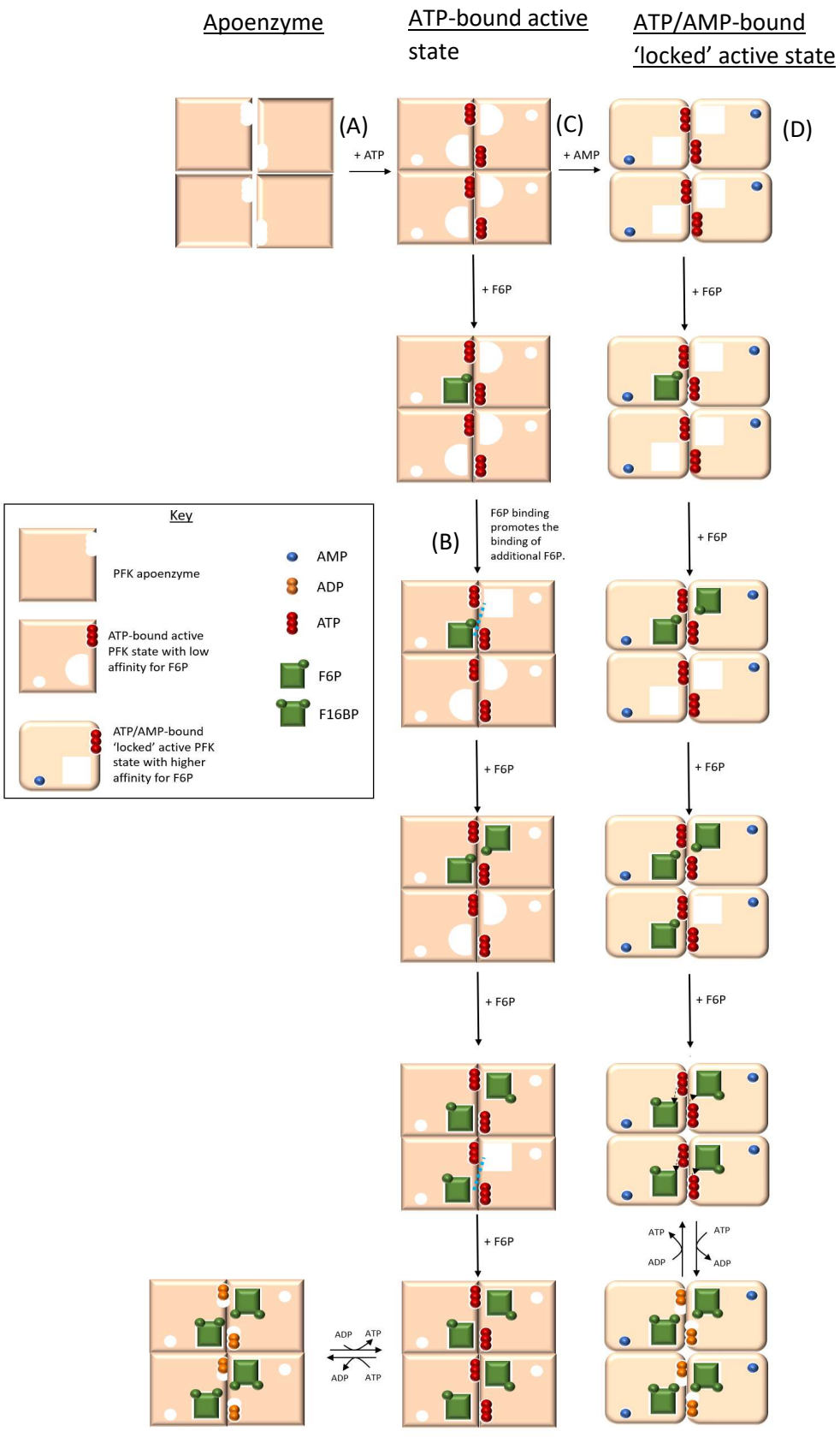

Figure 7.3: Model for trypanosomatid PFK enzyme mechanism.

Made using hypothesis (labelled A-D) as summarised in ***table 7.1***.

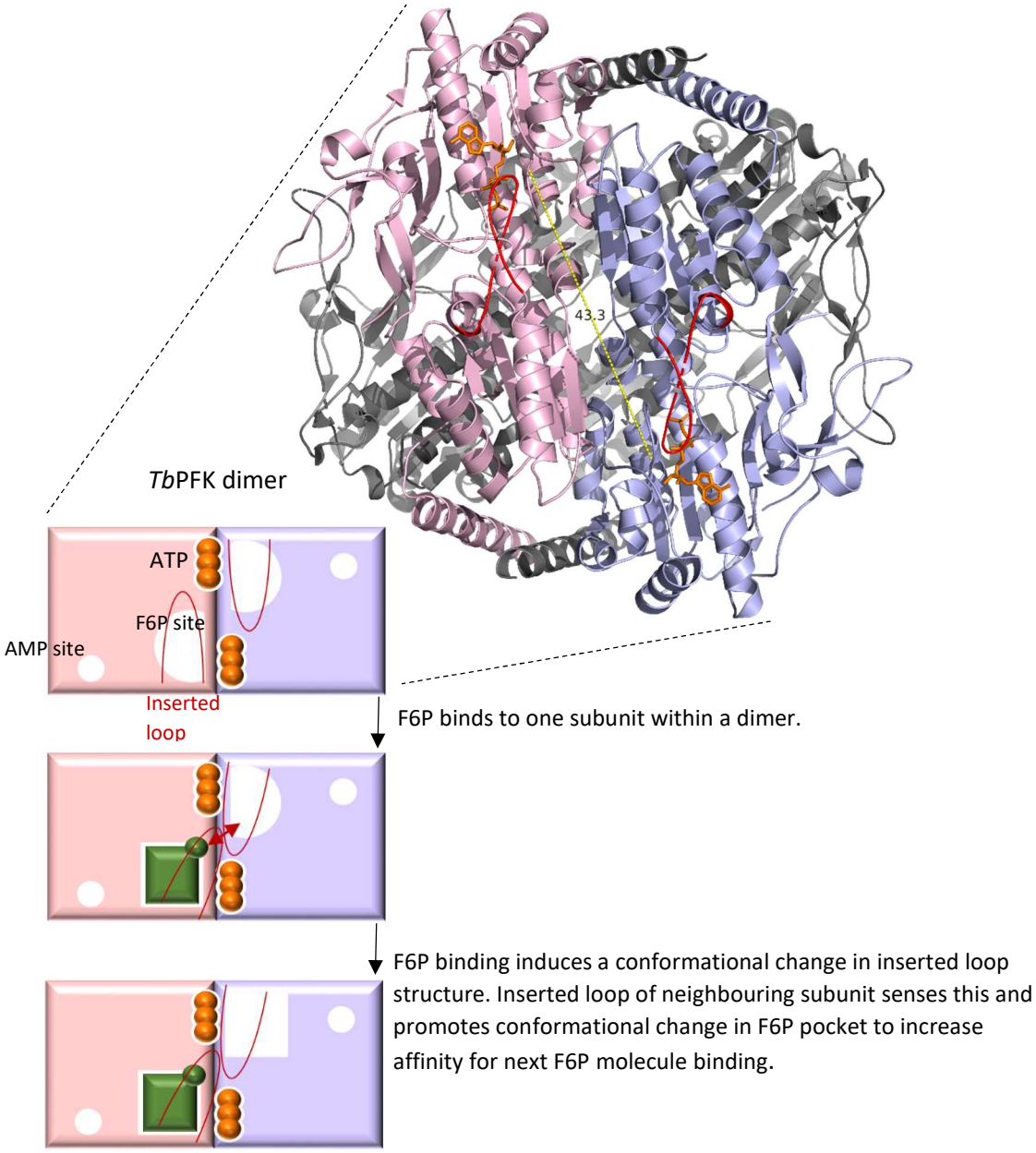

Figure 7.4: Could the 'inserted loop' feature communicate cooperativity in F6P binding?

ATP-bound (3F5M) TbPFK structure. Two neighbouring subunits within a dimer have been coloured pink and purple. Other dimer has been coloured grey. Inserted loop feature is coloured in red in both subunits and ATP shown as orange sticks in both subunits. Maximal distance between the two farthest residues on each inserted loop is given (yellow dashed lines) – 43.3 Å.

7.3. Enzyme kinetic assays revealed unique properties of trypanosomatid PFKs

7.3.1 Measuring PFK activities for various trypanosomatid species is vital for accurate metabolic control analysis.

As discussed in **section 1.3.5** in **chapter 1**, metabolic control analysis is a powerful method of characterising and ranking glycolytic targets according to their effectiveness in controlling overall glycolytic activity in the system. Computer modelling of these systems requires accurate and representative kinetic data for each enzyme (Haanstra et al., 2017). The data we have gathered for PFK activity in the three trypanosomatid species in this thesis will add the species-specific information required to build up a specific model of glycolysis in each organism.

While maximal activity and affinity constants for ATP and F6P were comparable between *T. brucei* and *T. cruzi* PFKs, *L. infantum* PFK had a considerably lower affinity for F6P, as well as a lower maximal activity. While perhaps a simplified approach, the cell and tissue type in which these parasites linger during their infective stage may help to answer why we see such variances in the enzyme activity between species; These environments are summarised for each trypanosomatid species in their human infective life cycles in **table 7.2**. Unlike *T. cruzi* and *L. infantum* parasites, *T. brucei's* life cycle, both in the insect and mammalian host stages is entirely extracellular. *T. cruzi* survives intracellularly in heart and digestive muscle tissues and *Leishmania* parasites evade immune detection by proliferation inside the phagolysosome of macrophages. The window of opportunity for maximal PFK inhibitor efficacy against trypanosomes is mainly in the bloodstream – where both drug bioavailability and trypanosomatid reliance on glycolysis will be at its highest. Glucose concentrations will vary according to extracellular fluid levels, insulin levels and the metabolic state of the host tissue of course, but even in their stage II tissue environments, *T. brucei* and *T. cruzi* parasites are in relatively high glucose environments in the brain, heart and digestive muscle tissues whether intracellular or extracellular (**table 7.2**). This may explain why both overall enzyme activity and affinity for substrates is comparable between *T. brucei* and *T. cruzi* PFKs. *Leishmania* parasites in contrast enter macrophage cells as promastigotes, where they proliferate and transform into an amastigote form and invade other cell types of the immune system intracellularly. Data for glucose levels within phagolysosomes could not be found at the time of writing. It is fair however to assume that phagolysosmes may have a separate metabolic environment to the cytosol of

muscle tissue cells. It is known that *Leishmania spp* are able to use sugars, but undergo metabolic quiescence (a slowing of the metabolism) in these environments (McConville, Saunders, Kloehn, & Dagley, 2015). As *Leishmania* PFK was most affected by AMP, it is possible that the metabolic environment in which *Leishmania* parasites proliferate may be energy deficient – i.e. have high levels of AMP. AMP therefore, more than in *T. brucei* and *T. cruzi* parasites, may act as a potent signaller for a metabolic switch for *Leishmania* spp. – significantly stimulating glycolysis within the trypanosomatid cell. The control of overall metabolic properties of trypanosomes is likely to be dictated mostly through regulation of the expression of the enzymes making up the metabolic pathways – reviewed by (Zikova et al., 2017). Still, AMP appears to play a significant role – greatly increasing the trypanosomatid PFK catalytic efficiency at times when glucose supplies may start to run low. The recent observation of *T. brucei* parasites in adipose and skin tissue adds another metabolic environment in which there may be a switch on the reliance of various metabolic pathways for survival (Capewell et al., 2016; Trindade et al., 2016). The PFK enzyme kinetic parameters gathered for these three disease causing trypanosomatid species in this thesis may provide up-to-date and reliable information for species-specific metabolic modelling studies. It is clear that despite their high sequence identity (69 – 72%) and homology in F6P and ATP binding sites, there are still differences in the overall enzyme activity between the trypanosomatid species.

We have tested trypanosomatid PFKs with gene sequences optimised for expression and purification from bacterial cells. The conclusions we draw from *in vitro* testing of these enzymes therefore must be limited; Post-translational modifications on the enzymes when expressed in the trypanosomatids for example may significantly affect their true *in vivo* activity. A more accurate analysis may require purification of PFK from whole cell lysates of the various trypanosomatid species. Although difficult to carry out due to lab safety requirements (Cat. 3 lab required even for non-human pathogenic *T. b. brucei* strains for example) and lower purification yields compared to *E. coli* expression, gathering kinetic values from *in vivo* PFK samples may give a more accurate picture of the enzyme activity in its true physiological form.

Parasite	Stage I environment	Stage II environment
T. brucei sspp.	Bloodstream. [Glucose] 18+ yr. old male = 4 – 5 mM[1]	Lymph and spinal fluids (extracellular). [Glucose] CSF = and 2.9 – 5.4 mM[2]. Skin and adipose tissues also reported[3,4].
T. cruzi	Bloodstream. [Glucose] 18+ yr. old male = 4 – 5 mM[1]	Heart + Digestive muscle tissue (intracellular) [Glucose] muscle tissue = 70 – 320 µM[5].
Leishmania spp.	Bloodstream. [Glucose] 18+ yr. old male = 4 – 5 mM[1]	Macrophages (intracellular, inside the phagolysosome). [Glucose] in phagolysosome of macrophages = no data available.

Table 7.2: Fact file for glucose concentrations in trypanosomatid human infective stage environments.

1. (Darzy et al., 2006) 2. (Wishart et al., 2008) 3. (Tanowitz, Scherer, Mota, & Figueiredo, 2017) 4. (Capewell et al., 2016) 5. (Cline, Jucker, Trajanoski, Rennings, & Shulman, 1998).

7.3.2 A physiologically relevant reverse PFK reaction.

In **chapter 5** we showed evidence for the 'reverse' PFK reaction carried out by trypanosomatid PFKs. We showed that the production of F6P and ATP from F16BP and ADP was catalysed by the PFK enzyme. Titrations of both ADP and F16BP showed hyperbolic or sigmoidal responses against the enzymes, and the reverse reaction could be inhibited by the CTCB compounds. As we have described in **chapter 6,** the mechanism of trypanosomatid PFK inhibition by these compounds involves the blocking of a dynamic loop that aids in the phosphotransfer from ATP onto F6P in the forward direction. By showing that this same mechanism can be blocked by the compounds in the reverse direction, we have accumulated evidence that indeed the PFK enzyme is able to catalyse the phosphotransfer in both directions. In **chapter 5** we discussed how the

kinetic parameters for the trypanosomatid PFKs in the reverse direction were feasibly close enough to expected F16BP and ADP concentrations to run in reverse under certain physiological conditions. We also discussed how in FBPase null mutants of *T. brucei*, indications of PFK running in reverse was recently observed by the lab of Dr Bringaud at the University of Bordeaux (unpublished, pers. comm.). Unless the FBPase enzyme is somehow inhibited or downregulated, it is still difficult to imagine under what conditions trypanosomatid PFKs would need to carry out the reverse reaction to produce F6P from F16BP *in vivo*. As many plant PPi-PFKs are known to run in reverse, it is tempting to postulate that the ability to run in reverse may be a consequence of trypanosomatid PFKs ancestral divergence to a PPi-PFK and back again (**section 1.4.1, chapter 1**). This is not likely the case however – we have shown through collaborative work with Dr Peter Fernandes within the Walkinshaw lab group, that human muscle, platelet and liver PFK isoforms can too be run in reverse under the correct *in vitro* conditions (data not shown). As mammalian PFKs did not have an evolutionary divergence to PPi-dependence, it is unlikely that the ability to run in reverse is due to this PPi-enzyme lineage.

Showing that the reverse reaction is possible and that it can be inhibited allowed us to reveal more detail into the catalytic mechanism carried out by trypanosomatid PFKs; As shown again in **figure 7.5**, the mechanism for *T. brucei* PFK phosphotransfer has been modelled based on bacterial PFK structures (Evans, 1992; McNae & Martinez-Oyanedel, 2009). The Asp229 residue is responsible for holding the F6P substrate in place, to facilitate the phosphotransfer reaction between it and ATP. This is the catalytic loop that is blocked by CTCB compounds binding to a pocket into which the loop sits. The fact that we can inhibit the reverse reaction shows that this loop is also responsible for the reverse phosphotransfer from F16BP back onto ADP to produce F6P and ATP. If this is the case, the interactions of F6P and F16BP with this Asp229 residue must be the same, allowing the binding of F6P or F16BP with similar affinity. It is interesting that in SPR we were able to record a binding response for F16BP alone against *T. brucei* PFK, but not F6P on its own (**section 4.4.2, chapter 4**). We have explained that ATP binding promotes a conformational change in PFK to an 'active' conformation, capable of binding F6P, and indeed when ATP was present a response for F6P binding in SPR could be recorded (**section 4.4.4, chapter 4**). In the presence of ATP a binding response for F16BP could not be measured. This is not surprising considering the phosphates would overlap. As the affinity for ATP is much greater than for F16BP (**table 7.3**), ATP will be bound preferentially. This suggests that the 'active' PFK enzyme state induced upon ATP binding promotes specificity for F6P as a substrate for the forward reaction over F16BP as a substrate for the reverse reaction.

	ADP	ATP	F6P	F16BP
SS K_d (µM)	558 ± 80	16 ± 2	No response	4600 ± 122
SS K_d (+ATP) (µM)	1677 ± 194	NA	Weak (>10 mM)	No response

Table 7.3: Dissociation constants for PFK substrates against TbPFK.

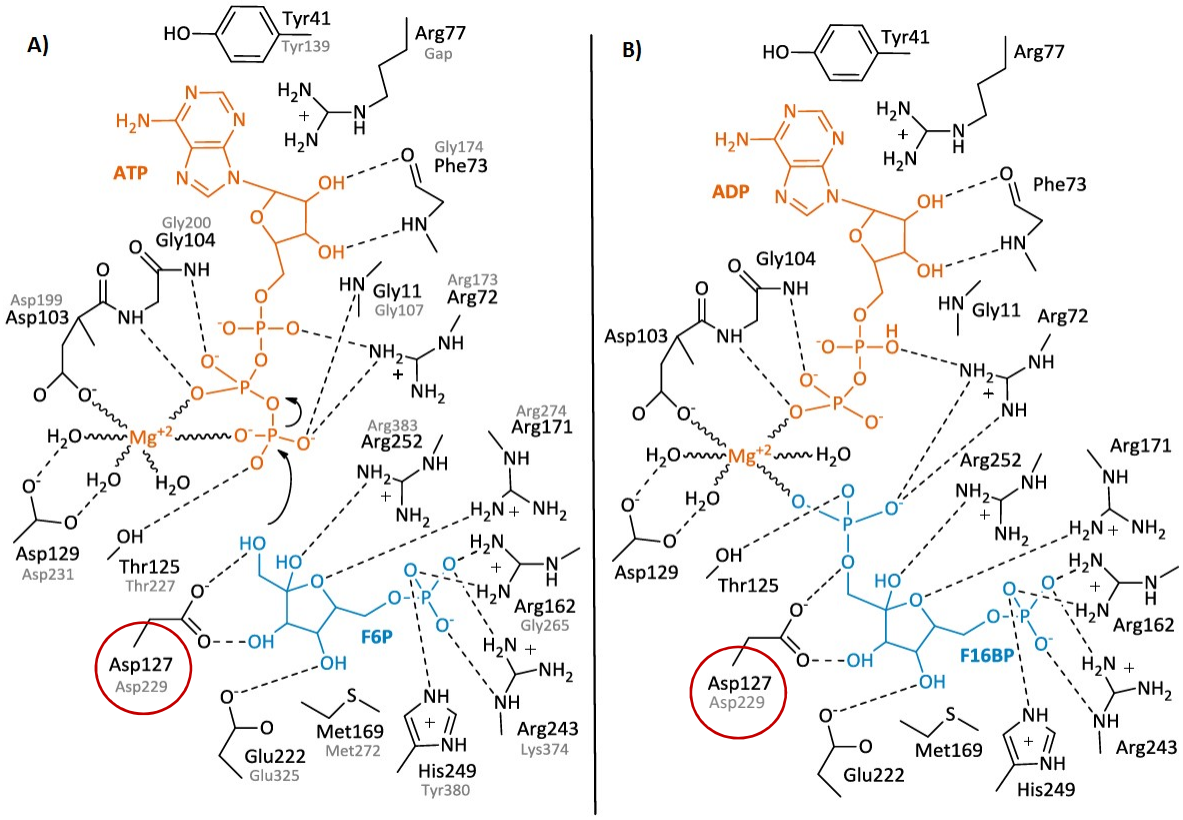

Figure 7.5: catalytic mechanism of bacterial ATP-dependant PFK.

Adapted from Evans et al(Evans, 1992). A) From E. coli crystal structure. Corresponding T. brucei PFK residues shown in grey B) from B. stearothermophilus structure.

Enzymes can speed up the rate of a reaction, but cannot alter the equilibrium of the reaction. Considering this, the thermodynamics of the forward and reverse reactions, and not the kinetics of the reaction may answer if the reverse reaction is feasible or not. The free energy change involved in the Ppi-kinase reaction is less than the ATP reaction (**figure 7.6**). This means for the

reverse reaction involving PPi, less of an energy cost is required. This may be the reason why most PFKs that are known to run in reverse *in vivo* (plant PPi-kinases) are able to do so.

$$\Delta G^{o} (PPi + F6P \rightarrow F16BP + Pi) = -2.1 \text{ Kcal/mol}$$

$$\Delta G^{o} (ATP + F6P \rightarrow F16BP + ADP) = -4.4 \text{ Kcal/mol.}$$

Figure 7.6: Free energy of PPi and ATP-kinase reactions.

7.4. CTCB compounds are excellent drug candidates against HAT.

The main driving force behind the work carried out in this PhD project has stemmed from the overall goal of the Seeding Drug Discovery program; to design novel small molecule inhibitors of *T. brucei* PFK as drug candidates against Human African Trypanosomiasis. We have shown in this thesis that inhibition of *T. brucei* PFK translates to equally potent killing of cultured *T. b. brucei* parasites. As PFK holds a lower ranking position in terms of flux control in *T. brucei* (**section 1.3.5, chapter 1**), it is important that inhibitors designed against the enzyme are selective against the parasite and not the human host enzyme. We have shown that the CTCB compounds are exactly that; they bind in a 1:1 stoichiometry to a unique allosteric pocket found proximal to the active site of *T. brucei* PFK. They are not promiscuous binders , do not compete with the physiological substrates of the enzyme, and are small molecules – the average size of the 636 CTCB compounds was 320 Da. The selectivity of the compounds over the human PFK enzyme is clearly due to the CTCB binding pocket, which is incomplete in the human PFK structure (**figure 7.7**) These attributes make the CTCB compounds very promising 'druggable' compounds. Effective drugs however must have many other attributes despite a specific and tight interaction with their target;

Out of the six CTCB compounds taken forward into dose-tolerance assays in mice, three showed cure of stage I HAT models in mice – CTCB 405, CTCB 470 and CTCB 508.

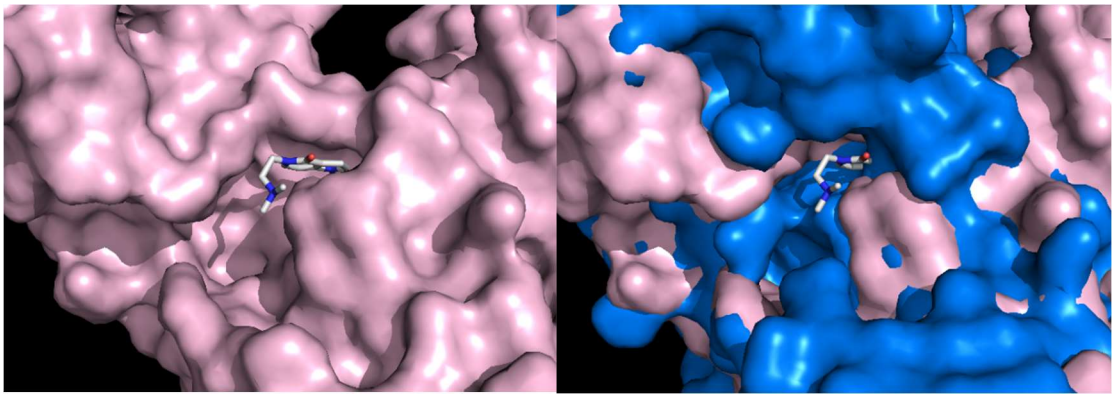

Figure 7.7 : The CTCB binding pocket is not present in Human PFK platelet isoform.

Overlay of TbPFK (pink) with CTCB 405 (sticks) bound (unpublished structure) with human PFK-P (4XYJ) (Blue). TbPFK-CTCB 405 structure resolution = 2.8 Å (per. comm I. McNae, UoE), human PFK-P resolution = 3.1 Å (Webb et al., 2015).

7.4.1 CTCB compounds were rapid killers of T. brucei parasites.

During *in vitro* assays to establish the EC_{50} ("effective concentration" required for 50% death of parasites) for CTCB compounds against cultured *T. b. brucei* parasites it was found that CTCB compounds killed the parasites much quicker than existing treatments such as Suramin and other compounds in development (Fexinidazole and SCYX-7158) (Jacobs et al., 2011). **Figure 7.8** shows the parasite killing profiles of CTCB 405 alongside these existing compounds against '*T. b. brucei* parasites of the GVR35Luc2 cell line. This cell line is derived from the GVR35 strain; it produces a luciferase enzyme that emits a luminescent signal with the addition of luciferin – showing the presence of ATP and thus providing an indication of cell viability. As we can see in **figure 7.8**, CTCB 405 rapidly blocks ATP production and kills cells within 30 minutes, compared to the other compounds which take at least 12 hours to elicit complete killing of the parasite culture. It is clear that the inhibition of the *T. brucei* PFK enzyme is a highly effective killer of the bloodstream form parasites, and validates our finding that CTCB potency against the enzyme correlates well with parasite death.

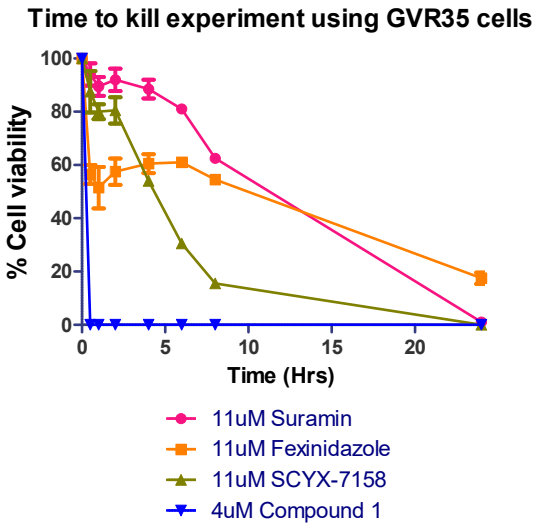

Figure 7.8: CTCB 405 blocks leads to a rapid cell death of T. b. brucei GVR35 trypanosomes.

GVR35Luc2 T. b. brucei cells modified for luciferase expression (gives luminescent signal when ATP is being produced. All cells tested in modified HMI-9 medium with 20% FCS. Data collected by L. Yen (UoE).

7.4.2 CTCB compounds had promising pharmacological profiles.

'ADME' (Absorption, Distribution, Metabolism and Excretion) profiles were generated for all CTCB compounds that were considered for testing in mice. **Table 7.4** shows the pharmacological profiles for the three CTCB compounds taken forward to show cure of stage I HAT in mice.

The CTCB compounds have strong target selectivity – with high potency against both the enzyme (IC_{50} / 0.2 µM) and cultured parasites (EC_{50} ~ 0.3 µM), the compounds in **table 7.4** show no inhibition of the human muscle PFK isoform ('*h*PFK) and kill human liver hepatocytes (HepG2 cells) at much higher concentrations. This is reflected in the high 'cellular selectivity' indices given – the ratio of EC_{50} (HepG2 cells) : EC_{50}(*T. b. brucei* cells).

CTCB compounds also show good metabolic stability – half-life in mouse liver microsomes (MLM) range from 15 – 25 minutes. Half-life values for existing drugs (in Human Liver Microsomes – HLM) range from 4 minutes (Midazolam) to as much as 66 minutes (Amobarbital) (Obach, 1999). Drug metabolism and clearance occurs predominantly in the liver and kidneys – many existing drug compounds are known to be cleared by liver hepatocytes (Obach, 1999). The CTCB compounds shown in **table 7.4** have moderate intrinsic clearance rates of 56 – 70 µL/min/mg in mouse liver microsomes. This sits in the middle of the range of known clearance rates of existing drugs in human microsomes – ranging from 0.52 – 189 µL/min/mg for the drugs Warfarin and Verapamil, respectively (Obach, 1999).

As we showed in **section 6.4.4, chapter 6**, the majority of CTCB compounds had very weak or no affinity for human serum albumin (HSA). This is shown indeed by the low binding rate of the CTCB compounds to both human and mouse plasma protein as shown in **table 7.4**. This ensures a high bioavailability of the inhibitor in the bloodstream – the environment which offers the window of opportunity for most effective killing of the trypanosomes due to their metabolic reliance on glycolysis. The IC_{50} and EC_{50} values for CTCB 405, '470 and '508 are all ~ 0.2 and ~0.3 µM respectively (**table 7.4**). With even a single dose of compound, the plasma concentration is ~3X higher than the EC_{50} requirement for each of the compounds – under these concentrations the parasite population in the blood should be completely killed. With a 3x 100 mg/Kg dose over 2 days the plasma compound levels for both 405 and 470 are greater than 4 µM at 2 hours following the last dose. Considering the compounds kill parasites *in vitro* in under 30 mins at this concentration (**figure 7.8**), there is an ample window of opportunity to clear the parasites from the blood considering all of these measured parameters. Again the IC_{50} and EC_{50} measurements show that effective inhibition of PFK correlated well with parasite death both *in vitro* and *in vivo*.

Parameter	CTCB-405	CTCB-470	CTCB-508
	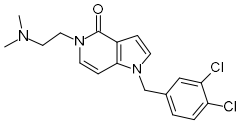	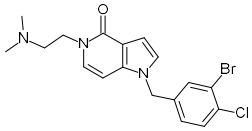	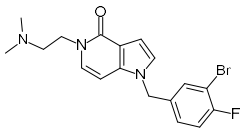
SELECTIVITY			
*Tb*PFK IC_{50} (µM)	0.19	0.21	0.20
*h*PFK IC_{50} (µM)	> 100	> 100	> 100
Tbb EC_{50} (µM)	0.37	0.31	0.3
HepG2 EC_{50} (µM)	20.8	12.3	33.4
Cellular Selectivity	56	39	111
METABOLIC STABILITY			
MLM Cl_{int} (µL/min/mg)	70	91	56
MLM $t_{1/2}$ (min)	19.6	15.2	24.6
HLM Cl_{int} (µL/min/mg)	<8.6	-	-
BINDING AND EFFLUX			
Mouse PPB (%unbound)	94.2%	94%	82%
Human PPB (%unbound)	93.7%	96.8%	79.3%

Table 7.4: ADME profiles for CTCB compounds that lead to a cure of stage I HAT in mice.

TbPFK = T. brucei PFK. hPFK = human muscle PFK. MLM = mouse liver microsomes. HLM = human liver microsomes. PPB = plasma protein binding.

Highest tolerated dose (HTD) studies were carried out in mice with five of the CTCB compounds and the plasma concentrations of compound were measured 2 hours after each dose. The blood concentration levels of CTCB 405, ‘470 and ‘508 in mice under various dosing regimens are given in **table 7.5**.

	Plasma conc. (µM) (2hr after final dose)		
Dose scheme	**CTCB 405**	**CTCB 470**	**CTCB 508**
1 x 50 mg/Kg dose	0.86	0.89	**0.78**
3 x 50 mg/Kg doses daily for 2 days	6.8	1.8	5.0
3 x 100 mg/Kg doses daily for 2 days	9.8	4.8	ND

Table 7.5: Mice blood plasma concentrations of CTCB compounds after oral administration.

Powdered stocks of CTCB compounds were administered using oral gavage to C41 strain mice. Blood samples measured by tail snips. Data collected by D. Malik (UoE) and Selcia Ltd.

7.4.3 CTCB compounds resulted in cure of stage I HAT.

The overarching focus of the SDD was to design small molecule inhibitors of *T. brucei* PFK as novel drug candidates against Human African Trypanosomiasis. All three of the CTCB compounds described in **table 7.4** resulted in a cure of stage I HAT in mice infected with *T. b. brucei* Lister 427 strain parasites. A relapse of parasites was observed when the same drugs were used in studies involving mice infected *with T. b. brucei* Lister-427 infected mice, however **figure 7.9** shows the clearance of fluorescent GVR35Luc2 *T. b. brucei* parasites from mice through oral dosing with CTCB 470 and CTCB 508. The relapse of parasites in the stage II HAT mice models was seen by a return of luminescent signal in the brain region, followed by the abdomen (data not shown). This suggests both that insufficient amounts of CTCB compound were available in the brain for a complete cure of the parasite population, and that perhaps a number of parasites were dormant in the adipose tissue of the abdomen or skin, as suggested by recent findings (Capewell et al., 2016; Trindade et al., 2016).

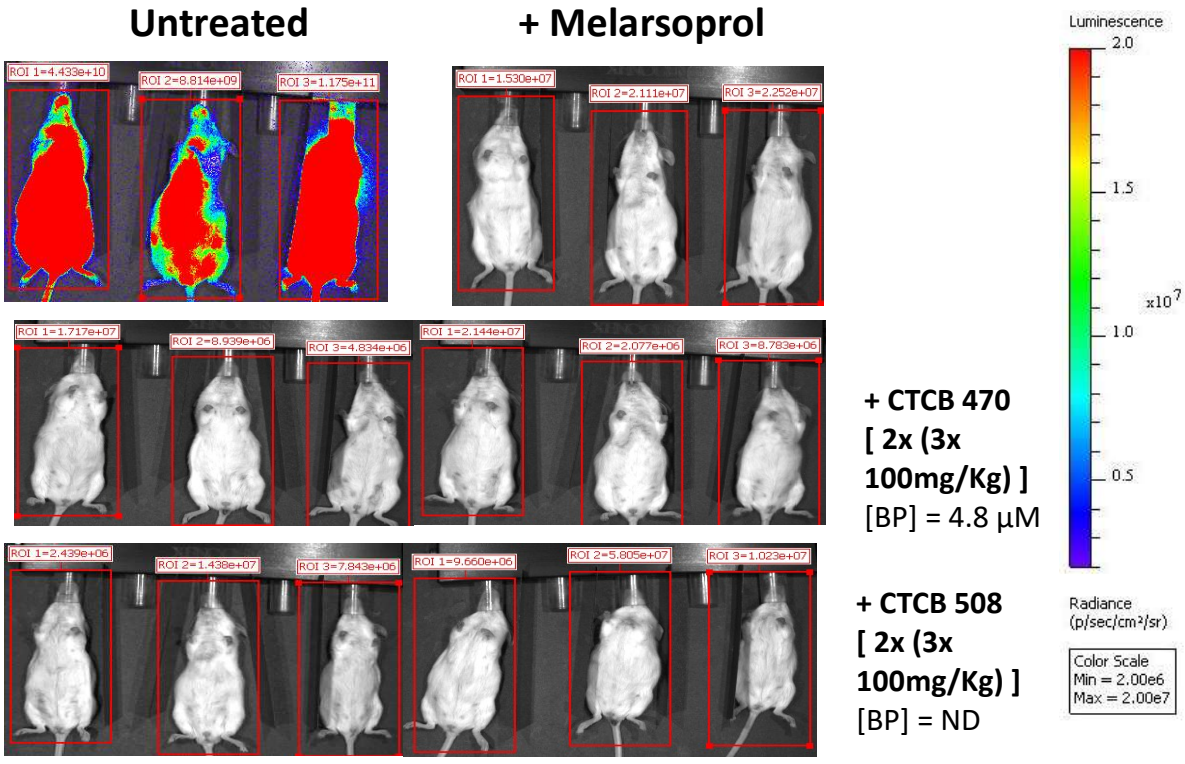

Figure 7.9: CTCB 470 and CTCB 508 result in a cure of stage I HAT in mice.

Imaging of stage I T. brucei brucei infected C41 mice at day 7 post treatment. Melarsoprol is an existing HAT treatment with high mortality rates and toxic side effects. Efficacy monitored using transgenic luminescent parasites (GVR35Luc2 strain). [BP] = concentration of compound in blood plasma. Data measured by D. Malik (UoE) using facilities provided by University of Glasgow.

7.4.4 Future directions for SDD project.

Going forward, the main focus of the SDD work will be to optimise the lead compound to increase penetration of compound into the brain, in order to kill parasites in the stage II form of the disease. The average molecular weight of the CTCB compounds was 319.9 Da, and the most successful azabenzimidazole scaffold series (like those shown in **table 7.4**) has scope for increased groups to be added or modified. The more basic compounds generally performed better when tested against the *in vitro* cultured *T. b. brucei* parasites (**section 6.2.5, chapter 6**) and the lead compounds taken forward for mice studies clearly have a suitable balance in affinity against the target enzyme (IC_{50}^{PFK}) and characteristics to effectively enter the parasite (EC_{50}). More work therefore will need to be carried out to improve the characteristics of the compounds for crossing the blood-brain-barrier. This is possible, as shown by the revisiting of *T. brucei* N-Myristoyltransferase Inhibitors from a group in Dundee, who managed to improve the brain penetration of their lead series to better improve its stage II HAT characteristics (Bayliss et al., 2017).

The latest implementation of Fexinidazole as an orally administered treatment of stage II HAT by the DNDi (Drugs for Neglected Diseases initiative) has been a remarkable success story (Pollastri, 2017). Despite this, it is still important to feed more potential drug compounds into the 'pipeline' of drug development against HAT – to ensure a range of possible treatments can be used to attempt to tackle drug resistance and availability. It would be extremely advantageous therefore to continue development of the CTCB compounds since they are tight and specific inhibitor compounds, have shown no toxicity in mice models, show excellent ADME profiles and have a known target and mode of action, as we have described in this thesis.

References.

Aguilar, Z., & Urbina, J. A. (1986). The phosphofructokinase of Trypanosoma (Schizotrypanum) cruzi: purification and kinetic mechanism. *Molecular and Biochemical Parasitology*, *21*(2), 103–111. https://doi.org/10.1016/0166-6851(86)90013-7

Akpunarlieva, S., Weidt, S., Lamasudin, D., Naula, C., Henderson, D., Barrett, M., … Burchmore, R. (2017). Integration of proteomics and metabolomics to elucidate metabolic adaptation in Leishmania. *Journal of Proteomics*, *155*, 85–98. https://doi.org/10.1016/j.jprot.2016.12.009

Albe, K. R., Butler, M. H., & Wright, B. E. (1990). Cellular concentrations of enzymes and their substrates. *Journal of Theoretical Biology*, *143*(2), 163–195. https://doi.org/10.1016/S0022-5193(05)80266-8

Albert, M. A., Haanstra, J. R., Hannaert, V., Van Roy, J., Opperdoes, F. R., Bakker, B. M., & Michels, P. a M. (2005). Experimental and in silico analyses of glycolytic flux control in bloodstream form Trypanosoma brucei. *Journal of Biological Chemistry*, *280*(31), 28306–28315. https://doi.org/10.1074/jbc.M502403200

Alsford, S., Eckert, S., Baker, N., Glover, L., Sanchez-Flores, A., Leung, K. F., … Horn, D. (2012a). High-throughput decoding of antitrypanosomal drug efficacy and resistance. *Nature*, *482*(7384), 232–236. https://doi.org/10.1038/nature10771

Alsford, S., Eckert, S., Baker, N., Glover, L., Sanchez-Flores, A., Leung, K. F., … Horn, D. (2012b). High-throughput decoding of antitrypanosomal drug efficacy and resistance. *Nature*, *482*(7384), 232–236. https://doi.org/10.1038/nature10771

Arechaga, I., Martínez-Costa, O. H., Ferreras, C., Carrascosa, J. L., & Aragón, J. J. (2010). Electron microscopy analysis of mammalian phosphofructokinase reveals an unusual 3-dimensional structure with significant implications for enzyme function. *The FASEB Journal : Official Publication of the Federation of American Societies for Experimental Biology*, *24*(12), 4960–4968. https://doi.org/10.1096/fj.10-165845

Auzat, I., & Garel, J. (1992). pH dependence of the reverse reaction catalyzed by phosphofructokinase I from Escherichia coli: Implications for the role of Asp 127. *Protein Science*, *1*, 254–258.

Bakker, B. M., Walsh, M. C., ter Kuile, B. H., Mensonides, F. I., Michels, P. a, Opperdoes, F. R., & Westerhoff, H. V. (1999). Contribution of glucose transport to the control of the glycolytic flux in Trypanosoma brucei. *Proceedings of the National Academy of Sciences of the United States of America*, *96*(August), 10098–10103. https://doi.org/10.1073/pnas.96.18.10098

Bakker, B. M., Westerhoff, H. V, Opperdoes, F. R., & Michels, P. a. . (2000). Metabolic control analysis of glycolysis in trypanosomes as an approach to improve selectivity and effectiveness of drugs. *Molecular and Biochemical Parasitology*, *106*(1), 1–10. https://doi.org/10.1016/S0166-6851(99)00197-8

Banaszak, K., Mechin, I., Obmolova, G., Oldham, M., Chang, S. H., Ruiz, T., … Rypniewski, W. (2011). The crystal structures of eukaryotic phosphofructokinases from Baker's yeast and rabbit skeletal muscle. *Journal of Molecular Biology*, *407*(2), 284–297. https://doi.org/10.1016/j.jmb.2011.01.019

Bapteste, E., Moreira, D., & Philippe, H. (2003). Rampant horizontal gene transfer and phospho-donor change in the evolution of the phosphofructokinase. *Gene*, *318*(1–2), 185–191. https://doi.org/10.1016/S0378-1119(03)00797-2

Barrett, M. P. (2006). The rise and fall of sleeping sickness, *367*, 1377–1378.

Barrett, M. P., & Croft, S. L. (2012). Management of trypanosomiasis and leishmaniasis. *British Medical Bulletin*, *104*, 175–196. https://doi.org/10.1093/bmb/lds031

Barros-Alvarez X, Gualdron-Lopez M, Acosta H, Caceres A.J, Graminha M.A.S, Michels P.A.M, Concepcion J.L, Q. W. (2014). Glycosomal Targets for Anti-Trypanosomatid Drug Discovery, 1679–1706.

Bayliss, T., Robinson, D. A., Smith, V. C., Brand, S., Mcelroy, S. P., Torrie, L. S., … Wyatt, P. G. (2017). Design and Synthesis of Brain Penetrant Trypanocidal N‐Myristoyltransferase Inhibitors. https://doi.org/10.1021/acs.jmedchem.7b01255

Bennett, B., Kimball, E., & Gao, M. (2009). Absolute metabolite concentrations and implied enzyme active site occupancy in Escherichia coli. *Nature Chemical …*, *5*(8), 593–599. https://doi.org/10.1038/nchembio.186.Absolute

Berens, R. Marr, J. (1977). Phosphofructokinase of Leishmania donovani and Leishmania braziliensis and its Role in Glycolysis. *J.protozool.*, *24*(2), 340–344.

Biéler, S., Waltenberger, H., Barrett, M. P., McCulloch, R., Mottram, J. C., Carrington, M., … Ndung'u, J. M. (2016). Evaluation of Antigens for Development of a Serological Test for Human African Trypanosomiasis. *PLOS ONE*, *11*(12), e0168074. Retrieved from https://doi.org/10.1371/journal.pone.0168074

Brimacombe, K. R., Walsh, M. J., Liu, L., Morgan, H. P., Mcnae, I., Fothergill-gilmore, L. A., … Boxer, M. B. (2014). Identification of ML251, a Potent Inhibitor of T. brucei and T. cruzi Phosphofructokinase, 8–13.

Brun, R., Blum, J., Chappuis, F., & Burri, C. (2010). Human African trypanosomiasis. *Lancet*, *375*(9709), 148–59. https://doi.org/10.1016/S0140-6736(09)60829-1

Caceres, A. J., Michels, P. A. M., & Hannaert, V. (2010). Genetic validation of aldolase and glyceraldehyde-3-phosphate dehydrogenase as drug targets in Trypanosoma brucei. *Molecular and Biochemical Parasitology*, *169*(1), 50–54. https://doi.org/10.1016/j.molbiopara.2009.09.001

Capewell, P., Cren-Travaillé, C., Marchesi, F., Johnston, P., Clucas, C., Benson, R. A., … MacLeod, A. (2016). The skin is a significant but overlooked anatomical reservoir for vector-borne African trypanosomes. *eLife*, *5*(September2016), 1–17. https://doi.org/10.7554/eLife.17716

Carlisle, M., Blakeleys, D., Hemmingsenzll, S. M., Kruger, J., Dennis, D. T., & Trevanionii, J. (1990). Pyrophosphate-dependent, *265*(30), 18366–18371.

Carter, N. S., & Fairlamb, A. H. (1993). Arsenical-resistant trypanosomes lack an unusual adenosine transporter. *Nature*, *361*(6408), 173–176. https://doi.org/10.1038/361173a0

Cascante, M., Boros, L. G., Comin-anduix, B., Atauri, P. De, Centelles, J. J., & Lee, P. W. (2002). Metabolic control analysis in drug discovery and disease, *20*(March), 243–249.

Chen, H., Engkvist, O., & Kogej, T. (2015). *Compound Properties and Their Influence on Drug Quality*. *The Practice of Medicinal Chemistry: Fourth Edition*. Elsevier Ltd. https://doi.org/10.1016/B978-0-12-417205-0.00015-8

Chevalier, N., Bertrand, L., Rider, M. H., Opperdoes, F. R., Rigden, D. J., & Michels, P. A. M. (2005). 6-phosphofructo-2-kinase and fructose-2,6-bisphosphatase in Trypanosomatidae., *272*, 3542–3560. https://doi.org/10.1111/j.1742-4658.2005.04774.x

Claustre, S., Denier, C., Lakhdar-ghazal, F., Lopez, C., Chevalier, N., Michels, P. A. M., … Sabatier, P. (2002). Articles Exploring the Active Site of Trypanosoma brucei Phosphofructokinase by Inhibition Studies : Specific Irreversible Inhibition †, *41*(32).

Cleghorn, L. a. T., Albrecht, S., Stojanovski, L., Simeons, F. R. J., Norval, S., Kime, R., … Gilbert, I. H. (2015). Discovery of Indoline-2-carboxamide Derivatives as a New Class of Brain-Penetrant Inhibitors of *Trypanosoma brucei*. *Journal of Medicinal Chemistry*, *1*(Figure 1), 150929154044000. https://doi.org/10.1021/acs.jmedchem.5b00596

Cline, G. W., Jucker, B. M., Trajanoski, Z., Rennings, A. J., & Shulman, G. I. (1998). A novel 13C NMR method to assess intracellular glucose concentration in muscle, in vivo. *The American Journal of Physiology*, *274*(2 Pt 1), E381-9.

Colasante, C., Peña Diaz, P., Clayton, C., & Voncken, F. (2009). Mitochondrial carrier family inventory of Trypanosoma brucei brucei: Identification, expression and subcellular localisation. *Molecular and Biochemical Parasitology*, *167*, 104–117. https://doi.org/10.1016/j.molbiopara.2009.05.004

Cooper, M. A. (2002). Optical biosensors in drug discovery. *Nature Reviews Drug Discovery*, *1*, 515. Retrieved from http://dx.doi.org/10.1038/nrd838

Cordeiro, A. T., & Thiemann, O. H. (2010). 16-Bromoepiandrosterone, an activator of the mammalian immune system, inhibits glucose 6-phosphate dehydrogenase from Trypanosoma cruzi and is toxic to these parasites grown in culture. *Bioorganic and Medicinal Chemistry*, *18*(13), 4762–4768. https://doi.org/10.1016/j.bmc.2010.05.008

Cordeiro, A. T., Thiemann, O. H., & Michels, P. a M. (2009). Inhibition of Trypanosoma brucei glucose-6-phosphate dehydrogenase by human steroids and their effects on the viability of cultured parasites. *Bioorganic and Medicinal Chemistry*, *17*(6), 2483–2489. https://doi.org/10.1016/j.bmc.2009.01.068

Creek, D. J., Mazet, M., Achcar, F., Anderson, J., Kim, D. H., Kamour, R., … Barrett, M. P. (2015). Probing the Metabolic Network in Bloodstream-Form Trypanosoma brucei Using Untargeted Metabolomics with Stable Isotope Labelled Glucose. *PLoS Pathogens*, *11*(3), 1–25. https://doi.org/10.1371/journal.ppat.1004689

Cronin, C. N., & Tipton, K. F. (1985). Purification and regulatory properties of phosphofructokinase from Trypanosoma (Trypanozoon) brucei brucei. *The Biochemical Journal*, *227*(1), 113–24. Retrieved from http://www.pubmedcentral.nih.gov/articlerender.fcgi?artid=1144815&tool=pmcentrez&rendertype=abstract

Cronin, C. N., & Tipton, K. F. (1987). Kinetic studies on the reaction catalysed by phosphofructokinase from Trypanosoma brucei. *The Biochemical Journal*, *245*(1), 13–8. Retrieved from http://www.pubmedcentral.nih.gov/articlerender.fcgi?artid=1148076&tool=pmcentrez&rendertype=abstract

Danchin, A., Dondon, L., & Daniel, J. (1984). Metabolic alterations mediated by 2-ketobutyrate in Escherichia coli K12. *Molecular and General Genetics MGG*, *193*(3), 473–478. https://doi.org/10.1007/BF00382086

Dardonville, C., Rinaldi, E., Barrett, M. P., Brun, R., Gilbert, I. H., & Hanau, S. (2004). Selective inhibition of Trypanosoma brucei 6-phosphogluconate dehydrogenase by high-energy intermediate and transition-state analogues. *Journal of Medicinal Chemistry*, *47*(Figure 2), 3427–3437. https://doi.org/10.1021/jm031066i

Darzy, K., Murray, R., Gleeson, H., Pezzoli, S., Thorner, M., & Shalet, S. (2006). The Impact of Short-Term Fasting on the Dynamics of 24-Hour Growth Hormone (GH) Secretion in Patients with Severe Radiation-Induced GH Deficiency. *Clinical Endocrinology & Metabolism*, *91*(3), 987–994.

de Koning, H. P. (2008). Ever-increasing complexities of diamidine and arsenical crossresistance in African trypanosomes. *Trends in Parasitology*, *24*(8), 345–349. https://doi.org/10.1016/j.pt.2008.04.006

Deramchia, K., Morand, P., Biran, M., Millerioux, Y., Mazet, M., Wargnies, M., … Bringaud, F. (2014). Contribution of pyruvate phosphate dikinase in the maintenance of the glycosomal ATP/ADP balance in the Trypanosoma brucei procyclic form. *Journal of Biological Chemistry*, *289*(25), 17365–17378. https://doi.org/10.1074/jbc.M114.567230

Dunaway, G. A. (1983). A review of animal phosphofructokinase isozymes with an emphasis on their physiological role. *Molecular and Cellular Biochemistry*, *52*(1), 75–91.

Dunaway, G. a, Kasten, T. P., Sebo, T., & Trapp, R. (1988). Analysis of the phosphofructokinase subunits and isoenzymes in human tissues. *The Biochemical Journal*, *251*(3), 677–83. Retrieved from

http://www.pubmedcentral.nih.gov/articlerender.fcgi?artid=1149058&tool=pmcentrez&rendertype=abstract

Ehrlich, P. (1913). Address in Pathology, ON CHEMIOTHERAPY: Delivered before the Seventeenth International Congress of Medicine. *British Medical Journal*, *2*(2746), 353–9. https://doi.org/10.1136/bmj.2.2746.353

Evans, P. R. (1992). Activity and allosteric regulation in bacterial phosphofructokinase. https://doi.org/10.1074/jbc.270.8.3828

Evans, P. R., Farrants, G. W., Hudson, P. J., & Britton, H. G. (1981). Phosphofructokinase: Structure and Control [and Discussion]. *Philosophical Transactions of the Royal Society of London. B, Biological Sciences*, *293*(1063), 53 LP-62. Retrieved from http://rstb.royalsocietypublishing.org/content/293/1063/53.abstract

Fasano, M., Curry, S., Terreno, E., Galliano, M., Fanali, G., Narciso, P., … Ascenzi, P. (2005). The extraordinary ligand binding properties of human serum albumin. *IUBMB Life*, *57*(December), 787–796. https://doi.org/10.1080/15216540500404093

Fernandes, a P., Nelson, K., & Beverley, S. M. (1993). Evolution of nuclear ribosomal RNAs in kinetoplastid protozoa: perspectives on the age and origins of parasitism. *Proceedings of the National Academy of Sciences of the United States of America*, *90*(December), 11608–11612. https://doi.org/10.1073/pnas.90.24.11608

Frearson, J. a, Brand, S., McElroy, S. P., Cleghorn, L. a T., Smid, O., Stojanovski, L., … Wyatt, P. G. (2010). N-myristoyltransferase inhibitors as new leads to treat sleeping sickness. *Nature*, *464*(7289), 728–32. https://doi.org/10.1038/nature08893

Freyer, M. W., & Lewis, E. A. (2008). Isothermal Titration Calorimetry : Experimental Design , Data Analysis , and Probing Macromolecule / Ligand Binding and Kinetic Interactions. *Methods in Cell Biology*, *84*(7), 79–113. https://doi.org/10.1016/S0091-679X(07)84004-0

Freymann, D. M., Wenck, M. A., Engel, J. C., Feng, J., Focia, P. J., Y, A. E. E., & Iii, S. P. C. (2000). Efficient identification of inhibitors targeting the closed active site conformation of the HPRT from Trypanosoma cruzi. *Chemistry & Biology*, *7*, 957–968.

Galland, N., & Michels, P. A. M. (2010). Comparison of the peroxisomal matrix protein import system of different organisms. Exploration of possibilities for developing inhibitors of the import system of trypanosomatids for anti-parasite chemotherapy. *European Journal of Cell Biology*, *89*(9), 621–637. https://doi.org/10.1016/j.ejcb.2010.04.001

GE Healthcare. (n.d.). Biacore T200. *Interactions*, *28-9808–83*(Edition AA), 9–22.

Ginger, M. L., Ngazoa, E. S., Pereira, C. A., Pullen, T. J., Kabiri, M., Becker, K., … Steverding, D. (2005). Intracellular positioning of isoforms explains an unusually large adenylate kinase gene family in the parasite Trypanosoma brucei. *The Journal of Biological Chemistry*, *280*(12), 11781–9. https://doi.org/10.1074/jbc.M413821200

Gobbi, P., Lo Presti, M. S., Fernández, A. R., Enders, J. E., Fretes, R., Gea, S., … Rivarola, H. W. (2007). Allopurinol is effective to modify the evolution of Trypanosoma cruzi infection in mice. *Parasitology Research*, *101*, 1459–1462. https://doi.org/10.1007/s00436-007-0644-2

Gutteridge, W. E. (1985). Existing chemotherapy and its limitations. *British Medical Bulletin*, *41*(2), 162–168.

Haanstra, J. R., Gerding, A., Dolga, A. M., Sorgdrager, F. J. H., Buist-Homan, M., Du Toit, F., … Bakker, B. M. (2017). Targeting pathogen metabolism without collateral damage to the host. *Scientific Reports*, *7*(December 2016), 1–15. https://doi.org/10.1038/srep40406

Haanstra, J. R., van Tuijl, A., Kessler, P., Reijnders, W., Michels, P. A. M., Westerhoff, H. V, … Bakker, B. M. (2008). Compartmentation prevents a lethal turbo-explosion of glycolysis in trypanosomes.

Proceedings of the National Academy of Sciences of the United States of America, *105*(46), 17718–23. https://doi.org/10.1073/pnas.0806664105

Hall, B. S., Bot, C., & Wilkinson, S. R. (2011). Nifurtimox activation by trypanosomal type I nitroreductases generates cytotoxic nitrile metabolites. *Journal of Biological Chemistry*, *286*(15), 13088–13095. https://doi.org/10.1074/jbc.M111.230847

Hassell, A. M., An, G., Bledsoe, R. K., Bynum, J. M., Carter, H. L., Deng, S. J. J., … Shewchuk, L. M. (2006). Crystallization of protein-ligand complexes. *Acta Crystallographica Section D: Biological Crystallography*, *63*(1), 72–79. https://doi.org/10.1107/S0907444906047020

Heinisch, J., Ritzel, R. G., von Borstel, R. C., Aguilera, A., Rodicio, R., & Zimmermann, F. K. (1989). The phosphofructokinase genes of yeast evolved from two duplication events. *Gene*, *78*(2), 309–321. https://doi.org/10.1016/0378-1119(89)90233-3

Holdgate, G. A. (2001). Making cool drugs hot: Isothermal titration calorimetry as a tool to study binding energetics. *BioTechniques*, *31*(1), 164–184.

Jacobs, R. T., Nare, B., Wring, S. a, Orr, M. D., Chen, D., Sligar, J. M., … Don, R. (2011). SCYX-7158, an orally-active benzoxaborole for the treatment of stage 2 human African trypanosomiasis. *PLoS Neglected Tropical Diseases*, *5*(6), e1151. https://doi.org/10.1371/journal.pntd.0001151

Kaiser, M., Bray, M. A., Cal, M., Trunz, B. B., Torreele, E., & Brun, R. (2011). Antitrypanosomal activity of fexinidazole, a new oral nitroimidazole drug candidate for treatment of sleeping sickness. *Antimicrobial Agents and Chemotherapy*, *55*(12), 5602–5608. https://doi.org/10.1128/AAC.00246-11

Keillor, J. W., Lherbet, C., Castonguay, R., Lapierre, D., Martinez-Oyanedel, J., Fothergill-Gilmore, L. A., & Walkinshaw, M. D. (2003). Expression, purification, crystallization and preliminary crystallographic analysis of Trypanosoma brucei phosphofructokinase. *Acta Crystallographica - Section D Biological Crystallography*, *59*(3), 532–534. https://doi.org/10.1107/S0907444902023478

Kemp, R. G., & Tripathi, R. L. (1993). Pyrophosphate-dependent phosphofructo-1-kinase complements fructose 1,6- bisphosphatase but not phosphofructokinase deficiency in Escherichia coli. *Journal of Bacteriology*, *175*(17), 5723–5724.

Khare, S., Nagle, A. S., Biggart, A., Lai, Y. H., Liang, F., Davis, L. C., … Wen, B. G. (2016). AC AT AR TI ER AT AR TI. *Nature Publishing Group*, 1–24. https://doi.org/10.1038/nature19339

Koshland, D. E., & Hamadani, K. (2002). Proteomics and Models for. https://doi.org/10.1074/jbc.R200014200

Koutinas, A. F., Saridomichelakis, M. N., Mylonakis, M. E., Leontides, L., Polizopoulou, Z., Billinis, C., … Papadopoulos, O. (2001). A randomised, blinded, placebo-controlled clinical trial with allopurinol in canine leishmaniosis. *Veterinary Parasitology*, *98*, 247–261. https://doi.org/10.1016/S0304-4017(01)00399-5

Kuntz, I. D., Chen, K., Sharp, K. A., & Kollman, P. A. (1999). The maximal affinity of ligands. *Proceedings of the National Academy of Sciences*, *96*(18), 9997–10002. https://doi.org/10.1073/pnas.96.18.9997

Lanteri, C. A., Tidwell, R. R., & Meshnick, S. R. (2008a). Phosphofructokinase Type 1 Kinetics, Isoform Expression, and Gene Polymorphisms in Cancer Cells. *Antimicrobial Agents and Chemotherapy*, *52*(3), 875–882. https://doi.org/10.1128/AAC.00642-07

Lanteri, C. A., Tidwell, R. R., & Meshnick, S. R. (2008b). The mitochondrion is a site of trypanocidal action of the aromatic diamidine DB75 in bloodstream forms of Trypanosoma brucei. *Antimicrobial Agents and Chemotherapy*, *52*(3), 875–882. https://doi.org/10.1128/AAC.00642-07

López, C., Chevalier, N., Hannaert, V., Rigden, D. J., Michels, P. a. M., & Ramirez, J. L. (2002). Leishmania donovani phosphofructokinase. *European Journal of Biochemistry*, *269*, 3978–3989. https://doi.org/10.1046/j.1432-1033.2002.03086.x

Lowry, O. H., Carter, J., Ward, J. B., & Glaser, L. (1971). The effect of carbon and nitrogen sources on the level of metabolic intermediates in *Escherichia coli*. *Journal of Biological Chemistry*, *246*(21), 6511–6521. https://doi.org/10.1007/s13213-011-0241-6

MacGregor, P., Savill, N. J., Hall, D., & Matthews, K. R. (2011). Transmission stages dominate trypanosome within-host dynamics during chronic infections. *Cell Host and Microbe*, *9*(4), 310–318. https://doi.org/10.1016/j.chom.2011.03.013

Marr, J. J., & Docampo, R. (1986). Chemotherapy for Chagas' disease: a perspective of current therapy and considerations for future research. *Reviews of Infectious Diseases*, *8*(6), 884–903.

Martinez-Oyanedel, J., McNae, I. W., Nowicki, M. W., Keillor, J. W., Michels, P. a M., Fothergill-Gilmore, L. a, & Walkinshaw, M. D. (2007). The first crystal structure of phosphofructokinase from a eukaryote: Trypanosoma brucei. *Journal of Molecular Biology*, *366*(4), 1185–98. https://doi.org/10.1016/j.jmb.2006.10.019

Masocha, W., Rottenberg, M. E., & Kristensson, K. (2007). Migration of African trypanosomes across the blood-brain barrier. *Physiology and Behavior*, *92*(1–2), 110–114. https://doi.org/10.1016/j.physbeh.2007.05.045

Matthews, K. R. (2005). The developmental cell biology of Trypanosoma brucei. *Journal of Cell Science*, *118*(2), 283–290. https://doi.org/10.1242/jcs.01649

Maxmen, A. (2017). Sleeping sickness can now be cured with pills. *Nature*, *550*(7677), 441. https://doi.org/10.1038/nature.2017.22856

McConville, M. J., Saunders, E. C., Kloehn, J., & Dagley, M. J. (2015). Leishmania carbon metabolism in the macrophage phagolysosome- feast or famine? [version 1; referees: 3 approved]. *F1000Research*, *4*(938). https://doi.org/10.12688/f1000research.6724.1

Mclintock, L. M. L., Turner, C. M. R., & Vickerman, K. (1993). Comparison of the effects of immune killing mechanisms on. *Parasite Immunology*, *15*, 475–480.

McNae, I., & Martinez-Oyanedel, J. (2009). of ATP-bound Phosphofructokinase from Trypanosoma brucei Reveals Conformational Transitions Different from those of Other Phosphofructokinases. *Journal of Molecular …*, *385*(5), 1519–33. https://doi.org/10.1016/j.jmb.2008.11.047

Mertens, E. (1991). Pyrophosphate-dependent phosphofructokinase, an anaerobic glycolytic enzyme? *FEBS Letters*, *285*(1), 1–5. https://doi.org/10.1016/0014-5793(91)80711-B

Michels, P. A. M., Bringaud, F., Herman, M., & Hannaert, V. (2006). Metabolic functions of glycosomes in trypanosomatids, *1763*, 1463–1477. https://doi.org/10.1016/j.bbamcr.2006.08.019

Michels, P. a, Chevalier, N., Opperdoes, F. R., Rider, M. H., & Rigden, D. J. (1997). The glycosomal ATP-dependent phosphofructokinase of Trypanosoma brucei must have evolved from an ancestral pyrophosphate-dependent enzyme. *European Journal of Biochemistry / FEBS*, *250*, 698–704.

Morrison, L. J., Vezza, L., Rowan, T., & Hope, J. C. (2016a). Animal African Trypanosomiasis : Time to Increase Focus on Clinically Relevant Parasite and Host Species. *Trends in Parasitology*, *xx*, 1–9. https://doi.org/10.1016/j.pt.2016.04.012

Morrison, L. J., Vezza, L., Rowan, T., & Hope, J. C. (2016b). Animal African Trypanosomiasis : Time to Increase Focus on Clinically Relevant Parasite and Host Species. *Trends in Parasitology*, *xx*, 1–9. https://doi.org/10.1016/j.pt.2016.04.012

Munday, J. C., Eze, A. A., Baker, N., Glover, L., Clucas, C., Aguinaga Andrés, D., … De Koning, H. P. (2014). Trypanosoma brucei aquaglyceroporin 2 is a high-affinity transporter for pentamidine and melaminophenyl arsenic drugs and the main genetic determinant of resistance to these drugs. *Journal of Antimicrobial Chemotherapy*, *69*(3), 651–663. https://doi.org/10.1093/jac/dkt442

Nakayama, Y., Kinoshita, A., & Tomita, M. (2005). Dynamic simulation of red blood cell metabolism and

its application to the analysis of a pathological condition. *Theoretical Biology & Medical Modelling*, *2*, 18. https://doi.org/10.1186/1742-4682-2-18

Nowicki, M. W., Tulloch, L. B., Worralll, L., McNae, I. W., Hannaert, V., Michels, P. a M., … Turner, N. J. (2008). Design, synthesis and trypanocidal activity of lead compounds based on inhibitors of parasite glycolysis. *Bioorganic and Medicinal Chemistry*, *16*, 5050–5061. https://doi.org/10.1016/j.bmc.2008.03.045

Nwagwu, M., & Opperdoes, F. R. (1982). Regulation of glycolysis in Trypanosoma brucei: hexokinase and phosphofructokinase activity. *Acta Tropica*, *39*(1), 61–72.

Obach, R. S. (1999). Prediction of human clearance of twenty-nine drugs from hepatic microsomal intrinsic clearance data: An examination of in vitro half-life approach and nonspecific binding to microsomes. *Drug Metabolism and Disposition*, *27*(11), 1350–1359. https://doi.org/10.1124/dmd.30.7.831

Pepin, J., & Milord, F. (1994). The treatment of human African trypanosomiasis. *Advances in Parasitology*, *33*, 1–47.

Perozzo, R., Folkers, G., & Scapozza, L. (2004a). Thermodynamics of Protein–Ligand Interactions: History, Presence, and Future Aspects. *Journal of Receptors and Signal Transduction*, *24*(1–2), 1–52. https://doi.org/10.1081/RRS-120037896

Perozzo, R., Folkers, G., & Scapozza, L. (2004b). Thermodynamics of Protein–Ligand Interactions: History, Presence, and Future Aspects. *Journal of Receptors and Signal Transduction*, *24*(1–2), 1–52. https://doi.org/10.1081/RRS-120037896

Pollastri, M. P. (2017). Fexinidazole: A New Drug for African Sleeping Sickness on the Horizon. *Trends in Parasitology*, *34*(3), 178–179. https://doi.org/10.1016/j.pt.2017.12.002

Price, N., & Nairn, J. (2009). *Exploring Proteins*. Oxford University Press.

Rafael Moreno-Sa´nchez,* Alvaro Marı´n-Herna´ndez, J. C. G.-P., & He´ctor Quezada, Rusely Encalada, Sara Rodrı´guez-Enrı´quez, and E. S. (2012). Cellular Biochemistry. *Cellular Biochemistry*, *1703*(1), 1692–1703. https://doi.org/10.1002/jcb.24039

Richardson, J. B., Lee, K., Mireji, P., Enyaru, J., Sistrom, M., Aksoy, S., … Caccone, A. (2017). Genomic analyses of African Trypanozoon strains to assess evolutionary relationships and identify markers for strain identification, 1–16.

Rider, M. H., Bertrand, L., Vertommen, D., Michels, P. A., Rousseau, G. G., & Hue, L. (2004). with a bifunctional enzyme that controls glycolysis, *579*, 561–579.

Rodríguez, E., Lander, N., & Ramirez, J. L. (2009). Molecular and biochemical characterisation of Trypanosoma cruzi phosphofructokinase, *104*(June), 745–748.

Schirmer, T., & Evans, P. R. (1990). Structural basis of the allosteric behaviour of phosphofructokinase. *Nature*, *343*, 140–145. https://doi.org/10.1038/343140a0

Schöneberg, T., Kloos, M., Brüser, A., Kirchberger, J., & Sträter, N. (2013). Structure and allosteric regulation of eukaryotic 6-phosphofructokinases. *Biological Chemistry*, *394*(8), 977–93. https://doi.org/10.1515/hsz-2013-0130

Schuster, R., & Holzhütter, H. G. (1995). Use of mathematical models for predicting the metabolic effect of large-scale enzyme activity alterations. Application to enzyme deficiencies of red blood cells. *European Journal of Biochemistry / FEBS*, *229*, 403–418. https://doi.org/10.1111/j.1432-1033.1995.0403k.x

Seyfang, a, & Duszenko, M. (1991). Specificity of glucose transport in Trypanosoma brucei. Effective inhibition by phloretin and cytochalasin B. *European Journal of Biochemistry / FEBS*, *202*, 191–196.

Silvester, E., McWilliam, K., & Matthews, K. (2017). The Cytological Events and Molecular Control of Life

Cycle Development of Trypanosoma brucei in the Mammalian Bloodstream. *Pathogens*, *6*(3), 29. https://doi.org/10.3390/pathogens6030029

Sirimulla, S., Bailey, J. B., Vegesna, R., & Narayan, M. (2013). Halogen Interactions in Protein − Ligand Complexes: Implications of Halogen Bonding for Rational Drug Design.

Stich, A., Abel, P. M., & Krishna, S. (2002). Human African Trypanosomiasis. *British Medical Journal*, *325*(July), 203–6. https://doi.org/10.1136/bmj.325.7357.203

T. Wybranowski, M. Cyrankiewicz, B. Ziomkowska, S. K. (2008). The HSA affinity of warfarin and flurbiprofen determined by fluorescence anisotropy measurements of camptothecin. *Biosystems*, *94*(3), 258–262. https://doi.org/10.1016/J.BIOSYSTEMS.2008.05.034

Tanowitz, H. B., Scherer, P. E., Mota, M. M., & Figueiredo, L. M. (2017). Adipose Tissue: A Safe Haven for Parasites? *Trends in Parasitology*, *33*(4), 276–284. https://doi.org/10.1016/j.pt.2016.11.008

Taylor, J. E., & Rudenko, G. (2006). Switching trypanosome coats: what's in the wardrobe? *Trends in Genetics*, *22*(11), 614–620. https://doi.org/10.1016/j.tig.2006.08.003

Teusink, B., Walsh, M. C., Van Dam, K., & Westerhoff, H. V. (1998). The danger of metabolic pathways with turbo design. *Trends in Biochemical Sciences*, *23*(98), 162–169. https://doi.org/10.1016/S0968-0004(98)01205-5

Trindade, S., Rijo-Ferreira, F., Carvalho, T., Pinto-Neves, D., Guegan, F., Aresta-Branco, F., … Figueiredo, L. M. (2016). Trypanosoma brucei Parasites Occupy and Functionally Adapt to the Adipose Tissue in Mice. *Cell Host & Microbe*, 1–12. https://doi.org/10.1016/j.chom.2016.05.002

Urich, R., Luksch, T., Frearson, J. A., Brenk, R., & Wyatt, P. G. (2014). The Design and Synthesis of Potent and Selective Inhibitors of Trypanosoma brucei Glycogen Synthase Kinase 3 for the Treatment of Human African Trypanosomiasis.

Van Bogaert, I., & Haemers, A. (1989). Eflornithine. A new drug in the treatment of sleeping sickness. *Pharmaceutisch Weekblad. Scientific Edition*, *11*(3), 69–75.

Verlinde, C. L., Hannaert, V., Blonski, C., Willson, M., Périé, J. J., Fothergill-Gilmore, L. a, … Michels, P. a. (2001). Glycolysis as a target for the design of new anti-trypanosome drugs. *Drug Resistance Updates : Reviews and Commentaries in Antimicrobial and Anticancer Chemotherapy*, *4*(1), 50–65. https://doi.org/10.1054/drup.2000.0177

Vickerman, K. (1978). Antigenic variation in trypanosomes. *Nature Parasitology Supp.*, *273*, 613–617.

Vincent, I. M., Creek, D., Watson, D. G., Kamleh, M. a., Woods, D. J., Wong, P. E., … Barrett, M. P. (2010). A molecular mechanism for eflornithine resistance in African trypanosomes. *PLoS Pathogens*, *6*(11), 1–9. https://doi.org/10.1371/journal.ppat.1001204

Wear, M. ., Blackburn, L., & Nowicki, M. . (2009a). What is SPR? Retrieved May 1, 2017, from http://ctcb.bio.ed.ac.uk/CTCB/SPR_-_BIAcore_T200.html

Wear, M. ., Blackburn, L., & Nowicki, M. . (2009b). What is SPR?

Wear, M. A., Nowicki, M. W., Blackburn, E. A., McNae, I. W., & Walkinshaw, M. D. (2017). Thermo-kinetic analysis space expansion for cyclophilin-ligand interactions – identification of a new nonpeptide inhibitor using Biacore™ T200. *FEBS Open Bio*, *7*(4), 533–549. https://doi.org/10.1002/2211-5463.12201

Wear, M. a., & Walkinshaw, M. D. (2006). Thermodynamics of the cyclophilin-A/cyclosporin-A interaction: A direct comparison of parameters determined by surface plasmon resonance using Biacore T100 and isothermal titration calorimetry. *Analytical Biochemistry*, *359*, 285–287. https://doi.org/10.1016/j.ab.2006.08.038

Webb, B. a., Forouhar, F., Szu, F.-E., Seetharaman, J., Tong, L., & Barber, D. L. (2015). Structures of human phosphofructokinase-1 and atomic basis of cancer-associated mutations. *Nature*.

https://doi.org/10.1038/nature14405

Wiedemar, N., Graf, F. E., Zwyer, M., Ndomba, E., Renggli, C. K., Cal, M., … Mäser, P. (2017). Beyond immune escape: A variant surface glycoprotein causes suramin resistance in *Trypanosoma brucei*. *Molecular Microbiology*, *0*. https://doi.org/10.1111/mmi.13854

Wilkinson, S. R., Taylor, M. C., Horn, D., Kelly, J. M., & Cheeseman, I. (2008). A mechanism for cross-resistance to nifurtimox and benznidazole in trypanosomes. *Proceedings of the National Academy of Sciences of the United States of America*, *105*(13), 5022–5027. https://doi.org/10.1073/pnas.0711014105

Wishart, D. S., Lewis, M. J., Morrissey, J. A., Flegel, M. D., Jeroncic, K., Xiong, Y., … Li, L. (2008). The human cerebrospinal fluid metabolome. *Journal of Chromatography B*, *871*(2), 164–173. https://doi.org/https://doi.org/10.1016/j.jchromb.2008.05.001

Wittinghofer, A. (1997). Signaling mechanistics: aluminum fluoride for molecule of the year. *Current Biology : CB*, *7*(11), R682-5. https://doi.org/10.1016/S0960-9822(06)00355-1

Yaginuma, H., Kawai, S., Tabata, K. V., Tomiyama, K., Kakizuka, A., Komatsuzaki, T., … Imamura, H. (2015). Diversity in ATP concentrations in a single bacterial cell population revealed by quantitative single-cell imaging. *Scientific Reports*, *4*(1), 6522. https://doi.org/10.1038/srep06522

Yang, Q., & Hou, P. (2017). Targeting PFKFB3 in the Endothelium for Cancer Therapy, *23*(3), 197–200. https://doi.org/10.1016/j.molmed.2017.01.008

Yernaux, C., Fransen, M., Brees, C., Stephan Lorenzen, L., & Michels, P. A. M. (2006). Trypanosoma brucei glycosomal ABC transporters: identification and membrane targeting. *Molecular Membrane Biology*, *23*(2), 157–172. https://doi.org/10.1080/09687860500460124

Yun, O., Priotto, G., Tong, J., Flevaud, L., & Chappuis, F. (2010). NECT is next: Implementing the new drug combination therapy for trypanosoma brucei gambiense sleeping sickness. *PLoS Neglected Tropical Diseases*, *4*(5). https://doi.org/10.1371/journal.pntd.0000720

Zhang, Chung, & Oldenburg. (1999). A Simple Statistical Parameter for Use in Evaluation and Validation of High Throughput Screening Assays. *Journal of Biomolecular Screening*. https://doi.org/10.1177/108705719900400206

Zikova, A., Verner, Z., Nenarokova, A., Michels, P., & Lukes, J. (2017). A paradigm shift : the mitoproteomes of procyclic and bloodstream Trypanosoma brucei are comparably complex. *PLoSPathogens*, 1–14.

Zwaig, N., & Lin, E. C. (1966). Feedback inhibition of glycerol kinase, a catabolic enzyme in Escherichia coli. *Science (New York, N.Y.)*, *153*(737), 755–757. https://doi.org/10.1126/science.153.3737.755